

## ABSTRACT

Title of dissertation:      STUDIES OF  $B_s$  PRODUCTION AND  
SEMILEPTONIC DECAY, AND OF  
ANTIDEUTERON PRODUCTION IN  
 $\Upsilon$  DECAY AND QUARK  
FRAGMENTATION AT *BABAR*

Brian Hamilton, Doctor of Philosophy, 2012

Dissertation directed by:   Professor Abolhassan Jawahery  
Department of Physics

I present a measurement of the inclusive semileptonic branching fraction of the  $B_s$  meson and  $B_s$  production rates relative to all  $B$  mesons using a data set collected with the *BABAR* detector at the PEP-II asymmetric energy electron-positron collider operating at center-of-mass energies above the  $\Upsilon(4S)$  resonance. The quantities are extracted simultaneously using inclusive yields of  $\phi$  mesons and  $\phi$  mesons in coincidence with a high momentum lepton. The  $B_s$  semileptonic branching fraction is found to be  $\mathcal{B}(B_s \rightarrow \ell\nu X) = 9.5_{-2.0}^{+2.5+1.1}$ , where the first uncertainty is statistical and the second is systematic. Additionally, I present measurements of antideuteron production using the *BABAR* data collected at collision center-of-mass energies corresponding to the masses of the  $\Upsilon(2S)$ ,  $\Upsilon(3S)$ , and  $\Upsilon(4S)$  resonances. Measurements of specific ionization for charged tracks in the *BABAR* detector are used to obtain the antideuteron production rate in decays of the  $\Upsilon(1S)$ ,  $\Upsilon(2S)$ , and  $\Upsilon(3S)$  resonances as well as in continuum  $e^+e^-$  annihilation to hadrons. The total rates observed

in the data are  $\mathcal{B}(\Upsilon(2S) \rightarrow \bar{d}X) = (2.62 \pm 0.10_{-0.28}^{+0.31}) \times 10^{-5}$ ,  $\mathcal{B}(\Upsilon(1S) \rightarrow \bar{d}X) = (2.85 \pm 0.47_{-0.29}^{+0.21}) \times 10^{-5}$ ,  $\mathcal{B}(\Upsilon(3S) \rightarrow \bar{d}X) = (2.45 \pm 0.14_{-0.24}^{+0.27}) \times 10^{-5}$ , and the cross section for antideuteron production in continuum  $e^+e^-$  annihilation is found to be  $\sigma(e^+e^-(10.58 \text{ GeV}) \rightarrow \bar{d}X) = (10.49 \pm 0.33_{-1.14}^{+1.28}) \text{ fb}$ . No significant production in  $\Upsilon(4S)$  decays is observed.

STUDIES OF  $B_s$  PRODUCTION AND SEMILEPTONIC DECAY,  
AND OF ANTIDEUTERON PRODUCTION IN  $\Upsilon$  DECAY AND  
QARK FRAGMENTATION AT *BABAR*

by

Brian Keith Hamilton

Dissertation submitted to the Faculty of the Graduate School of the  
University of Maryland, College Park in partial fulfillment  
of the requirements for the degree of  
Doctor of Philosophy  
2012

Advisory Committee:  
Professor Abolhassan Jawahery, Chair/Advisor,  
Associate Professor Zackaria Chacko,  
Professor Michael Coplan,  
Professor Nick Hadley,  
Associate Professor Douglas Roberts

© Copyright by  
Brian Keith Hamilton  
2012

## Acknowledgments

Many pages could be spent detailing all the people who, by their support, advice, or comments, have helped make this work possible. Here instead I will try to be brief and mention those those who have made the most direct contributions, with sincere apologies to everyone else. First among those who made this possible is of course my advisor, Hassan Jawahery, who has provided both the opportunity for this work to be done and guidance throughout my experience at UMD.

Thanks also to those who have been a part of the MD *BABAR* group during my time conducting this research: Doug Roberts, Ed Behn, Riccardo Cenci, Gabrielle Simi, and Elizabeth Twedt, who have been invaluable as a source of discussion, commentary, advice and guidance. Doug and Gabrielle in particular provided much assistance in my transition into the world of experimental particle physics. Riccardo's experience proved invaluable to the second measurement described here, which would have taken substantially longer without his collaboration.

I also wish to thank the *BABAR* community at large for much of the groundwork which has made the work presented here possible. In addition they provided much helpful advice and insightful discussion stemming from the parallel talks and reviews centered on the analyses presented herein.

More personally, I would like to extend thanks to my family for their support and encouragement as I went off to pursue my passions in graduate school. And finally, thanks to my wife, whose support has kept me going throughout my years here. I do not know how I could have persevered without her to lean on.

# Table of Contents

List of Tables	vi
List of Figures	vii
1 Introduction	1
2 Physics at Flavor Factories	4
2.1 The Standard Model . . . . .	4
2.1.1 Matter fields . . . . .	4
2.1.2 Gauge sector . . . . .	6
2.1.3 Electroweak symmetry breaking and the CKM matrix . . . . .	7
2.1.4 Physics of hadrons . . . . .	9
2.1.5 $B$ Physics . . . . .	11
2.2 Physics Beyond the Standard Model . . . . .	14
3 The <i>BABAR</i> Experiment	17
3.1 PEP-II . . . . .	17
3.2 Detector . . . . .	18
3.2.1 Tracking . . . . .	19
3.2.2 Calorimetry . . . . .	24
3.2.3 Dedicated particle identification . . . . .	25
3.2.4 Instrumented Flux Return (IFR) . . . . .	27
3.2.5 Trigger . . . . .	29
3.3 Event Reconstruction and Data Analysis . . . . .	31
3.3.1 Reconstruction . . . . .	32
3.3.2 Simulation . . . . .	35
3.4 The <i>BABAR</i> Dataset . . . . .	37
4 Measurement of $\mathcal{B}(B_s \rightarrow \ell\nu X)$	40
4.1 Analysis Technique Overview . . . . .	41
4.2 Analysis Method . . . . .	44
4.2.1 Event Selection . . . . .	46
4.2.2 Inclusive $\phi$ reconstruction and $\phi$ -lepton selection . . . . .	47
4.2.3 Below-threshold Subtraction . . . . .	54
4.2.4 Extraction of $f_s$ and $\mathcal{B}(B_s \rightarrow \ell\nu X)$ . . . . .	55
4.3 Consistency Checks and Validation . . . . .	62
4.3.1 Validation of Continuum Subtraction . . . . .	62
4.3.2 Simulation Study of a Pure $B_s$ Samples . . . . .	62
4.3.3 Analysis on $e$ and $\mu$ Event Samples . . . . .	63
4.3.4 Effect of Multibody $B\bar{B}n\pi$ Events . . . . .	64
4.4 Estimates of Systematic Uncertainties . . . . .	65
4.5 Results . . . . .	69

5	Measurement of Antideuteron Production	74
5.1	Previous Work	75
5.2	Analysis Technique Overview	75
5.3	Track Selection	76
5.4	dEdxCombPull	79
5.5	Efficiency Correction	82
5.5.1	Trigger/Filter Efficiency	83
5.5.2	Geometric Acceptance	83
5.5.3	Reconstruction Efficiency	87
5.5.4	Annihilation in Material	90
5.6	Determination of Antideuteron Differential Yields	92
5.6.1	CM Momentum Bins	92
5.6.2	Fit shapes	93
5.6.3	Fit Strategy	95
5.6.4	Fit Validation	99
5.6.5	On/Off Subtraction	99
5.6.6	Determination of Differential Rates	102
5.6.7	Determination of Total Rate	105
5.7	Systematic Uncertainties	107
5.7.1	Fit Biases	108
5.7.2	Statistical Uncertainty in Simulated Datasets	108
5.7.3	Acceptance Fraction	109
5.7.4	Annihilation Fraction	109
5.7.5	Event Filter	110
5.7.6	Reconstruction and Selection Efficiency	110
5.7.7	Background Shape	114
5.7.8	Fake Antideuterons	114
5.7.9	Total Rate	117
5.8	Summary and Final Results	117
6	Conclusions and Future Prospects	127
A	Results of $\phi$ Yield Fits	130
A.1	$\phi$	130
A.2	$\phi$ -lepton	138
B	Results of Antideuteron Yield Fits	146
B.1	$\Upsilon(2S)$	146
B.1.1	$\Upsilon(2S)$ on-resonance negative tracks	146
B.1.2	$\Upsilon(2S)$ on-resonance positive tracks	148
B.1.3	$\Upsilon(2S)$ off-resonance negative tracks	150
B.1.4	$\Upsilon(2S)$ off-resonance positive tracks	152
B.2	$\Upsilon(3S)$	154
B.2.1	$\Upsilon(3S)$ on-resonance negative tracks	154
B.2.2	$\Upsilon(3S)$ on-resonance positive tracks	156

B.2.3	$\Upsilon(3S)$ off-resonance negative tracks . . . . .	158
B.2.4	$\Upsilon(3S)$ off-resonance positive tracks . . . . .	160
B.3	$\Upsilon(4S)$ and Continuum . . . . .	162
B.3.1	$\Upsilon(4S)$ and Continuum on-resonance negative tracks . . . . .	162
B.3.2	$\Upsilon(4S)$ and Continuum on-resonance positive tracks . . . . .	164
B.3.3	$\Upsilon(4S)$ and continuum off-resonance negative tracks . . . . .	166
B.3.4	$\Upsilon(4S)$ and continuum off-resonance positive tracks . . . . .	168
B.4	$\Upsilon(1S)$ . . . . .	170
B.4.1	$\Upsilon(1S)$ signal region negative tracks . . . . .	170
B.4.2	$\Upsilon(1S)$ signal region positive tracks . . . . .	171
B.4.3	$\Upsilon(1S)$ sideband negative tracks . . . . .	172
B.4.4	$\Upsilon(1S)$ sideband positive tracks . . . . .	173

Bibliography		174
--------------	--	-----

## List of Tables

2.1	Some of the key parameters in the $B$ meson systems as of the 2010 edition of the Review of Particle Physics. The mass and lifetime averages for the lighter $B$ s are dominated by hadron collider measurements, while the mass splitting and semileptonic branching fractions are dominated by $B$ factory measurements. . . . .	13
3.1	Signal events generated and run conditions used for deuteron simulation	36
3.2	$BABAR$ Runs 1-6 summary . . . . .	37
3.3	$BABAR$ $\Upsilon$ running summary . . . . .	38
4.1	Event selection criteria. * Total energy is computed assuming the pion mass for charged tracks. As in Sec. 3.3.1Reconstructionsubsection.3.3.1, $p_n$ refers to the $n$ th highest momentum track found in the event. . . .	46
4.2	Relative multiplicative and additive systematic uncertainties for the measurement of $\mathcal{B}(B_s \rightarrow \ell\nu X)$ . . . . .	66
5.1	Event filter efficiency in each period of $\Upsilon(4S)$ running . . . . .	84
5.2	Nominal fit parameters. The columns give the name of the variable, a brief description, and whether or not the variable is “split” across the various categories listed. The possible categories that variables may be split over are the charge of the track, whether it comes from on or off-resonance data, and which of the $n_{\text{bins}}$ bins of deuteron $p_{\text{CM}}$ it belongs to. Some exist only in particular categories, and those are indicated as such rather than split or no split. . . . .	97
5.3	Differential rates and associated uncertainties in $\Upsilon(2S)$ decay. Uncertainties are given as a percent of the measured yield. . . . .	122
5.4	Differential rates and associated uncertainties in $\Upsilon(3S)$ decay. Uncertainties are given as a percent of the measured yield. . . . .	123
5.5	Differential rates and associated uncertainties in $\Upsilon(1S)$ decay measured via the $\Upsilon(2S) \rightarrow \pi^+\pi^-\Upsilon(1S)$ transition. Uncertainties are given as a percent of the measured yield. . . . .	124
5.6	Differential rates and associated uncertainties in $\Upsilon(4S)$ decay. Uncertainties are given as a percent of the measured yield. . . . .	125
5.7	Differential rates and associated uncertainties in continuum $e^+e^-$ annihilation. Uncertainties are given as a percent of the measured yield.	126
6.1	Antideuteron total production rate results in $\Upsilon(1S, 2S, 3S)$ decay and continuum $e^+e^-$ annihilation . . . . .	128

## List of Figures

1.1	Cross section for $e^+e^- \rightarrow$ hadrons at CESR in the 10 GeV region of center-of-mass energy. From the Annual Review of Nuclear and Particle Science, vol 43 [1] . . . . .	2
2.1	Lowest-order diagrams describing neutral meson oscillations in the $B^0$ system. . . . .	10
2.2	General structure of internal (right) and external (left) spectator diagrams. The color-singlet nature of the initial state tends to suppress internal diagrams. The products of the virtual $W$ in these graphs may be a lepton-neutrino pair or a quark ( $q$ ) antiquark ( $\bar{q}'$ ) pair. . . .	11
2.3	Level diagrams of the $b\bar{b}$ bound states showing the $B\bar{B}$ threshold. From the 2012 Review of Particle Physics [12] . . . . .	12
3.1	Section of the <i>BABAR</i> detector transverse to the beam axis. The labelled height is given in mm. The acronyms are defined in the following sections. . . . .	19
3.2	SVT structure . . . . .	20
3.3	Diagram showing a single Drift Chamber (DCH) superlayer. . . . .	22
3.4	Measurement of $dE/dx$ (in arbitrary units) vs track momentum in the DCH. The curves are the Bethe-Bloch predictions derived from control samples. . . . .	23
3.5	Cutaway view of half of the EMC with dimensions labelled in mm. Note the asymmetric layout with larger coverage in the direction of the boost. . . . .	24
3.6	Diagram of the DIRC showing the basic principle of operation . . . .	26
3.7	Layout of the RPCs in the flux return. . . . .	28
3.8	The deviation of the track parameters from separate fits to each half of cosmic ray muon tracks. The parameters shown are the distance of closest approach in the transverse plane ( $d_0$ ), the direction in that plane $\Phi_0$ , and the distance of closest approach along the detector axis ( $z_0$ ), as well as the dip angle $\lambda$ . The width of the distributions give the resolution on these parameters as determined by the reconstruction code. . . . .	33
3.9	Measurement of $R_b$ in the FinalScan dataset from [31] . . . . .	39
4.1	One possible spectator decay chain leading to $\phi$ production in $B_s$ decay. $X_1$ and $X_2$ may be any of the possible products of the $b \rightarrow c$ transition. . . . .	43

4.2	Two possible sets of spectator diagrams for $\phi$ production in $B$ decay. The first process is suppressed both by the number of final states accessible to the virtual $W$ and also kinematically due to the pair of charm quarks in the final state, while the second process involves a color-suppressed $D$ decay. Note also that in contrast to the fully-inclusive systems $X_1$ and $X_2$ in Fig. 4.1 One possible spectator decay chain leading to $\phi$ production in $B_s$ decay. $X_1$ and $X_2$ may be any of the possible products of the $b \rightarrow c$ transition figure.4.1, both processes involve an exclusive process at the quark level. . . . .	43
4.3	$\tilde{R}_b$ and $\tilde{f}_s$ for FinalScan mixed simulation sample . . . . .	45
4.4	MultiHadron selection efficiencies as a function of center-of-mass (CM) energy in simulated (a) $B_s^{(*)}\bar{B}_s^{(*)}$ events, (b) $B\bar{B}$ events, (c) continuum events. . . . .	48
4.5	A chart of the parent of selected leptons in $B_s\bar{B}_s$ simulation events . . . . .	49
4.6	Invariant mass distribution of $\phi \rightarrow K^+K^-$ candidates in (a) the $\phi$ sample and (b) the $\phi$ -lepton sample in the CM energy bin $10.8275 \text{ GeV} \leq E_{\text{CM}} \leq 10.8425 \text{ GeV}$ . The background shape is shown by the dashed curve and the total fit by the solid curve. . . . .	50
4.7	$\phi$ counting efficiency in simulated (a) $B_s^{(*)}\bar{B}_s^{(*)}$ events, (b) $B\bar{B}$ events, (c) continuum events. . . . .	52
4.8	$\phi$ -lepton efficiency running in simulated (a) $B\bar{B}$ events and (b) continuum events. These quantities are not normalized as true efficiencies as only their ratios at different energies are used. . . . .	53
4.9	(a) $\phi$ -lepton efficiency in events with one semileptonic $B_s$ decay, (b) $\phi$ -lepton efficiency in events with both $B_s$ mesons decaying semileptonically, (c) the lepton selection efficiency (per track) for leptons from charm decays, (d) $\phi$ efficiency in events in which a lepton was found but neither $B_s$ decayed semileptonically . . . . .	54
4.10	Result of $f_s$ extraction in FinalScan mixed simulation. The blue histogram is the true value and the red points with error bars are the analysis output. . . . .	58
4.11	$\chi^2$ vs $\mathcal{B}(B_s \rightarrow \ell\nu X)$ in the mixed simulation sample. Note the asymmetric character of the minimum. The value of $\mathcal{B}(B_s \rightarrow \ell\nu X)$ used in simulation is 9.3% . . . . .	61
4.12	$udsc$ -only sample after subtraction. . . . .	63
4.13	$f_s$ calculated in a sample of only $B_s$ events. . . . .	64
4.14	Relative (top) event, (center) $\phi$ and (bottom) $\phi$ -lepton yields, normalized to the $\mu^+\mu^-$ yields. Corrections for detector efficiency have not been applied. The dotted vertical line indicates the $B_s$ production threshold. Note the greater prominence of the $\Upsilon(10860)$ peak in the $\phi$ and $\phi$ -lepton yields compared with the MultiHadronic yield. . . . .	70

4.15	(a) $f_s$ result in data. Black (inner) error bars are statistical errors, blue (outer) error bars are statistical errors added in quadrature with systematic errors. (b) $\chi^2$ as a function of $\mathcal{B}(B_s \rightarrow \ell\nu X)$ . Note the asymmetric character of the minimum. . . . .	72
4.16	Predictions in a coupled-channel analysis (taken from Ref. [33]) for (a) the contribution to $R$ from the various $B$ meson thresholds and (b) the contributions from production of each of the states $B\bar{B}$ , $B\bar{B}^*$ , $B^*\bar{B}$ , $B^*\bar{B}^*$ , $B_s\bar{B}_s$ , $B_s^*\bar{B}_s$ , $B_s\bar{B}_s^*$ and $B_s^*\bar{B}_s^*$ . For comparison, the <i>BABAR</i> results for (c) $R_b$ and (d) $f_s$ are shown beside the predictions. Note that the predictions only extend out to 10.9 GeV while the measurements extend to 11.2 GeV . . . . .	73
5.1	Track momentum vs $dE/dx$ in the drift chamber for positive tracks in a subset of data. Note that deuterons appear well-separated between 500 MeV and 1.5 GeV . . . . .	77
5.2	dEdxCombPull distribution with cut on number of samples in the DCH (filled circles) and before the cut (open circles) for comparison. The data sample used here are positive tracks from the $\Upsilon(4S)$ dataset. The deuteron peak is clear near zero, and at higher values of the $dE/dx$ residual we see another peak, likely from tritons. . . . .	79
5.3	The distribution of the number of photons in the DIRC best-fit ring for simulated primary deuterons (the red histogram peaking near 1) and simulated generic $\Upsilon(2S)$ decay tracks (the blue histogram peaking near 20, with a small peak near 4). The relative scaling between the two distributions is arbitrary. . . . .	80
5.4	dEdxCombPull (blue) compared to dEdxDchPull (black) and dEdxSvtPull (red) for positive tracks. Note the improvements in the background around the deuteron and triton peaks. . . . .	81
5.5	Geometrical acceptance fractions using the $\Upsilon(2S)$ (black) and the $\Upsilon(3S)$ (blue) boost . . . . .	84
5.6	Generator-level angular distribution of coalescence candidates in light quark fragmentation at $E_{\text{CM}} = m_{\Upsilon(4S)}$ . . . . .	86
5.7	Acceptance fractions for $\Upsilon(4S)$ boost with (black) flat angular distribution, (blue) $1 + \cos^2\theta$ and (red) fitted angular distribution . . . . .	86
5.8	Reconstruction efficiency and uncertainties in $\Upsilon(2S)$ signal Monte Carlo	87
5.9	Reconstruction efficiency and uncertainties in $\Upsilon(4S)$ signal Monte Carlo	89
5.10	Calculated antideuteron reconstruction asymmetry due to annihilation in detector material based on rescaling the corresponding antiproton asymmetry . . . . .	91
5.11	Background shape fit to the $dE/dx$ pull distribution for tracks in generic Monte Carlo at the $\Upsilon(4S)$ . The solid blue line represents the total fit while the dotted yellow and red lines are the exponential and Gaussian components, respectively. . . . .	93
5.12	Distribution of the variable dEdxCombPull for background species in generic Monte Carlo at $\Upsilon(4S)$ . . . . .	95

5.13	The result of a fit of the function in Eq. 5.6Fit shape to the $dE/dx$ pull for simulated deuterons at $E_{\text{CM}} = m_{\Upsilon(4S)}$	96
5.14	Pull distributions from toy study in $\Upsilon(2S)$ data	100
5.15	$\Upsilon(1S)$ $m_{\text{recoil}}$ signal and sideband boundaries. The upper and lower sidebands extend respectively to the low and high borders of the plot.	102
5.16	Results of a fit to the $\Upsilon(1S)$ $m_{\text{Recoil}}$ spectrum, used to obtain the number of $\Upsilon(1S)$ events in the signal region and sidebands.	105
5.17	Result of generator-level coalescence study using a coalescence momentum $p_0 = 160$ MeV fit to a fireball spectrum (Eq. 5.9Determination of Total Rate). See the text for comments on the agreement between the simulated data points and the fitted function.	106
5.18	Number of photons in DIRC for (black circles) positive deuterons in the signal region passing all other selections and for (red triangles) simulated primary deuterons.	111
5.19	Number of $dE/dx$ samples in the Drift Chamber for (black circles) positive deuterons in the signal region passing all other selections and for (red triangles) simulated primary deuterons.	112
5.20	Relative efficiency of the selection on the number of $dE/dx$ samplings in the DCH for data control samples and signal simulation. For most of the parameter space the two are offset by a constant factor.	112
5.21	Ratio of efficiencies of DOCA selection in well-identified antiprotons in data and simulation.	113
5.22	Fits to x-y DOCA distributions in $\Upsilon(4S)$ signal simulation (top) and $\Upsilon(4S)$ data (bottom). In the former, the green and red dotted curves are the Gaussian and Crystal Ball components of the signal shape, while in the latter the red dotted curve is the total signal shape and the purple is the background shape.	116
5.23	Results for differential rate of antideuteron production in (a) $\Upsilon(2S)$ and (b) $\Upsilon(3S)$ decays. The black (inner) error bars show the statistical uncertainty returned from the unbinned fit, while the red (outer) error bars show the sum of the statistical and systematic uncertainty.	119
5.24	Results for differential rate of antideuteron production in $\Upsilon(1S)$ decay from $\Upsilon(2S) \rightarrow \pi^+\pi^-\Upsilon(1S)$ with the previous results from CLEO overlaid as open triangles with dotted error bars. The black (inner) error bars show the statistical uncertainty returned from the unbinned fit, while the red (outer) error bars show the sum of the statistical and systematic uncertainty.	120
5.25	Results for differential rate of antideuteron production in (a) $\Upsilon(4S)$ and (b) continuum. The black (inner) error bars show the statistical uncertainty returned from the unbinned fit, while the red (outer) error bars show the sum of the statistical and systematic uncertainty. We observe no significant production in $\Upsilon(4S)$ decays, as expected.	121

A.1	Fits to $K^+K^-$ invariant mass distributions in the region $E_{\text{CM}} = 10.55 - 10.64$ GeV. The blue curve is the total fit, and the red curve is the background. . . . .	130
A.2	Fits to $K^+K^-$ invariant mass distributions in the region $E_{\text{CM}} = 10.64 - 10.73$ GeV. The blue curve is the total fit, and the red curve is the background. . . . .	131
A.3	Fits to $K^+K^-$ invariant mass distributions in the region $E_{\text{CM}} = 10.73 - 10.82$ GeV. The blue curve is the total fit, and the red curve is the background. . . . .	132
A.4	Fits to $K^+K^-$ invariant mass distributions in the region $E_{\text{CM}} = 10.82 - 10.91$ GeV. The blue curve is the total fit, and the red curve is the background. . . . .	133
A.5	Fits to $K^+K^-$ invariant mass distributions in the region $E_{\text{CM}} = 10.91 - 11.00$ GeV. The blue curve is the total fit, and the red curve is the background. . . . .	134
A.6	Fits to $K^+K^-$ invariant mass distributions in the region $E_{\text{CM}} = 11.00 - 11.09$ GeV. The blue curve is the total fit, and the red curve is the background. . . . .	135
A.7	Fits to $K^+K^-$ invariant mass distributions in the region $E_{\text{CM}} = 11.09 - 11.18$ GeV. The blue curve is the total fit, and the red curve is the background. . . . .	136
A.8	Fits to $K^+K^-$ invariant mass distributions in the region $E_{\text{CM}} = 11.18 - 11.21$ GeV. The blue curve is the total fit, and the red curve is the background. . . . .	137
A.9	Fits to $\phi$ -lepton sample $K^+K^-$ invariant mass distributions in the region $E_{\text{CM}} = 10.55 - 10.64$ GeV. The blue curve is the total fit, and the red curve is the background. . . . .	138
A.10	Fits to $\phi$ -lepton sample $K^+K^-$ invariant mass distributions in the region $E_{\text{CM}} = 10.64 - 10.73$ GeV. The blue curve is the total fit, and the red curve is the background. . . . .	139
A.11	Fits to $\phi$ -lepton sample $K^+K^-$ invariant mass distributions in the region $E_{\text{CM}} = 10.73 - 10.82$ GeV. The blue curve is the total fit, and the red curve is the background. . . . .	140
A.12	Fits to $\phi$ -lepton sample $K^+K^-$ invariant mass distributions in the region $E_{\text{CM}} = 10.82 - 10.91$ GeV. The blue curve is the total fit, and the red curve is the background. . . . .	141
A.13	Fits to $\phi$ -lepton sample $K^+K^-$ invariant mass distributions in the region $E_{\text{CM}} = 10.91 - 11.00$ GeV. The blue curve is the total fit, and the red curve is the background. . . . .	142
A.14	Fits to $\phi$ -lepton sample $K^+K^-$ invariant mass distributions in the region $E_{\text{CM}} = 11.00 - 11.09$ GeV. The blue curve is the total fit, and the red curve is the background. . . . .	143
A.15	Fits to $\phi$ -lepton sample $K^+K^-$ invariant mass distributions in the region $E_{\text{CM}} = 11.09 - 11.18$ GeV. The blue curve is the total fit, and the red curve is the background. . . . .	144

A.16	Fits to $\phi$ -lepton sample $K^+K^-$ invariant mass distributions in the region $E_{\text{CM}} = 11.18 - 11.21$ GeV. The blue curve is the total fit, and the red curve is the background. . . . .	145
B.1	Fit to $\Upsilon(2S)$ $p_{\text{CM}}$ bin 1-6 for on-resonance negative tracks. The blue curve shows the total fit, the red, purple and yellow dotted curves the signal, Gaussian and Exponential components. . . . .	146
B.2	Fit to $\Upsilon(2S)$ $p_{\text{CM}}$ bin 7-9 for on-resonance negative tracks. The blue curve shows the total fit, the red, purple and yellow dotted curves the signal, Gaussian and Exponential components. . . . .	147
B.3	Fit to $\Upsilon(2S)$ $p_{\text{CM}}$ bin 1-6 for on-resonance positive tracks. The blue curve shows the total fit, the red, green, purple and yellow dotted curves the signal, triton, Gaussian and Exponential components. . . .	148
B.4	Fit to $\Upsilon(2S)$ $p_{\text{CM}}$ bin 7-9 for on-resonance positive tracks. The blue curve shows the total fit, the red, green, purple and yellow dotted curves the signal, triton, Gaussian and Exponential components. . . .	149
B.5	Fit to $\Upsilon(2S)$ $p_{\text{CM}}$ bin 1-6 for off-resonance negative tracks. The blue curve shows the total fit, the purple and yellow dotted curves the Gaussian and Exponential components. . . . .	150
B.6	Fit to $\Upsilon(2S)$ $p_{\text{CM}}$ bin 7-9 for off-resonance negative tracks. The blue curve shows the total fit, the red, purple and yellow dotted curves the signal, Gaussian and Exponential components. . . . .	151
B.7	Fit to $\Upsilon(2S)$ $p_{\text{CM}}$ bin 1-6 for off-resonance positive tracks. The blue curve shows the total fit, the red, green, purple and yellow dotted curves the signal, triton, Gaussian and Exponential components. . . .	152
B.8	Fit to $\Upsilon(2S)$ $p_{\text{CM}}$ bin 1-6 for off-resonance positive tracks. The blue curve shows the total fit, the red, green, purple and yellow dotted curves the signal, triton, Gaussian and Exponential components. . . .	153
B.9	Fit to $\Upsilon(3S)$ $p_{\text{CM}}$ bin 1-6 for on-resonance negative tracks. The blue curve shows the total fit, the red, purple and yellow dotted curves the signal, Gaussian and Exponential components. . . . .	154
B.10	Fit to $\Upsilon(3S)$ $p_{\text{CM}}$ bin 7-9 for on-resonance negative tracks. The blue curve shows the total fit, the red, purple and yellow dotted curves the signal, Gaussian and Exponential components. . . . .	155
B.11	Fit to $\Upsilon(3S)$ $p_{\text{CM}}$ bin 1-6 for on-resonance positive tracks. The blue curve shows the total fit, the red, green, purple and yellow dotted curves the signal, triton, Gaussian and Exponential components. . . .	156
B.12	Fit to $\Upsilon(3S)$ $p_{\text{CM}}$ bin 7-9 for on-resonance positive tracks. The blue curve shows the total fit, the red, green, purple and yellow dotted curves the signal, triton, Gaussian and Exponential components. . . .	157
B.13	Fit to $\Upsilon(3S)$ $p_{\text{CM}}$ bin 1-6 for off-resonance negative tracks. The blue curve shows the total fit, the red, purple and yellow dotted curves the signal, Gaussian and Exponential components. . . . .	158

B.14	Fit to $\mathcal{Y}(3S)$ $p_{\text{CM}}$ bin 7-9 for off-resonance negative tracks. The blue curve shows the total fit, the red, purple and yellow dotted curves the signal, Gaussian and Exponential components. . . . .	159
B.15	Fit to $\mathcal{Y}(3S)$ $p_{\text{CM}}$ bin 1-6 for off-resonance positive tracks. The blue curve shows the total fit, the red, green, purple and yellow dotted curves the signal, triton, Gaussian and Exponential components.y . .	160
B.16	Fit to $\mathcal{Y}(3S)$ $p_{\text{CM}}$ bin 1-6 for off-resonance positive tracks. The blue curve shows the total fit, the red, green, purple and yellow dotted curves the signal, triton, Gaussian and Exponential components. . . .	161
B.17	Fit to $\mathcal{Y}(4S)$ data $p_{\text{CM}}$ bin 1-6 for on-resonance negative tracks. The blue curve shows the total fit, the red, purple and yellow dotted curves the signal, Gaussian and Exponential components. . . . .	162
B.18	Fit to $\mathcal{Y}(4S)$ data $p_{\text{CM}}$ bin 7-9 for on-resonance negative tracks. The blue curve shows the total fit, the red, purple and yellow dotted curves the signal, Gaussian and Exponential components. . . . .	163
B.19	Fit to $\mathcal{Y}(4S)$ data $p_{\text{CM}}$ bin 1-6 for on-resonance positive tracks. The blue curve shows the total fit, the red, green, purple and yellow dotted curves the signal, triton, Gaussian and Exponential components. . . .	164
B.20	Fit to $\mathcal{Y}(4S)$ data $p_{\text{CM}}$ bin 7-9 for on-resonance positive tracks. The blue curve shows the total fit, the red, green, purple and yellow dotted curves the signal, triton, Gaussian and Exponential components. . . .	165
B.21	Fit to $\mathcal{Y}(4S)$ data $p_{\text{CM}}$ bin 1-6 for off-resonance negative tracks. The blue curve shows the total fit, the red, purple and yellow dotted curves the signal, Gaussian and Exponential components. . . . .	166
B.22	Fit to $\mathcal{Y}(4S)$ data $p_{\text{CM}}$ bin 7-9 for off-resonance negative tracks. The blue curve shows the total fit, the red, purple and yellow dotted curves the signal, Gaussian and Exponential components. . . . .	167
B.23	Fit to $\mathcal{Y}(4S)$ data $p_{\text{CM}}$ bin 1-6 for off-resonance positive tracks. The blue curve shows the total fit, the red, green, purple and yellow dotted curves the signal, triton, Gaussian and Exponential components. . . .	168
B.24	Fit to $\mathcal{Y}(4S)$ data $p_{\text{CM}}$ bin 1-6 for off-resonance positive tracks. The blue curve shows the total fit, the red, green, purple and yellow dotted curves the signal, triton, Gaussian and Exponential components. . . .	169
B.25	Fit to $\mathcal{Y}(1S)$ $p_{\text{CM}}$ bin 1-6 for negative tracks in the signal region. The blue curve shows the total fit, the red, purple and yellow dotted curves the signal, Gaussian and Exponential components. . . . .	170
B.26	Fit to $\mathcal{Y}(1S)$ $p_{\text{CM}}$ bin 1-6 for positive tracks in the signal region. The blue curve shows the total fit, the red, purple and yellow dotted curves the signal, Gaussian and Exponential components. . . . .	171
B.27	Fit to $\mathcal{Y}(1S)$ $p_{\text{CM}}$ bin 1-6 for negative tracks in the sideband region. The blue curve shows the total fit, the red, purple and yellow dotted curves the signal, Gaussian and Exponential components. . . . .	172
B.28	Fit to $\mathcal{Y}(1S)$ $p_{\text{CM}}$ bin 1-6 for positive tracks in the sideband region. The blue curve shows the total fit, the red, purple and yellow dotted curves the signal, Gaussian and Exponential components. . . . .	173

# Chapter 1

## Introduction

The  $B$ -factory datasets provide an opportunity to explore a vast range of phenomena in the relatively clean environment of  $e^+e^-$  collisions. The center-of-mass energy of the collision is known up to initial state radiative effects and may be tuned to explore processes at different energies and search for rare decay products from different particles and resonances. The cross section for  $e^+e^-$  annihilation to hadrons in the 10 GeV center-of-mass energy region at the Cornell Electron Storage Ring is shown in Figure 1. These features are exploited in this work to measure the  $B_s$  semileptonic fraction  $\mathcal{B}(B_s \rightarrow \ell\nu X)$  and the ratio of inclusive production of  $B_s$  mesons to all  $B$  mesons in the region above the  $\Upsilon(4S)$  resonance. This measurement makes use of a dataset collected with the *BABAR* detector during a scan in  $e^+e^-$  center-of-mass energies from 10.56 GeV to 11.20 GeV in 5 MeV steps. Also presented here is a measurement of antideuteron production in various CM energy regions probed by the *BABAR* experiment.

The measurement of  $\mathcal{B}(B_s \rightarrow \ell\nu X)$  provides a verification of the spectator model for semileptonic decays of heavy flavored mesons. In addition it serves as a valuable input to hadron collider measurements, where  $B_s$  mesons are produced copiously. At these experiments it is difficult to obtain an absolute normalization for branching fraction measurements, and so it is common to measure ratios of

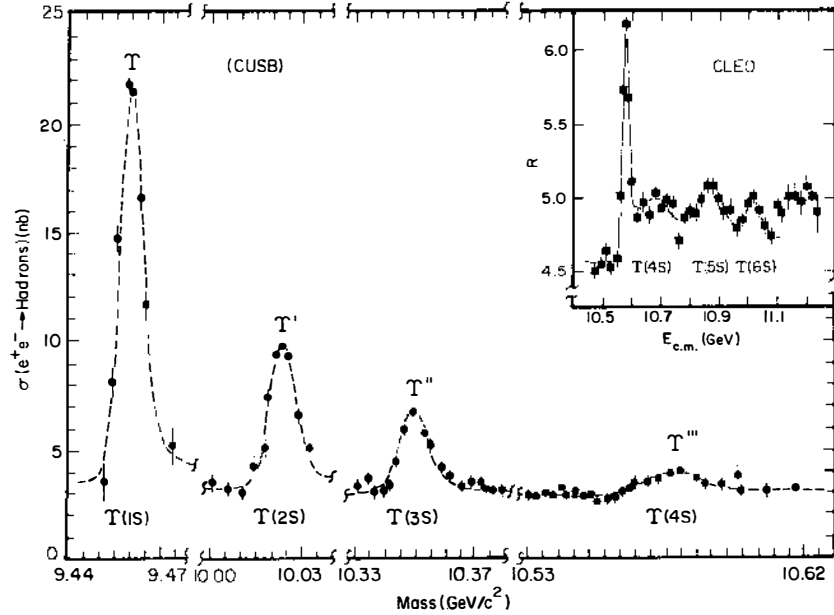


Figure 1.1: Cross section for  $e^+e^- \rightarrow \text{hadrons}$  at CESR in the 10 GeV region of center-of-mass energy. From the Annual Review of Nuclear and Particle Science, vol 43 [1]

branching fractions, allowing the measurement to be normalized to a related mode or to a more inclusive decay mode. The latter part of the  $B_s$  measurement provides information on a region of center-of-mass energy in which multiple  $b\bar{b}$  resonances contribute to the production of  $B$  and  $B_s$  mesons, allowing for tests of Coupled-Channel analyses of electron-positron annihilation into pairs of  $B$  hadrons in this region.

The current understanding of processes involving fundamental particles is encapsulated by the Standard Model, a quantum field theory describing the weak, electromagnetic, and strong interactions in a single framework. The forces are described via the invariance of the theory under different kinds of gauge transformation. Despite its apparent success in describing the interactions of matter, it is silent as to the nature of the dark matter and dark energy inferred indirectly from astrophys-

ical observations. One possible source of information on the dark matter is in the spectrum of cosmic ray antinuclei. This represents an attractive search channel for annihilating dark matter, as backgrounds from astrophysical sources are expected to be low. It is important to understand the production of antinuclei in quark and gluon jets in order to predict the expected antinuclei signal from dark matter annihilation into colored particles. The antideuteron measurement from the *BABAR* data, presented in this dissertation, provides important input for testing models of antinucleus formation in quark and gluon fragmentation.

In Chapter 2 I describe the Standard Model and discuss the use of antinuclei as a probe for dark matter. In Chapter 3 a brief description of the *BABAR* experiment is presented. The measurement of  $B_s$  production and semileptonic decay is presented in Chapter 4, and the measurements of antideuteron production are described in Chapter 5.

## Chapter 2

### Physics at Flavor Factories

In this chapter, I briefly discuss the theoretical background relevant to the measurements presented in this dissertation. First the standard model is outlined, followed by a discussion of the necessity of extending the Standard Model beyond its current form.

#### 2.1 The Standard Model

Our current understanding of the physics of elementary particles and their interactions is described (almost) completely by a single quantum field theory known as the Standard Model of Particle Physics (SM). The SM consists of the Glashow-Weinberg-Salam model (laid out in the 1960's beginning with Refs. [2, 3, 4]) of the unified electroweak interaction combined with an  $SU(3)$  gauge theory of the strong interaction. A set of scalar fields serves to break the symmetry of the vacuum [5, 6, 7, 8] providing mass terms for the force carriers of the weak interaction and the fermions. Each ingredient is outlined in more detail below.

##### 2.1.1 Matter fields

The matter fields of the SM are chiral (that is, the two helicity eigenstates of Dirac spinors are treated differently) and exist in three generations, which differ

only in their couplings to the Higgs field (discussed later). The fermions are divided into two broad categories, the leptons and the quarks, depending on whether or not they participate in the strong force. The group structure of the strong interaction ( $SU(3)_C$ ) implies that the quarks, which do interact strongly, have three degenerate states of strong-force charge while the leptons, which do not, exist as single strong-force neutral states.

All of the left-handed helicity particle states (and their right-handed antiparticle conjugates) participate in the electroweak interaction. This interaction has a group structure of  $SU(2) \otimes U(1)$ , and the left-handed spinors are paired as doublets under this interaction, each fermion having a pair within its generation (the neutrinos for the leptons, and the down-type quarks for the up-type quarks). The left-chiral antifermions (right-chiral fermions) are singlets in this space. We write  $Q_i$ , ( $i = 1, 2, 3$ ) for the left handed quark doublets and  $U_i$  and  $D_i$  for the singlets, so that the quarks may be listed as

$$Q_1 = \begin{pmatrix} u_L \\ d_L \end{pmatrix} \quad Q_2 = \begin{pmatrix} c_L \\ s_L \end{pmatrix} \quad Q_3 = \begin{pmatrix} t_L \\ b_L \end{pmatrix} \quad (2.1)$$

$$U_1 = u_R \quad U_2 = c_R \quad U_3 = t_R \quad (2.2)$$

$$D_1 = d_R \quad D_2 = s_R \quad D_3 = b_R. \quad (2.3)$$

with  $\psi_L \equiv \frac{1}{2}(1 - \gamma^5)L$ . Similarly, the leptons are denoted

$$L_1 = \begin{pmatrix} \nu_{eL} \\ e_L \end{pmatrix} \quad L_2 = \begin{pmatrix} \nu_{\mu L} \\ \mu_L \end{pmatrix} \quad L_3 = \begin{pmatrix} \nu_{\tau L} \\ \tau_L \end{pmatrix} \quad (2.4)$$

$$E_1 = e_R \quad E_2 = \mu_R \quad E_3 = \tau_R. \quad (2.5)$$

There are no singlet neutrino fields in the usual formulation of the standard model, a fact which will be revisited in Section 2.2. The fermion part of the Standard Model Lagrangian before electroweak symmetry breaking is then

$$\mathcal{L}_{\text{Matter}} = \bar{\Psi}(i\gamma^\mu D_\mu)\Psi, \quad (2.6)$$

for  $\Psi = Q_i, U_i, D_i, L_i, E_i$  with  $D_\mu$  the covariant derivative to be discussed below and  $U(1)$  hypercharge assignments of  $Y = 1/3, 4/3, -2/3, -1$  and  $-2$  respectively. The explicit  $SU(2)_L \otimes U(1)_Y$  symmetry forbids fermion masses, a fact which (along with gauge field masses) is addressed by electroweak symmetry breaking.

### 2.1.2 Gauge sector

The gauge group of the SM is  $SU(2)_L \otimes U(1)_Y \otimes SU(3)_C$ , such that the Yang-Mills Lagrangian before electroweak symmetry breaking is given by

$$\mathcal{L}_{\text{YM}} = -\frac{1}{2}\text{Tr} [\mathbb{W}^{\mu\nu}\mathbb{W}_{\mu\nu}] - \frac{1}{4}B^{\mu\nu}B_{\mu\nu} - \frac{1}{2}\text{Tr} [\mathbb{G}^{\mu\nu}\mathbb{G}_{\mu\nu}] \quad (2.7)$$

where  $\mathbb{W} \equiv W^i\sigma^i/2$  is the matrix of  $SU(2)_L$  gauge bosons (here  $\sigma^i$  are the Pauli matrices) and  $\mathbb{G} \equiv G^a\lambda^a/2$  is the matrix of gluons (with  $\lambda^a$  the Gell-Mann matrices). For simplicity the gauge fields associated with the tensors  $W_{\mu\nu}, B_{\mu\nu}, G_{\mu\nu}$  are here notated similarly as  $W_\mu, B_\mu, G_\mu$  with the number of Lorentz indices distinguishing them in context. The covariant derivative then includes the couplings to the various gauge fields  $D_\mu = \partial_\mu - ig\mathbb{W}_\mu - ig'\frac{Y}{2}B_\mu - ig_3\mathbb{G}_\mu$ , where the term for the gluon fields acts only on the quark fields. The Lagrangian cannot include explicit mass terms for the gauge fields, and so the observed masses of the weak vector bosons  $W$  and  $Z$

must be generated by the mechanism of “spontaneous symmetry breaking” discussed below.

### 2.1.3 Electroweak symmetry breaking and the CKM matrix

Fermion and gauge boson masses are generated by the mechanism of spontaneous symmetry breaking in the  $SU(2)_L \otimes U(1)_Y$  electroweak sector. Briefly, an  $SU(2)_L$  doublet of scalar fields  $\Phi = (\phi^+, \phi^0)$  (hypercharge 1,  $SU(3)_C$  singlet) is added to the model with the Lagrangian

$$\mathcal{L}_{\text{Higgs}} = (D^\mu \Phi)^\dagger (D_\mu \Phi) - \mu^2 \Phi^\dagger \Phi - \frac{\lambda}{4!} (\Phi^\dagger \Phi)^2 - \mathcal{L}_{\text{Yukawa}}, \quad (2.8)$$

and Yukawa couplings to the fermions

$$\mathcal{L}_{\text{Yukawa}} = h_{ij}^U \bar{Q}_i (i\sigma_2) \Phi^c U_j + h_{ij}^D \bar{Q}_i \Phi D_j + h_{ij}^L \bar{L}_i \Phi E_j, \quad (2.9)$$

where the Yukawa coupling constants  $h_{ij}^X$  are, in general, complex.

The case  $\mu^2 < 0$  leads to a broken  $SU(2)_L \otimes U(1)_Y$  symmetry due to the existence of a continuum of possible minimum states, which are related to each other by  $SU(2)_L \otimes U(1)_Y$  transformations. The choice of a particular vacuum, which without loss of generality may be taken to be one in which  $\langle \phi^0 \rangle \neq 0$ , spontaneously breaks the symmetry of the ground states and generates mass terms for the Weak gauge fields  $W_\mu^\pm \equiv (W_\mu^1 \pm iW_\mu^2)/\sqrt{2}$  and  $Z_\mu = W_\mu^3 \cos \theta_W + B_\mu \sin \theta_W$ . Here we have introduced an important parameter of the SM, the Weinberg angle  $\sin \theta_W \equiv g'/\sqrt{g^2 + g'^2}$ . There remains an unbroken  $U(1)_Q$  gauge interaction (the orthogonal to the  $Z$ ) with charges given by  $Q = T^3 + Y/2$ , with  $T^3$  the  $SU(2)_L$  weak isospin

quantum number ( $= \pm 1/2$ ), which describes the photon and its interactions and reproduces the celebrated theory of quantum electrodynamics at low energies. The up-type quarks have  $+2/3$  charge, the down-types  $-1/3$ , the charged leptons  $-1$ , and the neutrinos  $0$ . Three components of the Higgs field doublet become the longitudinal degrees of freedom of the  $W$  and  $Z$ , with one real scalar  $H$  remaining. This is the Higgs boson, which is the “smoking gun” of this kind of symmetry breaking.

The Yukawa couplings generate mass matrices for the fermions. Any such complex matrices may be diagonalized via a bi-unitary transformation  $M \rightarrow V_1^{-1} M V_2$  in the  $SU(3)$  flavor space. The mass matrix for the leptons is generated by the  $h_{ij}^L \bar{L}_i \Phi E_j$  term and leads to three lepton masses and massless neutrinos. In the case of the quarks, the diagonalization of the matrices generated by  $h_{ij}^U \bar{Q}_i (i\sigma_2) \Phi^c U_j$  and  $h_{ij}^D \bar{Q}_i \Phi D_j$  results in mass eigenstates that are, in general, not also eigenstates of the weak interaction: the two bases differ by a unitary transformation [9, 10, 11]. This matrix, known as the Cabibbo-Kobayashi-Maskawa (CKM) matrix, is fully defined by just four parameters: three mixing angles and one complex phase with components denoted  $V_{ij}$  with  $i \in \{u, c, t\}$  and  $j \in \{d, s, b\}$  so that e.g.  $V_{ub}$  is the factor associated with  $b \rightarrow u$  quark transitions. The complex phase is very important as it is the only term in the SM which is not invariant under the combined transformations of charge conjugation and spatial parity ( $CP$ ), and can give rise to  $CP$ -violating processes.

### 2.1.4 Physics of hadrons

Isolated quarks are never observed due to the nature of the strong interaction. This phenomenon is known as confinement, and its direct consequence is that the spectrum of strongly-interacting particles we observe are bosonic (meson) or fermionic (baryon) bound states of quarks, with quantum numbers corresponding to  $q\bar{q}$  or  $\epsilon^{ijk}q_iq_jq_k$  combinations, respectively. Here  $\epsilon^{ijk}$  is the fully antisymmetric rank-three Levi-Civita symbol. An important phenomenon for understanding physics at the  $B$  factories is the phenomenon of neutral meson mixing. Neutral mesons and their antiparticles such as the  $K^0$ , the  $D^0$  and the  $B^0$  do not carry any conserved charges in the standard model, and thus the process  $B^0 \leftrightarrow \bar{B}^0$  is allowed through the second-order box diagrams such as those in Fig. 2.1, and in general the particle will oscillate between the two states. In the absence of  $CP$ -violating effects the  $CP$  eigenstates  $|B^0\rangle \pm |\bar{B}^0\rangle$  would also be eigenstates of the Hamiltonian describing all interactions of the particles, resulting in  $CP$ -odd and  $CP$ -even particle states with mass difference  $\Delta m$  and lifetime difference  $\Delta\Gamma$ . A nonzero CKM phase results in the true mass eigenstates being slightly misaligned from the  $CP$  eigenstates, causing interference effects which are measurable at collider experiments.

As QCD is flavor diagonal, the lightest mesons with heavy quark flavors ( $c$  and  $b$ ) are stable against strong decay and instead decay via weak transitions. These processes involve energies above the scale at which QCD begins to become perturbative ( $\Lambda_{\text{QCD}} \sim 200 \text{ MeV}$ ), and inclusive decay rates may be calculated to a fair approximation at the quark level ignoring the QCD interactions among the quarks

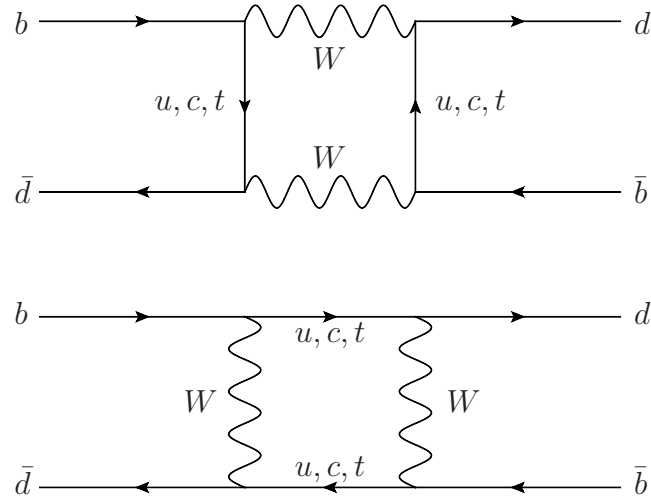


Figure 2.1: Lowest-order diagrams describing neutral meson oscillations in the  $B^0$  system.

inside of the initial and final hadronic system. This level of calculation is sometimes referred to as calculation with a spectator diagram, as the light quark in the meson is treated as a “spectator” which does not actively participate in the reaction. Spectator diagrams may also be used to select transitions which are expected to be suppressed, either due to quark-level transitions involving off-diagonal CKM matrix elements, Pauli exclusion from identical quarks in the final state, or color-suppressed decays. Feynman diagrams showing various spectator processes are shown in Fig. 2.2. Semileptonic decays in particular are amenable to this sort of treatment due to the lack of any strong interaction between the hadronic system and the lepton neutrino pair. Such a calculation would suggest that the different inclusive semileptonic partial widths of the  $B$ -type mesons should all be the same, split only by higher-order effects, providing a simple test of our theoretical understanding of these processes.

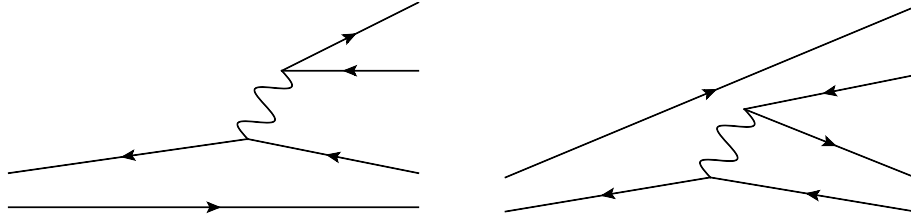


Figure 2.2: General structure of internal (right) and external (left) spectator diagrams. The color-singlet nature of the initial state tends to suppress internal diagrams. The products of the virtual  $W$  in these graphs may be a lepton-neutrino pair or a quark ( $q$ ) antiquark ( $\bar{q}$ ) pair.

### 2.1.5 $B$ Physics

The spectrum of  $b\bar{b}$  bound states, shown in Fig. 2.3, includes the  $\Upsilon(4S)$  state with which has a mass just  $\approx 20$  MeV above the threshold for  $B^0\bar{B}^0$  and  $B^+B^-$  production. This state has  $J^{PC}$  quantum numbers of  $1^{--}$  and thus may be produced in  $e^+e^- \rightarrow \gamma^*$  reactions. It subsequently decays nearly 100% of the time to the light  $b$ -flavored mesons in a  $P$ -wave state with a very small  $Q$ -value. Operation of electron-positron colliders at this center-of-mass energy has allowed for a rich program of precision physics with  $B$  mesons. This arrangement also makes possible time-dependent measurements of the  $B$  system by use of asymmetric colliders which produce a boost to the entire event so that distance along the boost axis serves as a proxy variable for decay time. Precision measurements have been made of many observables in the  $B^0\bar{B}^0$  and  $B^+B^-$  systems, including the mixing parameters  $\Delta m_d$  and  $\Delta\Gamma_d$ , the inclusive semileptonic branching fractions  $\mathcal{B}(B^0 \rightarrow \ell\nu X)$  and  $\mathcal{B}(B^+ \rightarrow \ell\nu X)$ , and various CP-violating observables.

The structure at 10.860 GeV, tentatively classified as the  $\Upsilon(5S)$ , provides an opportunity to study the  $B_s$  system at  $e^+e^-$  colliders, as the  $B_s$  production thresh-

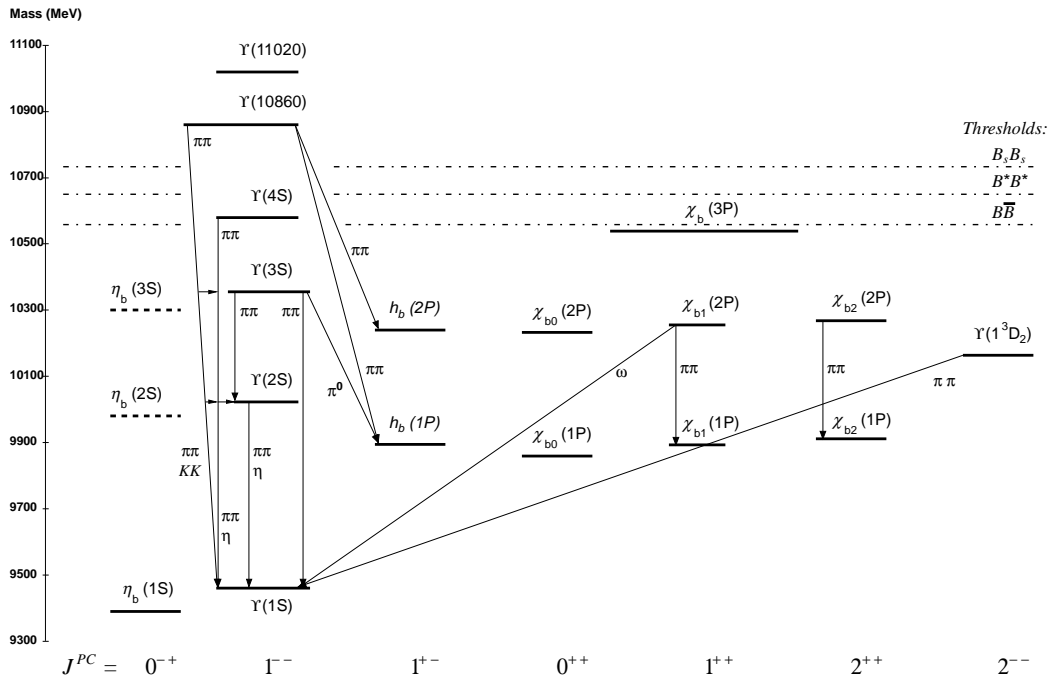


Figure 2.3: Level diagrams of the  $b\bar{b}$  bound states showing the  $B\bar{B}$  threshold. From the 2012 Review of Particle Physics [12]

old lies at 10.733 GeV. This resonance has a smaller production cross-section than the  $\gamma(4S)$  and decays only  $\approx 20\%$  of the time to  $B_s$  mesons. As a result, parameters describing the  $B_s$  system have been measured primarily at hadron colliders, where measurements of inclusive quantities are very difficult. The fully-inclusive semileptonic decay rate, a measurement of which is presented in this thesis, is unmeasured as of the 2011 PDG update [13]. Table 2.1 shows the 2011 averages of some key measurements in the  $B$  systems.

As of this writing, the SM has been verified to an impressive extent. The  $W$  and  $Z$  have both been studied extensively, the existence of three generations of leptons and of six quark flavors and the  $SU(3)_C$  structure of QCD have been verified. In July of 2012 the discovery of a new particle with mass 125 GeV consistent with a

Table 2.1: Some of the key parameters in the  $B$  meson systems as of the 2010 edition of the Review of Particle Physics. The mass and lifetime averages for the lighter  $B$ s are dominated by hadron collider measurements, while the mass splitting and semileptonic branching fractions are dominated by  $B$  factory measurements.

	$B^+$	$B^0$	$B_s$
$m$ (MeV)	$5279.17 \pm 0.29$	$5279.50 \pm 0.30$	$5366.3 \pm 0.6$
$\tau$ ( $10^{-12}s$ )	$1.519 \pm 0.007$	$1.641 \pm 0.008$	$1.472^{+0.024}_{-0.026}$
$\Delta m$ ( $ps^{-1}$ )	N/A	$0.507 \pm 0.005$	$17.77 \pm 0.12$
$\Delta\Gamma/\Gamma$	N/A	$< 0.01$	$0.092^{+0.051}_{-0.054}$
Semileptonic BF (%)	$10.99 \pm 0.28$	$10.33 \pm 0.28$	?

Higgs boson was announced by the ATLAS and CMS experiments operating at the LHC collider. The CKM matrix has been constrained and verified to 10% or better by multiple measurements of quantities related by CKM parameters, including  $|V_{ub}|$ ,  $\mathcal{B}(B^+ \rightarrow \tau^+\nu_\tau)$ , and  $\sin 2\beta$  as measured in  $B^0 \rightarrow J/\psi K_S^0$ .

In Chapter 4 of this dissertation, I provide a measurement of the inclusive semileptonic branching fraction  $\mathcal{B}(B_s \rightarrow \ell\nu X)$  using data collected with *BABAR* at center-of-mass energies extending from the  $B\bar{B}$  threshold and scanning across the  $\Upsilon(4S)$ ,  $\Upsilon(5S)$ , and  $\Upsilon(11020)$  to 11.2 GeV. In addition,  $B_s$  meson production in this energy region is studied. This provides a check of  $B_q$  production models in this region, and in particular of coupled-channel calculations of the electron-positron cross-section to  $B$ -hadrons just above the  $B\bar{B}$  threshold which predict negligible  $B_s$  production away from the peak of the  $\Upsilon(5S)$  resonance.

## 2.2 Physics Beyond the Standard Model

The SM has been known for some time to be incomplete due to the absence of a description of gravitational effects (or indeed the ability to calculate the classical gravitational effects of beyond leading-order processes in the matter fields) and the lack of a stabilizing mechanism for the Higgs mass parameter in a Wilsonian understanding of renormalization in the context of the lack of a gravitational model (the hierarchy problem). The relatively recent discovery of the phenomenon of neutrino flavor oscillations [14] is another example of phenomena not encompassed by the SM. The presence of non-SM contributions to the large-scale energy density of the universe in the form of dark matter and dark energy present additional frontiers for exploring beyond the standard model. For a discussion of cosmological evidence for non-baryonic matter (dark matter) and dark energy, see the review of Big Bang Cosmology in Ref. [13].

Though much of the parameter space for weakly-interacting dark matter candidates, e.g. light neutralinos in supersymmetric models, is outside of the reach of  $B$ -factory experiments, searches for low mass ( $< 10$  GeV) dark matter particles in  $\mathcal{T}$  decays [15] are possible and have been performed (for example the study in Ref. [16]).

A possible window for indirect dark matter searches is to look for evidence of annihilating galactic dark matter via examining the spectrum of gamma radiation and antimatter cosmic rays. The latter is particularly attractive, as antimatter nuclei species are not produced in very large numbers by astrophysical sources, while

pair annihilation of dark matter particles would produce equal amounts of matter and antimatter, leading to a direct injection of antimatter into the cosmic ray spectrum [17]. Thus there is significant interest in measurements of cosmic ray antinuclei as a low-background probe of galactic dark matter annihilation. There is currently a program in place for spectrometry on cosmic rays in orbit, with a particular interest on antimatter fluxes. Limits on the astrophysical flux of cosmic-ray antideuterons is expected to improve by a factor of 1000 at the upcoming experiments AMS-02 and GAPS, from  $10^{-4}[\text{m}^2\text{ssr GeV}]^{-1}$  to  $10^{-7}$  [18]. Given that astrophysical sources are expected to contribute at the level of  $10^{-9}$ , the detection of an anomalous antideuteron flux at these experiments would be evidence for a new primary source of antideuterons, possibly annihilation of dark matter to colored particles.

Theoretical difficulties exist in predicting the detailed spectrum of antideuterons produced in a given model of annihilating dark matter, due to the fact that the formation of light (anti)nuclei in quark and gluon fragmentation is not well understood. Estimates may be performed by assuming that nucleons nearby one-another with very little relative momentum may “stick” together. The simplest such estimate involves relating the production of a nucleus of mass  $A$  to the  $A$ th power of the nucleon differential production cross-section, ignoring the correlated production of baryons [17]. A slightly more sophisticated approach is to use Monte Carlo simulations of hadronization to construct a large sample of fragmented quark or gluon initial states. The final states are then checked for the existence of prompt nucleons with small relative momenta, assuming that those below some momentum threshold will combine [18]. This approach has been applied to understanding previous

measurements [19], but is sensitive to the particular generator chosen for the fragmentation [17]. Ultimately, accurate measurements of antideuteron production in the fragmentation of quarks and gluons is needed help test the predictions of these models. The second analysis presented here (in Chapter 5) is a measurement of the differential production rate of antideuterons in quark and gluon fragmentation in the kinematic regime of 10 GeV  $e^+e^-$  center-of-mass energy.

## Chapter 3

### The *BABAR* Experiment

The *BABAR* experiment is built around a general-purpose magnetic spectrometer optimized for detecting the results of collisions in the PEP-II asymmetric-energy electron-positron collider. Electron and positron beams for PEP-II were accelerated using part of SLAC National Accelerator Laboratory's 2-mile long linear accelerator and injected into the storage rings, where they were brought into collision at the heart of the *BABAR* detector.

#### 3.1 PEP-II

The PEP-II asymmetric *B*-factory consists of electron and positron rings designed for high instantaneous luminosity and optimized for the *BABAR* experiment. The electron ring, referred to as the High Energy Ring (HER), is injected at 9 GeV (for  $\Upsilon(4S)$  running), with a design beam current of 0.75 A, while the positron ring, referred to as the Low Energy Ring (LER), is injected at 3.1 GeV with a design current of 2.15 A. More typical currents for early running are 0.7 and 1.3A, with later running reaching peak currents of over 2.0 and 3.2A, respectively. The beams consist of a maximum of 1658 bunches with a 4.2 ns bunch spacing. Transverse beam sizes are  $< 6 \mu\text{m}$  in the y direction (vertical to the beam orbit plane) and  $120 \mu\text{m}$  in x (in the beam orbit plane). Typical CM energy spreads in collision were

on the order of 5 MeV. Running at other values of  $\sqrt{s}$  was achieved by adjusting the energy of the HER as necessary to achieve the desired CM energy. The highest value of instantaneous luminosity achieved with PEP-II during *BABAR*'s lifetime was  $10^{34} \text{ cm}^{-2}\text{s}^{-1}$ .

## 3.2 Detector

The *BABAR* detector is described in detail in Ref. [20]. As mentioned above, it is a general-purpose magnetic spectrometer, shown in Fig. 3.1, consisting of a number of subdetectors performing measurements of charged particle trajectories, ionization energy loss, calorimetry and particle identification. The overall apparatus is asymmetric in anticipation of the effects of the boost of the  $e^+e^-$  CM frame in the laboratory frame: consider a photon leaving the origin at an angle  $\theta_{\text{CM}}$  to the boost axis, in the laboratory frame we have

$$\cos \theta_{\text{lab}} = \frac{p'_z}{|p'|} = \frac{p'_z}{E'} = \frac{\gamma E \cos \theta_{\text{CM}} + \beta \gamma E}{\gamma E + \beta \gamma E \cos \theta_{\text{CM}}} = \frac{\cos \theta_{\text{CM}} + \beta}{1 + \beta \cos \theta_{\text{CM}}}. \quad (3.1)$$

Where primed momenta and energies are those measured in the laboratory frame. The boost is slightly offset from the z-axis of the *BABAR* co-ordinate system, which is along the axis of the detector: for  $\Upsilon(4S)$  running we have  $\vec{\beta} = (-0.0091, 0, 0.48508)$ . In the following, the various subdetectors are described and their function and capabilities outlined, highlighting their relevance to the analyses described in this dissertation. Figures are adapted from [20].

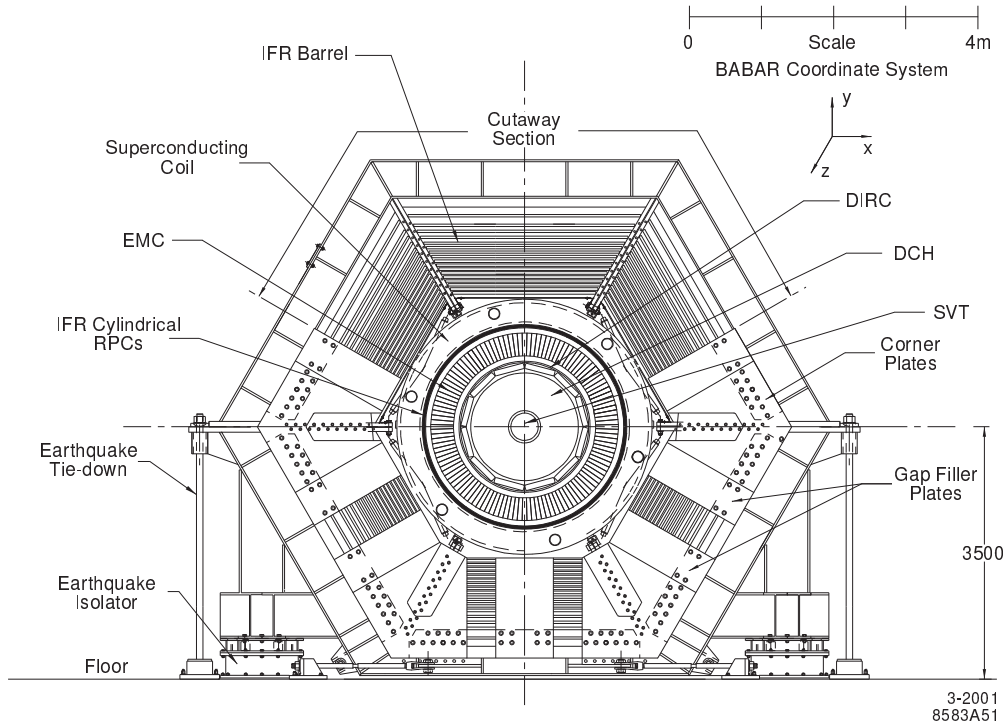


Figure 3.1: Section of the *BABAR* detector transverse to the beam axis. The labelled height is given in mm. The acronyms are defined in the following sections.

### 3.2.1 Tracking

The tracking subsystems are designed to detect and parameterize the paths of charged particles passing through the *BABAR* detector and measure the amount of ionization they produce as they pass through the active material. Near the interaction point there are five parameters of interest describing the path of a charged particle: the transverse momentum  $p_T$ , the dip angle of the helix  $\lambda$ , the orientation in the transverse plane  $\phi_0$ , and the distances of closest approach to the origin in the transverse plane ( $d_0$ ) and along the detector axis ( $z_0$ ). Measurements of these parameters are accomplished through a pair of complimentary subdetectors in the nearly uniform 1.5-Tesla field of *BABAR*'s superconducting solenoidal electromagnet.

The magnet itself is composed of filaments of Nb-Ti, wound into strands which are in turn combined into cables used to wind the solenoid. The magnet is kept at an operating temperature of 4.5K using liquid He. Mapping of the field from the magnet prior to the installation of tracking components shows that the  $\phi$  component of the magnetic field does not exceed 1mT and the radial component is less than 50 mT for most of the tracking volume. The innermost tracking subsystem is the Silicon Vertex Tracker (SVT), a five-layer silicon-based semiconductor tracker. The physical arrangement of the SVT is shown in Fig. 3.2.

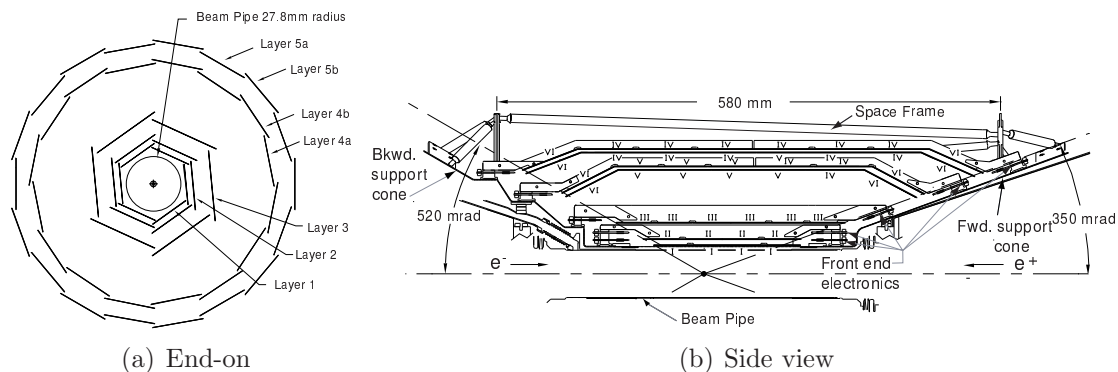


Figure 3.2: SVT structure

The SVT consists of three inner layers starting just outside the beam-pipe for tracking as close to the interaction point as possible. Two additional layers further out provide measurements in the region between the inner layers of the silicon tracker and the beginning of the drift chamber. The first layer is located 32 mm from the interaction region, with subsequent layers at 40, 55, 127, and 144 mm. Each layer is a collection of silicon modules with readouts on both ends. The modules are composed of 300 micron-thick n-type silicon substrate sandwiched between  $p^+$  and  $n^+$  strips (with the latter implanted on top of p-type stops). The strips are along

the  $z$  and  $\phi$  directions with differing pitches between 50 and 210  $\mu\text{m}$ , depending on the layer and direction, allowing for three-dimensional hit coordinates when the substrate is ionized by a passing charged particle. Internal alignment of the system is monitored offline: briefly, the procedure uses large samples of  $e^+e^- \rightarrow \mu^+\mu^-$  events with constraining information from the known interaction energy to determine the best-fit position of each of the 52 modules using track fits in the SVT alone. The entire apparatus is then treated as a solid body for global alignment with the DCH using information from both trackers. The global alignment is needed because while the DCH is ultimately supported by the mechanical structure of the rest of the detector, the SVT is not, and so they are mechanically independent.

The SVT provides precision measurements of charged particle positions near the interaction region, as well as stand-alone tracking for particles with transverse momenta too low for DCH tracking (less than 120 MeV, corresponding to a radius of curvature of 266 mm) down to 50 MeV, crucial to the reconstruction of  $D^*$  decays. Hit resolutions achieved with the apparatus are 10-30 microns in  $\phi$  and 20-40 microns in  $z$ . Layer number,  $z$ , and  $\phi$  information may be used directly in track fitting. For higher- $p_T$  tracks, the SVT contributes mostly to determination of track angles and distances of closest approach. Resolutions on the former are  $\sigma_{\phi_0} = 0.43$  mrad and  $\sigma_{\tan\lambda} = 0.53 \times 10^{-3}$ .

The DCH begins at an inner radius of 236 mm from the interaction region and extends out to 809 mm. It consists of a gas filled chamber in which wires of different diameter and composition are strung axially. The chamber is divided by the wires into cells, with each cell consisting of aluminum field wires held at 0 V



a more than 98% efficient reconstruction of charged particles with  $p_T > 500$  MeV, with a transverse momentum resolution of  $\sigma_{p_T}/p_T = (0.13p_T + 0.45)\%$ .

Both tracking subdetectors provide measurements of ionization charge deposited along the track, allowing for separation of particle species of different masses by measurements of specific ionization energy loss ( $dE/dx$ ) with resolutions on the order of 7% in the DCH, and 14% using a truncated mean measurement in the SVT. These  $dE/dx$  measurements provide excellent  $K/\pi$  separation below 700 MeV, as can be seen in Fig. 3.4, and are the primary identification mechanism for antideuterons in the analysis presented in Chapter 5.

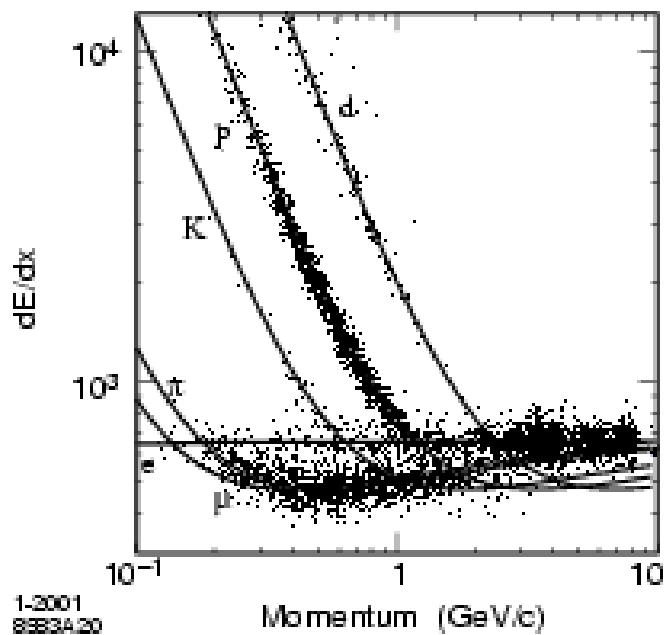


Figure 3.4: Measurement of  $dE/dx$  (in arbitrary units) vs track momentum in the DCH. The curves are the Bethe-Bloch predictions derived from control samples.

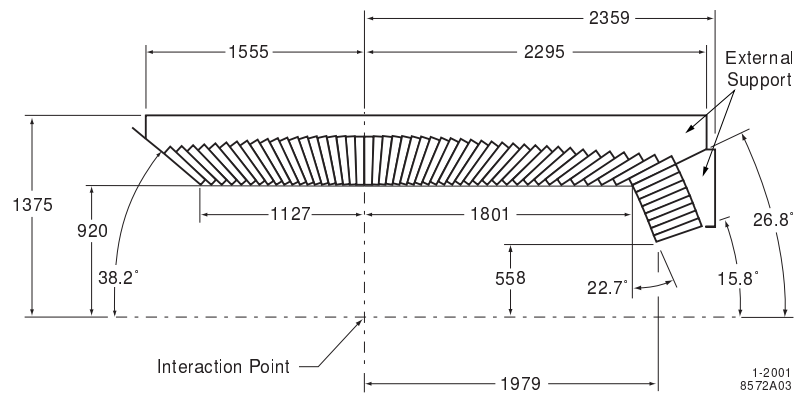


Figure 3.5: Cutaway view of half of the EMC with dimensions labelled in mm. Note the asymmetric layout with larger coverage in the direction of the boost.

### 3.2.2 Calorimetry

The *BABAR* detector incorporates a crystal-based Electromagnetic Calorimeter (EMC) for measurement of photon energies and identification of electrons. The EMC consists of 5760 trapezoidal Thallium-doped Cesium Iodide (CsI(Tl)) crystals arranged in 56 rings about the detector axis from the interaction region covering polar angles between 0.277 and 2.456 radians (see Fig. 3.5). Each ring in the barrel region contains 120 crystals (80-120 in the endcap between 0.277 and 0.469 radians).

Photodetectors mounted to the back of each crystal (which is isolated from its neighbors by reflective foil) measure the light emitted by electromagnetic showers in the bulk of the crystal. The depth of each crystal is at least 16 radiation lengths ( $X_0$ ) of CsI(Tl), ensuring good containment of EM showers. On-line calibration of the light response of each crystal is performed using a light pulser system consisting of optical fibers connecting the rear of each crystal to a xenon flash lamp light source.

After reconstruction and calibration, the energy resolution for photons is

$$\frac{\sigma_E}{E} = \frac{2.32\%}{\sqrt[4]{E(\text{GeV})}} \oplus 1.85\%,$$

and the angular resolutions achieved with the crystals can be parameterized as

$$\sigma_\theta = \sigma_\phi = \frac{3.87}{\sqrt{E(\text{GeV})}} \text{mrad}$$

As well as measuring photon energies, the EMC serves as a powerful tool for electron identification. The momentum of tracks with an associated EMC energy deposit may be compared with the calorimetric energy deposited to distinguish electrons ( $E/p$  near unity) from muons (which are minimum ionizing at *BABAR* energies) or light hadrons. In the analysis described in Chapter 4, this capability contributes to electron identification in hadronic events as well as helping to distinguish  $e^+e^- \rightarrow \mu^+\mu^-$  events from  $e^+e^- \rightarrow e^+e^-$  (Bhabha scattering) events.

### 3.2.3 Dedicated particle identification

In the barrel of the detector situated between the end of the DCH and the EMC are bars of high-quality fused silica serving as a radiator for *BABAR*'s Detector of Internally-Reflected Cherenkov light (DIRC). The bars are arranged into twelve groups of twelve bars each, with highly polished surfaces to promote total internal reflection of Cherenkov light emitted by passing charged particles. The key principle underlying the DIRC is that photon propagation angles are preserved by total internal reflection, and therefore the Cherenkov angle of light emitted by a charged particle may be measured after being transported out of the active area of the detector, reducing the amount of material before the EMC.

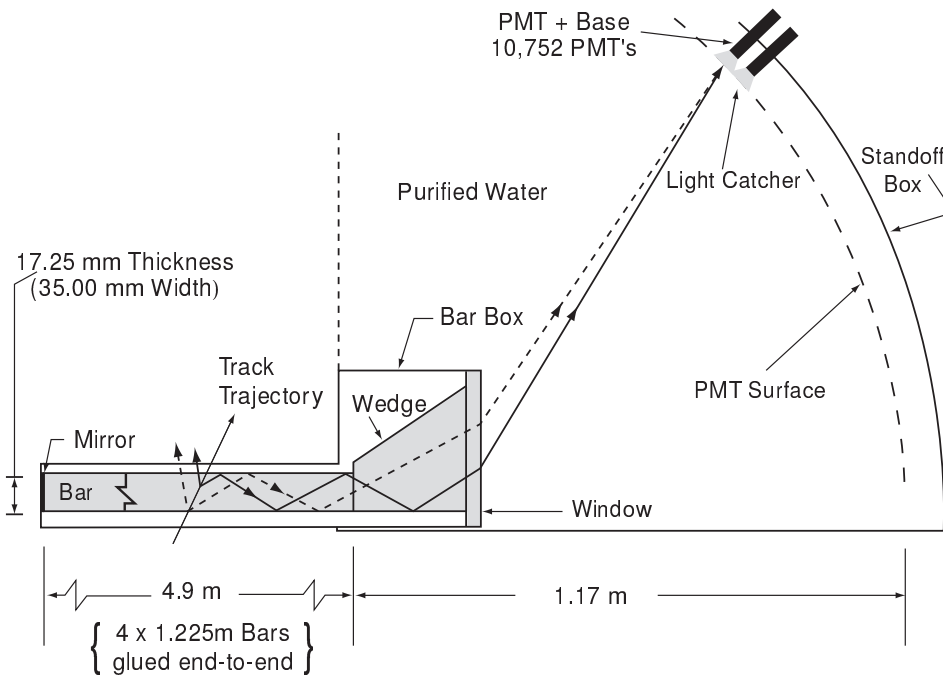


Figure 3.6: Diagram of the DIRC showing the basic principle of operation

The reflected light makes its way to the rear end of the detector (there is a reflector at the forward end of the bars) to the DIRC's standoff box containing the instrumentation used to measure the Cherenkov light. The standoff box is filled with 6,000 liters of purified water ( $n \approx 1.346$  compared to fused silica  $n \approx 1.473$ ), divided into 12 sectors which are each instrumented with 896 photomultiplier tubes (PMT). The signals from the PMTs provide both position and timing information on the detected photon. The former is used to reconstruct the Cherenkov ring, and the latter aids in discrimination against background. Timing calibration of the PMTs is performed online using 1 ns light pulses from LEDs to calibrate relative timings among the PMTs, while tracks from data are used to determine the global timing offset with respect to track arrival time. The measured time resolution is

$\sigma_t = 1.7\text{ns}$ , and the overall width of the Cherenkov angle distribution for dimuon events is 2.5 mrad.

The DIRC is a very good instrument for charged particle identification for tracks with  $\beta \approx 1$ , making it an excellent compliment to  $dE/dx$  information, which is not useful for tracks above 700 MeV. Such PID information is used extensively in Chapter 4, while in Chapter 5 the DIRC is used as a veto, due to the fact that no maximum-likelihood fit to DIRC information with the deuteron mass hypothesis is performed in the *BABAR* reconstruction code.

### 3.2.4 Instrumented Flux Return (IFR)

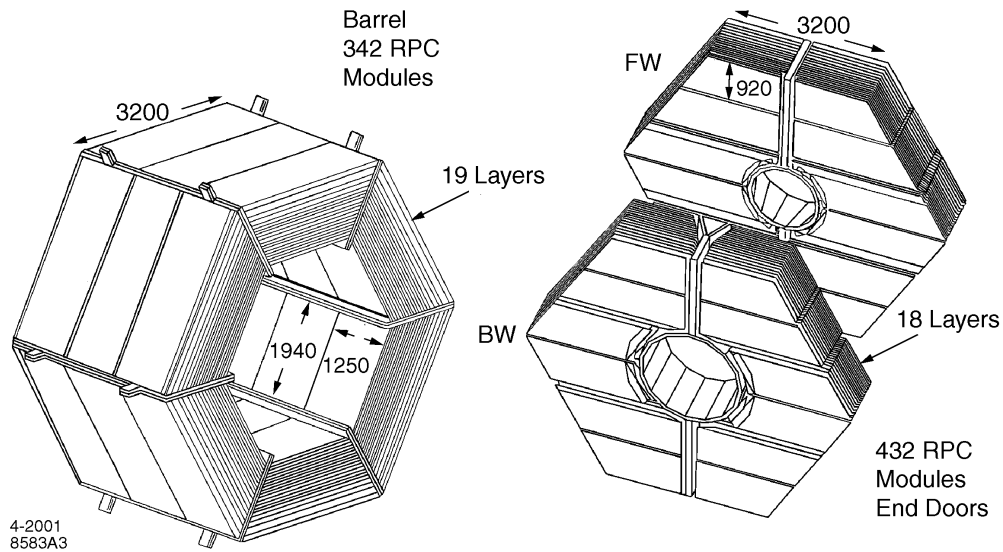


Figure 3.7: Layout of the RPCs in the flux return.

The magnetic field outside of *BABAR*'s 1.5 Tesla solenoid is shaped by a large steel Instrumented Flux Return (IFR). Rather than solid passive material, the flux return is layered and was instrumented with two different technologies over the life

of the experiment (the original instrumentation was upgraded part-way into the running of the experiment). The original configuration used 19 layers (in the barrel region, in the endcaps there is one fewer layer) of resistive plate chambers (RPCs) as detectors with the steel of the flux return acting as a hadron absorber. The RPCs consist of two layers of bakelite with a gap in between which is supported by polycarbonate spacers. Readout strips in  $z$  and  $\phi$  are connected to graphite which is on the surface of the bakelite.

Charged particles traversing the gaps in the RPCs ionize the gas in the gap, and charge is ultimately collected on the strips outside of the bakelite. Nominally the RPCs in the IFR provide good performance for muon identification: tracking the muons through the material of the steel flux return and comparing to the expected amount of material a  $\mu^\pm$  of that momentum would be expected to penetrate (compared to, say, a  $\pi^\pm$ ) allows for 80-90% muon ID efficiency across a wide range of polar angle and momentum, with  $< 10\%$  charged pion misidentification rate.

Early on in data-taking, the performance of the majority of the RPCs in the IFR system began degrading considerably, a problem attributed partially to the initial manufacturing process and partially to overheating of the modules in early running. The decision was made to replace much of the active systems in the forward endcap of the IFR in 2002 and in the barrel sections during shutdowns in 2004 and 2006. The RPCs in the forward endcap were replaced with second generation modules, while the barrel RPCs were replaced with 12 layers of Limited Streamer Tubes (LST) plus additional brass absorbers where the remaining layers of RPCs once were.

The LST modules consist of rectangular gas cells with a single silver-plated anode wire running down the long axis of the tube, with the inside surface of the cells coated in a layer of graphite. When a charged particle traverses the cell, the gas amplifies the ionization into an avalanche. The location of the cell itself gives the  $r$  and  $\phi$  coordinates of the hit. For a more precise  $z$  position, the outside of the cell has strips running in the  $\phi$  direction. The avalanche inside the cell induces a signal on the nearest strips, providing segmentation along the tube which would otherwise not exist. The upgrade was successful in bringing detection efficiencies in the IFR in line with geometrical acceptance. A more detailed description of the upgrade may be found in Ref. [21].

### 3.2.5 Trigger

While in operation, PEP-II reached instantaneous luminosities in excess of  $10^{34}\text{cm}^{-2}\text{s}^{-1}$  with beam currents exceeding 2 A in the HER and 3 in the LER. At these luminosities, the total inelastic collision rate is 66 Hz while the rate for large-angle Bhabha scattering events is around 530 Hz. Beam-induced background rates for tracks in the DCH are two orders of magnitude larger. *BABAR* uses a two-level trigger system to reduce the total rate of recorded events below 120 Hz, accepting inelastic collisions with high efficiency while simultaneously rejecting as many background events as possible while accumulating minimal dead time.

The lower level trigger, referred to as the Level 1 (L1) trigger, is implemented in hardware with a selection rate of 1 kHz at design luminosity ( $3.3 \times 10^{33}\text{cm}^2\text{s}^{-1}$ ). It

operates on results of triggering information sent from the DCH, EMC and IFR while up to four events are buffered awaiting triggering decisions. Trigger primitives are formed from simplified reconstruction algorithms for each of the three subdetectors and passed on to the global trigger. The kinds of primitives include: the presence of short, long, or high- $p_T$  track segments in the DCH; the presence of minimum ionizing (100 + MeV), intermediate (250 + MeV), or high (700 + MeV) deposits in the EMC barrel, minimum ionizing signals in the forward endcap or very high (1 GeV) deposits in the backward region; and single or dimuon signals in the IFR for different  $\phi$  sectors. The global trigger then makes the final decision based on these primitives. The combined L1 trigger is greater than 99.9% efficient in selecting most  $B\bar{B}$  event topologies, while also retaining more than 99% of  $q\bar{q}$  events and dimuon events ( $\tau^+\tau^-$  events are slightly worse at  $> 94\%$ ).

The second level of triggering is the Level 3 (L3) trigger. The L3 trigger operates in software using better tracking and clustering algorithms to reconstruct the event. It is built on *BABAR*'s usual data processing framework, allowing for the inclusion of different kinds of software modules to customize the trigger. Level 3 filters include the presence of one high- $p_T$  track (600 MeV) or two lower- $p_T$  tracks (250 MeV) originating from the interaction region (less than 1 cm transverse for the single track case or 1.5 for the two-track case). Similarly the EMC filter requires two clusters with at least 350 MeV in the CM and an estimated invariant mass above 1.5 GeV, or four clusters with an invariant mass above 1.5 GeV. In addition, a veto for Bhabha events is incorporated using  $E/p$  information at this level. Efficiencies for  $B\bar{B}$  remain high, with only modest reductions in  $q\bar{q}$ ,  $\mu\mu$  and  $\tau\tau$  efficiencies from

L1 to L3.

### 3.3 Event Reconstruction and Data Analysis

Event reconstruction proceeds offline, with the goal of converting detector hit information and trigger primitives into analysis objects. In the process, the events are tagged according to whether or not they satisfy some simple cuts related to background classification. Here I list the definitions for particular tags which are used in the analyses described below. (I use the subscript  $n$  to refer to parameters describing the  $n$ -th highest momentum track or the  $n$ -th highest energy calorimeter cluster)

- BGFMultiHadron:  $> 2$  charged tracks,  $R2 < 0.98$  [22].
- BGFMuMu:  $p_1 > 4 \text{ GeV}$ ,  $p_2 > 2 \text{ GeV}$ ,  $3.5 > \theta_1 + \theta_2 < 2.8$ ,  $E_1 + E_2 < 2 \text{ GeV}$
- BGF Tau: 2 charged tracks, total charge = 0,  $p_1 + p_2 < 9 \text{ GeV}$ ,  $E_1 + E_2 < 5 \text{ GeV}$ ,  $E_1/p_1$  or  $E_2/p_2 < 0.8$ ,  $\sqrt{s} - p_1 - p_2 > 0 \text{ GeV}$ ,  $(p_{T1} + p_{T2})/(\sqrt{s} - p_1 - p_2) > 0.07$
- BGF TwoProng: 2 charged tracks, total charge 0,  $p_1$  or  $p_2 > 1 \text{ GeV}$ ,  $E_1 < 3 \text{ GeV}$ ,  $|\cos \theta_1 + \cos \theta_2| > 0.1$  (reject cosmics),  $\cos \theta_1 > -0.75$  (in EMC),  $p_1 > 4 \text{ GeV}$  or  $|p_{T1} - p_{T2}| < 0.3$
- BGF NeutralHadron:  $R2 < 0.95$  and either: 2 charged tracks, 3 clusters  $> 0.1 \text{ GeV}$  and 2 clusters  $> 0.5 \text{ GeV}$ ; 1 charged track, 4 clusters  $> 0.1 \text{ GeV}$  and 2 clusters  $> 0.5 \text{ GeV}$ ; or 0 charged tracks, 6 clusters  $> 0.1 \text{ GeV}$  and 3 clusters  $> 0.5 \text{ GeV}$ .

Below I outline the general procedure for reconstructing analysis objects at *BABAR*.

### 3.3.1 Reconstruction

As discussed in Sec. 3.2.1, the ultimate goal of tracking and track reconstruction is to obtain the five parameters describing the momentum near the origin and the distance of closest approach to the origin of a given charged particle. Track finding at *BABAR* builds on information from L3 tracks, with track segments found at that level fit to a helix to find the largest, cleanest tracks in the event and to add additional hits which may have been missed at L3. Additional DCH segments which are not already assigned to a track fit are used to seed searches for additional tracks separately from the L3 seed tracks. The resulting DCH tracks are refit using a Kalman filter [23] method in which the track is composed of piecewise helix segments taking into account expected energy loss in the detector material.

These tracks are extrapolated into the SVT in an attempt to match them with SVT hits, again taking into account expected material losses and possible multiple scattering in the SVT. Hits from the SVT are then added, with any ambiguities resolved by choosing the series of hits with more layers and/or smaller residuals, and the entire track is refit using both DCH and SVT information. Standalone SVT tracks are then searched for in the remaining hits in the SVT. Finally, SVT-only tracks are matched up with DCH-only tracks in an attempt to completely reconstruct those tracks which may have a kink due to interaction with the support tube

which lies between the two trackers. When combining candidates into a composite candidate (e.g. the  $\phi \rightarrow K^+K^-$  decay in Chapter 4), the parameters of the daughter tracks are adjusted to find a best-fit vertex point.

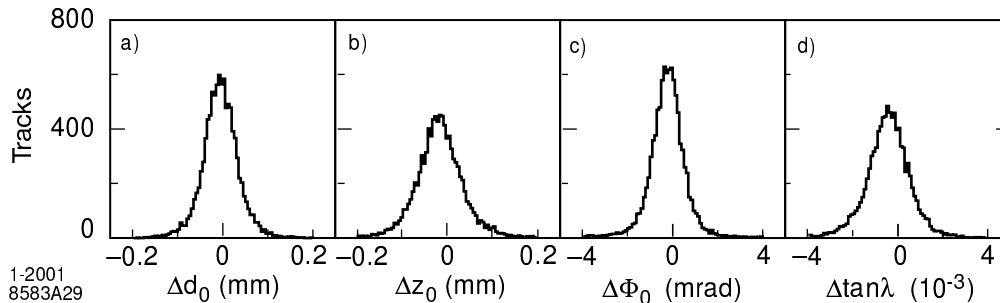


Figure 3.8: The deviation of the track parameters from separate fits to each half of cosmic ray muon tracks. The parameters shown are the distance of closest approach in the transverse plane ( $d_0$ ), the direction in that plane  $\Phi_0$ , and the distance of closest approach along the detector axis ( $z_0$ ), as well as the dip angle  $\lambda$ . The width of the distributions give the resolution on these parameters as determined by the reconstruction code.

The TrkFixup procedure was added to track reconstruction in a more recent version of the reconstruction software to better filter out poorly reconstructed tracks and tracks which travel back to the detector axis after reaching a maximum distance. A thorough description of the efficiency of the entire procedure can be found in [24]. Track parameter resolutions are studied by fitting cosmic rays passing through the detector as two separate tracks and comparing their respective parameters at the IP. The resulting distribution of deviations is shown in Fig. 3.8.

Electromagnetic showers in the calorimeter will typically spread beyond the dimensions of a single crystal, and so reconstruction in the calorimeter involves finding clusters of energy deposits. In addition, calorimeter reconstruction must

also identify when what would otherwise be one cluster originated from two distinct showers which have overlapped, e.g. from a highly boosted  $\pi^0$  decay. Clusters are seeded by individual crystal energy deposits above 10 MeV. Surrounding crystals are added if their energy is above 1 MeV, or if they are adjacent to a crystal above 3 MeV. Crystals that are local maxima are identified on the requirement that they both exceed the energy of their neighbors and their energy times the factor  $(N - 2.5)/2$ , with  $N$  the number of adjacent crystals with  $E > 2$  MeV, is larger than the energy of any neighboring crystal above 2 MeV.

The cluster is then divided into bumps based on each of the identified local maxima by weighting each crystal by a factor exponential in its distance to the currently computed centroid. The bump energy is then computed as a sum over each crystal energy multiplied by the bump weight for that crystal. The centroid is then recomputed (using a logarithmic energy weighting) and the process repeated iteratively until the centroid is stable. A small correction ( $\pm 2.6$  mrad) is applied to the polar angle of the centroid in the forward and backward directions to account for the fact that the calorimeter is slightly non-projective. Bumps with tracks pointing to them are associated with the track, and the remaining bumps are neutral candidates, usually assuming a photon hypothesis.

### 3.3.2 Simulation

The production of simulated events for use in *BABAR* analyses may be broken down into several stages. The initial state is produced using one of several gen-

erators EVTGEN [25] for  $B\bar{B}$ , JETSET [26] for  $q\bar{q}$ , or KK2F [27] for leptons, with kinematics accounting for the spread in beam energies at PEP-II. Partonic initial states are fragmented with JETSET, and color-neutral particles are decayed using EVTGEN, selecting from a list of exclusive decay modes with various corresponding decay models giving the angular distribution to be sampled. Hadronic or semileptonic modes which are not explicitly parameterized are generated semi-inclusively by generating the quark model level decays and calling JETSET to fragment the result. The resulting decay is rejected if it is already listed among the exclusive decays in EVTGEN, and accepted otherwise.

This process of decaying particles proceeds recursively until only very long lived particles remain ( $\gamma, p, n, \mu, e$  and their respective antiparticles). Each particle with a non-negligible lifetime has a lifetime chosen at generation, and long lived particles which may decay within the tracking volume are flagged for special treatment. The whole event is boosted into the lab frame and the list of stable and long-lived particles is passed on to a full GEANT4 [28] detector simulation to simulate their propagation through and interaction with the detector and its magnetic field. Long lived particles that reach their decay flight length inside the detector without being absorbed are decayed as generated.

The analyses presented in this dissertation make use of simulated generic  $B\bar{B}$ , and  $\mathcal{T}(nS)$  decays, as well as  $c\bar{c}$  and  $uds$  events for each of BABAR's data collection periods. Of particular interest are events generated specifically for the analysis in Chapter 4 for each of the points comprising the FinalScan (discussed in the next section). The following modes were generated:  $\mu^+\mu^-$  (1, 140/pb<sup>-1</sup>),  $c\bar{c}$  (2, 600/pb<sup>-1</sup>),

$uds$  ( $3,550/\text{pb}^{-1}$ ),  $B\bar{B}$  ( $2,000/\text{pb}^{-1}$ ),  $B_s\bar{B}_s$  ( $1,200/\text{pb}^{-1}$ ),  $B_s^*\bar{B}_s$  ( $600/\text{pb}^{-1}$ ), and  $B_s^*\bar{B}_s^*$  ( $600/\text{pb}^{-1}$ ).

Table 3.1: Signal events generated and run conditions used for deuteron simulation

Run Period	Events	Conditions
Run1	100k	Oct2000
Run2	300k	Jan2002/Feb2002
Run3	160k	Mar2003
Run4	500k	Feb2004
Run5	650k	Dec2005/Jan2006
Run6	380k	May2007

Custom simulation was also generated for the analysis described in Chapter 5 for a sample of simulated deuterons originating from the interaction point. Deuterons are used rather than antideuterons because the version of GEANT4 used in *BABAR* does not include antideuterons. This sample consists of events with a single deuteron, two antibaryons, and five light hadrons ( $\pi^\pm, \pi^0, K^\pm$ ) equally in every combination allowed by conservation of baryon number, charge, and strangeness, distributed evenly in the available phase space. The total number of events generated are  $\approx 1 \times 10^6$  million at the  $\Upsilon(2S)$ ,  $0.1 \times 10^6$  at the  $\Upsilon(3S)$  and  $2.11 \times 10^6$  at the  $\Upsilon(4S)$ . The  $\Upsilon(4S)$  events are distributed in running times according to luminosity (see Table 3.1).

### 3.4 The *BABAR* Dataset

During its operation life, *BABAR* collected data over seven running periods. Runs 1-6 consist of data taking at  $E_{\text{CM}} = m_{\Upsilon(4S)}$ , taking advantage of the reaction

Table 3.2: *BABAR* Runs 1-6 summary

Run Period	Date	On-Resonance	Off-Resonance
Run1	Oct1999-Oct2000	20.4 fb <sup>-1</sup>	2.56 fb <sup>-1</sup>
Run2	Feb2001-Jun2002	61.3 fb <sup>-1</sup>	6.83 fb <sup>-1</sup>
Run3	Dec2002-Jun2003	32.3 fb <sup>-1</sup>	2.44 fb <sup>-1</sup>
Run4	Sep2003-Jul2004	99.6 fb <sup>-1</sup>	10.02 fb <sup>-1</sup>
Run5	Apr2005-Aug2006	132.3 fb <sup>-1</sup>	14.28 fb <sup>-1</sup>
Run6	Jan2007-Sep2007	78.3 fb <sup>-1</sup>	7.75 fb <sup>-1</sup>

$e^+e^- \rightarrow \Upsilon(4S) \rightarrow B\bar{B}$  to collect a sample of 464 million  $B\bar{B}$  pairs from late October 1999 to September of 2007 [29]. The  $\Upsilon(4S)$  running periods also include data taken at a CM energy 40 MeV below the  $\Upsilon(4S)$  mass (20 MeV below the  $B\bar{B}$  threshold) as a sample for off-resonance subtraction. Table 3.2 gives the dates of each run period and the approximate integrated luminosity collected (values from Ref. [29]). This entire dataset is used in Chapter 5 to measure continuum production of antideuterons, while a subset of Run6 On- and Off-Resonance data are used in Chapter 4 to estimate  $B\bar{B}$  and continuum backgrounds in that analysis.

Table 3.3: *BABAR*  $\Upsilon$  running summary

Run Period	Date	On-Resonance	Off-Resonance
$\Upsilon(3S)$	Dec2007-Feb2008	28.0 fb <sup>-1</sup>	2.62 fb <sup>-1</sup>
$\Upsilon(2S)$	Feb2008-Mar2008	13.6 fb <sup>-1</sup>	1.42 fb <sup>-1</sup>

During *BABAR*'s seventh run, data collection was performed to find and run on the peaks of the  $\Upsilon(3S)$  and  $\Upsilon(2S)$  resonances in order to collect very large ( $\mathcal{O}(10^8)\Upsilon$ ) samples for bottomonium spectroscopy. These data eventually led to the discovery of the  $\eta_b$ , the ground state of the  $b\bar{b}$  system [30]. Data were also collected

below-resonance for these samples as well (30 MeV below the nominal running point), and the samples are summarized in Table 3.3. These data are used in Chapter 5 to measure antideuteron production in the decay of  $\Upsilon(2S)$ ,  $\Upsilon(3S)$  and  $\Upsilon(1S)$  mesons.

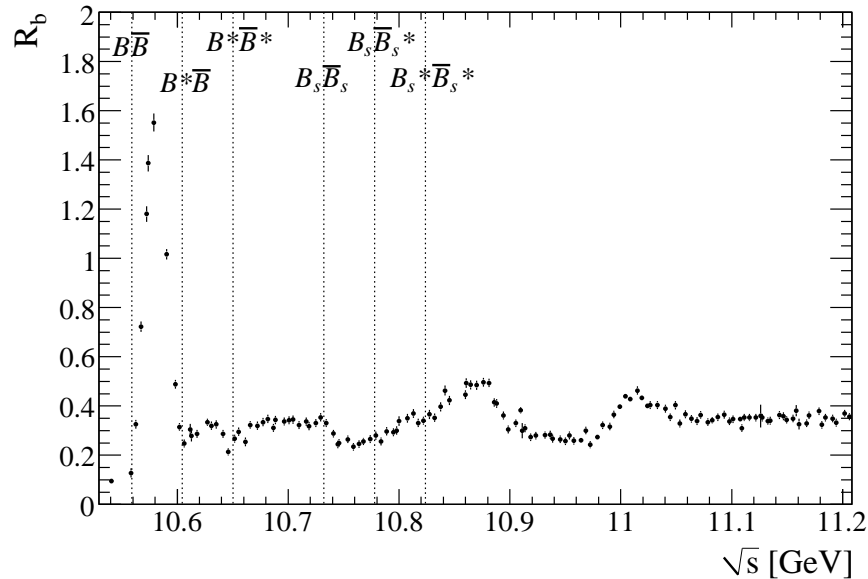


Figure 3.9: Measurement of  $R_b$  in the FinalScan dataset from [31]

Finally, beginning in the last days of March of 2008, a scan was performed adjusting the collision energy in steps of 5 MeV starting at the  $B\bar{B}$  threshold and ending at 11.2 GeV, just short of the  $\Lambda_b\bar{\Lambda}_b$  threshold. Approximately  $25 \text{ pb}^{-1}$  were collected at each point. In addition, several  $100 \text{ pb}^{-1}$  points were collected at various energies around the feature known as the  $\Upsilon(11020)$  resonance. A measurement of  $R_b \equiv \sigma_{b\bar{b}}/\sigma_{\mu\mu}^0$  was performed in Ref. [31], and I include the result in Fig. 3.4 to illustrate the features contained in the scan dataset. In total,  $4.1 \text{ fb}^{-1}$  were collected, with  $3.3 \text{ fb}^{-1}$  above the  $B_s$  threshold. This is the primary dataset for the measurement in Chapter 4.

## Chapter 4

### Measurement of $\mathcal{B}(B_s \rightarrow \ell\nu X)$

As discussed in Chapter 2, the current understanding of the  $B_s$  system is less advanced in comparison to the  $B^0$  and  $B^\pm$  systems. The lack of an analog to the  $\Upsilon(4S) \rightarrow B\bar{B}$  production mechanism for  $B_s$  has prevented progress on measuring absolute branching ratios and studying inclusive processes. And  $\Upsilon(5S)$  running at the  $B$ -factories is hindered by small cross-sections and poorly-measured production rates of  $B$  and  $B_s$  at that energy. From here on we refer to  $B^0$  and  $B^\pm$  collectively as  $B$ . Away from the  $\Upsilon(5S)$  peak, production of  $B_s$  is even less well-understood: while there have been several measurements of  $B_s$  production relative to  $B$  at the  $\Upsilon(5S)$  peak [32], there is little information about production elsewhere in the region, which would be useful to test theoretical predictions such as the coupled-channel analysis of  $B\bar{B}$  production in electron-positron annihilation above threshold performed by Törnqvist [33].

The inclusive semileptonic decay branching fraction is one piece of information in particular that suffers from the lack of a clean production mechanism for  $B_s$  mesons. This quantity allows for tests of spectator calculations as well as of more sophisticated theoretical predictions of the rate. It also provides a normalization for (semi)exclusive measurements involving leptons in the final states at, for example, LHCb. Measurements of  $\mathcal{B}(B \rightarrow \ell\nu X)$  performed at the  $\Upsilon(4S)$  [34, 35, 36] are

currently systematically limited, with world-average values of the individual isospin states of  $\mathcal{B}(B^+ \rightarrow \ell\nu X) = (10.99 \pm 0.28)\%$  and  $\mathcal{B}(B^0 \rightarrow \ell\nu X) = (10.33 \pm 0.28)\%$  [13]. By contrast, the measurement presented here is the first measurement of the fully-inclusive semileptonic branching fraction of the  $B_s$  meson to be published. The most relevant previous work is a measurement of the semi-inclusive branching fraction  $\mathcal{B}(B_s \rightarrow D_s \ell\nu X) = (7.6 \pm 2.4)$  [37] performed at the Z pole by the ALEPH Collaboration.

The goal of this analysis is to measure simultaneously both the inclusive semileptonic branching fraction  $\mathcal{B}(B_s \rightarrow \ell\nu X)$  and the production of  $B_s$  mesons relative to the total production rate of  $B_s$  and  $B$  mesons ( $f_s$ ) as a function of CM energy. For this analysis, we use the FinalScan dataset (4.15 fb<sup>-1</sup> taken above the  $\Upsilon(4S)$  resonance, described in more detail in section 3.4). In addition, we make use of a dataset consisting of 18.55 fb<sup>-1</sup> taken on the  $\Upsilon(4S)$  resonance and a dataset of 7.89 fb<sup>-1</sup> taken at a CM energy 40 MeV below the  $\Upsilon(4S)$  to estimate contributions from  $B\bar{B}$  and continuum  $e^+e^- \rightarrow q\bar{q}$ , respectively.

## 4.1 Analysis Technique Overview

This analysis makes use of inclusive measurements of the rate of  $b$ -like hadronic events, the production rate of events containing  $\phi$  mesons, and the production rate of events containing both a high-momentum lepton and  $\phi$  mesons to determine  $f_s$  in different bins of CM energy ( $E_{\text{CM}}$ ), and to obtain simultaneously a measurement of  $\mathcal{B}(B_s \rightarrow \ell\nu X)$ . The technique is based on the observation that decays of  $B_s$  mesons

are much more likely to contain  $\phi$  mesons than  $B$  decays, due to the CKM-favored decay chain  $b \rightarrow c \rightarrow s$ , which in the simplest Cabibbo-favored spectator diagrams leads to  $B_s \rightarrow D_s \rightarrow \phi$  in inclusive transitions (Fig. 4.1). By contrast,  $\phi$  production in  $B$  decay has no such straightforward channel, needing to proceed through either color-suppressed decays of  $D$  mesons or after  $D_s$  production in  $b \rightarrow c\bar{c}s$  decay (Fig. 4.2), which quark-model calculations suggest to be only  $\approx 15\%$  of all  $B$  decays. Indeed, the inclusive branching fraction  $\mathcal{B}(B \rightarrow \phi X)$  is measured to be  $(3.41 \pm 0.13)\%$  [38], whereas the combination  $\mathcal{B}(B_s \rightarrow D_s X) \times \mathcal{B}(D_s \rightarrow \phi X)$  is estimated to be  $\approx 15\%$ , as the world average value of  $\mathcal{B}(B_s \rightarrow D_s X)$  is  $(0.93 \pm 0.25)$  [13] while the value for the latter is  $(0.157 \pm 0.01)$  [13]. This large difference in rates is the primary means for separating the  $B_s$  contribution from the others in the inclusive quantities to be measured.

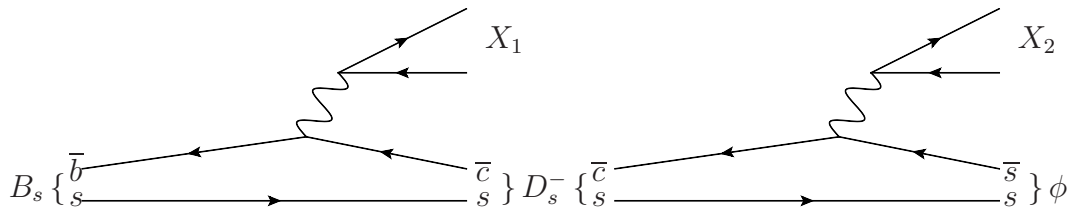


Figure 4.1: One possible spectator decay chain leading to  $\phi$  production in  $B_s$  decay.  $X_1$  and  $X_2$  may be any of the possible products of the  $b \rightarrow c$  transition.

The difference in  $\phi$  production rate discussed above is also true in events with semileptonic  $B_{(s)}$  decays, with the  $\phi$  meson originating either directly from the  $B_{(s)}$  which decayed semileptonically in the Cabibbo-favored chain or from the decay of the other  $B_{(s)}$  meson in the event. To reduce the contribution from events where products of hadronic  $B_{(s)}$  decays have themselves decayed semileptonically, we select

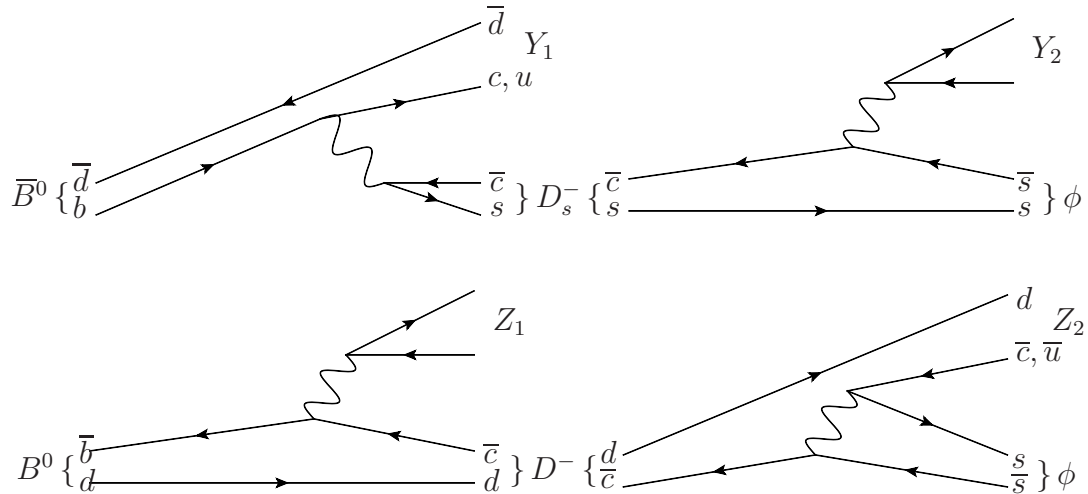


Figure 4.2: Two possible sets of spectator diagrams for  $\phi$  production in  $B$  decay. The first process is suppressed both by the number of final states accessible to the virtual  $W$  and also kinematically due to the pair of charm quarks in the final state, while the second process involves a color-suppressed  $D$  decay. Note also that in contrast to the fully-inclusive systems  $X_1$  and  $X_2$  in Fig. 4.1, both processes involve an exclusive process at the quark level.

only leptons with high momentum in the CM frame. The selection is discussed in more detail below.

In summary, the procedure for extracting the quantities of interest can be summarized as follows:

- The ratio of the rates of  $e^+e^- \rightarrow b$ -hadron events to  $e^+e^- \rightarrow \mu^+\mu^-$  is measured in bins of CM energy based on (slightly modified) versions of the event filters described in Section 3.3.1. Residual continuum  $e^+e^- \rightarrow q\bar{q}$  contributions are subtracted based on measurements made below the  $B\bar{B}$  threshold. We refer to the result as the MultiHadronic yield.
- The yield of events containing  $\phi$  mesons in  $b$  hadron-like events is determined by reconstructing  $\phi \rightarrow K^+K^-$  decays and fitting the invariant mass distribution of the  $K^+K^-$  pairs. Residual continuum contributions are subtracted as

above, and we refer to the result as the ” $\phi$ -yield”. This measurement is used in conjunction with the previous to determine  $f_s$  as a function of CM energy.

- The yield of events containing both a  $\phi$  meson and a high-momentum lepton is similarly measured and corrected for continuum contributions. The result is referred to as the ” $\phi$ -lepton” yield. This, in combination with  $f_s$ , allows the semileptonic branching fraction to be extracted via a  $\chi^2$  minimization procedure.

## 4.2 Analysis Method

The simulation sample for this analysis (described previously) is divided into two sets; one is a mixture of the various modes intended to roughly represent the contents of the final scan dataset. This is referred to as the mixed sample. A sample consisting of approximately 20 times the number of  $B^{(*)}\bar{B}^{(*)}$  events relative to the mixed sample is used as a supplemental high-statistics test sample. Finally, the remaining FinalScan simulation is used to evaluate the various energy-dependent efficiencies needed for this analysis.

The mixed sample is constructed by mixing simulated events according to their relative cross-sections, measured at the  $\Upsilon(4S)$  and scaled by  $m_{\Upsilon(4S)}^2/E_{\text{CM}}^2$ , in combination with the measured integrated luminosities at each point for continuum and dimuon events. Then ad-hoc choices of  $R_B = \sigma_{B_q\bar{B}_q}/\sigma_{\mu\mu}$  (motivated by the  $R_b \equiv \sigma_{b\bar{b}}/\sigma_{\mu\mu}$  measurement in [31]) and  $f_s = N_{B_s}/(N_{B_s} + N_B)$  (purely ad-hoc) are used to determine the number of  $B\bar{B}$  and  $B_s\bar{B}_s$  simulated events to add to the mix

(Fig. 4.3). The  $B_s\bar{B}_s$  sample consists of either 100%  $B_s\bar{B}_s$ , 75%-25%  $B_s\bar{B}_s B_s^*\bar{B}_s$  or 50%-25%-25%  $B_s\bar{B}_s B_s^*\bar{B}_s B_s^*\bar{B}_s$  depending on which thresholds are open at the given value of  $E_{\text{CM}}$ . To distinguish these choices from the (unknown) true values of  $R_b$  and  $f_s$ , we use the symbols  $\tilde{R}_b$  and  $\tilde{f}_s$  for our choices.

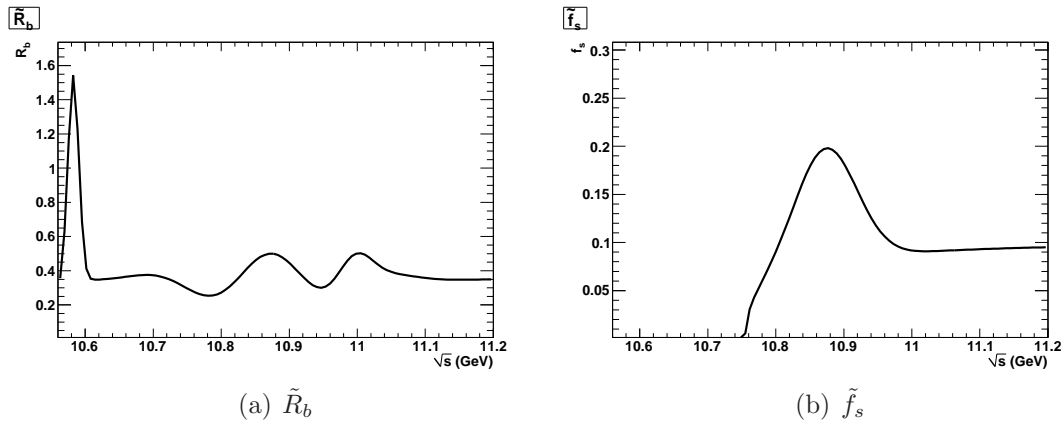


Figure 4.3:  $\tilde{R}_b$  and  $\tilde{f}_s$  for FinalScan mixed simulation sample

To ensure adequate statistics in each bin, the scan points (nominally 5 MeV steps) are regrouped into 15 MeV wide bins of CM energy ( $E_{\text{CM}}$ ). In each bin, events are analyzed as described in the following sections.

### 4.2.1 Event Selection

For this analysis, two separate event-level selections are used: (1) to select  $b$  hadron events, and (2) to select  $e^+e^- \rightarrow \mu^+\mu^-$ . The hadronic event selection is based on the *BABAR* event filter **isBCMutiHadron** described in section 3.3.1, with a modified requirement on the ratio of the second to the zeroth Fox-Wolfram moments[22]. The dimuon selection is based on the isBCMumu event filter. The requirements for these selections are listed in Table 4.1.

Table 4.1: Event selection criteria. \* Total energy is computed assuming the pion mass for charged tracks. As in Sec. 3.3.1,  $p_n$  refers to the  $n$ th highest momentum track found in the event.

Multi-hadronic selection	Dimuon selection
Passes BGFMultiHadron (Sec. 3.3.1)	Passes BGFMuMu (Sec. 3.3.1)
$\geq 3$ passing GoodTracksLoose	Invariant mass $(p_1, p_2) > 7.5$ GeV
4.5 GeV Total Energy*	$p_1$ and $p_2$ colinear to within $10^\circ$
Prim. vertex within 0.5 cm in $r$ , 6 cm in $z$	$\cos \theta_{p_1} < 0.7485$
$R2 < 0.2^\dagger$	$p_1$ energy in EMC $> 0, < 1$ GeV

For each type of simulation sample (generic  $B\bar{B}$ , generic  $B_s^{(*)}\bar{B}_s^{(*)}$ , generic  $u\bar{u}, d\bar{d}, s\bar{s}$ , and generic  $c\bar{c}$ ) the multihadronic selection is applied and the efficiency of the selection is computed at each scan point. The resulting estimated efficiency is fit to a polynomial to describe the efficiency as a function of  $E_{\text{CM}}$ ; this polynomial is either linear or quadratic, where the decision to use one or the other is made on the basis of whether or not a statistically significant (nonzero to better than two times its uncertainty) quadratic term can be determined by the fit. Other efficiency factors are similarly computed and fit so that all efficiencies used in this analysis are functions of  $E_{\text{CM}}$ . The fits to the multihadron efficiencies are shown in Fig. 4.4.

In each CM bin the number of events passing the hadronic event selection is normalized to the number of events passing the dimuon selection, so that the resulting number is approximately independent of luminosity.

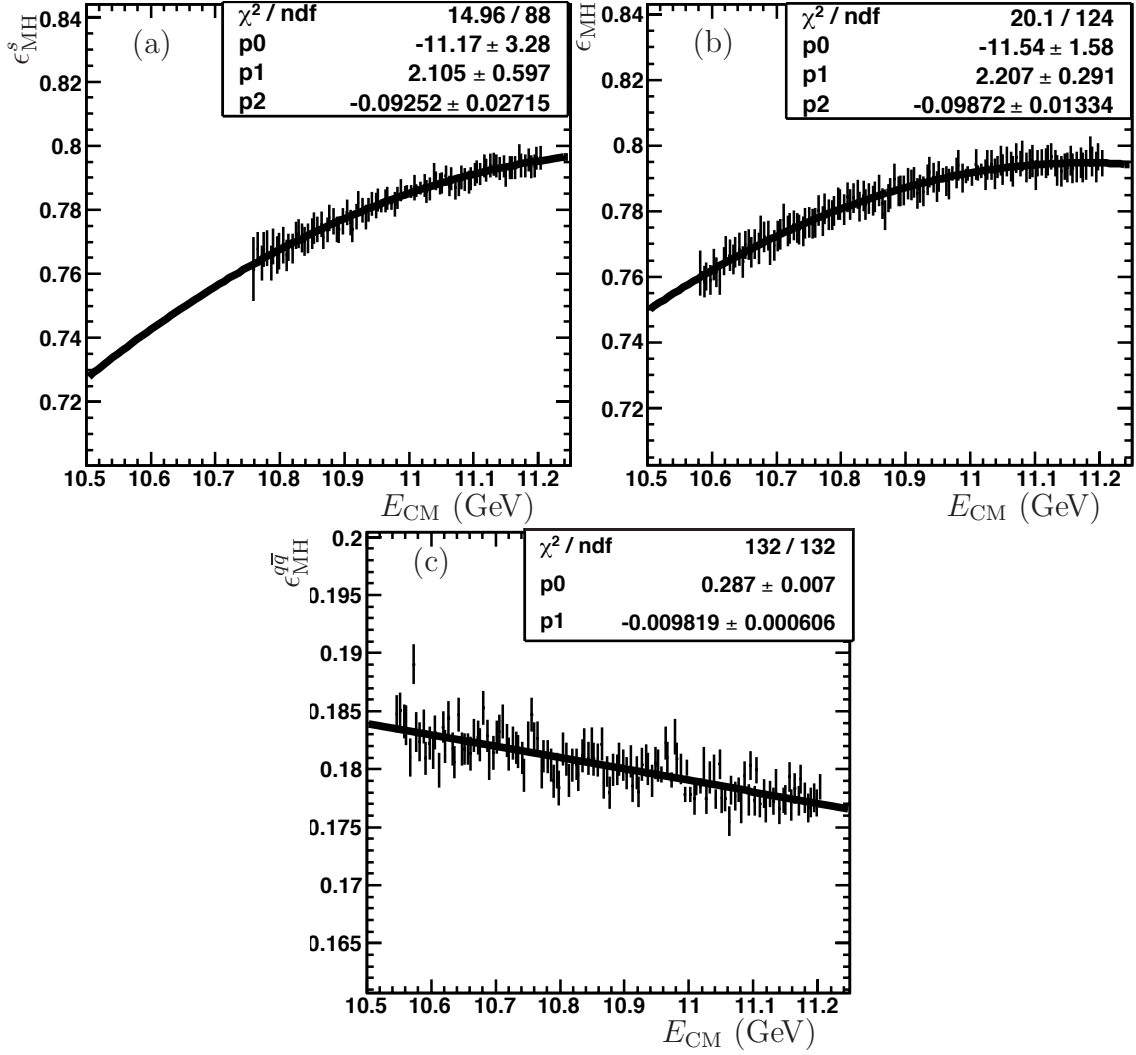


Figure 4.4: MultiHadron selection efficiencies as a function of CM energy in simulated (a)  $B_s^{(*)} \bar{B}_s^{(*)}$  events, (b)  $B \bar{B}$  events, (c) continuum events.

#### 4.2.2 Inclusive $\phi$ reconstruction and $\phi$ -lepton selection

We reconstruct  $\phi$  meson candidates in events passing the multihadronic selection by forming pairs of oppositely-charged tracks, requiring the tracks to pass the loosest level of charged  $K$  particle identification. The track pair is fitted to a common vertex, and those for which the  $\chi^2$  cumulative probability is greater than 0.1% are selected as  $\phi$  candidates. This raw list of candidates is then reduced by

selecting at most one  $\phi$  candidate per event. The candidate chosen is the one with the best-identified kaon daughters according to the following criteria: each daughter is assigned a weight based on the highest level of particle identification criteria it has passed. The various kaon PID levels and their respective weights are: (super loose, 1; very loose, 3; loose, 7; tight, 15; very tight, 31; super tight, 63). The candidate with the largest sum of daughter weights is selected if the sum is greater than 65, otherwise no candidate is selected for the event. The above requirement effectively imposes the condition that at least one daughter passes the super tight criteria while the other passes at least the very loose criteria. The mass distribution of the  $\phi$  candidates is fit, using a procedure described later in this chapter, to determine the yield of  $\phi$  mesons in the sample.

To construct the  $\phi$ -lepton sample, the events are also examined for the presence of a track with momentum greater than 900 MeV/ $c$  that passes tight PID criteria identifying it as an  $e$  or  $\mu$  candidate. A chart illustrating the sources of leptons selected in  $B_s\bar{B}_s$  simulation is shown in Fig. 4.5: it can be seen that leptons from  $B_s$  semileptonic decay dominate the sample, with leptons from charm semileptonic decays representing less than 1/4 of the total events.

To determine the total yield of  $\phi$  mesons in a given CM energy bin, the invariant mass distribution of the  $\phi$  candidates is fit to the function

$$f(M; N, b, c) \equiv NV(m_{KK}; m_\phi, \Gamma_\phi, \sigma) + Nc(1 + bm_{KK})\sqrt{1 - \left(\frac{2m_K}{m_{KK}}\right)^2}, \quad (4.1)$$

with  $m_K$  the world-average mass value [13] of the  $K^\pm$ .  $V(m_{KK}; m_\phi, \Gamma_\phi, \sigma)$  is a

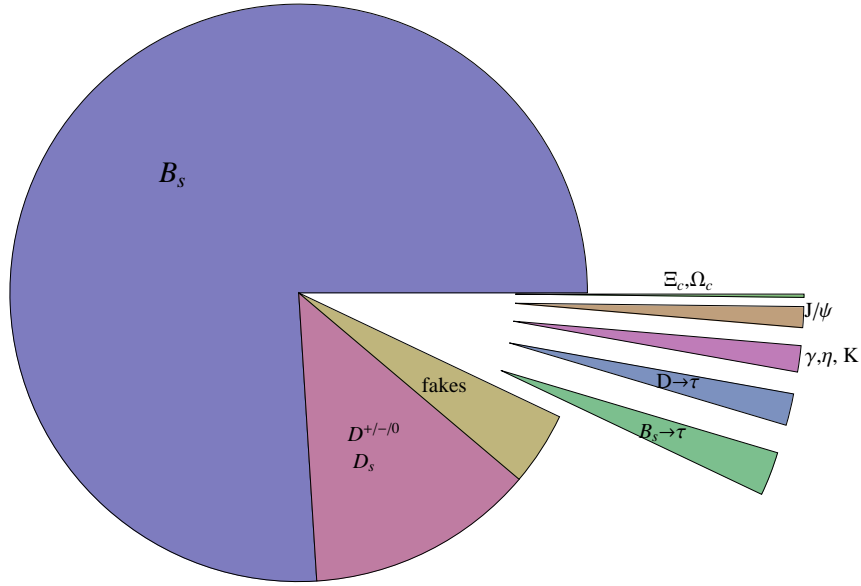


Figure 4.5: A chart of the parent of selected leptons in  $B_S\bar{B}_S$  simulation events

Voigt profile (the convolution of a Breit-Wigner function  $1/((m_{KK} - m_\phi)^2 + \Gamma_\phi^2/4)$  with a Gaussian resolution function) normalized to unity, so that  $N$  is the number of events in the peak. We fix the mean ( $m_\phi$ ) and Breit-Wigner width ( $\Gamma_\phi$ ) to the world average values of the  $\phi$  mass and natural width [13], and the width of the Gaussian resolution ( $\sigma$ ) by first performing fits in all CM energy bins with the parameter left free. The fit is then repeated, fixing  $\sigma_\phi$  to the weighted mean of all of the resolution values obtained across the scan. The value in data determined by this method is  $\sigma = 1.61 \pm 0.04(\text{stat})$  MeV. The combinatoric background is modeled as the product of a linear term and a threshold cutoff function parameterized by the slope of the linear term ( $b$ ) and a relative scaling ( $c$ ). Sample results of the fit for a particular bin of  $E_{\text{CM}}$  are shown in Fig. 4.6. The remainder may be found in Appendix A.

The efficiency of this procedure in estimating the number of events containing a  $\phi$  meson in various simulated event types is shown in Fig. 4.7. For  $B\bar{B}$  and

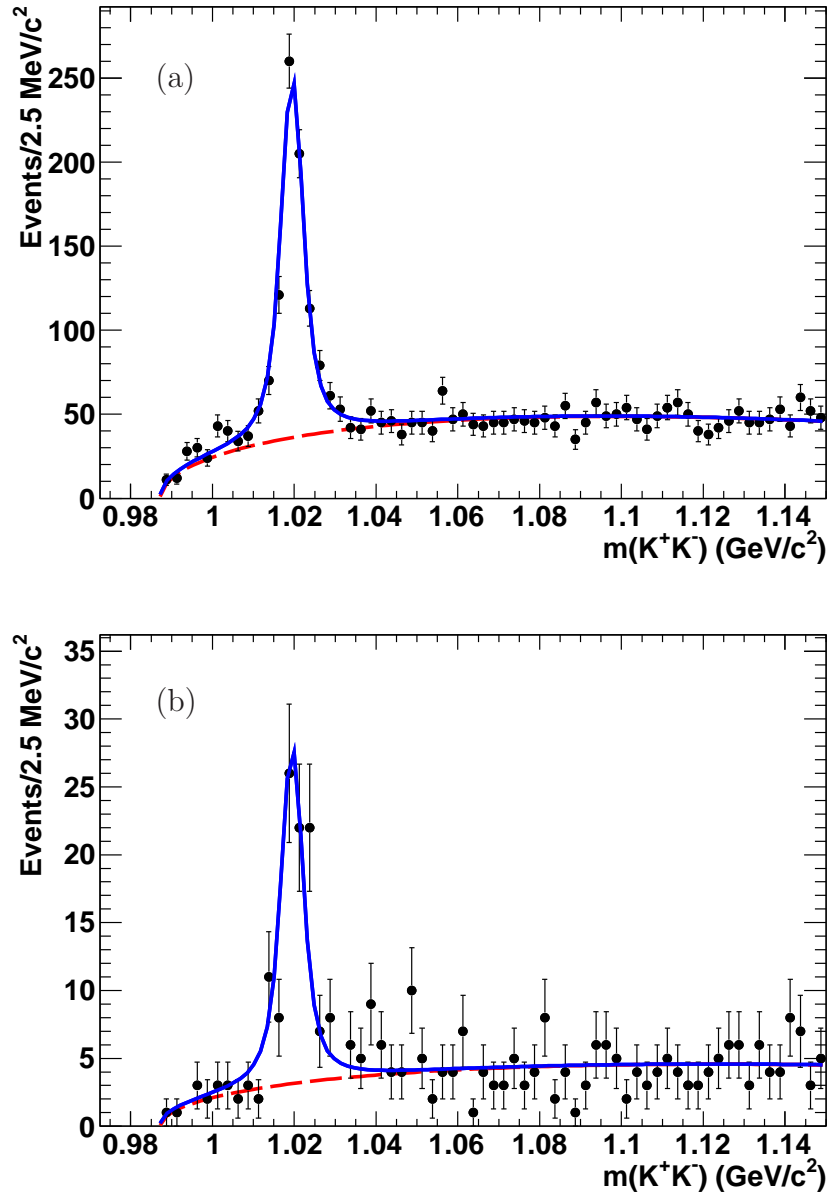


Figure 4.6: Invariant mass distribution of  $\phi \rightarrow K^+K^-$  candidates in (a) the  $\phi$  sample and (b) the  $\phi$ -lepton sample in the CM energy bin  $10.8275 \text{ GeV} \leq E_{\text{CM}} \leq 10.8425 \text{ GeV}$ . The background shape is shown by the dashed curve and the total fit by the solid curve.

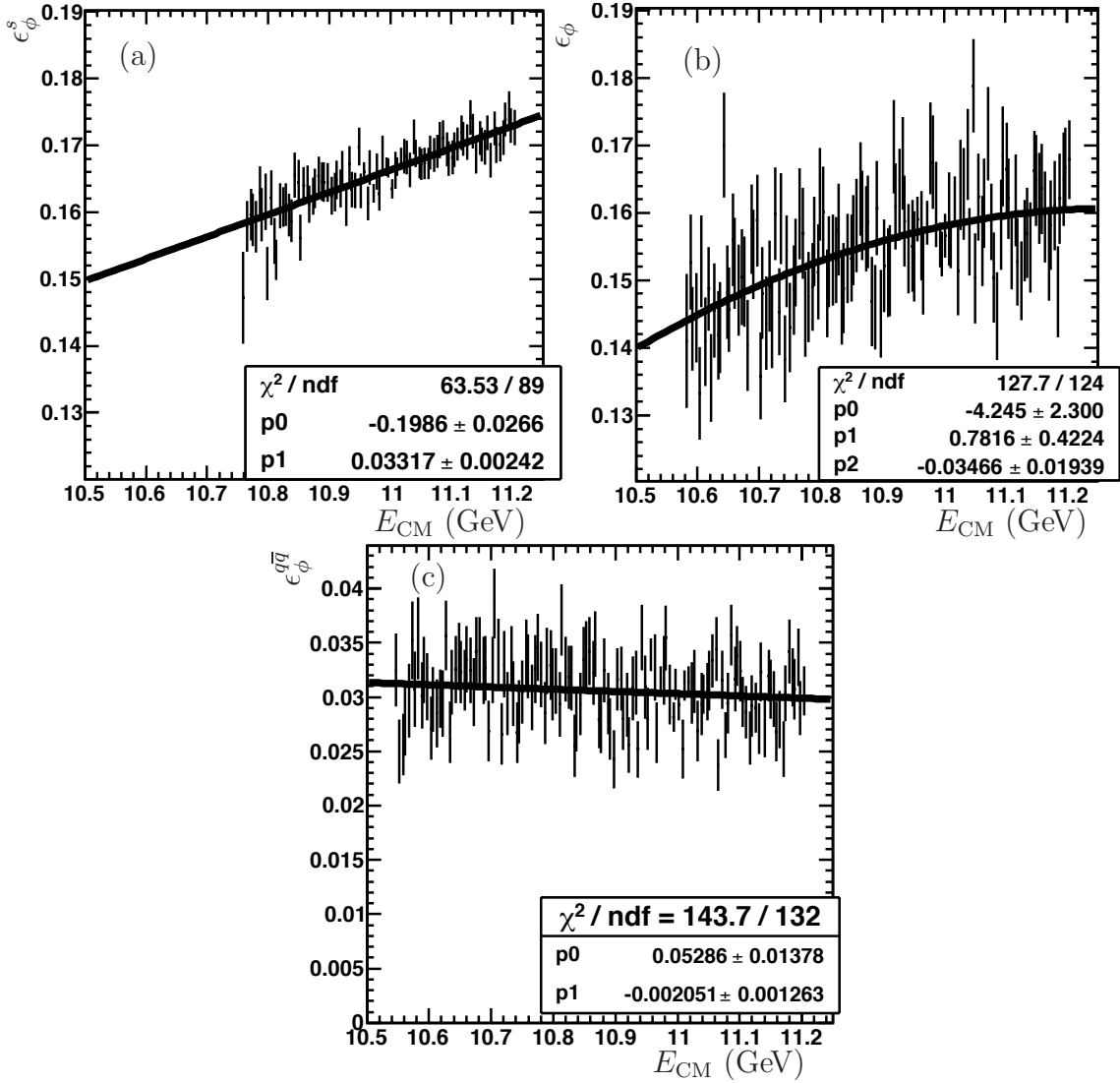


Figure 4.7:  $\phi$  counting efficiency in simulated (a)  $B_s^{(*)} \bar{B}_s^{(*)}$  events, (b)  $B \bar{B}$  events, (c) continuum events.

continuum events, only the ratio of  $\phi$ -lepton efficiencies at different energies will be used. So for those samples the fitted number of events at each point is normalized to the total number of generated events. The results are shown in Fig. 4.8.

For  $B_s$  events, we define four separate efficiencies with respect to the  $\phi$ -lepton yield:

- The  $\phi$ -lepton efficiency in events with one semileptonic  $B_s$  decay. ( $\epsilon_{\phi\ell}^s$ )

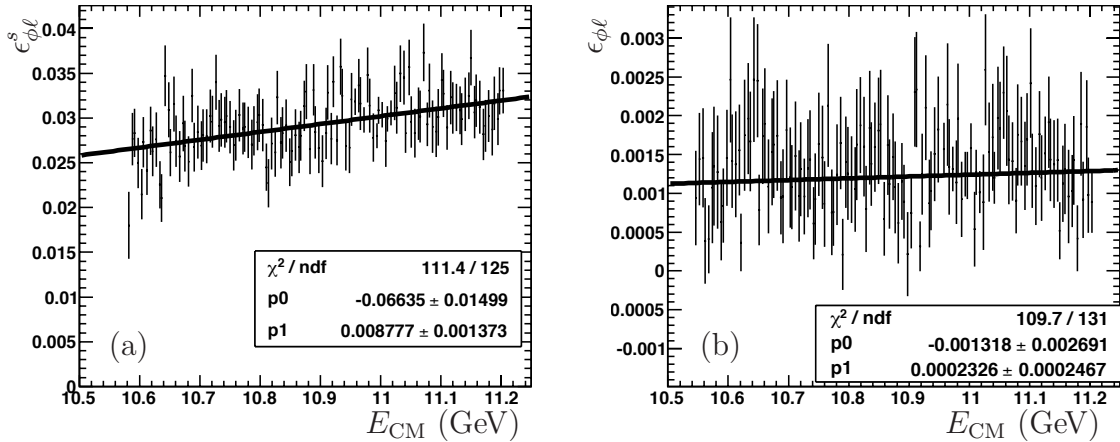


Figure 4.8:  $\phi$ -lepton efficiency running in simulated (a)  $B_s \bar{B}_s$  events and (b) continuum events. These quantities are not normalized as true efficiencies as only their ratios at different energies are used.

- The  $\phi$ -lepton efficiency in events with both  $B_s$  mesons decaying semileptonically. ( $\epsilon_{\phi\ell\ell}^s$ )
- The lepton selection efficiency (per track) for leptons from charm decays. ( $\epsilon_\ell^D$ )
- The  $\phi$  efficiency in events in which a lepton was found but neither  $B_s$  decayed semileptonically. ( $\epsilon_\phi^D$ ).

The dependence of these four quantities on  $E_{\text{CM}}$  is shown in Fig. 4.9.

As in the event selection, the yields from the  $\phi$  and  $\phi$ -lepton fits in each bin of  $E_{\text{CM}}$  are normalized by the number of events passing the dimuon event selection.

### 4.2.3 Below-threshold Subtraction

After each yield is normalized to the number of dimuon events, the remaining contributions of continuum  $e^+e^- \rightarrow q\bar{q}$ ,  $q = u, d, s, c$  events to each of the measured yields are removed. This is accomplished by measuring each of the corresponding yields in the below-threshold data sample. The below-threshold value of each yield is

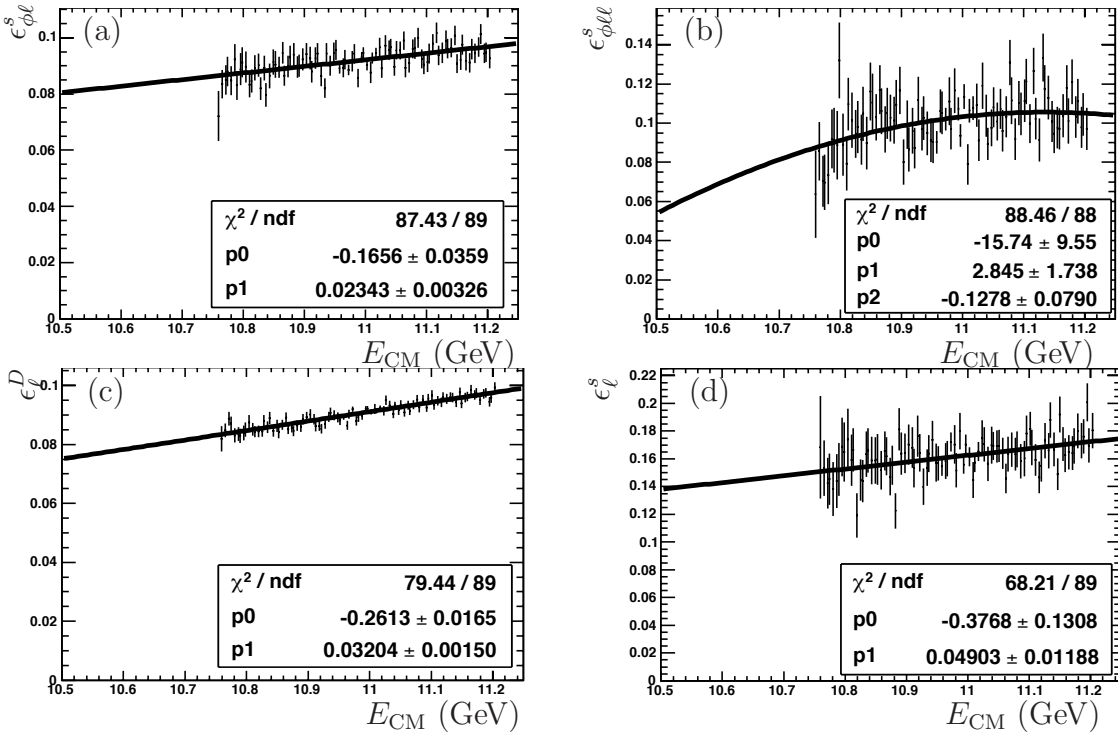


Figure 4.9: (a)  $\phi$ -lepton efficiency in events with one semileptonic  $B_s$  decay, (b)  $\phi$ -lepton efficiency in events with both  $B_s$  mesons decaying semileptonically, (c) the lepton selection efficiency (per track) for leptons from charm decays, (d)  $\phi$  efficiency in events in which a lepton was found but neither  $B_s$  decayed semileptonically

subtracted from each  $E_{CM}$  bin after corrections for energy-dependent reconstruction efficiencies as evaluated in simulation.

This procedure is only strictly correct when the cross sections for the relevant processes scale with CM energy in the same way as  $\sigma(e^+e^- \rightarrow \mu^+\mu^-)$ , that is  $1/E_{CM}^2$ . This is not necessarily the case for some processes contributing to the yield of  $b$  hadron events. In particular, the presence of initial state radiation (ISR)  $e^+e^- \rightarrow \gamma\gamma(1S, 2S, 3S)$  and two photon  $e^+e^- \rightarrow e^+e^-\gamma^*\gamma^* \rightarrow e^+e^-X_h$  events, which do not scale with energy as  $1/E_{CM}^2$ , may affect the below-threshold subtraction by introducing a small energy dependence on the estimated yield that must be subtracted from each bin. The average size of this effect is estimated to be less than 2%

of the below-resonance event yield and is accounted for in systematic uncertainties in the final result, which are discussed in greater detail in section 4.4.

#### 4.2.4 Extraction of $f_s$ and $\mathcal{B}(B_S \rightarrow \ell\nu X)$

After the removal of continuum contributions via below-threshold subtraction, the yields from  $b$  events can be expressed as a sum of contributions from  $B\bar{B}$  and  $B_s\bar{B}_s$  events, the cross section ratio  $R_B \equiv \sum_{q=\{u,d,s\}} \sigma(e^+e^- \rightarrow B_q\bar{B}_q) / \sigma_{\mu^+\mu^-}$ , and the related reconstruction efficiencies, as follows:

$$C_h = R_B [f_s \epsilon_h^s + (1 - f_s) \epsilon_h] \quad (4.2)$$

$$C_\phi = R_B [f_s \epsilon_\phi^s P(B_s\bar{B}_s \rightarrow \phi X) + (1 - f_s) \epsilon_\phi P(B\bar{B} \rightarrow \phi X)] \quad (4.3)$$

$$C_{\phi\ell} = R_B [f_s \epsilon_{\phi\ell}^s P(B_s\bar{B}_s \rightarrow \phi\ell X) + (1 - f_s) \epsilon_{\phi\ell} P(B\bar{B} \rightarrow \phi\ell X)] \quad (4.4)$$

(with energy dependence implicit in all terms here and elsewhere), where

$$f_s \equiv \frac{N_{B_s}}{N_{B_u} + N_{B_d} + N_{B_s}} \quad (4.5)$$

and  $\epsilon_X(\epsilon_X^s)$  is the efficiency for a  $B_{u,d}$  ( $B_s$ ) pair to contribute to the event or  $\phi$  yields as described above. Not all of the relevant efficiencies in  $B_s$   $\phi$ -lepton events appear yet in the equations, as  $\epsilon_{\phi\ell}^s P(B_s\bar{B}_s \rightarrow \phi\ell X)$  must first be broken into contributions from different processes. The products  $\epsilon_{\phi\ell} P(B\bar{B} \rightarrow \phi\ell X)$  and  $\epsilon_\phi P(B\bar{B} \rightarrow \phi X)$  are determined directly from the  $\Upsilon(4S)$  data sample, by first repeating the usual procedures to measure the MultiHadronic,  $\phi$  and  $\phi$ -lepton yields in these data and then applying the above relationships with  $f_s = 0$ .

From these relationships,  $f_s$  can be extracted from the ratio of Eqns. (4.2) and (4.3) if one knows the probability for a  $B_s\bar{B}_s$  event to yield a  $\phi$  meson. We

construct this quantity from the rates of processes in the  $B_s$  decay that lead to a  $\phi$  meson:

$$\begin{aligned} P(B_s \rightarrow \phi X) &= \mathcal{B}(B_s \rightarrow D_s^{(*)} X) \mathcal{B}(D_s \rightarrow \phi X) + \mathcal{B}(B_s \rightarrow c\bar{c}\phi) \\ &+ \mathcal{B}(B_s \rightarrow DD_s X) \mathcal{B}(D \rightarrow \phi X). \end{aligned} \quad (4.6)$$

With this estimate in hand, we can then express the probability for a  $B_s\bar{B}_s$  system to produce at least one  $\phi$ : this is  $2P(B_s \rightarrow \phi X)$  minus the probability that both mesons produce a  $\phi$  lepton (removing a double-counting of such events as we wish to compute the probability for *at least one*  $\phi$  to be produced rather than the expected number of  $\phi$  mesons produced)

$$P(B_s\bar{B}_s \rightarrow \phi X) = 2P(B_s \rightarrow \phi X) - P(B_s \rightarrow \phi X)^2. \quad (4.7)$$

We use the 2011 world averages [13] of the inclusive branching fractions  $\mathcal{B}(B_s \rightarrow D_s X)$ ,  $\mathcal{B}(D_s \rightarrow \phi X)$ , and  $\mathcal{B}(D \rightarrow \phi X)$ . Here and in the following,  $D$  refers to the sum of  $D^\pm$  and  $D^0$  contributions. Also needed now are estimates of the unmeasured branching fractions  $\mathcal{B}(B_s \rightarrow c\bar{c}\phi)$  and  $\mathcal{B}(B_s \rightarrow DD_s X)$ . The former accounts for direct  $B_s \rightarrow \phi$  production, a substantial fraction of which arises from  $B_s$  to charmonium decays. We use the central value from the simulation, 1.7%, which is roughly consistent with the known rate of charmonium production in  $B$  decays. For the latter quantity we use a naive quark model prediction of 15% for  $b \rightarrow c\bar{c}s$ . The uncertainties associated with these estimates are accounted for as part of the systematic errors, discussed in section 4.4. With Eqns (4.6) and (4.7) in hand, we can obtain  $f_s$  as a function of  $E_{\text{CM}}$  across the FinalScan region. Applying this procedure to the mixed sample, we extracted values of  $f_s$  shown in Fig. 4.10 for the mixed

simulation sample, found to be consistent with the respective input values.

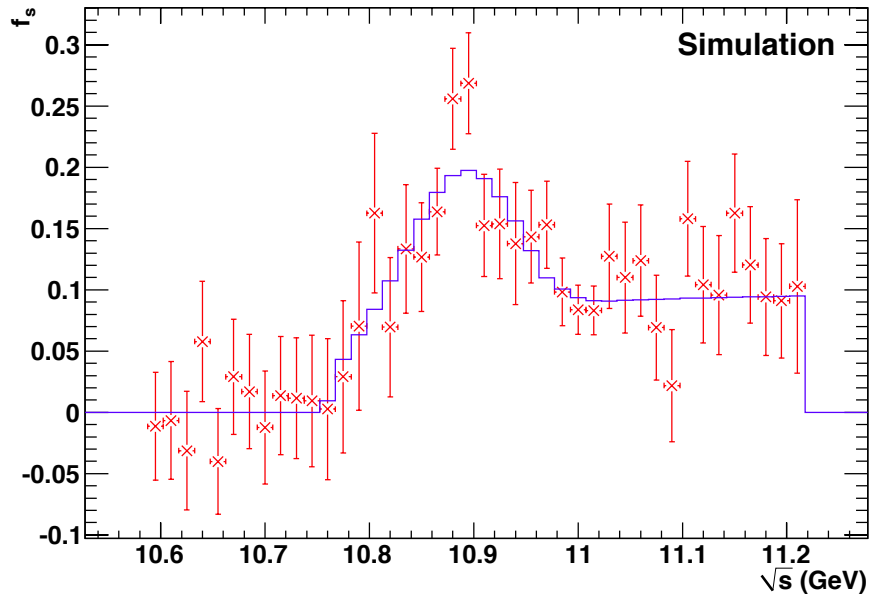


Figure 4.10: Result of  $f_s$  extraction in FinalScan mixed simulation. The blue histogram is the true value and the red points with error bars are the analysis output.

To extract  $\mathcal{B}(B_s \rightarrow \ell\nu X)$ , we use (4.4) to construct a  $\chi^2$ -like quantity from the measured and expected values of  $P(B_s\bar{B}_s \rightarrow \phi\ell X)$  for  $E_{\text{CM}} > 2m_{B_s}$ . The expected values are clearly functions of the semileptonic branching fraction  $\mathcal{B}(B_s \rightarrow \ell\nu X)$ . By minimizing this  $\chi^2$  with respect to  $\mathcal{B}(B_s \rightarrow \ell\nu X)$  we obtain a best-fit estimate of the branching fraction. The following processes contribute to  $C_{\phi\ell}$  from  $B_s\bar{B}_s$  events: primary leptons originating from semileptonic decays of  $B_s$ , secondary leptons resulting from semileptonic decays of charmed mesons produced in  $B_s$  decay, and  $\pi^\pm$  or  $K^\pm$  misidentified as  $e^\pm$  or  $\mu^\pm$ . The contributions from primary leptons is further divided into events where one  $B_s$  decays semileptonically and events where both  $B_s$  mesons decay semileptonically, with efficiencies for each case evaluated separately as discussed above and shown in Fig. 4.9.

To estimate the contribution from secondary leptons, we consider events with up to two leptons originating from  $D^\pm$ ,  $D^0$ , or  $D_s^\pm$  decays. The selection efficiency is taken to be the product of the per-lepton efficiency,  $\epsilon_\ell^D$ , and the  $\phi$  counting efficiency,  $\epsilon_\phi^D$ , also discussed above and shown in Fig. 4.9. The contribution to the  $\phi$ -lepton yield from events where no true leptons passed the selection but a misidentified hadron did is estimated from  $B^{(*)}_s\bar{B}_s^{(*)}$  simulation to be 3.3% of the total number of  $\phi$ -lepton candidates in  $B_s\bar{B}_s$  events.

For the expected and measured  $\phi$ -lepton yields, we find:

$$\begin{aligned} \epsilon_{\phi\ell}^s P(B_s\bar{B}_s \rightarrow \phi\ell X)_{\text{Measured}} &= (1 - 0.033) \\ &\times \left( C_{\phi\ell} \frac{f_s \epsilon_h^s + (1 - f_s) \epsilon_h}{f_s C_h} - \frac{(1 - f_s) \epsilon_{\phi\ell} P(B\bar{B} \rightarrow \phi\ell X)}{f_s} \right), \end{aligned} \quad (4.8)$$

$$\begin{aligned} \epsilon_{\phi\ell}^s P(B_s\bar{B}_s \rightarrow \phi\ell X)_{\text{Primary}} &= (2\epsilon_{\phi\ell}^s - \epsilon_{\phi\ell\ell}^s) \mathcal{B}(D_s \rightarrow \phi X) \\ &\times [-2 + \mathcal{B}(D_s \rightarrow \phi X)] [\mathcal{B}(B_s \rightarrow \ell\nu X)]^2 \\ &+ \mathcal{B}(B_s \rightarrow \ell\nu X) \epsilon_{\phi\ell}^s \left[ \mathcal{B}(D_s \rightarrow \phi X) \right. \\ &\left. + [1 - \mathcal{B}(D_s \rightarrow \phi X)] P(B_s \rightarrow \phi X) \right], \end{aligned} \quad (4.9)$$

$$\begin{aligned}
\epsilon_{\phi\ell}^s P(B_s \bar{B}_s \rightarrow \phi\ell X)_{\text{Secondary}} = & \\
& 2\epsilon_{\ell}^D \epsilon_{\phi}^D \left\{ \left[ \mathcal{B}(D_s \rightarrow \ell\nu\phi) + \mathcal{B}(D_s \rightarrow \ell\nu X)\mathcal{B}(D_s \rightarrow \phi X) \right. \right. \\
& - \left. \mathcal{B}(D_s \rightarrow \ell\nu\phi)\mathcal{B}(D_s \rightarrow \phi X) \right] [\mathcal{B}(B_s \rightarrow \ell\nu X)]^2 \\
& + \left[ P(B_s \rightarrow \phi X)(\mathcal{B}(D_s \rightarrow \ell\nu\phi) - \mathcal{B}(D_s \rightarrow \ell\nu X)) \right. \\
& - \mathcal{B}(D_s \rightarrow \ell\nu\phi) \\
& - \mathcal{B}(B_s \rightarrow D_s X)\mathcal{B}(D_s \rightarrow \ell\nu\phi) \\
& - \mathcal{B}(B_s \rightarrow D_s X)\mathcal{B}(D_s \rightarrow \ell\nu X)\mathcal{B}(D_s \rightarrow \phi X) \\
& + \mathcal{B}(B_s \rightarrow D_s X)\mathcal{B}(D_s \rightarrow \ell\nu\phi)\mathcal{B}(D_s \rightarrow \phi X) \\
& + \mathcal{B}(B_s \rightarrow \ell\nu X)(\mathcal{B}(D_s \rightarrow \phi X) - 2) \\
& \times \left. \sum_{i \in u, d, s} \mathcal{B}(B_s \rightarrow D_s^{(*)-} D_i(X))\mathcal{B}(D_i \rightarrow \ell\nu X) \right] \\
& + \mathcal{B}(B_s \rightarrow D_s X)P(B_s \rightarrow \phi X) [\mathcal{B}(D_s \rightarrow \ell\nu X) - \mathcal{B}(D_s \rightarrow \ell\nu\phi)] \\
& + \mathcal{B}(B_s \rightarrow D_s X)\mathcal{B}(D_s \rightarrow \ell\nu\phi) \\
& + [\mathcal{B}(B_s \rightarrow \phi X) + \mathcal{B}(D_s \rightarrow \phi X) - P(B_s \rightarrow \phi X)\mathcal{B}(D_s \rightarrow \phi X)] \\
& \times \left. \sum_{i \in u, d, s} \mathcal{B}(B_s \rightarrow D_s^{(*)-} D_i(X))\mathcal{B}(D_i \rightarrow \ell\nu X) \right\}, \tag{4.10}
\end{aligned}$$

$$\begin{aligned}
\epsilon_{\phi\ell}^s P(B_s \bar{B}_s \rightarrow \phi\ell X)_{\text{Expected}} = & \left\{ \epsilon_{\phi\ell}^s \times 0.591 \times \mathcal{B}(B_s \rightarrow \ell\nu X) \right. \\
& - (2\epsilon_{\phi\ell}^s - \epsilon_{\phi\ell\ell}^s) \times 0.289 \times (\mathcal{B}(B_s \rightarrow \ell\nu X))^2 \\
& + \epsilon_{\phi}^D \epsilon_{\ell}^D [0.1375 - 0.2721 \times \mathcal{B}(B_s \rightarrow \ell\nu X) \\
& \left. + 0.1339 \times (\mathcal{B}(B_s \rightarrow \ell\nu X))^2 \right\}, \tag{4.11}
\end{aligned}$$

where Eq. (4.11) is the sum of Eqs. (4.9) and (4.10) after substituting the values of known quantities. The first two lines in Eq. (4.11) expresses the contribution from

primary leptons and the following two lines those from secondary leptons. Eqs. (4.8) and (4.11) describe respectively the measured and expected values used to form the  $\chi^2$ , along with the statistical uncertainties of each of the measured quantities and the uncertainties in the energy-dependent efficiencies.

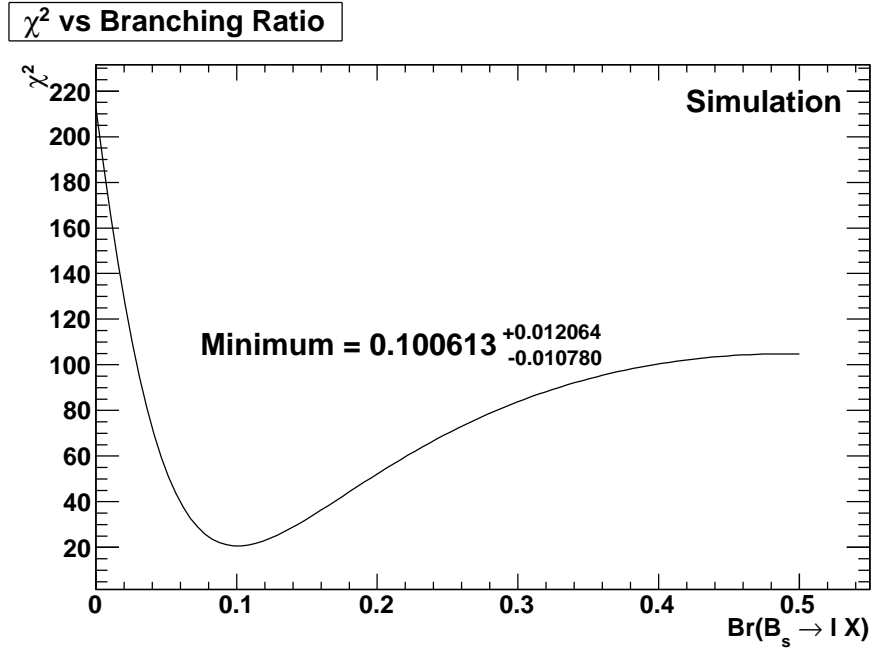


Figure 4.11:  $\chi^2$  vs  $\mathcal{B}(B_s \rightarrow \ell\nu X)$  in the mixed simulation sample. Note the asymmetric character of the minimum. The value of  $\mathcal{B}(B_s \rightarrow \ell\nu X)$  used in simulation is 9.3%

Note that the branching fraction  $\mathcal{B}(B_s \rightarrow \ell\nu X)$  appears quadratically in the expression for the expected value of  $\epsilon_{\phi\ell}^s P(B_s \bar{B}_s \rightarrow \phi\ell X)$ , specifically coming from cases where both or neither  $B_s$  decays semileptonically. Hence, in the  $\chi^2$  minimization there are a pair of minima with asymmetric curvature. The  $\chi^2$  as a function of  $\mathcal{B}(B_s \rightarrow \ell\nu X)$ , as obtained in the mixed simulation sample, can be seen in Fig. 4.11.

### 4.3 Consistency Checks and Validation

In the following section, we describe additional checks performed to validate the analysis technique.

#### 4.3.1 Validation of Continuum Subtraction

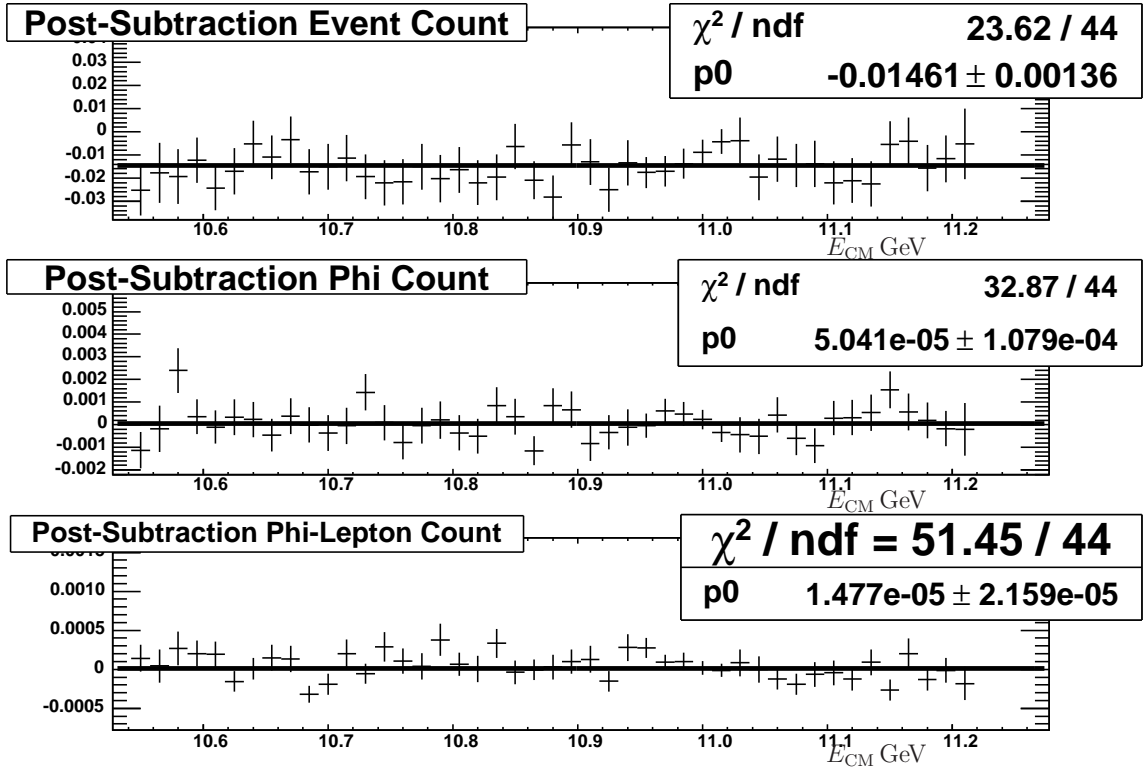
To test the continuum subtraction we run the analysis on the mixed sample with  $B\bar{B}$  and  $B_s\bar{B}_s$  events removed, so that only  $\mu\mu$ ,  $uds$  and  $c\bar{c}$  simulated events remain. The results are shown in Fig. 4.12. We find that the continuum subtraction overcorrects the number of MultiHadron events by a small but statistically significant amount of about  $\approx 1\%$  of the total subtraction. We apply a correction for this effect and take 100% of the resulting change as a systematic uncertainty.

#### 4.3.2 Simulation Study of a Pure $B_s$ Samples

We perform the analysis on a sample of simulated  $\mu\mu$  and pure  $B_s\bar{B}_s$  events, skipping the continuum subtraction step. The resulting values of  $f_s$  as a function of  $E_{\text{CM}}$  are shown in Fig. 4.13. The branching fraction extracted in the high-statistics sample is  $(9.074 \pm 0.11)\%$  (the true value in the simulation is  $9.3\%$ ).

#### 4.3.3 Analysis on $e$ and $\mu$ Event Samples

In the nominal analysis, we combine semileptonic decays to  $e$  and  $\mu$  into a flavor averaged value of  $\mathcal{B}(B_s \rightarrow \ell\nu X)$ . As a standard check in *BABAR* semileptonic analyses, we run the analysis separately using only  $e$  or  $\mu$  events. We find a result

Figure 4.12:  $udsc$ -only sample after subtraction.

of  $(11.8^{+1.6}_{-1.5})\%$  in data for  $e$ -only data and  $(8.6^{+1.2}_{-1.1})\%$  for  $\mu$ -only data. Both are consistent with the average value and with each other within the statistical precision.

#### 4.3.4 Effect of Multibody $B\bar{B}n\pi$ Events

For most of the CM energy range covered by the dataset, reactions leading to three or four body final states,  $B\bar{B}n\pi$ , are kinematically allowed, but neglected in the analysis. To check for a possible systematic effect from these events, we generate additional simulated events in the modes  $e^+e^- \rightarrow B\bar{B}\pi$  and  $e^+e^- \rightarrow B\bar{B}\pi\pi$  with each allowed combination of  $B^0, \bar{B}^0, B^+, B^-, \pi^+, \pi^-, \pi^0$  in equal proportion. These events are added to the mixed simulation sample in various proportions (one-third,

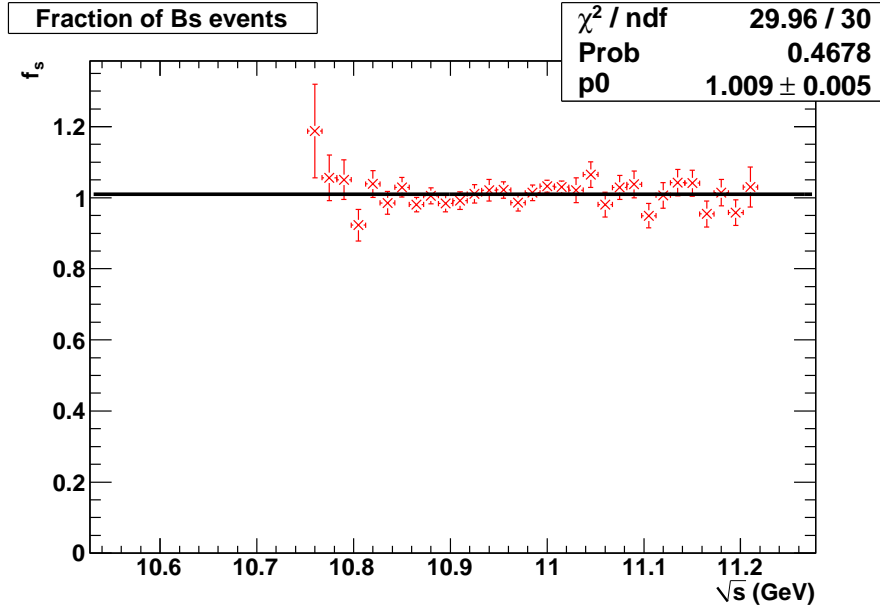


Figure 4.13:  $f_s$  calculated in a sample of only  $B_s$  events.

one-half or two-thirds of the total number of  $B\bar{B}$  events in the sample) to test the robustness of the  $f_s$  extraction against possible large contamination from multibody final states. It was found that significant systematic deviations from the true value of  $f_s$  in the samples occurred only in the case where two-thirds of the  $B\bar{B}$  events were multibody. Therefore no additional systematic uncertainty is assigned for this source.

#### 4.4 Estimates of Systematic Uncertainties

The most significant source of systematic uncertainties are due to the uncertainties in the values of various branching fractions used in Eqn. 4.11. The inclusive  $B_s \rightarrow D_s$  rate is the most poorly known of these ( $0.93 \pm 0.25$ ). We evaluate the contribution from these sources by changing their values in the analysis to  $\pm 1\sigma$  of the

central value and noting the change in the resulting values of  $f_s$  and  $\mathcal{B}(B_s \rightarrow \ell\nu X)$ . In Table 4.2 we note the contribution of  $\mathcal{B}(B_s \rightarrow D_s X)$  separately from the other branching fractions. The remainder are divided into those that contribute an uncertainty which scales with  $\mathcal{B}(B_s \rightarrow \ell\nu X)$  (multiplicative), and those that do not (additive). We present each of these as single entries with the quadrature sum of the contribution from all of the branching fractions in the respective category. The effect of  $\mathcal{B}(B_s \rightarrow D_s X)$  is a relative uncertainty of  $(+8.72/ - 13.58)\%$  while the remaining branching fractions contribute a (multiplicative) relative uncertainty of  $(+0.52/ - 0.54)\%$  and an (additive) absolute uncertainty of  $(+0.56/ - 0.64) \times 10^{-3}$ .

For the unmeasured branching fractions, we assign a 50% uncertainty to the estimated values used in the analysis and evaluate their contribution using the same procedure as above. We find the uncertainty from  $\mathcal{B}(B_s \rightarrow c\bar{c}\phi)$  to be  $\pm 3.20\%$  and from  $\mathcal{B}(B_s \rightarrow DD_s X)$  to be  $(+1.12/ - 1.16)\%$ . Each is included as a separate entry in Table 4.2.

Uncertainties from the event and lepton selections are determined by varying the  $R2$  and lepton  $p_{\text{CM}}$  selections by  $\pm 0.02$  and  $\pm 100$  MeV, respectively, and recording the change in  $\mathcal{B}(B_s \rightarrow \ell\nu X)$ . The large variation chosen for the lepton momentum selection allows us to use this as an estimate of our sensitivity to the decay model used in simulating  $B_s$  semileptonic decays. We find that varying the  $R2$  requirement by 0.02 changes the result by  $(+0.08/ - 0.60)\%$  and that varying the lepton momentum requirement by 100 MeV changes the result by  $(+1.99/ - 2.79)\%$ . These are combined as a single entry in Table 4.2.

Next we consider the uncertainty from the shape parameters of the fit to the

Table 4.2: Relative multiplicative and additive systematic uncertainties for the measurement of  $\mathcal{B}(B_s \rightarrow \ell\nu X)$ .

<b>Multiplicative Systematics</b>	<b>Relative Uncertainty (%)</b>
$\mathcal{B}(B_s \rightarrow D_s^{(*)} X)$	+8.72/−13.58
$\mathcal{B}(B_s \rightarrow c\bar{c}\phi)$ (Unmeasured)	$\pm 3.20$
$\mathcal{B}(B_s \rightarrow DD_s X)$ (Unmeasured)	+1.12/−1.16
Other Branching Fractions	+0.52/−0.54
Event and Lepton Selection	+1.99/−2.85
Fixed Fit Parameters	+0.49/−0.15
Background Parameterization	$\pm 0.93$
PID and Lepton Fake Rate	$\pm 3.21$
$P(B_{u,d}\bar{B}_{u,d} \rightarrow \phi)$	+1.47/−1.69
Simulation Branching Fractions	$\pm 2.59$
ISR and $2\gamma$ Background	+1.57/−7.14
Correction to Event Subtraction	+1.88/−4.59
Technique bias	+0.39/−10.00
<b>Total Multiplicative</b>	(+10.87/−19.92)%
<b>Additive Systematics</b>	<b>Uncertainty (<math>\times 10^{-3}</math>)</b>
Other Branching Fractions	+0.56/−0.64
$P(B_{u,d}\bar{B}_{u,d} \rightarrow \phi\ell\nu)$	+4.30/−3.90
<b>Total Additive</b>	(+4.34/−3.95) $\times 10^{-3}$
<b>Total Systematic</b>	(+11.20/−19.34) $\times 10^{-3}$

$K^+K^-$  mass distribution  $m_\phi$ ,  $\Gamma_\phi$  and  $\sigma_\phi$ , as well as the specific choice of binning (as the fits are carried out as binned likelihood fits). For the parameters listed above, we find changes of (+0.10, −0.01)%, (+0.11/−0.09)%, and (+0.10/−0.06)%, respectively, while the binning effect contributes an uncertainty of +0.43%. Furthermore, it can be seen in the fits (see Appendix A) that at some points there is a slight excess of events near  $2m_{K^\pm}$  compared to the fit value. To determine the effect of these events and a possible contribution from scalar resonances contributing near

threshold, we change the background parameterization to

$$\sqrt{1 - \frac{2m_K}{x}} \left( 1 + bx + \frac{r}{(x - m_0)^2 + g^2/4} \right) \quad (4.12)$$

with  $r$  and  $g$  allowed to float, and  $m_0$  fixed to 980 (without fixing  $m_0$ , the Breit-Wigner tail piece is not easily distinguished from the linear contribution by the fit).

We repeat the entire analysis with the new fit function to estimate the effect of this addition. We find that this changes the result for  $\mathcal{B}(B_s \rightarrow \ell\nu X)$  by  $\pm 0.93\%$ . The fit parameter uncertainties are listed as a single entry in Table 4.2, with the background shape uncertainty included separately.

To estimate the uncertainty from PID criteria, we repeat the analysis with PID tweaking (corrections for known data-simulation differences) disabled for each selector. As with the other systematics, the difference in the result divided by the original output is taken to be the fractional systematic uncertainty from this source. To estimate an uncertainty from the correction for fake leptons, we take the fake rates computed in samples that are 100%  $B_s\bar{B}_s$  and 100%  $B_s^*\bar{B}_s^*$  and assign this dependence on the sample composition as an additional systematic uncertainty. The contribution from each selector and from the fake rate are combined in Table 4.2.

As the  $\Upsilon(4S)$  and below-threshold data samples have finite size, we must estimate the effects of the statistical uncertainty in  $P(B\bar{B} \rightarrow \phi X)$  and  $P(B\bar{B} \rightarrow \phi\ell X)$  on our result. It is found that the contribution from the uncertainty on the  $\phi$  yield is multiplicative while the contribution to the  $\phi$ -lepton yield is additive.

Another source of systematic uncertainty is due to out-of-date branching frac-

tions used in the simulation. We estimate our sensitivity to these effects by reevaluating the efficiencies using a scheme to skip events in such a way as to effectively rescale the efficiencies by the difference in the simulated value and the value from [13].

We estimate the contribution from non- $1/E_{\text{CM}}^2$  background sources, such as ISR and 2-photon events, by estimating the average deviation from  $1/E_{\text{CM}}^2$  caused by these events and modifying the below-threshold subtraction of the MultiHadronic event yield by this amount. In addition, as noted above we include an uncertainty due to the small over-subtraction which was found to occur in this same part of the analysis.

Finally, we include systematic uncertainties arising from the fact that the analysis tends to over-estimate the branching fraction by an amount about equal to the reported statistical error, whereas at low statistics the technique used here has a small bias. Evidence for the latter comes from pseudo-data samples derived from the simulated dataset. The former is taken from toy studies where the input branching ratio is artificially adjusted before re-running the analysis. As neither source has a well-understood origin, we assign a systematic error for this effect rather than attempting to apply a correction to the result.

## 4.5 Results

After applying the analysis technique to the FinalScan dataset, we find  $26000 \pm 6100$   $B_s \bar{B}_s$  events. The normalized event,  $\phi$  and  $\phi$ -lepton yields, hereafter denoted

$C_h$ ,  $C_\phi$  and  $C_{\phi\ell}$ , after the subtraction of continuum contributions are shown Fig. 4.14.

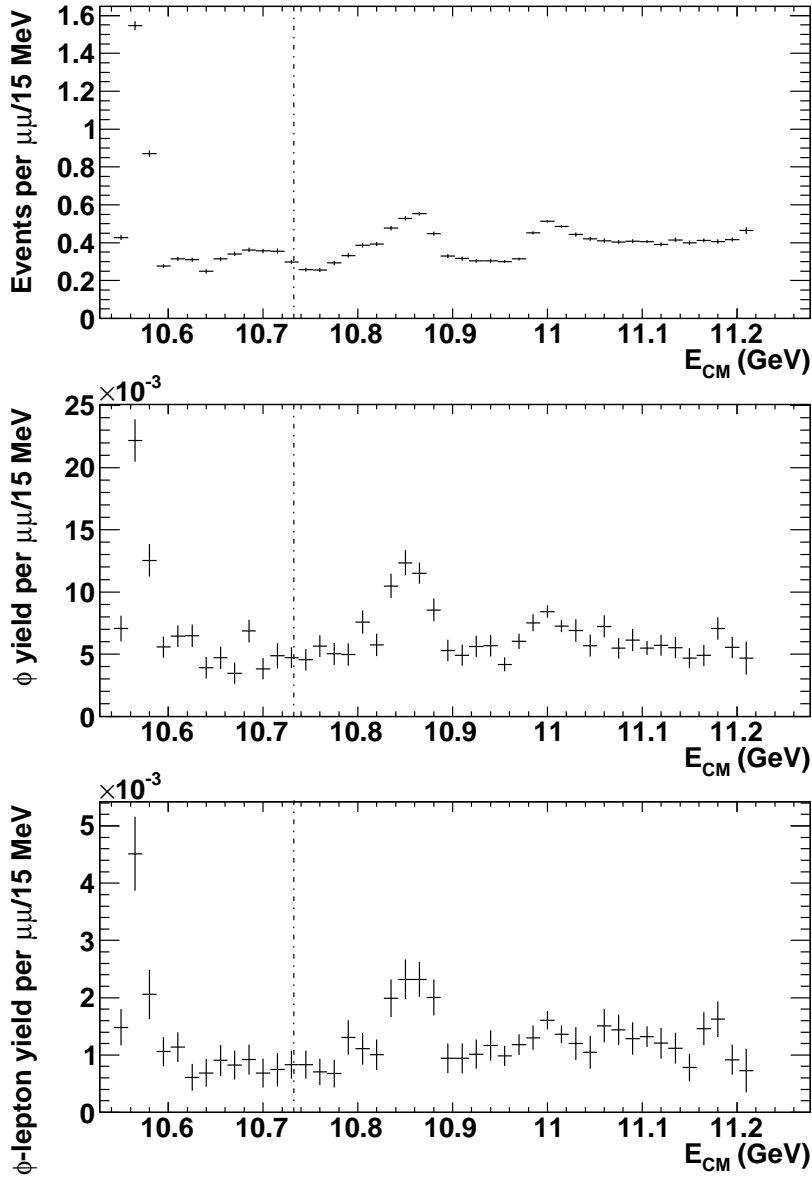


Figure 4.14: Relative (top) event, (center)  $\phi$  and (bottom)  $\phi$ -lepton yields, normalized to the  $\mu^+\mu^-$  yields. Corrections for detector efficiency have not been applied. The dotted vertical line indicates the  $B_s$  production threshold. Note the greater prominence of the  $\Upsilon(10860)$  peak in the  $\phi$  and  $\phi$ -lepton yields compared with the MultiHadronic yield.

Due to small statistics we again combine neighboring bins to present  $f_s$  as a

function of  $E_{\text{CM}}$  in Fig. 4.15(a) along with systematic uncertainties to be discussed. The ratio,  $f_s$ , peaks around the  $\Upsilon(5S)$  mass, and is not significantly large elsewhere, possibly indicating a large suppression of  $B_s$  production away from that resonance (in agreement with the coupled channel analysis [33], the results of which are shown in Figure 4.16). The observed excess below the  $B_s$  threshold appears to be due to an anomalous increase in  $\phi$  production in that region, but it is not statistically significant ( $1.5\sigma$ ). The observed deficit at very high values of  $E_{\text{CM}}$  has a similarly small significance ( $1.3\sigma$ ).

The minimization of the  $\chi^2$  with respect to  $\mathcal{B}(B_s \rightarrow \ell\nu X)$  in data results in a best-fit value of  $9.5^{+2.5+1.1}_{-2.0-1.9}$ . The systematic uncertainties on this quantity are discussed in Section 4.4. The semileptonic branching fraction is consistent with theoretical calculations in Refs. [39] and [40], which predict the semileptonic partial widths of the  $B^0$  and  $B_s$  to differ only at the level of 1%.

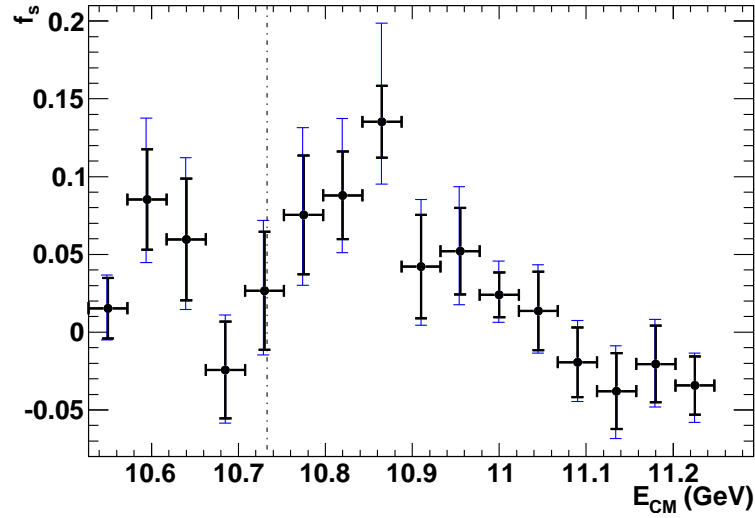
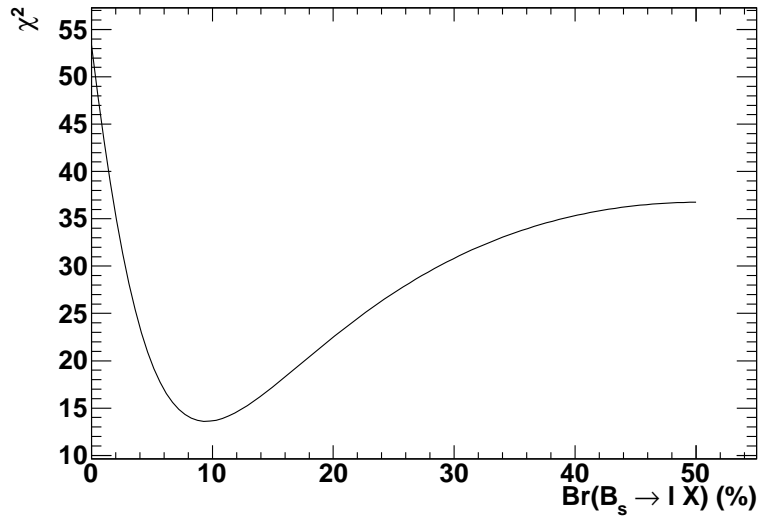
(a)  $f_s$ (b)  $\chi^2$  vs  $\mathcal{B}(B_s \rightarrow \ell\nu X)$ 

Figure 4.15: (a)  $f_s$  result in data. Black (inner) error bars are statistical errors, blue (outer) error bars are statistical errors added in quadrature with systematic errors. (b)  $\chi^2$  as a function of  $\mathcal{B}(B_s \rightarrow \ell\nu X)$ . Note the asymmetric character of the minimum.

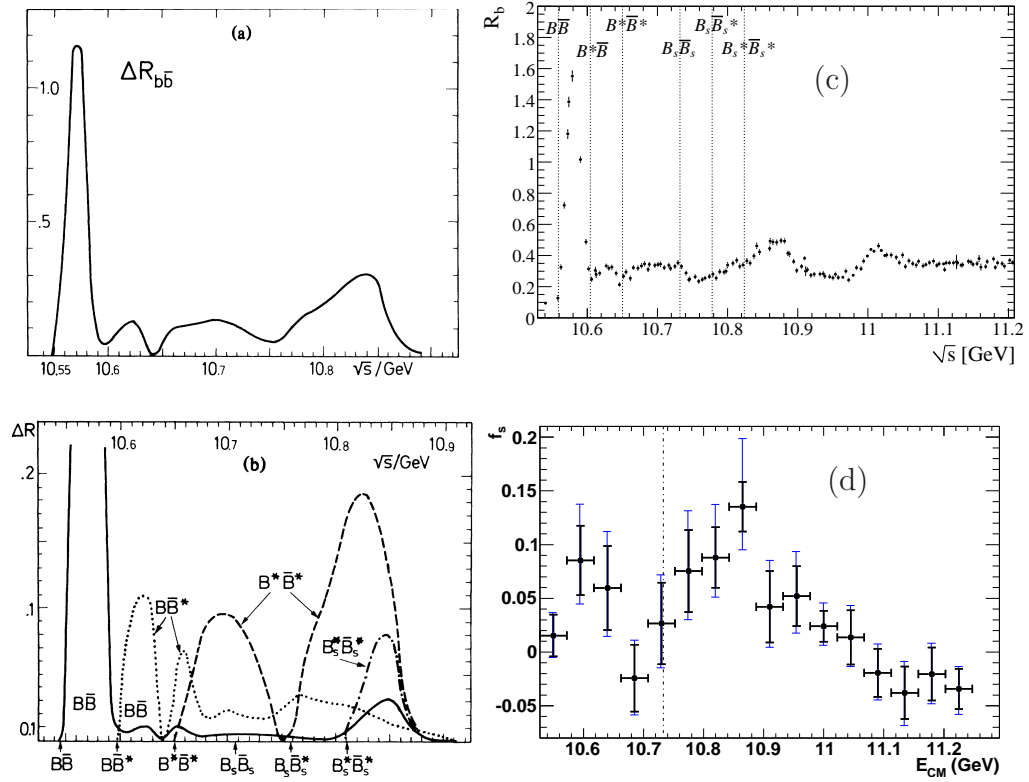


Figure 4.16: Predictions in a coupled-channel analysis (taken from Ref. [33]) for (a) the contribution to  $R$  from the various  $B$  meson thresholds and (b) the contributions from production of each of the states  $B\bar{B}$ ,  $B\bar{B}^*$ ,  $B^*\bar{B}$ ,  $B^*\bar{B}^*$ ,  $B_s\bar{B}_s$ ,  $B_s^*\bar{B}_s$ ,  $B_s\bar{B}_s^*$  and  $B_s^*\bar{B}_s^*$ . For comparison, the BABAR results for (c)  $R_b$  and (d)  $f_s$  are shown beside the predictions. Note that the predictions only extend out to 10.9 GeV while the measurements extend to 11.2 GeV

## Chapter 5

### Measurement of Antideuteron Production

As discussed in Chapter 2, cosmic ray antideuteron flux provides a low-background channel for indirect detection of annihilating dark matter. While, Experimental limits on the flux of antideuterons are expected to improve rapidly in the coming years, expected flux calculations suffer from large uncertainties in production models [18].

Measurements of antideuteron production at electron-positron colliders with different CM energies allow for models of light nucleon production in quark and gluon fragmentation to be calibrated and tested against real data. One popular calculational scheme is the so-called coalescence model, as discussed in Ref. [17]. Differential spectra are obtained in this picture by running Monte Carlo simulations of fragmenting partons, looking for multiple nucleons in a single event which are nearby in phase space. Here “nearby” is defined as a relative momentum in the two-body center of mass frame of the antiproton and antineutron of  $p_0 \lesssim \Lambda_{\text{QCD}} \sim 200 \text{ MeV}$ . The exact cutoff  $p_0$  is generally calibrated by matching some overall production rate in data, and varies greatly with different fragmentation models. See Ref. [17] for a more thorough and quantitative discussion. Uncertainties due to hadronization models and calibration of the overall rate constitute a dominant source of uncertainty in predictions of primary antideuteron flux in models with annihilating galactic dark matter. In this work we contribute measurements of

antideuteron production from  $\Upsilon$  decays and in continuum  $e^+e^-$  annihilation at CM energies around 10 GeV. Our measurements are obtained as differential rates in terms of antideuteron momentum in the CM frame.

## 5.1 Previous Work

Previously, antideuteron production in  $e^+e^-$  collisions was studied by ALEPH at LEP using data taken running at  $\sqrt{s} = m_Z$  [19], and in the region of the  $\Upsilon$  resonances by ARGUS at DORIS-II [41] and (most recently) by CLEO at CESR [42]. CLEO performed measurements of inclusive antideuteron production in  $\Upsilon(1S)$  and  $\Upsilon(2S)$  decays, as well as direct production (where only  $\Upsilon \rightarrow Ng$  decays are considered, removing the contribution from re-annihilation to light quarks). In addition, upper limits were set on antideuteron production in  $\Upsilon(4S)$  decays and continuum ( $e^+e^- \rightarrow q\bar{q}$ ,  $q = u, d, s, c$ ). The *BABAR* dataset represents a vastly larger sample at the  $\Upsilon(2S)$  and continuum off-resonance than that used by CLEO, and in addition this analysis includes the use of the entire  $\Upsilon(4S)$  dataset to determine continuum production of antideuterons.

## 5.2 Analysis Technique Overview

We identify antideuterons by use of specific ionization ( $dE/dx$ ) measurements provided by the tracking subdetectors. Reconstruction of Cherenkov emission angles in the DIRC does not include the deuteron mass hypothesis as a possibility, and in addition the threshold for Cherenkov radiation from deuterons in quartz is 1.74 GeV.

Furthermore the ambiguous region where particle discrimination from  $dE/dx$  runs out but before Cherenkov radiation in the DIRC radiator begins is large, from around 1.6 GeV to 1.74 GeV. Therefore we restrict ourselves to a momentum region where there is no expected DIRC signal from antideuterons and use that information as a veto against lighter species with anomalously large  $dE/dx$ . We weight candidates by the inverse of the efficiency and acceptance for an antideuteron with the given track parameters and bin them by deuteron CM momentum. The distribution of normalized residuals of the candidates with respect to the Bethe-Bloch  $dE/dx$  expectation under the deuteron mass hypothesis is used to extract production yields in each bin by use of an unbinned simultaneous maximum likelihood fit to the weighted data. For on-resonance yields, an on-off subtraction is performed to obtain only the contributions from decays of the resonance.

### 5.3 Track Selection

Events are first selected from those passing the tagbit BGFMutliHadron while failing BGFMuMu, BGFTau, BGFTwoProng and BGFNeutralHadron, all defined in Chapter 3. This ensures a starting point of events with multiple charged tracks due to inelastic  $e^+e^-$  reactions to hadrons.

The analysis starts with a base set of well-reconstructed charged tracks from the GoodTracksLoose track list, which have passed quality requirements and point back towards the interaction point ( $d_0 < 1.5\text{cm}$ ,  $z_0 < 10\text{cm}$ ). This selection is first refined by kinematic cuts in the laboratory frame. The track is required to be

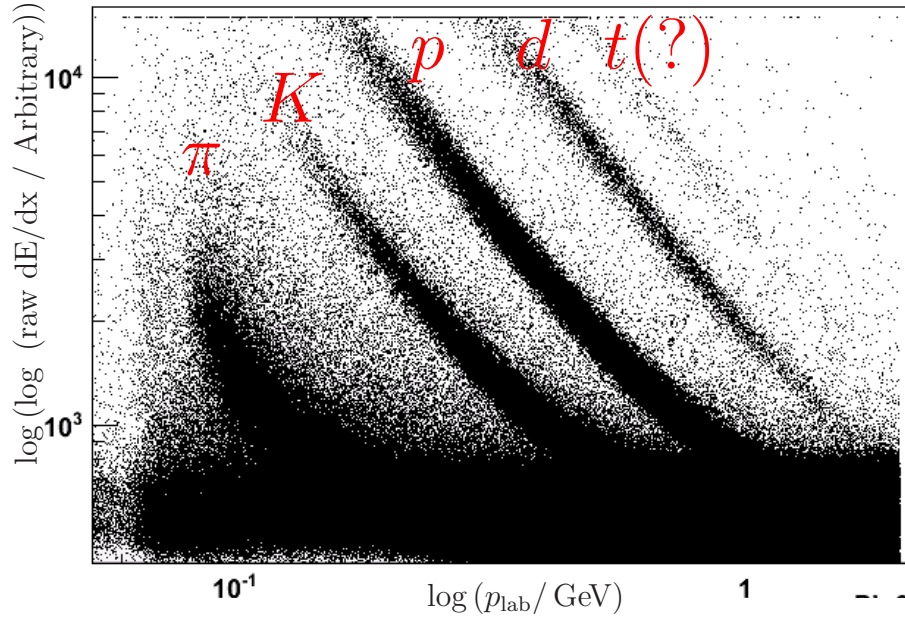


Figure 5.1: Track momentum vs  $dE/dx$  in the drift chamber for positive tracks in a subset of data. Note that deuterons appear well-separated between 500 MeV and 1.5 GeV

within the polar angle region  $-0.8 < \cos\theta_{\text{lab}} < 0.92$ , and have a momentum in the laboratory frame of  $0.5 \text{ GeV} < |p_{\text{lab}}| < 1.5 \text{ GeV}$ . The polar angle restriction ensures that the track passes through all of the DCH layers, ensuring good quality measurements of  $p_T$  and  $dE/dx$ . The momentum restriction is needed due to our reliance on measurements of specific ionization for this analysis. The *BABAR* DIRC ring-finding algorithms perform maximum likelihood analyses assuming that tracks incident on the quartz radiator bars are one of  $e$ ,  $\mu$ ,  $\pi$ ,  $K$  or  $p$ . Therefore, there is no high-level particle identification for antideuteron candidates from this subsystem, and so we restrict ourselves to a momentum region below 1.5 GeV where antideuterons are well-separated from other tracks in  $dE/dx$ . In Fig. 5.1  $dE/dx$  vs momentum for all tracks in a subsample of data is shown to illustrate this region.

To further ensure high-quality measurements of  $dE/dx$  on candidate tracks, we

require at least 24 separate specific ionization measurements in the DCH. Because at 1.5 GeV deuterons are still moving quite slowly, and hence are highly ionizing, this cut is very efficient ( $> 90\%$ ) for (anti)deuterons while simultaneously removing background tracks (mostly protons and kaons) with anomalously high  $dE/dx$  due to few or poor-quality measurements. The effect of this cut is illustrated in Fig. 5.2. The variable  $dEdxCombPull$ , explained in detail in the next section, is the normalized deviation of the measured  $dE/dx$  with respect to the Bethe-Bloch expectation: (anti)deuteron tracks are expected to cluster in a roughly gaussian shape around zero.

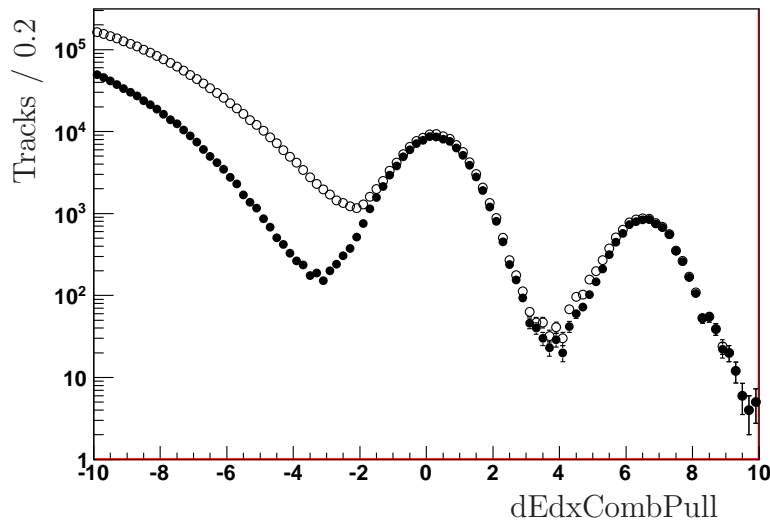


Figure 5.2:  $dEdxCombPull$  distribution with cut on number of samples in the DCH (filled circles) and before the cut (open circles) for comparison. The data sample used here are positive tracks from the  $\Upsilon(4S)$  dataset. The deuteron peak is clear near zero, and at higher values of the  $dE/dx$  residual we see another peak, likely from tritons.

Since the momentum cut ensures that true (anti)deuterons are moving too slowly to radiate in the DIRC, we use information from that subsystem as a veto

to further reduce background. We require a poor fit to all mass hypotheses in the DIRC by requiring fewer than 10 photons to be associated with the best-fit ring. This selection was found to be as effective as requiring a very poor log-likelihood for the DIRC fit under the proton mass hypothesis.

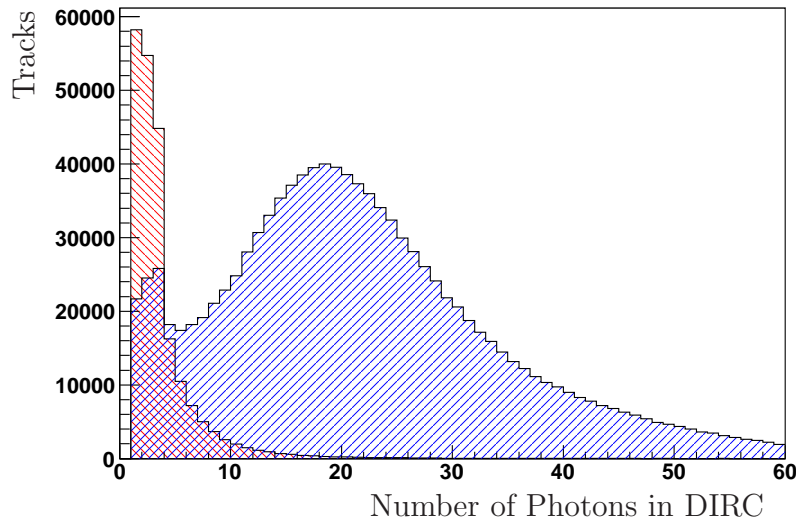


Figure 5.3: The distribution of the number of photons in the DIRC best-fit ring for simulated primary deuterons (the red histogram peaking near 1) and simulated generic  $\Upsilon(2S)$  decay tracks (the blue histogram peaking near 20, with a small peak near 4). The relative scaling between the two distributions is arbitrary.

#### 5.4 dEdxCombPull

We construct a variable which corresponds to the normalized deviation of the specific ionization  $dE/dx$  from the expected value as determined by the Bethe-Bloch formula [13]. For each track, the raw  $dE/dx$  information from the detector, after truncation to remove the landau tail [20], is corrected and converted to physical units using the latest calibration information based on the track’s trajectory through the

detector material. The deviation of this quantity from the expectation is normalized to the expected resolution based again on the material traversed by the track and the number of measured hits with good  $dE/dx$  information in the detector. This quantity is computed for both the SVT ( $dEdxSvtPull$ ) and the DCH ( $dEdxDchPull$ ).

$$dEdxPull \equiv \frac{\left(\frac{dE}{dx}\right)_{\text{meas.}} - \left(\frac{dE}{dx}\right)_{\text{exp.}}}{\sigma \frac{dE}{dx}} \quad (5.1)$$

Assuming Gaussian deviations and ideal calibration, this procedure would result in the signal being distributed as a Gaussian with a mean of zero and a width of one. We use the simulated prompt deuteron sample described in Section 3.3.2 to determine the shape of the expected distribution in signal events, which will be described in Section 5.6.2.

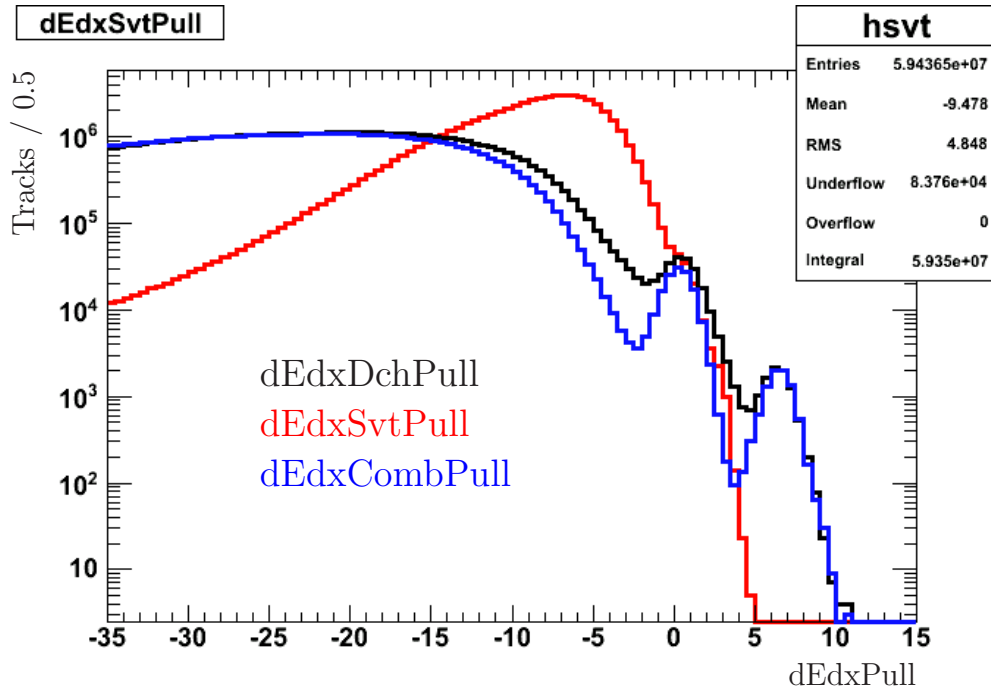


Figure 5.4:  $dEdxCombPull$  (blue) compared to  $dEdxDchPull$  (black) and  $dEdxSvtPull$  (red) for positive tracks. Note the improvements in the background around the deuteron and triton peaks.

To maximize the amount of information in this variable and improve signal and background separation, we combine the normalized deviations of  $dE/dx$  as measured in the DCH *and* the SVT. As the two subdetector systems are composed of different material, the expected  $dE/dx$  is different, and thus they cannot be simply averaged without some initial rescaling or correction. Therefore the measured value from the SVT and its associated resolution are rescaled by the ratio of the expected values in the SVT and DCH to obtain a weighted average of the two independent quantities. The residual of this new variable with respect to the DCH expectation is  $dEdxCombPull$ .

$$dEdxComb \equiv \left[ \frac{\left(\frac{dE}{dx}\right)_{DCH}^{meas}}{\sigma_{DCH}^2} + \frac{\left(\frac{dE}{dx}\right)_{SVT}^{meas} \frac{dE^{exp}}{dx_{SVT}}}{\sigma_{SVT}^2 \frac{dE^{exp}}{dx_{DCH}}} \right] \left( \frac{1}{\sigma_{DCH}^2} + \frac{1}{\sigma_{SVT}^2 \left[ \frac{dE^{exp}}{dx_{DCH}} \right]^2} \right)^{-1} \quad (5.2)$$

$$dEdxCombPull \equiv \left( dEdxComb - \left(\frac{dE}{dx}\right)_{DCH}^{exp} \right) \left( \frac{1}{\sigma_{DCH}^2} + \frac{1}{\sigma_{SVT}^2 \left[ \frac{dE^{exp}}{dx_{DCH}} \right]^2} \right)^{1/2} \quad (5.3)$$

While the measurement of  $dE/dx$  in the SVT is of lower resolution than that in the DCH, owing to the fewer number of track hits in the device, the addition of this information is found to be helpful in reducing background in the signal region. This can be seen clearly in Fig. 5.4

## 5.5 Efficiency Correction

We correct the raw  $dEdxCombPull$  distribution for detector acceptance and detection efficiency, so that the yields obtained by fitting the distributions would

correspond to production rates. Each track contributing to the distribution is therefore weighted by the inverse of the detection efficiency for an (anti)deuteron of the given track parameters. The antideuteron efficiency is split into four qualitatively different factors whose product is the total efficiency. These are: 1) the probability for an event containing an (anti)deuteron to successfully pass all filter and trigger requirements, 2) the fraction of (anti)deuterons with the given value of  $|p_{\text{CM}}|$  passing the kinematic restrictions, 3) the probability for an (anti)deuteron with the given lab momentum and polar angle to be successfully reconstructed and pass all selection requirements, and 4) the probability for an antideuteron with the given lab momentum and polar angle to survive without undergoing annihilation interactions in the detector material. The procedures used to obtain each of these factors are described below.

### 5.5.1 Trigger/Filter Efficiency

The per-event efficiency for a signal event to pass the trigger and also the applied background filters is estimated using simulated generic  $\Upsilon(2S)$  decays (or  $e^+e^- \rightarrow q\bar{q}$ ,  $q = u, d, s$  events) containing at least four promptly produced (anti)nucleons. These events have a topology most similar to the signal events of interest. For such events we find an efficiency in simulation of  $(93.38 \pm 0.04)\%$  (where the uncertainty is from the statistics of the simulated sample). For  $\Upsilon(1S)$  from the decay chain  $\Upsilon(2S) \rightarrow \pi^+\pi^-\Upsilon(1S)$ , we restrict the simulated sample to those events in which there is such a decay in addition to the required number of prompt (anti)nucleons.

In this sample we find a slightly higher efficiency of  $(97.15 \pm 0.05)\%$ , consistent with the presence of the extra charged pions. Finally, for continuum events we use a subsample of Run1-Run6  $e^+e^- \rightarrow q\bar{q}$ ,  $q = u, d, s$  simulation satisfying the four-nucleon requirement. In this sample we find an average efficiency across the six  $\Upsilon(4S)$  running periods of  $(83.75 \pm 0.07 \pm 0.21)\%$ , where the first uncertainty is due to simulation statistics and the second is associated with uncertainties in the relative luminosity of each run. The run-by-run efficiencies are given in Table 5.1.

Table 5.1: Event filter efficiency in each period of  $\Upsilon(4S)$  running

Run Number	Luminosity Fraction (%)	Efficiency (%)
1	$4.80 \pm 0.03$	$83.96 \pm 0.16$
2	$14.46 \pm 0.09$	$83.59 \pm 0.16$
3	$7.61 \pm 0.04$	$84.05 \pm 0.15$
4	$23.47 \pm 0.14$	$83.83 \pm 0.15$
5	$31.20 \pm 0.19$	$83.75 \pm 0.15$
6	$18.46 \pm 0.14$	$83.47 \pm 0.15$
Average	-	$83.75 \pm 0.06 \pm 0.21$

### 5.5.2 Geometric Acceptance

Due to the large mass of (anti)deuterons, the CM boost at *BABAR* dramatically changes the kinematics of the particles: a deuteron at rest in the CM frame gains around 1 GeV of longitudinal momentum in the lab frame. The region defined by the selection on  $\cos\theta_{lab}$  and  $p_{lab}$  has highly nontrivial boundaries in the  $e^+e^-$  CM frame. We account for this effect separately from tracking and reconstruction efficiencies discussed above and below, respectively. Tracks are reweighted by the fraction of solid angle in the CM frame for which a deuteron with that particular

CM momentum would pass the kinematic selection in the lab frame. In the case of continuum production we use the fraction of solid angle weighted by the polar angle distribution obtained in a coalescence model calculation.

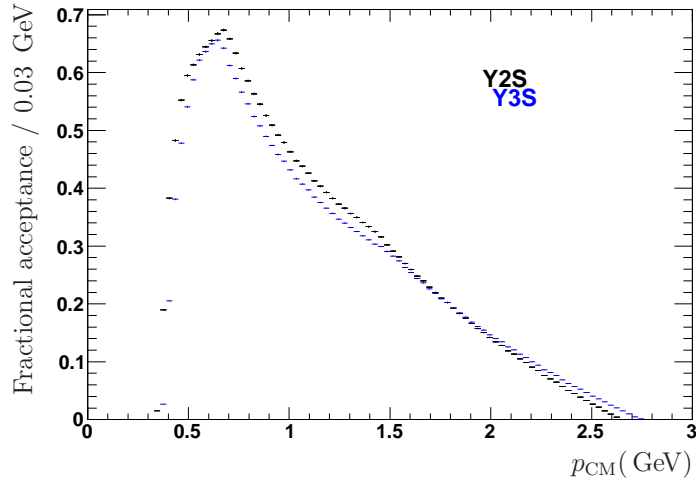


Figure 5.5: Geometrical acceptance fractions using the  $\Upsilon(2S)$  (black) and the  $\Upsilon(3S)$  (blue) boost

We calculate this quantity by Monte Carlo methods. In a given slice of CM momentum  $p^* < p_i^* < p^* + \Delta p^*$ , we generate random values of  $\phi$  and  $\cos\theta$  in the CM frame from a uniform distribution (for  $\Upsilon(2S)$  and  $\Upsilon(3S)$ ) or from an angular distribution obtained from simulation as discussed below. Tracks from  $\Upsilon$  decay must be isotropic in the CM frame due to the fact that  $\Upsilon$  resonances are produced unpolarized in collisions of unpolarized PEP-II beams. We construct four-vectors from these values and the deuteron mass and boost each into the laboratory frame. The fraction of tracks which pass the selection in the lab frame is the corresponding weight for that value of  $p_{\text{CM}}$ . Fig. 5.5 shows the resulting acceptance fractions for 30 MeV-wide  $p_{\text{CM}}$  bins.

For the continuum measurement, an isotropic distribution cannot be assumed, and so we use a coalescence calculation based on JETSET generating  $e^+e^- \rightarrow u\bar{u}, e^+e^- \rightarrow d\bar{d}$  and  $e^+e^- \rightarrow s\bar{s}$  events. The events are checked for (anti)proton and (anti)neutron pairs satisfying the ‘‘coalescence’’ requirement that their relative momentum in their two-body center of mass frame is less than 160 MeV. Candidate (anti)deuterons are then formed from the pairs by adding their respective four-momenta. The distribution of these candidates in  $\cos\theta_{\text{CM}}$  is fit to the function  $p_0(\frac{1}{2} + p_1 \frac{3}{8}x^2)$  ( $x = \cos\theta$ ) to find a linear combination of the isotropic distribution and the parton level  $1 + \cos^2\theta$  distribution which was representative of the generated distribution. This combination is in turn used to generate the acceptance fractions for continuum events using the method outlined above. See Fig. 5.6.

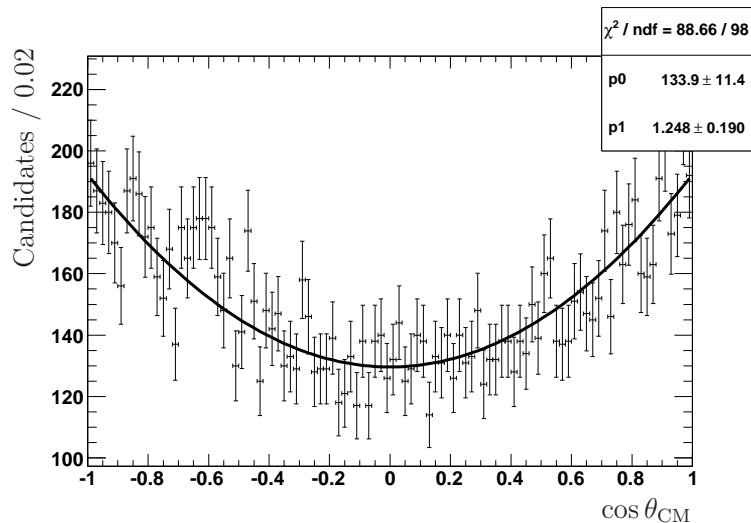


Figure 5.6: Generator-level angular distribution of coalescence candidates in light quark fragmentation at  $E_{\text{CM}} = m_{\Upsilon(4S)}$

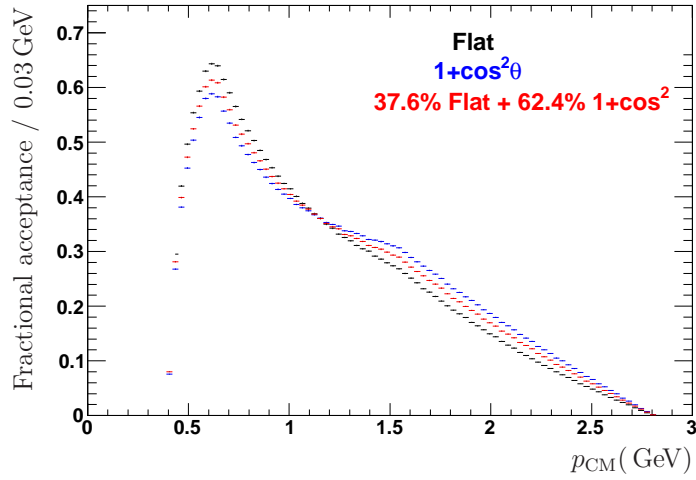


Figure 5.7: Acceptance fractions for  $\Upsilon(4S)$  boost with (black) flat angular distribution, (blue)  $1 + \cos^2 \theta$  and (red) fitted angular distribution

### 5.5.3 Reconstruction Efficiency

Reconstruction efficiencies are evaluated using the samples of simulated primary deuterons in bins of laboratory momentum and polar angle. The number of reconstructed deuteron tracks passing all selection requirements is normalized to the number generated within the bin in events passing the applied event filters. This is done so that the event filter efficiency, which is strongly dependent on multiplicity and is thus quite different in data and the simulated samples, can be considered separately as described above. The bins are chosen to keep the distribution of uncertainties approximately flat from bin to bin. The resulting efficiency in  $\Upsilon(2S)$  events and the relative uncertainty in each bin is shown in Fig. 5.8.

For 4S running we use the same procedure in the combined signal simulation dataset for that running mode, such that the efficiency obtained is a run-averaged value. These are shown in Fig. 5.9.

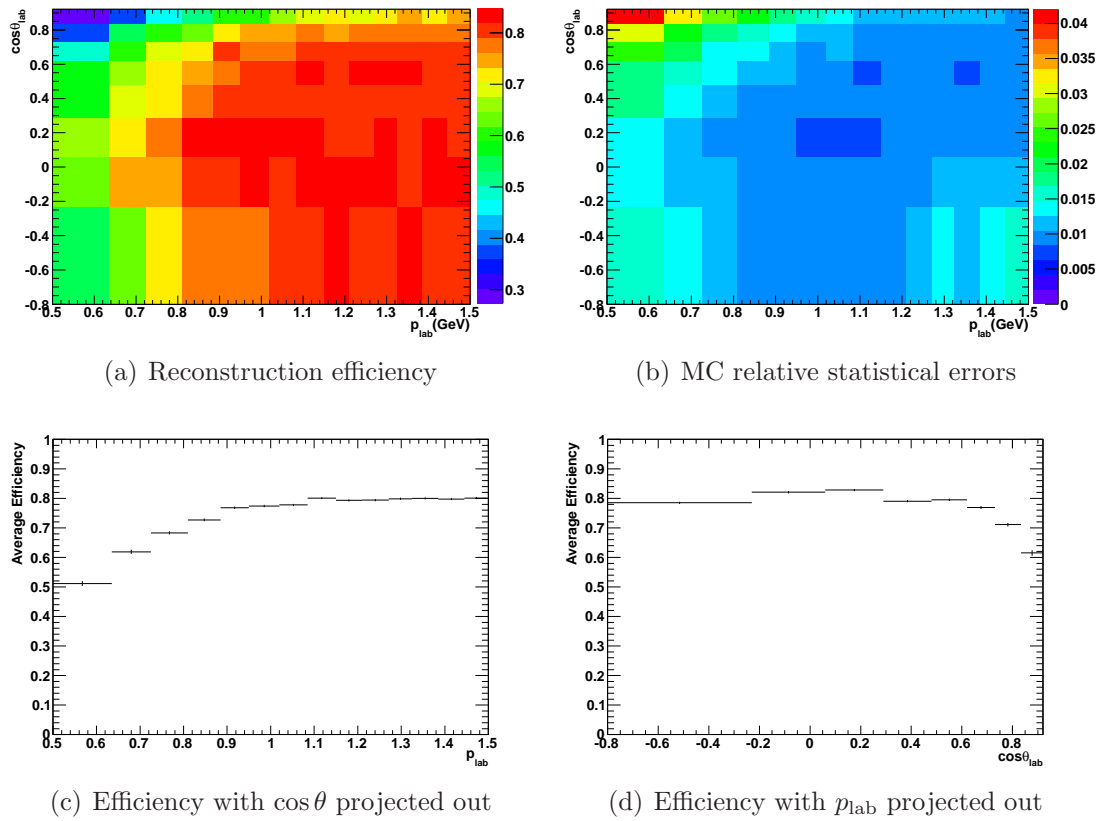


Figure 5.8: Reconstruction efficiency and uncertainties in  $\mathcal{T}(2S)$  signal Monte Carlo

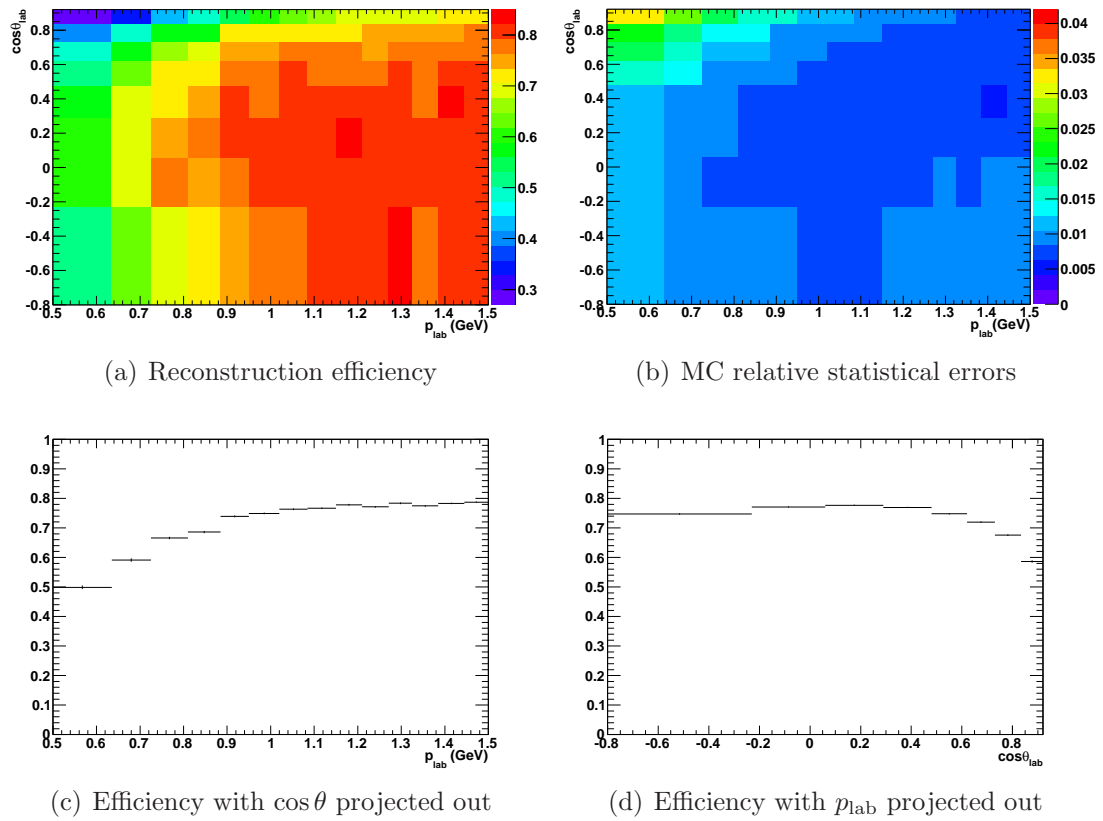


Figure 5.9: Reconstruction efficiency and uncertainties in  $\mathcal{T}(4S)$  signal Monte Carlo

### 5.5.4 Annihilation in Material

Finally, we must account for the fact that our nominal signal simulation code simulates primary deuterons rather than antideuterons. As mentioned in Section 3.3.2, *BABAR*'s GEANT4 release does not include antideuterons. While tracking is expected to be identical between the two species, traversing the *BABAR* detector material will in general generate an asymmetry due to partial (the separate annihilation of either the  $\bar{p}$  or  $\bar{n}$  from the antideuteron; sometimes called “stripping”) or total annihilations of antideuterons. The annihilation of antideuterons in various materials was studied in [43], where it was found that for a wide range of target atomic masses, the cross-section for antideuteron annihilation is 1.4 to 1.5 times that for antiprotons.

In order to estimate the contribution of annihilation in material to the overall antideuteron efficiency, we use the asymmetry between protons and antiprotons generated by *BABAR*'s GEANT4 simulation. This takes into account the detailed material modeling of the *BABAR* detector, which has been verified by extensive simulation and data studies. This asymmetry is related to the annihilation cross-section for antiprotons by

$$1 - A_p = e^{-\sigma_p n t} \quad (5.4)$$

where  $\sigma$  is the annihilation cross section,  $n$  the number density of nuclei in the material and  $t$  the material thickness traversed. The expected asymmetry for antideuterons is then

$$1 - A_d = e^{-\sigma_d n t} = (e^{-\sigma_p n t})^{\sigma_d/\sigma_p} = (1 - A_p)^{\sigma_d/\sigma_p} \quad (5.5)$$

allowing us to use the GEANT4 prediction for antiproton annihilation to generate an estimate of antideuteron annihilation with the known ratio of cross sections. A numerical calculation of the survival probability of antideuterons as a function of momentum at  $\cos\theta = 0$  using the known material properties and thicknesses with cross-sections from [13] was used to cross check the GEANT4 output and the two were found to be in agreement. The resulting values for the antideuteron reconstruction asymmetry,  $A_d$ , can be found in Fig. 5.10.

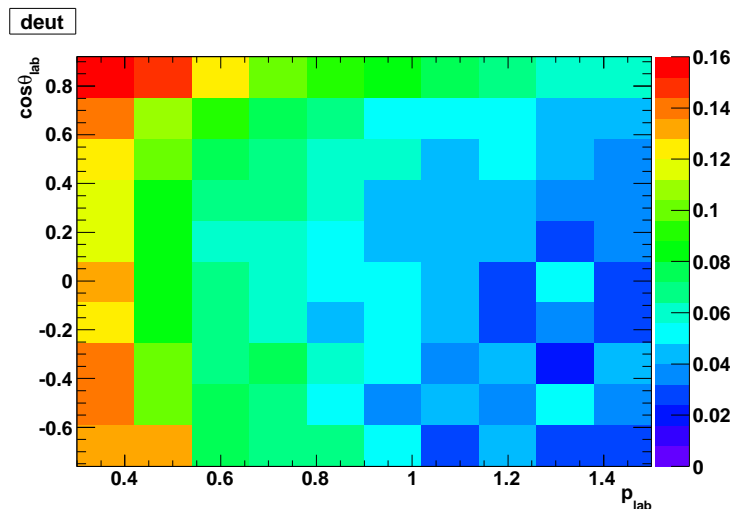


Figure 5.10: Calculated antideuteron reconstruction asymmetry due to annihilation in detector material based on rescaling the corresponding antiproton asymmetry

The total weight applied to each track is then the inverse of the product of each of the four factors discussed above.

## 5.6 Determination of Antideuteron Differential Yields

The extraction of the antideuteron differential production rate proceeds via a simultaneous weighted unbinned extended maximum-likelihood fit, resulting in a

measurement of the yield per unit CM momentum which is then normalized either to the number of  $\Upsilon$  mesons or by the total luminosity. Below we lay out the steps taken to bin the data by CM momentum, the signal and background shapes to be used, the simultaneous structure of the fit, and the determination of the normalization for each mode.

### 5.6.1 CM Momentum Bins

The antideuteron yield is to be extracted as a function of antideuteron CM momentum for each of the data samples. To do this we construct variable-size bins such that each bin contains approximately the same number of negatively-charged tracks in the signal region  $dE_{dx}CombPull > -0.5$ . The process begins by first counting the total number of such tracks and dividing by the number of desired bins (5 for the measurement in  $\Upsilon(1S)$ , 10 otherwise). This number represents the ideal or “target” number of tracks per bin for the algorithm. Starting from 100 MeV, the width of the first bin is increased in 50 MeV steps until the number of signal-region tracks is greater than the target number. The next bin edge is then set by starting from 100 MeV and moving in 50 MeV steps until the total number of signal-region tracks in the first two bins is greater than twice the target number and the number in the second bin alone is greater than 70% of the target number. This process continues iteratively until the total number of remaining tracks above the current bin’s low edge is less than the target, in which case the final bin’s upper edge is set at the upper limit of the CM momentum range (typically around 2.4 GeV). The

bins for the  $\Upsilon(2S)$  measurement then start from a lower bound of 0.35 GeV, and their upper edges are 0.55, 0.70, 0.80, 0.90, 1.00, 1.15, 1.30, 1.55, and 2.25 GeV.

### 5.6.2 Fit shapes

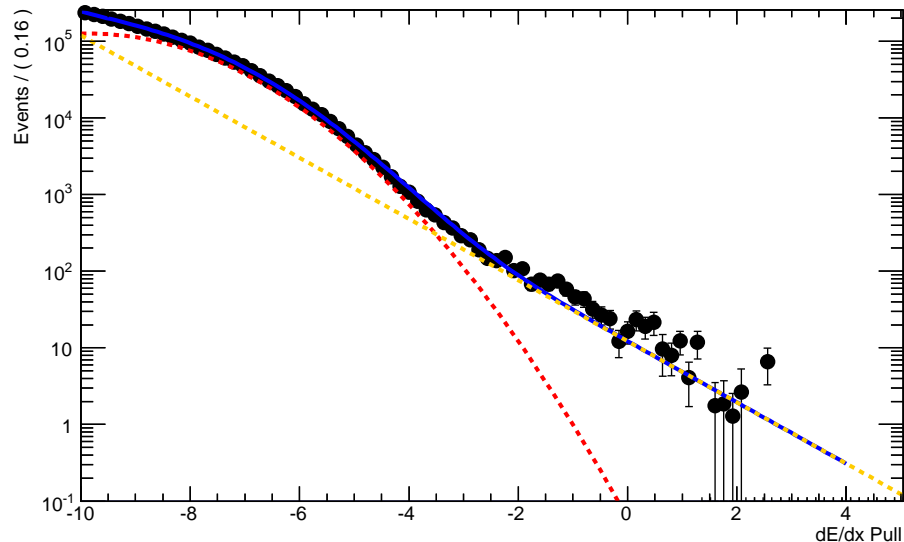


Figure 5.11: Background shape fit to the  $dE/dx$  pull distribution for tracks in generic Monte Carlo at the  $\Upsilon(4S)$ . The solid blue line represents the total fit while the dotted yellow and red lines are the exponential and Gaussian components, respectively.

We model the background distribution in  $dE/dx$  CombPull as the sum of a Gaussian and an exponential function. The relative area of the gaussian and exponential pieces are fixed across the various  $p_{CM}$  bins, as it was found that the additional free parameters destabilized the minimization processes for the fit, leading to unreliable statistical uncertainties calculated from the fit. This shape is found to provide an adequate description of the background across a large range of  $dE/dx$  CombPull and  $p_{CM}$ . We use one of several alternative shapes to estimate the systematic uncertainty

in the obtained yields from fits with a given background shape, as described in 5.7. The result of a fit using this shape to simulated generic inelastic events at the  $\Upsilon(4S)$  is shown in Fig. 5.11, and the simulated shapes in  $dE/dx$ CombPull of various species of particles are shown for reference in 5.12.

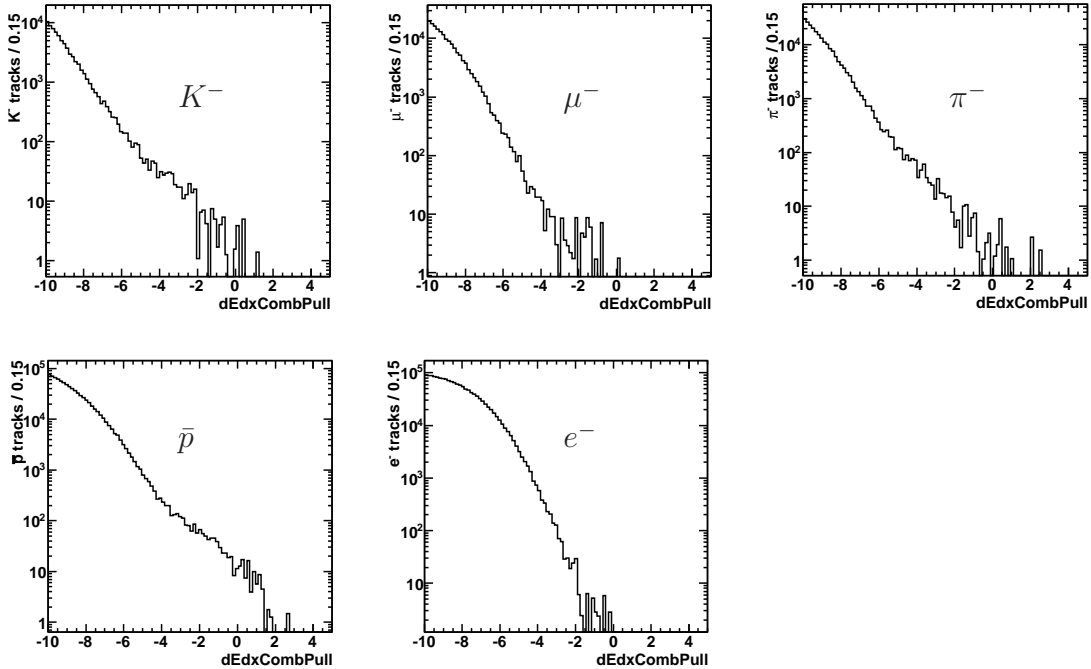


Figure 5.12: Distribution of the variable  $dE/dx$ CombPull for background species in generic Monte Carlo at  $\Upsilon(4S)$ .

The shape of the signal peak in simulated primary deuterons is found to deviate from the ideal of a pure Gaussian with zero mean and width equal to one. Instead the simulated data exhibit a long exponential tail towards negative values – corresponding to values of  $dE/dx$  below the Bethe-Bloch expectation. We parameterize this shape by a piecewise combination of an exponential function and a gaussian peak. The two piecewise components are constrained by imposing the conditions that both the resulting function and its first derivative be continuous

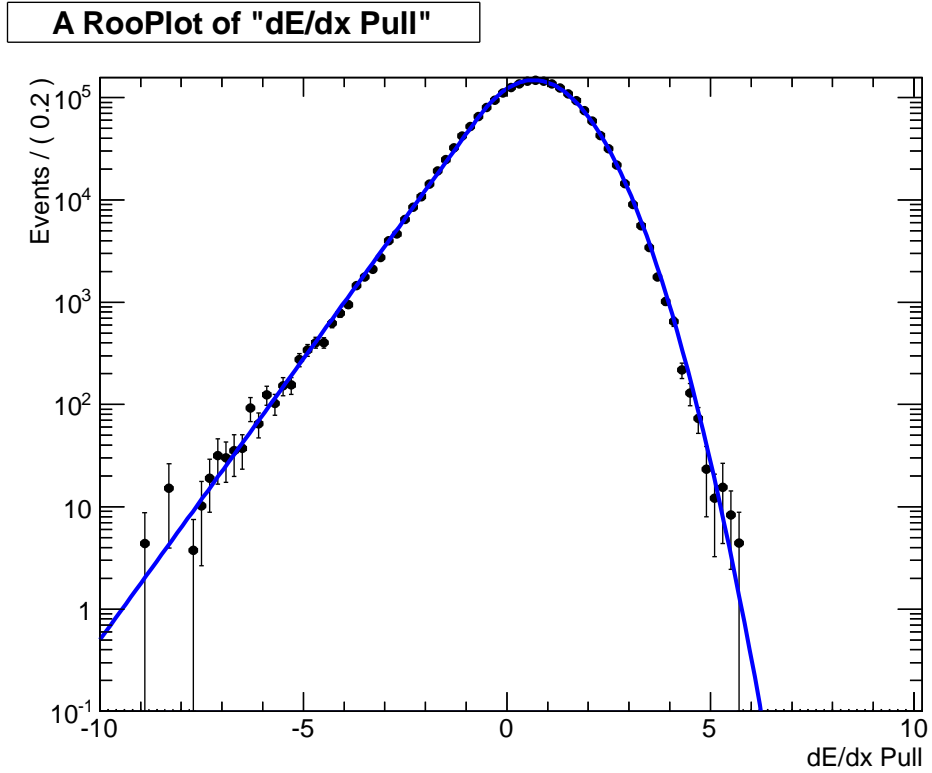


Figure 5.13: The result of a fit of the function in Eq. 5.6 to the  $dE/dx$  pull for simulated deuterons at  $E_{\text{CM}} = m_{\Upsilon(4S)}$

across the boundary between the two pieces. The resulting function is given by

$$f(x) = \begin{cases} e^{-\frac{(x-\mu)^2}{2\sigma^2}}, & x \geq \mu - \alpha\sigma \\ e^{\frac{\alpha(x-\mu)}{\sigma} + \alpha^2/2}, & x < \mu - \alpha\sigma. \end{cases} \quad (5.6)$$

This parameterization has the advantage of being fairly simple, introducing only the extra parameter  $\alpha$ , which may be understood as the distance from the Gaussian mean at which the function changes from gaussian to exponential (in units of the gaussian width  $\sigma$ ). A fit of this function to the  $\Upsilon(4S)$  sample of simulated deuterons is shown in Fig. 5.13.

### 5.6.3 Fit Strategy

As noted above, we proceed with a separate simultaneous unbinned weighted maximum-likelihood fit to each of the datasets ( $\Upsilon(2S)$  inclusive,  $\Upsilon(2S) \rightarrow \pi^+\pi^-\Upsilon(1S)$ ,  $\Upsilon(3S)$  inclusive and the entire  $\Upsilon(4S)$  on/off dataset). Each candidate is weighted by the inverse of the product of the efficiency, acceptance and annihilation factors described in Section 5.5 to correct for detector effects and divided into bins of  $p_{\text{CM}}$  using the algorithm described in Section 5.6.1. The candidates are divided into on- and off-resonance samples (or, in the case of  $\Upsilon(2S) \rightarrow \pi^+\pi^-\Upsilon(1S)$ , into  $\Upsilon(1S)$  signal and sideband regions of the mass recoiling against the  $\pi^+\pi^-$  system), and also separated according to the sign of their electric charge. The categories are thus defined by each combination of the variables  $p_{\text{CM}}$ , on/off, and charge, and the distributions for each category are fit simultaneously to a probability distribution function consisting of the sum of the signal and background functions described above. In addition, a second peak is added to the fit function which is the same shape used for the signal peak. This second peak accounts for the contribution of tracks with  $dE/dx$  larger than the deuteron expectation, believed to be the contribution from tritons ( ${}^3_1\text{H}^+$ ) from material interaction.

The simultaneous fitting procedure “splits” some variables among the different categories such that each category has its own respective value after the fit, while other variables are constrained to be equal between different categories. A list of all parameters in the fit and whether or not they are divided (split) among the different possible values for a given category variable is given in Table 5.2.

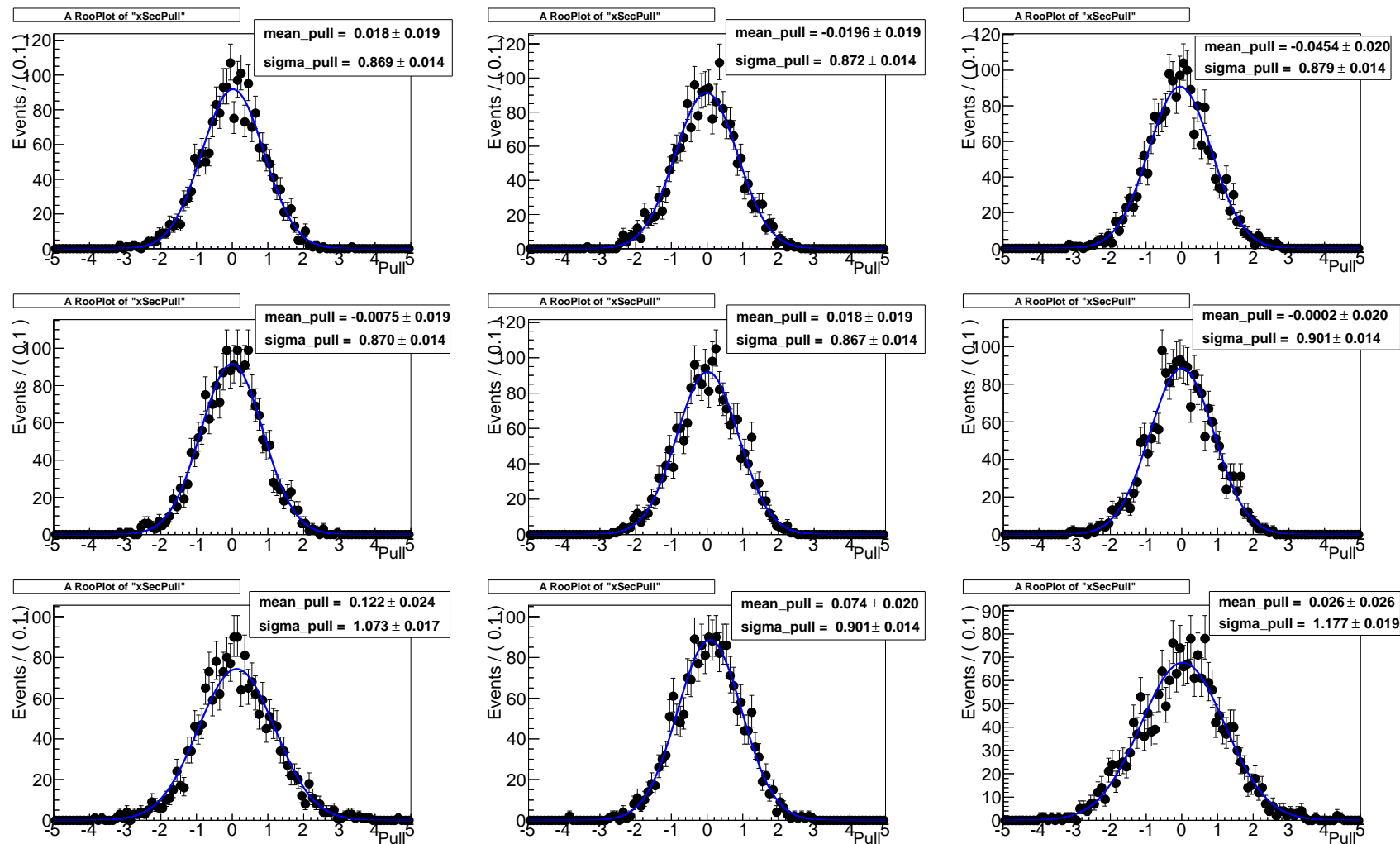
Table 5.2: Nominal fit parameters. The columns give the name of the variable, a brief description, and whether or not the variable is “split” across the various categories listed. The possible categories that variables may be split over are the charge of the track, whether it comes from on or off-resonance data, and which of the  $n_{\text{bins}}$  bins of deuteron  $p_{\text{CM}}$  it belongs to. Some exist only in particular categories, and those are indicated as such rather than split or no split.

Name	Description	Charge	On/Off	$p_{\text{cm}}$	#
$N_{\text{deut}}$	(anti)deuteron yield	split	split	split	$4n_{\text{bins}}$
$N_{\text{trit}}$	triton yield	+ only	split	split	$2n_{\text{bins}}$
$N_{\text{bkg}}$	background normalization	split	split	split	$4n_{\text{bins}}$
$f_{\text{bkg}}$	ratio of gaus and exp areas	no split	no split	no split	1
$t$	exponential parameter	no split	no split	no split	1
$\mu_{\text{bkg}}$	mean of BG gaussian	no split	no split	no split	1
$\mu_{\text{deut}}$	mean of deuteron peak	no split	no split	no split	1
$\mu_{\text{trit}}$	mean of triton peak	no split	no split	no split	1
$\sigma_{\text{bkg}}$	width of BG gaussian	no split	no split	split	$n_{\text{bins}}$
$R_{\text{bkg}}$	On/Off ratio of BG $\sigma$	no split	Off Only	no split	1
$\sigma_{\text{deut}}$	width of deuteron peak	no split	no split	no split	1
$\sigma_{\text{trit}}$	width of triton peak	no split	no split	no split	1
$\alpha_{\text{deut}}$	deuteron tail parameter	no split	no split	no split	1
$\alpha_{\text{trit}}$	triton tail parameter	no split	no split	no split	1
<b>Total parameters in nominal fit</b>				$11n_{\text{bins}} + 10$	

To improve convergence of the fitting algorithms, the fit is divided into stages and the results of each stage are used as starting parameters for the next stage of minimization. First, the background and signal shapes are fit to the appropriate simulated datasets, then the combined signal and background functions with starting parameters from simulation are fit to the data without any category splits. The subsequent stages then involve applying the on/off category, charge and  $p_{\text{CM}}$  categories in turn. Each of these stages uses a binned likelihood along with a likelihood scan to ensure the best minimum is found, while the final fit is performed as an unbinned fit to make the best use of the sometimes-limited statistics.

#### 5.6.4 Fit Validation

Validation of the fits proceed via a toy Monte Carlo study, where pseudo-datasets are generated from the functions used in the fit (with final fit parameters) and refit using the same functions. For each pseudo-dataset, the nominal result is subtracted from the result for that dataset and the difference is normalized by the reported statistical uncertainty. The distribution of these pulls is used to check for bias or over- or under-estimation of the statistical uncertainty. For the  $\Upsilon(2S)$  measurements we find evidence for a small (percent level) bias in the yields in some bins, with the largest effect being 12%. The pull distribution for each  $p_{\text{CM}}$  bin in the  $\Upsilon(2S)$  measurement is shown in Fig. 5.14.

Figure 5.14: Pull distributions from toy study in  $\Upsilon(2S)$  data

### 5.6.5 On/Off Subtraction

For measurements of inclusive  $\Upsilon(2S)$  and  $\Upsilon(3S)$  antideuteron production rates, we subtract the fitted yields in off-resonance data from the respective yields on-resonance, after rescaling by the factors  $\frac{\int \mathcal{L}_{\text{on}} dt}{\int \mathcal{L}_{\text{off}} dt}$  for the differing size of the datasets and  $\frac{(E_{\text{CM}}^{\text{off}})^2}{(E_{\text{CM}}^{\text{on}})^2}$  for the  $\approx 1/E_{\text{CM}}^2$  running of the continuum cross sections.

For the measurement of the rate in  $\Upsilon(1S)$  from  $\Upsilon(2S) \rightarrow \pi^+\pi^-\Upsilon(1S)$  decay, we search for candidate  $\pi^+\pi^-$  pairs passing a loose multivariate PID selector. The pairs are fit to a common vertex which is constrained to be within the beamspot (the overlap region of the two beams). The mass recoiling against this two-pion system is calculated as

$$m_{\text{recoil}} = \sqrt{(E_{\text{beam}} - E_{\pi\pi})^2 - (\vec{p}_{\text{beam}} - \vec{p}_{\pi\pi})^2} \quad (5.7)$$

using the known beam energy and total momentum, and each pair of pions is considered a separate candidate  $\Upsilon$  decay. The variable  $m_{\text{recoil}}$  peaks at  $m_{\Upsilon(1S)} = 9.460$  for pions from  $\Upsilon(2S) \rightarrow \pi^+\pi^-\Upsilon(1S)$  events (with a tail on the upper side from decays with final state photons) and is flat otherwise with a downward slope towards larger values. We define three regions of interest in this variable: the signal region (9.453, 9.472) GeV, the upper sideband (9.474, 9.488) GeV, and the lower sideband (9.432, 9.452) GeV. Antideuteron yields are extracted for the signal and summed sideband candidates and the sideband yields are subtracted from the yields in the signal region after rescaling by the relative sizes of the intervals in  $m_{\text{recoil}}$  to obtain the contribution from  $\Upsilon(1S)$  decay. Note that events may be counted more than once in this procedure if they contain multiple candidate two-pion systems; in sim-

plified Monte Carlo studies this was found not to generate any bias in the resulting subtracted yields. In addition we verify that the integral of the background in the sidebands divided by their width in  $m_{\text{recoil}}$  matches the value in the signal region by fitting the signal and background peak with a triple-gaussian peak function on top of a polynomial background. The sideband average is found to match to the average value of the polynomial in the signal region to better than 0.1%. This verifies that no additional scaling of the sidebands is needed.

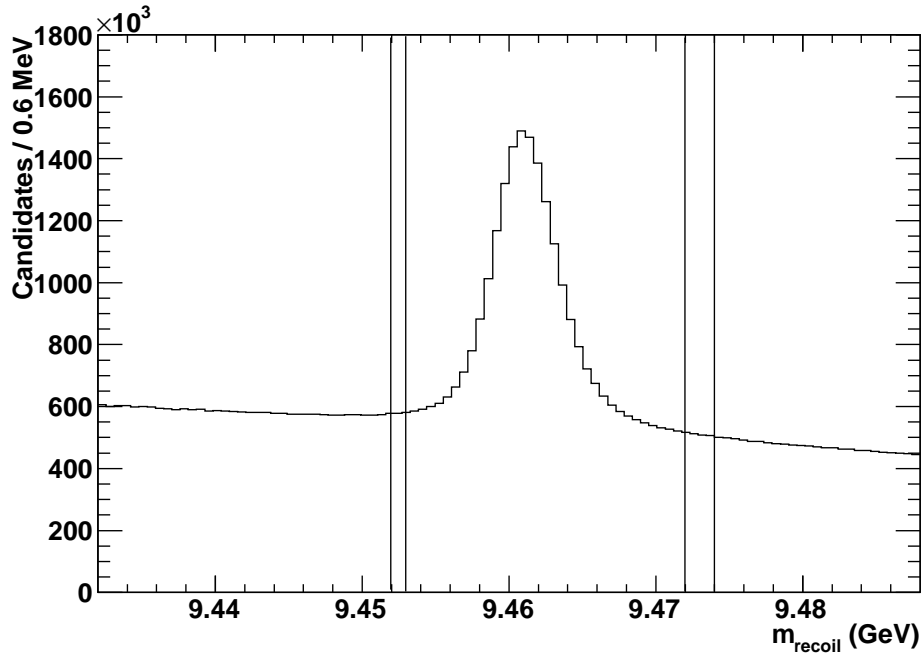


Figure 5.15:  $\Upsilon(1S)$   $m_{\text{recoil}}$  signal and sideband boundaries. The upper and lower sidebands extend respectively to the low and high borders of the plot.

In the  $\Upsilon(4S)$  dataset we generate both an inclusive  $\Upsilon(4S)$  result using the same method as the  $\Upsilon(2S)$  and  $\Upsilon(3S)$  inclusive rate measurements and a measurement using the sum of the on- and off-resonance yields. The former measurement constrains the antideuteron production in  $\Upsilon(4S)$  decays, expected to be extremely small due

to large kinematic restrictions in  $B$  decay, combined with the very small branching fraction for  $\Upsilon(4S)$  to decay to non  $B\bar{B}$  final states. The latter measurement provides the differential cross-section for antideuteron production in continuum  $e^+e^- \rightarrow q\bar{q}$ , given the negligible contributions from the  $\Upsilon(4S)$  decays in the dataset.

### 5.6.6 Determination of Differential Rates

Fitted and subtracted yields in each bin are normalized first by dividing out the bin width in GeV to obtain a measurement of yield/GeV, also removing the effect of varying bin size. The inclusive  $\Upsilon(2S)$ ,  $\Upsilon(3S)$ , and  $\Upsilon(4S)$  measurements are then normalized by the number of  $\Upsilon$  mesons expected in the dataset, given by the integrated luminosity times the effective cross section for each species. The effective cross-section for  $\Upsilon(4S)$  production at *BABAR* has been determined to be 1.1 nb. The effective cross-sections for  $\Upsilon(2S)$  and  $\Upsilon(3S)$  production are found by dividing the result of an Upsilon-counting procedure [44, 45], summarized below, by the result of an offline measurement of the luminosity in the datasets used for Upsilon-counting [29].

The Upsilon-counting procedure used by *BABAR* involves finding the number of hadronic events from Upsilon decay by measuring the total number of hadronic events in on-resonance running and subtracting off the expected number of continuum hadronic events based on the number of  $e^+e^- \rightarrow e^+e^-X_h$  two-photon events. Off-resonance data is used to find the ratio of cross sections of two-photon events to all continuum processes, which is then adjusted to the on-resonance ratio us-

ing known energy dependences. The offline luminosity measurement is performed by analyzing the number of  $e^+e^- \rightarrow e^+e^-(\gamma)$  Bhabha events in the dataset. Also used are  $e^+e^- \rightarrow \mu^+\mu^-$  events, but the latter luminosity measurement has large(r) systematics due to uncertainties accounting for in the  $\Upsilon \rightarrow \mu^+\mu^-$  cross-section.

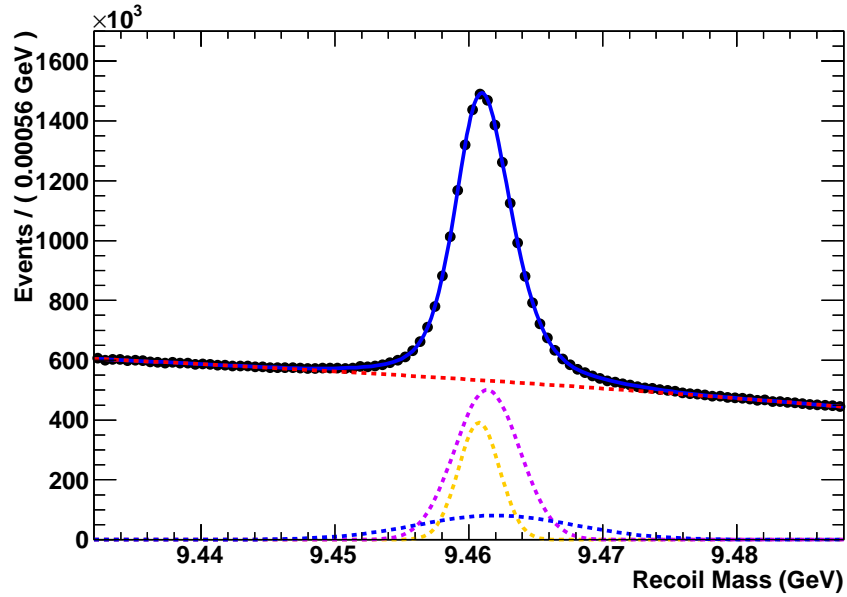
Using the effective cross-sections found by combining the two measurements, we find  $(98.3 \pm 1.2) \times 10^6 \Upsilon(2S)$  events,  $(116.1 \pm 1.4) \times 10^6 \Upsilon(3S)$  events, and  $(466.8 \pm 2.8) \times 10^6 \Upsilon(4S)$  events.

The yield in  $\pi^+\pi^-\Upsilon(1S)$  events (after correcting for antideuteron efficiency and acceptance in  $\Upsilon(2S)$  events) is related to the branching fraction  $\mathcal{B}(\Upsilon(1S) \rightarrow \bar{d}X)$  by

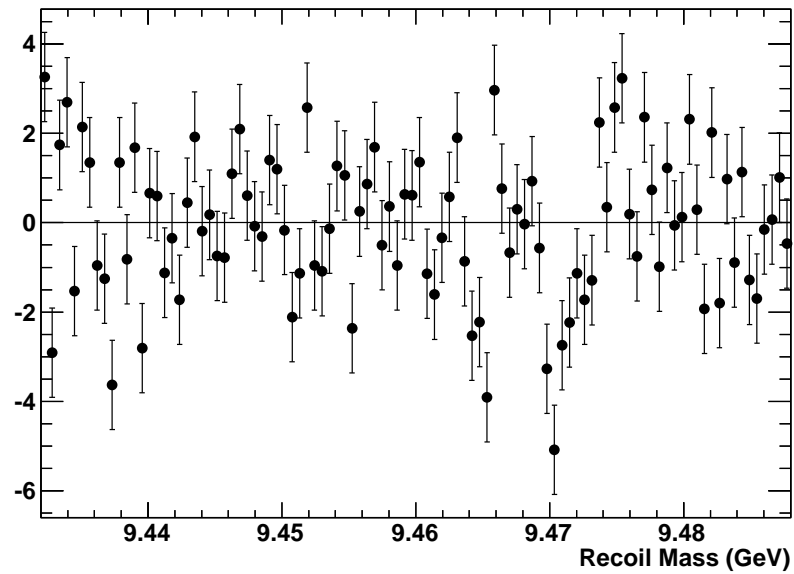
$$N_{\bar{d}} = N_{\pi^+\pi^-\Upsilon(1S)} \epsilon_{\pi^+\pi^-|\text{MH}} (f_{\text{sig}} - f_{\text{sb}}) \mathcal{B}(\Upsilon(1S) \rightarrow \bar{d}X), \quad (5.8)$$

where  $\epsilon_{\pi^+\pi^-|\text{MH}}$  is the efficiency for reconstructing the  $\pi^+\pi^-$  system and  $(f_{\text{sig}} - f_{\text{sb}})$  is the fraction of the total signal yield in the signal region minus the fraction of the total signal yield in the sidebands. To obtain the correctly-normalized branching fraction we must know the number of  $\pi^+\pi^-\Upsilon(1S)$  events multiplied by probability  $\epsilon_{\pi^+\pi^-|\text{MH}}$  for reconstructing the recoiling pion system, given that the event has passed the trigger and background filters. Therefore we reconstruct the recoiling  $\pi^+\pi^-$  system as above but without any selection on the presence of antideuteron candidates. A fit to the  $m_{\text{recoil}}$  distribution gives the reconstructed yield. The trigger and filter efficiency for this is estimated from simulation and divided out. The signal distribution used is a sum of three Gaussian functions and the background is a second-order polynomial. The results are shown in Fig. 5.16. The fitted signal

yield is  $(10.240 \pm 0.025) \times 10^6 \Upsilon(2S) \rightarrow \pi^+\pi^-\Upsilon(1S)$  events.



(a) 1S recoil mass fit



(b) Recoil mass fit normalized residuals

Figure 5.16: Results of a fit to the  $\Upsilon(1S)$   $m_{\text{Recoil}}$  spectrum, used to obtain the number of  $\Upsilon(1S)$  events in the signal region and sidebands.

Obtaining all of the values needed for the normalization, we find that the

fraction of the signal PDF in the signal window is 95.456% and the fraction in the sidebands is 2.752%, so that  $f_{\text{sig}} - f_{\text{bg}} = 92.705\%$ . In a sample of 30,937 simulated  $\Upsilon(2S)$  decays in this mode, we find an efficiency of  $(98.17 \pm 0.08)\%$  for the trigger and filter. The final number of  $\Upsilon(1S)$  events for normalization is found to be  $(9.670 \pm 0.025) \times 10^6$ .

### 5.6.7 Determination of Total Rate

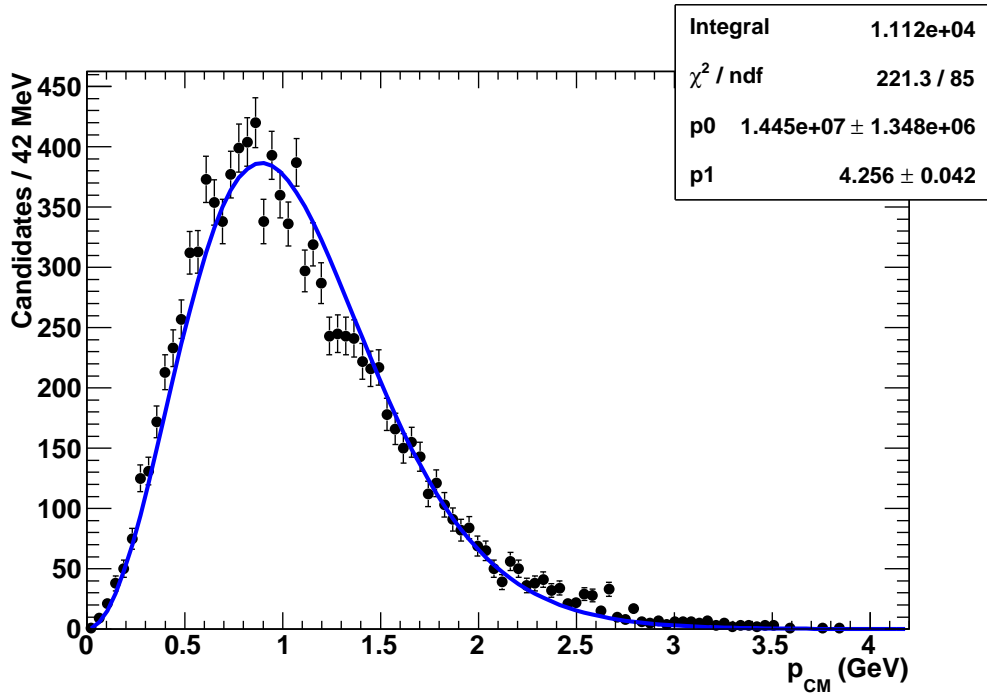


Figure 5.17: Result of generator-level coalescence study using a coalescence momentum  $p_0 = 160$  MeV fit to a fireball spectrum (Eq. 5.9). See the text for comments on the agreement between the simulated data points and the fitted function.

To obtain the total rate of antideuteron production in the datasets studied in this analysis, we fit the differential spectra to a simple fireball model, where the energy distribution of antideuterons in the collision CM frame follows a thermal

distribution function

$$P(E) = \alpha v^2(E) e^{-\beta E} = \alpha \frac{E^2 - m_d^2}{E^2} e^{-\beta E} \quad (5.9)$$

with  $\alpha$  an overall normalization,  $\beta$  a free parameter analogous to thermodynamic temperature, and  $m_d$  the world-average deuteron mass. This distribution was used by CLEO in Ref. [42]. We find that this distribution is a good fit to the distribution of deuteron and antideuteron candidates produced in a coalescence scheme using JETSET with higher statistics than expected in data. Candidates were formed from generated (anti)proton and (anti)neutron pairs produced directly or via very short-lived resonances (that is, daughters of long lived heavy baryons such as hyperons were rejected) with invariant masses below a threshold corresponding to a given coalescence momentum. The result is shown in figure 5.17. Although the agreement between the generated spectrum and the fit is not perfect, the function is an adequate representation of the spectrum at the level of the statistical accuracy of the current data. Therefore we perform a  $\chi^2$  fit of Eq. 5.9 to the measured differential spectra to obtain the total production rate given the measured differential yields. Since the function has no analytic normalization, we use the following procedure to estimate the systematic uncertainty in the total yield. The parameter  $\beta$  is fixed to obtain the statistical uncertainty on the yield  $\alpha / \int P(E) dE$ . The statistical uncertainty in fitting for  $\beta$  is taken as a systematic uncertainty by evaluating the change in the yield after fixing  $\beta = \beta_0 + \sigma_\beta$ , where  $\beta_0$  is the best fit value and  $\sigma_\beta$  the statistical uncertainty on  $\beta_0$ .

## 5.7 Systematic Uncertainties

Systematic uncertainties in the differential rate measurements originate largely from the determination of efficiencies in simulation. We evaluate the size of these uncertainties by comparing the distributions in data control samples and in simulation of variables used in the selection. Additionally, biases found during validation as discussed in Section 5.6.4 are incorporated as systematic errors. Below we describe the procedures used to evaluate the systematic uncertainties in the yields from each source, with the obtained values summarized in Tables 5.3 - 5.7.

### 5.7.1 Fit Biases

Validation of the fit using toy pseudo-datasets reveals biases at the level of several percent for the fitted antideuteron yields. We use the deviation from zero of the mean of the normalized residuals and the deviation from one of their RMS width to assign uncertainties as fractions of the reported statistical error. For the  $\mathcal{T}(2S)$ , these deviations range from less than one percent to three percent, except in the three highest momentum bins, where we find deviations on the order of ten percent.

### 5.7.2 Statistical Uncertainty in Simulated Datasets

As the simulated sample of primary deuterons has finite statistics, the efficiencies used to reweight the data have finite statistical uncertainties. We evaluate the effect of these uncertainties on the fitted yields by a procedure in which the fit is

performed many times with different values for the various efficiencies. Before the fit begins, the efficiencies as a function of lab momentum, lab polar angle, and CM momentum are chosen from a gaussian distribution with mean equal to the nominal value and width equal to the statistical uncertainty on that value. The newly-obtained weights are then applied to the tracks in place of the nominal weights and the fit is performed. We assign the maximum deviation from the nominal yield of these outputs as the systematic uncertainty. For some bins, we find that depending on the weights the fit may find one of two nearby values for the fitted yield, leading to a larger systematic uncertainty from this source.

### 5.7.3 Acceptance Fraction

In the case of the measurement in continuum  $e^+e^-$  annihilation, we perform the above procedure, but additionally take half the difference between the nominal acceptance fractions and a set generated from a pure  $1 + \cos^2 \theta$  distribution.

### 5.7.4 Annihilation Fraction

The systematic uncertainty due to the correction for the annihilation of antideuterons in the detector material is computed as above, where for the width of the distribution of values used as input we use the statistical uncertainty added in quadrature with approximately 30% (actually  $1/\sqrt{12}$ ) of the size of the deviation of the survival probability from unity. This is to account for additional uncertainty in this quantity due to the technique used to compute it (Section 5.5.4).

### 5.7.5 Event Filter

The uncertainty in the event filter efficiency is taken as the difference between the efficiency in the four nucleon events and the efficiency in the subset of those events in which there exists a proton or antiproton within the angular acceptance  $\cos \theta \in [-0.80, 0.92]$ .

### 5.7.6 Reconstruction and Selection Efficiency

Previous studies [24] at *BABAR* have demonstrated that the tracking efficiency for tracks passing the GoodTracksLoose selection (used as the basis for this analysis) is well-modeled in simulation. Typical systematic uncertainties are at the per-mil level, and therefore we do not assign additional systematic uncertainties from tracking at this level.

For the additional selection criteria employed in this analysis –  $x - y$  DOCA  $< 0.44$  mm, at least 24 measurements of  $dE/dx$  in the DCH, less than 10 photons in the DIRC best-fit ring – we construct control samples from data, which are used to compare to simulated distributions of the variables. A sample of positive deuterons with high purity is selected by applying all analysis cuts and using tracks in the dEdxCombPull region (0,1.5), which is far from significant contamination from other species in both the  $\pi, K, p, \mu e$  and tritium regions.

The efficiency for the requirement on the number of DIRC photons - less than 10 associated “signal” photons in the DIRC best fit ring - is checked by comparing the control sample distribution of the number of such photons with that obtained in

the sample of simulated primary deuterons. We find acceptable agreement between simulation and data (see Fig. 5.18) and do not assign any additional systematic uncertainty for this selection.

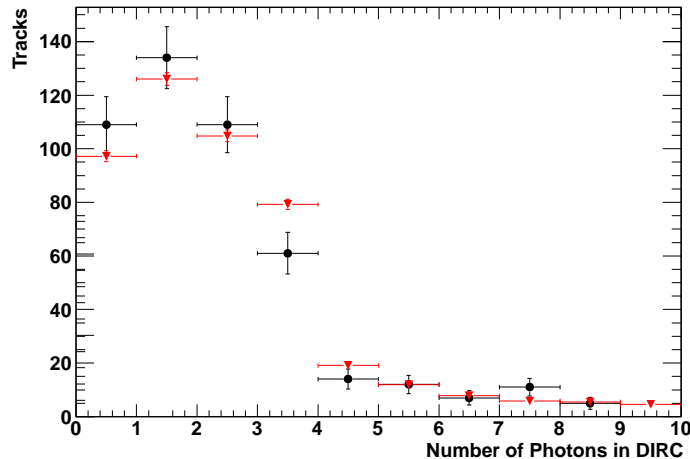


Figure 5.18: Number of photons in DIRC for (black circles) positive deuterons in the signal region passing all other selections and for (red triangles) simulated primary deuterons.

The same data and simulation samples find poorer agreement for the number of  $dE/dx$  samples in the DCH. Figure 5.20 illustrates, for a restricted range of momentum and polar angle, the disagreement between the two samples.

To evaluate the effect on the selection efficiency, we bin the control sample and the simulated data in CM momentum and polar angle. In each bin we compute the efficiency of the  $dE/dx$  selection by taking the ratio of the number of candidates in that bin with and without that selection, with all other selections left unchanged between the two. We then take the ratio of the efficiency histogram in data to that in simulation. The results are shown in Fig. 5.20, where it can be seen that the simulation underestimates the efficiency of this selection by about 7-8%. We apply

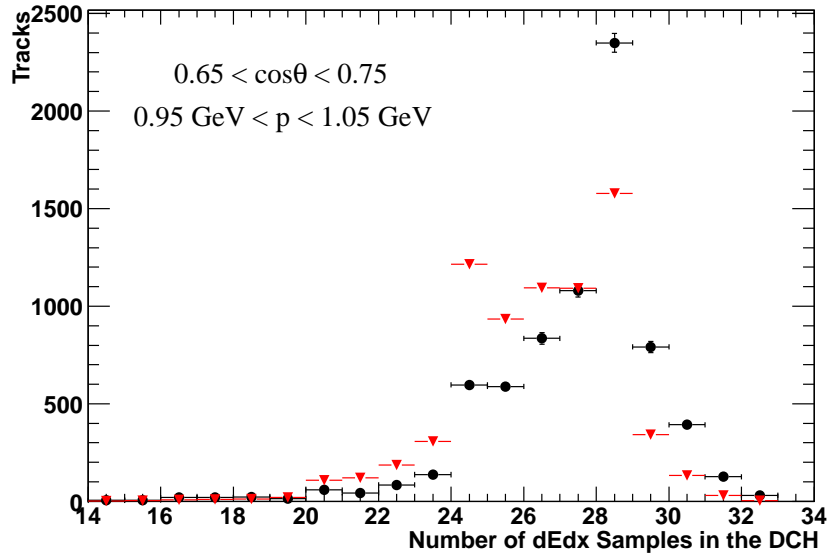
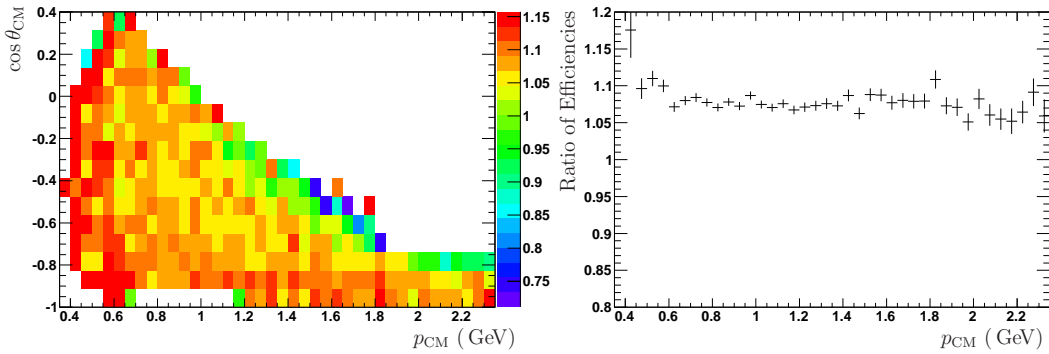


Figure 5.19: Number of  $dE/dx$  samples in the Drift Chamber for (black circles) positive deuterons in the signal region passing all other selections and for (red triangles) simulated primary deuterons.



(a) Ratio in CM momentum vs polar angle plane

(b) Ratio averaged over polar angle

Figure 5.20: Relative efficiency of the selection on the number of  $dE/dx$  samplings in the DCH for data control samples and signal simulation. For most of the parameter space the two are offset by a constant factor.

a correction to the fitted yields to correct for this effect.

The track selection also includes a requirement on the distance of closest approach in the transverse plane. We perform a similar check as above using control

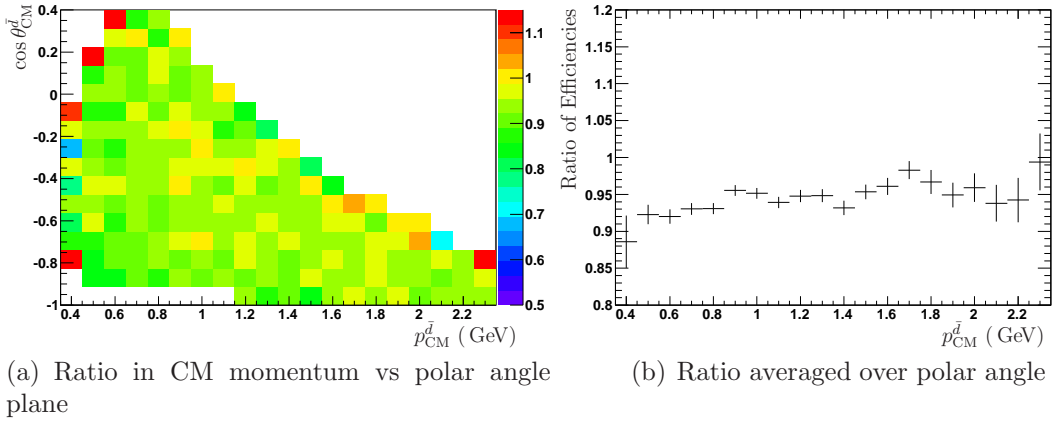


Figure 5.21: Ratio of efficiencies of DOCA selection in well-identified antiprotons in data and simulation.

samples consisting of well-identified antiprotons in data and simulated  $\Upsilon(2S)$  decays. We find disagreement at the level of 5-7% with the opposite sign of the disagreement in the cut on the number of  $dE/dx$  samples. The results can be seen in Fig. 5.21. This effect is accounted for as a uniform, one-sided 5.5% systematic uncertainty on the fitted yields.

The *BABAR* track fitting routine does not attempt track fits using the deuteron mass hypothesis. We check that the effects of fitting to the wrong mass hypothesis are well-modeled in simulation by comparing well-identified antiprotons in data and simulation fitted as protons and as pions. We compare the ratio of the efficiencies for our DOCA selection in these samples under each mass hypothesis, and we find that the simulation reproduces this ratio to better than 1% over a large momentum range. We therefore do not assign any additional systematic error due to this effect.

### 5.7.7 Background Shape

We perform the fit using an alternate background shape function to evaluate the uncertainty due to the shape of the background underneath the signal peak. The alternate background shape used involves the sum of two gaussian functions. The mean and width of the second gaussian is fixed by fitting to simulation, while the relative normalization is fixed by a fit to data. The difference between the yields in this fit and the nominal one is taken to be the systematic uncertainty due to the parameterization of the background.

### 5.7.8 Fake Antideuterons

The vast majority of deuterons recorded by the *BABAR* detector are created by nuclear interactions in material. When these reactions occur in outer material, such as the calorimeter or outer wall of the drift chamber, there is some probability that they will be created propagating inwards towards the interaction point, mimicking antideuterons. To estimate the number of backward going deuterons (fake antideuterons) passing our selection, we exploit the full range of x-y DOCA for the GoodTracksLoose list, shown in figure 5.22. Using the simulated signal deuterons, we find that the distribution for deuterons originating from the interaction region may be parameterized by the sum of a Gaussian function and a Crystal Ball shape (a Gaussian Peak with a power-law tail on one side). The long tail of the signal shape flattens out four orders of magnitude below the signal peak. In data, we observe that the distribution flattens out only two orders below the peak, which we

ascribe to the presence of backward-going tracks, and we parameterize this with the addition of a slowly falling exponential. The integral of this exponential function inside of the cut region of x-y DOCA  $< 0.04$  cm gives the expected contamination from backward-going tracks.

This fitting procedure is performed simultaneously across the various momentum bins so that an estimate for the contamination in each bin is obtained. We assign an asymmetric systematic uncertainty from the result, as this contribution can only decrease the yield.

### 5.7.9 Total Rate

Systematic uncertainties in the total rate from toy Monte Carlo studies are obtained from the distributions of the total visible rate (integral over the bins) in each of the toy studies. The uncertainty is obtained from the distribution of results in the same manner as for the uncertainty in each bin. Uncertainties from data/simulation agreement in efficiencies evaluated in simulation studies are carried over as uncertainties in the total yield.

## 5.8 Summary and Final Results

In conclusion we measure the production rate of antideuterons in  $\Upsilon(1S)$ ,  $\Upsilon(2S)$  and  $\Upsilon(3S)$  decay as well as in continuum  $e^+e^-$  annihilation. The final results and the statistical and systematic uncertainties for the various datasets are summarized in Figures 5.23-5.25 and Tables 5.3-5.7. The measured differential yields with statistical (black error bars) and statistical plus systematic uncertainties added in quadrature

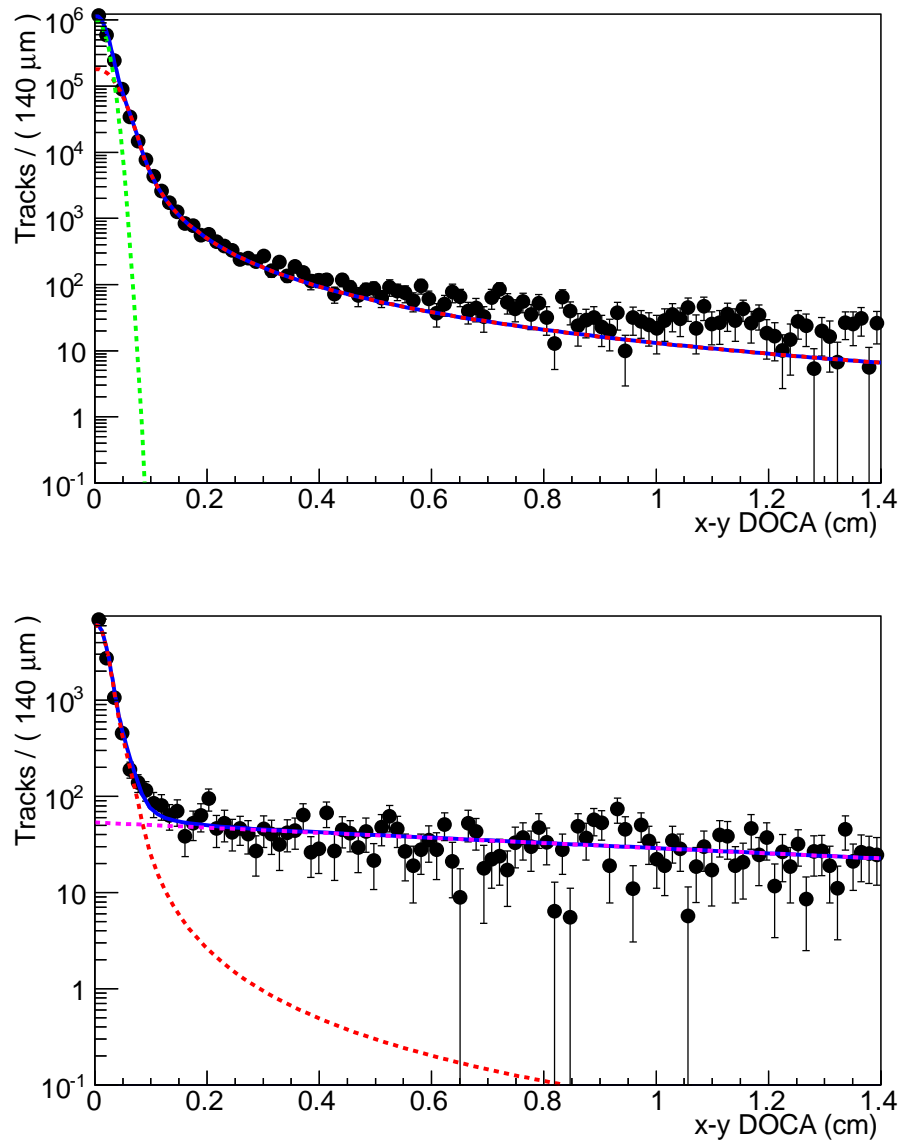


Figure 5.22: Fits to x-y DOCA distributions in  $\Upsilon(4S)$  signal simulation (top) and  $\Upsilon(4S)$  data (bottom). In the former, the green and red dotted curves are the Gaussian and Crystal Ball components of the signal shape, while in the latter the red dotted curve is the total signal shape and the purple is the background shape.

(red error bars) for all modes can be seen in the following figures. Total production rates, using the fireball spectrum to model the shape, are  $\mathcal{B}(\Upsilon(2S) \rightarrow \bar{d}X) = (2.62 \pm 0.10_{-0.28}^{+0.31}) \times 10^{-5}$ ,  $\mathcal{B}(\Upsilon(3S) \rightarrow \bar{d}X) = (2.45 \pm 0.14_{-0.24}^{+0.27}) \times 10^{-5}$ ,  $\mathcal{B}(\Upsilon(1S) \rightarrow \bar{d}X) = (2.85 \pm 0.47_{-0.29}^{+0.21}) \times 10^{-5}$ , and  $\sigma(e^+e^-(10.58 \text{ GeV}) \rightarrow \bar{d}X) = (10.49 \pm 0.33_{-1.14}^{+1.28})$  fb. We find no evidence of significant antideuteron production in  $\Upsilon(4S)$  decays. These results are in good agreement with the previous results from CLEO [42], and represents a significant improvement in the  $\Upsilon(2S)$  rate and the first measurement for  $\Upsilon(3S)$  decay and continuum  $e^+e^-$  annihilation.

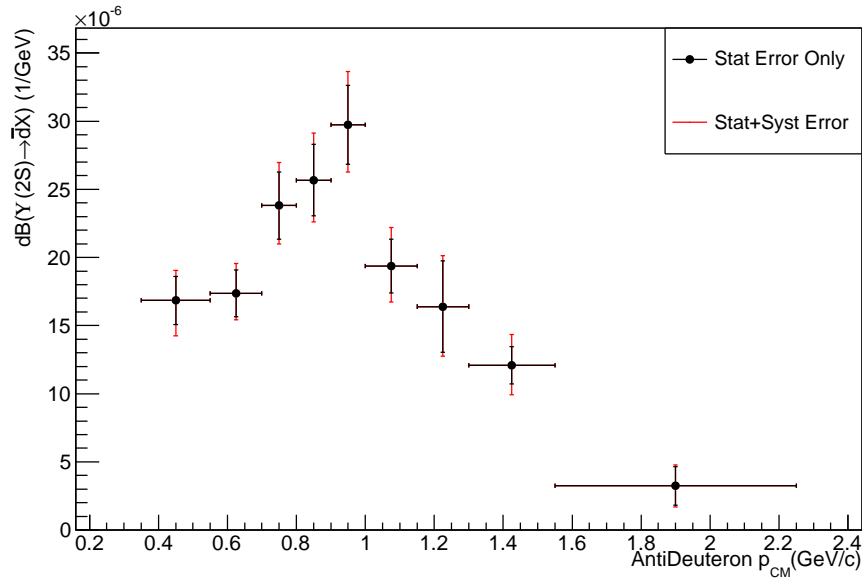
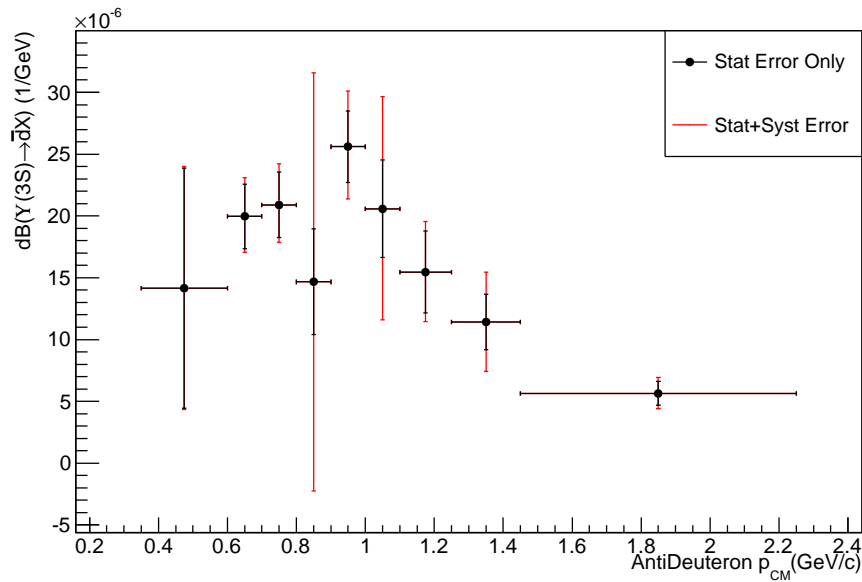

 (a)  $\Upsilon(2S)$ 

 (b)  $\Upsilon(3S)$ 

Figure 5.23: Results for differential rate of antideuteron production in (a)  $\Upsilon(2S)$  and (b)  $\Upsilon(3S)$  decays. The black (inner) error bars show the statistical uncertainty returned from the unbinned fit, while the red (outer) error bars show the sum of the statistical and systematic uncertainty.

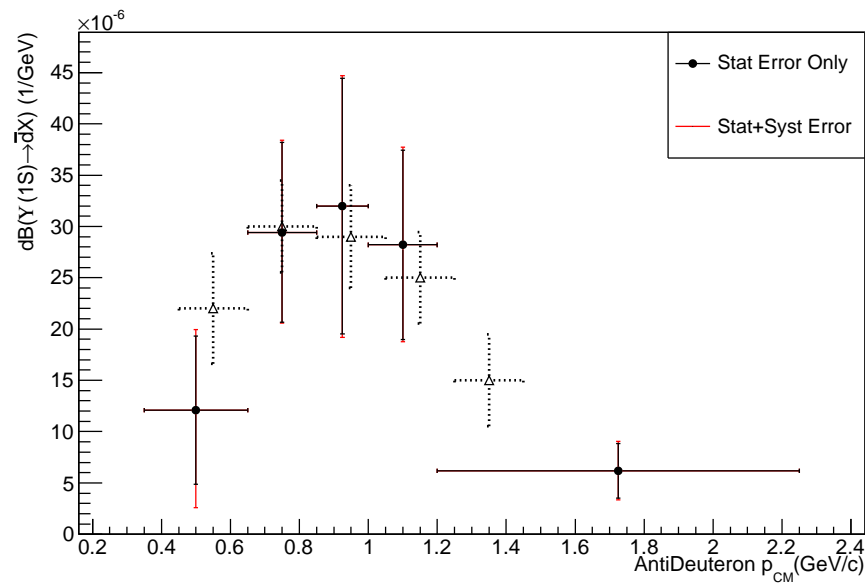
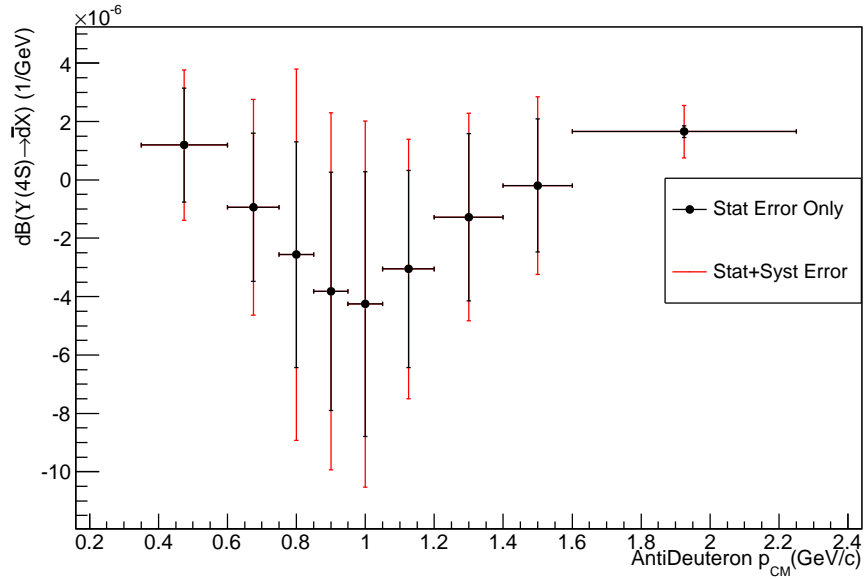
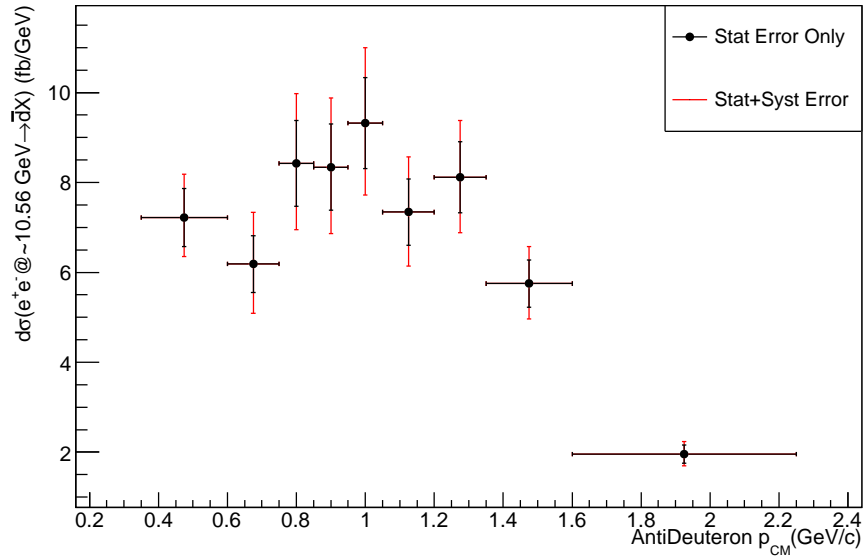


Figure 5.24: Results for differential rate of antideuteron production in  $\Upsilon(1S)$  decay from  $\Upsilon(2S) \rightarrow \pi^+\pi^-\Upsilon(1S)$  with the previous results from CLEO overlaid as open triangles with dotted error bars. The black (inner) error bars show the statistical uncertainty returned from the unbinned fit, while the red (outer) error bars show the sum of the statistical and systematic uncertainty.



(a)  $\Upsilon(4S)$



(b) continuum  $e^+e^-$

Figure 5.25: Results for differential rate of antideuteron production in (a)  $\Upsilon(4S)$  and (b) continuum. The black (inner) error bars show the statistical uncertainty returned from the unbinned fit, while the red (outer) error bars show the sum of the statistical and systematic uncertainty. We observe no significant production in  $\Upsilon(4S)$  decays, as expected.

Table 5.3: Differential rates and associated uncertainties in  $\Upsilon(2S)$  decay. Uncertainties are given as a percent of the measured yield.

Bin edge (GeV)	0.35-0.55	0.70	0.80	0.90	1.00	1.15	1.30	1.55	2.25
Branching Ratio ( $\times 10^{-6}/\text{GeV}$ )	1.18	1.30	1.79	1.93	2.23	1.45	1.23	0.91	0.24
Stat error (%)	10.48	9.23	9.65	9.47	9.08	9.43	18.96	10.43	40.99
Toy MC	1.48	0.94	0.69	1.08	1.27	0.86	3.26	1.68	7.94
Sim Stats	2.82	1.87	2.46	2.65	2.69	3.97	3.24	6.89	5.21
Acceptance Stats	0.81	1.39	2.23	2.47	2.51	3.65	3.27	6.82	5.26
Annihilation	2.80	2.14	2.63	2.79	2.80	4.17	3.55	7.07	4.86
Background	0.43	0.79	0.62	1.77	1.62	2.84	1.15	2.82	10.90
Fake $\bar{d}$	-10.25	-1.73	-1.45	-1.26	-1.90	-3.43	-3.64	-1.79	-0.47
DOCA	+5.82	+5.82	+5.82	+5.82	+5.82	+5.82	+5.82	+5.82	+5.82
Event selection	2.30	2.30	2.30	2.30	2.30	2.30	2.30	2.30	2.30
Normalization	1.20	1.20	1.20	1.20	1.20	1.20	1.20	1.20	1.20
Total syst (%)	+7.71 -11.43	+7.22 -4.61	+7.71 -5.25	+8.11 -5.79	+8.14 -6.00	+9.79 -8.59	+9.29 -8.11	+13.98 -12.83	+17.35 -16.35
Total error (%)	+13.01 -15.51	+11.72 -10.32	+12.35 -10.99	+12.47 -11.10	+12.19 -10.88	+13.60 -12.76	+21.12 -20.62	+17.44 -16.54	+44.51 -44.13

Table 5.4: Differential rates and associated uncertainties in  $\Upsilon(3S)$  decay. Uncertainties are given as a percent of the measured yield.

Bin edge (GeV)	0.35-0.60	0.70	0.80	0.85	0.95	1.10	1.25	1.50	2.25
Branching Ratio ( $\times 10^{-6}/\text{GeV}$ )	0.99	1.50	1.57	1.10	1.92	1.54	1.16	0.86	0.42
Stat error (%)	68.66	12.14	11.84	27.14	10.48	17.85	19.91	18.37	15.87
Toy MC	1.53	0.04	0.63	5.09	0.29	2.84	1.63	4.29	2.09
Sim Stats	4.58	3.24	3.63	103.44	6.50	35.72	9.31	22.13	10.36
Acceptance Stats	2.93	2.48	3.43	3.20	6.10	4.28	9.04	9.87	4.57
Annihilation	5.88	2.76	3.12	3.90	6.12	4.21	1.67	10.03	4.60
Background	0.15	0.29	0.25	0.57	0.49	0.41	0.35	0.31	3.48
Fake $\bar{d}$	-3.39	-1.73	-1.22	-2.31	-1.88	-1.42	-2.38	-1.65	-0.91
DOCA	+5.82	+5.82	+5.82	+5.82	+5.82	+5.82	+5.82	+5.82	+5.82
Event selection	2.30	2.30	2.30	2.30	2.30	2.30	2.30	2.30	2.30
Normalization	1.20	1.20	1.20	1.20	1.20	1.20	1.20	1.20	1.20
Total syst (%)	+10.35 -9.21	+8.06 -5.84	+8.70 -6.59	+103.88 -103.75	+12.57 -11.30	+36.89 -36.46	+14.65 -13.65	+27.33 -26.75	+14.37 -13.17
Total error (%)	+69.44 -69.28	+14.57 -13.47	+14.69 -13.55	+107.37 -107.24	+16.36 -15.41	+40.98 -40.59	+24.72 -24.14	+32.93 -32.45	+21.41 -20.62

Table 5.5: Differential rates and associated uncertainties in  $\Upsilon(1S)$  decay measured via the  $\Upsilon(2S) \rightarrow \pi^+\pi^-\Upsilon(1S)$  transition. Uncertainties are given as a percent of the measured yield.

Bin edge (GeV)	0.35-0.65	0.85	1.00	1.20	2.25
Branching Ratio ( $\times 10^{-6}/\text{GeV}$ )	0.84	2.21	2.40	2.12	0.46
Stat error (%)	59.88	27.73	36.23	30.47	39.96
Toy MC	1.03	0.82	0.46	0.74	0.68
Sim Stats	6.19	0.72	1.16	2.38	7.40
Acceptance Stats	15.52	0.85	2.37	2.62	7.63
Annihilation	16.81	1.28	2.28	2.72	7.97
Background	5.90	0.65	2.72	2.03	4.39
Fake $\bar{d}$	-44.39	-2.04	-6.97	-4.11	-5.18
DOCA	+5.82	+5.82	+5.82	+5.82	+5.82
Event selection	1.11	1.11	1.11	1.11	1.11
Normalization	0.24	0.24	0.24	0.24	0.24
Total syst (%)	+25.16 -50.69	+6.26 -3.07	+7.41 -8.35	+7.73 -6.54	+15.21 -14.98
Total error (%)	+64.95 -78.46	+28.43 -27.90	+36.98 -37.18	+31.44 -31.17	+42.76 -42.68

Table 5.6: Differential rates and associated uncertainties in  $\Upsilon(4S)$  decay. Uncertainties are given as a percent of the measured yield.

Bin edge (GeV)	0.35-0.60	0.75	0.85	0.95	1.05	1.20	1.40	1.60	2.25
Branching Ratio ( $\times 10^{-8}/\text{GeV}$ )	8.55	-6.54	-18.36	-27.62	-30.77	-22.04	-8.96	-1.12	12.27
Stat error (%)	156.15	265.84	144.00	101.07	100.90	104.73	218.70	1387.35	11.43
Toy MC	15.90	13.79	4.16	1.43	6.46	10.35	20.60	121.40	31.96
Sim Stats	77.73	163.81	112.73	67.22	56.07	51.53	93.69	707.49	2.24
Acceptance Stats	76.84	160.63	121.09	64.01	55.62	51.79	89.51	707.69	37.66
Annihilation	80.93	168.46	97.10	67.97	57.63	53.49	97.50	738.27	2.20
Background	4.39	10.78	8.72	1.27	2.83	6.85	9.44	21.04	13.21
Fake $\bar{d}$	-1.05	-5.07	-2.19	-2.13	-2.06	-3.93	-10.60	-46.84	-0.68
DOCA	+5.82	+5.82	+5.82	+5.82	+5.82	+5.82	+5.82	+5.82	+5.82
Event selection	2.30	2.30	2.30	2.30	2.30	2.30	2.30	2.30	2.30
Normalization	0.60	0.60	0.60	0.60	0.60	0.60	0.60	0.60	0.60
Total syst (%)	+137.14 -137.02	+285.24 -285.22	+192.18 -192.10	+115.24 -115.11	+98.22 -98.07	+91.61 -91.51	+163.86 -164.10	+1249.65 -1250.52	+51.61 -51.28
Total error (%)	+207.82 -207.74	+389.91 -389.90	+240.15 -240.09	+153.28 -153.19	+140.81 -140.70	+139.14 -139.08	+273.28 -273.42	+1867.18 -1867.76	+52.86 -52.54

Table 5.7: Differential rates and associated uncertainties in continuum  $e^+e^-$  annihilation. Uncertainties are given as a percent of the measured yield.

Bin edge (GeV)	0.35-0.60	0.75	0.85	0.95	1.05	1.20	1.35	1.60	2.25
Cross-section (0.1fb/ GeV)	5.04	4.64	6.32	6.26	6.99	5.51	6.09	4.31	1.47
Stat error (%)	8.89	9.45	10.53	10.69	10.08	9.36	9.07	8.52	9.68
Toy MC	0.65	0.01	0.02	0.64	0.25	0.24	0.56	0.55	0.72
Sim Stats	3.70	5.62	6.10	6.09	5.51	4.86	4.31	3.67	2.43
Acceptance Stats	3.23	5.44	5.86	6.09	5.46	4.76	4.18	3.54	4.31
Annihilation	4.31	5.67	6.34	6.13	5.69	4.87	4.26	3.39	1.52
Background	0.11	7.80	3.99	3.84	5.56	5.48	4.14	3.65	2.18
Fake $\bar{d}$	-0.53	-2.14	-1.91	-2.83	-2.72	-4.73	-4.94	-4.04	-1.72
DOCA	+5.82	+5.82	+5.82	+5.82	+5.82	+5.82	+5.82	+5.82	+5.82
Event selection	4.61	4.61	4.61	4.61	4.61	4.61	4.61	4.61	4.61
Normalization	0.60	0.60	0.60	0.60	0.60	0.60	0.60	0.60	0.60
Total syst (%)	+9.93 -8.07	+14.48 -13.43	+13.53 -12.37	+13.50 -12.51	+13.38 -12.35	+12.47 -12.00	+11.28 -10.85	+10.32 -9.44	+9.36 -7.52
Total error (%)	+13.33 -12.01	+17.29 -16.42	+17.15 -16.24	+17.22 -16.45	+16.75 -15.94	+15.59 -15.22	+14.47 -14.14	+13.39 -12.72	+13.47 -12.26

## Chapter 6

### Conclusions and Future Prospects

Both measurements presented here constitute significant improvements over the previous state of knowledge of the respective quantities. For the  $B_s$  semileptonic branching fraction we find  $\mathcal{B}(B_s \rightarrow \ell\nu X) = 9.5_{-2.0}^{+2.5+1.1}$ . This measurement is the first published result for this parameter, and the  $f_s$  measurement (Figure 4.15(a)) represents the first attempt at probing  $B_s$  production in the region around the  $\Upsilon(5S)$  rather than at the peak. The latter shows good agreement with the predictions of an earlier coupled-channel calculation performed in [33]. The measurements of antideuteron production rates are in good agreement with the previous measurements for  $\Upsilon(1S)$  decay [42], and they improve on previous measurements at the  $\Upsilon(2S)$  and represents the first measurement of this process in continuum  $e^+e^-$  collisions in the 10 GeV center-of-mass region. These results are listed in Table 6.1 and the differential rates are shown in Figures 5.23, 5.24 and 5.25.

Future  $e^+e^-$  colliders operating in this energy region will allow for exploration

Table 6.1: Antideuteron total production rate results in  $\Upsilon(1S, 2S, 3S)$  decay and continuum  $e^+e^-$  annihilation

Process	Rate
$\mathcal{B}(\Upsilon(2S) \rightarrow \bar{d}X)$	$(2.62 \pm 0.10_{-0.28}^{+0.31}) \times 10^{-5}$
$\mathcal{B}(\Upsilon(3S) \rightarrow \bar{d}X)$	$(2.45 \pm 0.14_{-0.24}^{+0.27}) \times 10^{-5}$
$\mathcal{B}(\Upsilon(1S) \rightarrow \bar{d}X)$	$(2.85 \pm 0.47_{-0.29}^{+0.21}) \times 10^{-5}$
$\sigma(e^+e^-_{(10.58 \text{ GeV})} \rightarrow \bar{d}X)$	$(10.49 \pm 0.33_{-1.14}^{+1.28}) \text{ fb}$

of these kinds of measurements with much improved precision. The Belle-II experiment at the upgraded Super KEK-B facility currently in progress and the planned SuperB facility will collect datasets on the scale of  $50,000 \text{ fb}^{-1}$ . These large datasets will be able to provide precision measurements of continuum antideuteron production. The improvements in systematics are possible with better simulation, especially improved simulation of antideuteron material interactions. Also required is careful investigations of the agreement between data and simulation and deuteron reconstruction using the deuteron mass hypothesis in dedicated PID devices.

The large instantaneous luminosities at future facilities of  $\approx 10^{36} \text{ cm}^{-2} \text{ s}^{-1}$  will allow for scans of much greater detail in the CM energy region of 10 GeV. The scan used here represents a very short ( $\sim 1$  week) running period at *BABAR* luminosities: a scan with luminosity on the order of  $10 \text{ fb}^{-1}$  per point is feasible in about a month of running at the Super *B*-factories. Combined with improved measurements of  $\mathcal{B}(B_s \rightarrow D_s X)$ , this will allow for higher-precision tests of coupled-channel models of *B* and *B<sub>s</sub>* production above the  $\Upsilon(4S)$ . Other improvements required include a careful treatment of the contribution of Initial State Radiation  $e^+e^- \rightarrow \gamma^* \Upsilon(nS)$  and two-photon  $e^+e^- \rightarrow e^+e^- \gamma^* \gamma^* \rightarrow e^+e^- X_h$  events.

Appendix A  
 Results of  $\phi$  Yield Fits  
 A.1  $\phi$

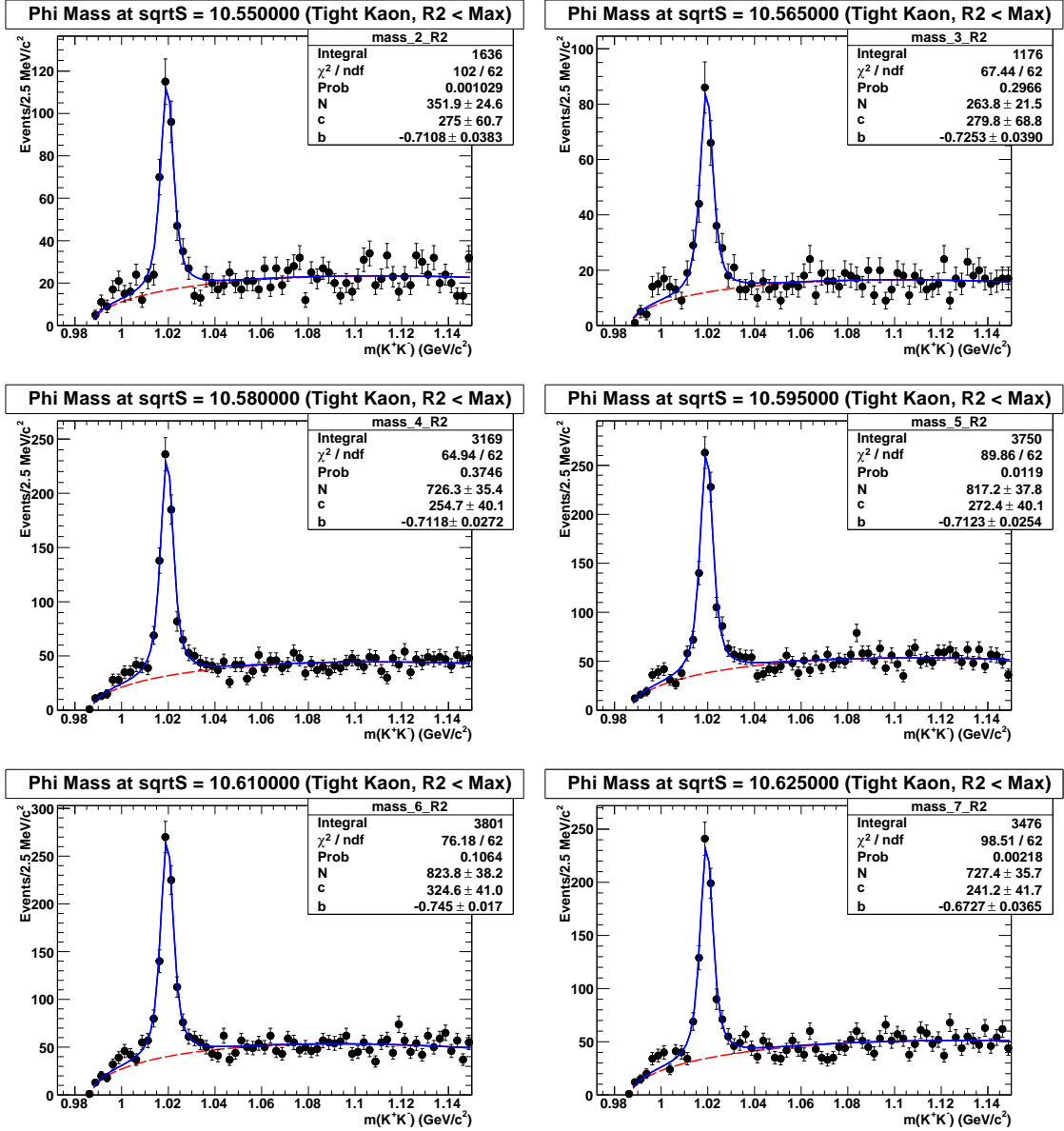


Figure A.1: Fits to  $K^+K^-$  invariant mass distributions in the region  $E_{\text{CM}} = 10.55 - 10.64$  GeV. The blue curve is the total fit, and the red curve is the background.

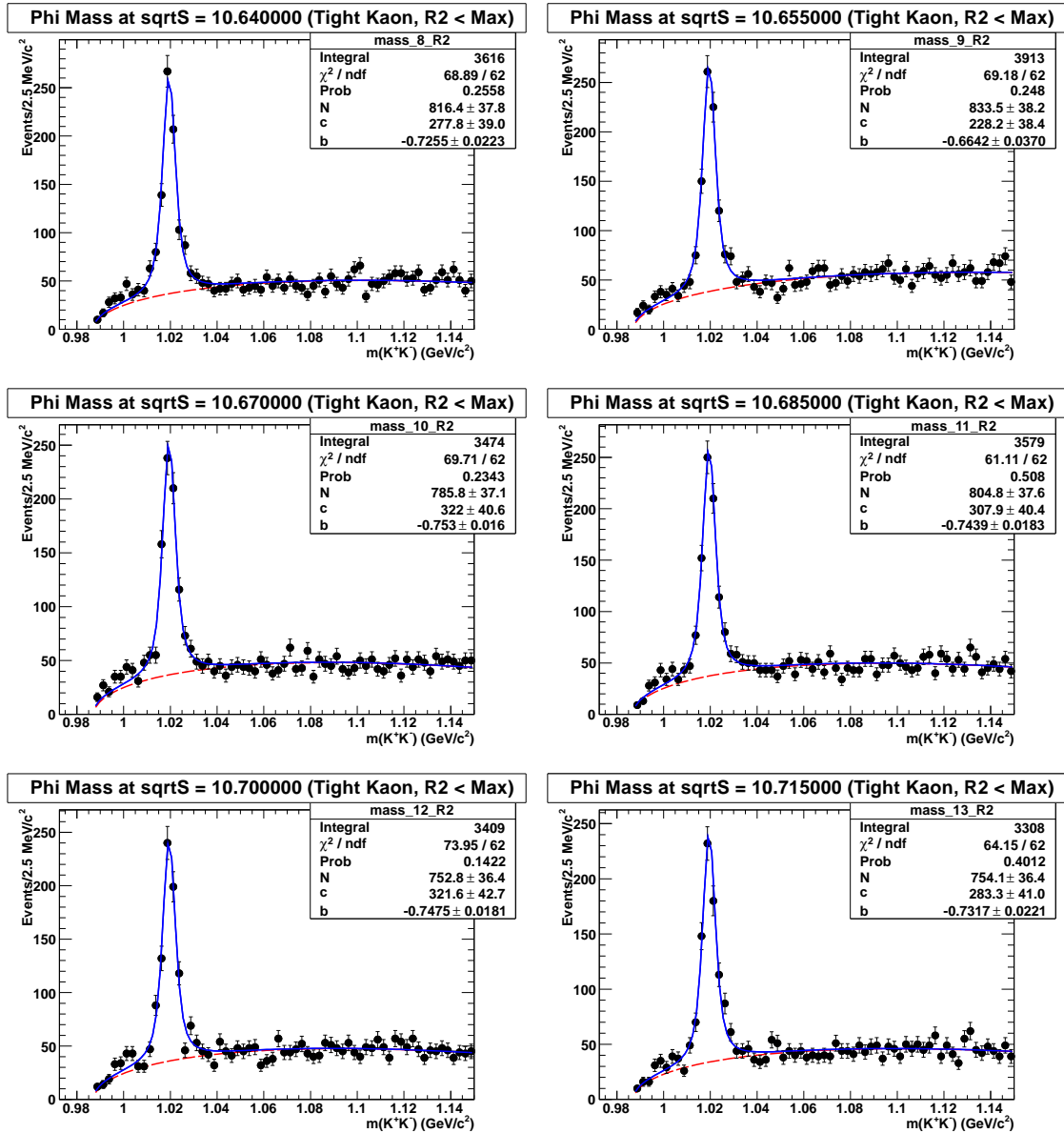


Figure A.2: Fits to  $K^+K^-$  invariant mass distributions in the region  $E_{CM} = 10.64 - 10.73$  GeV. The blue curve is the total fit, and the red curve is the background.

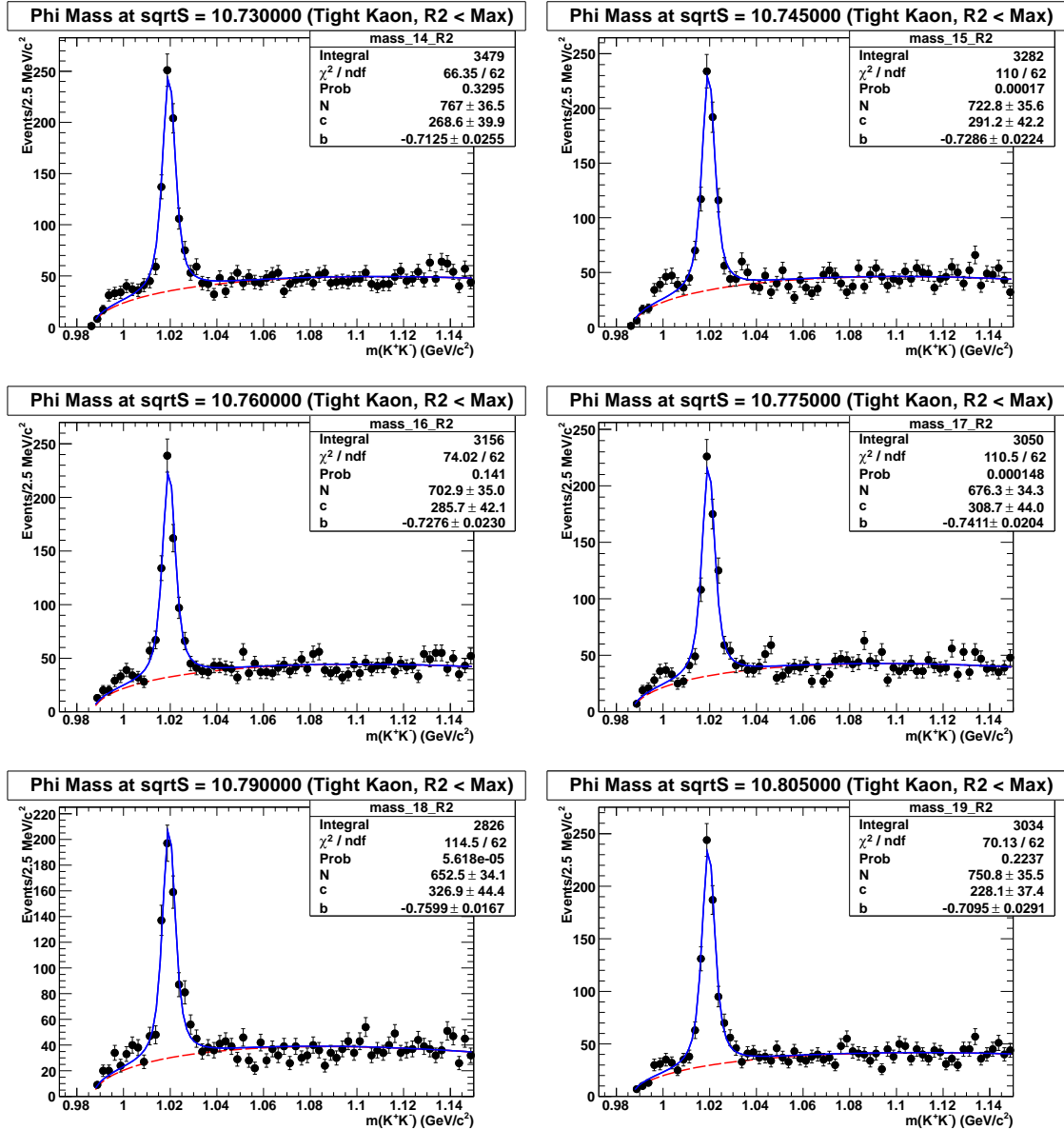


Figure A.3: Fits to  $K^+K^-$  invariant mass distributions in the region  $E_{\text{CM}} = 10.73 - 10.82$  GeV. The blue curve is the total fit, and the red curve is the background.

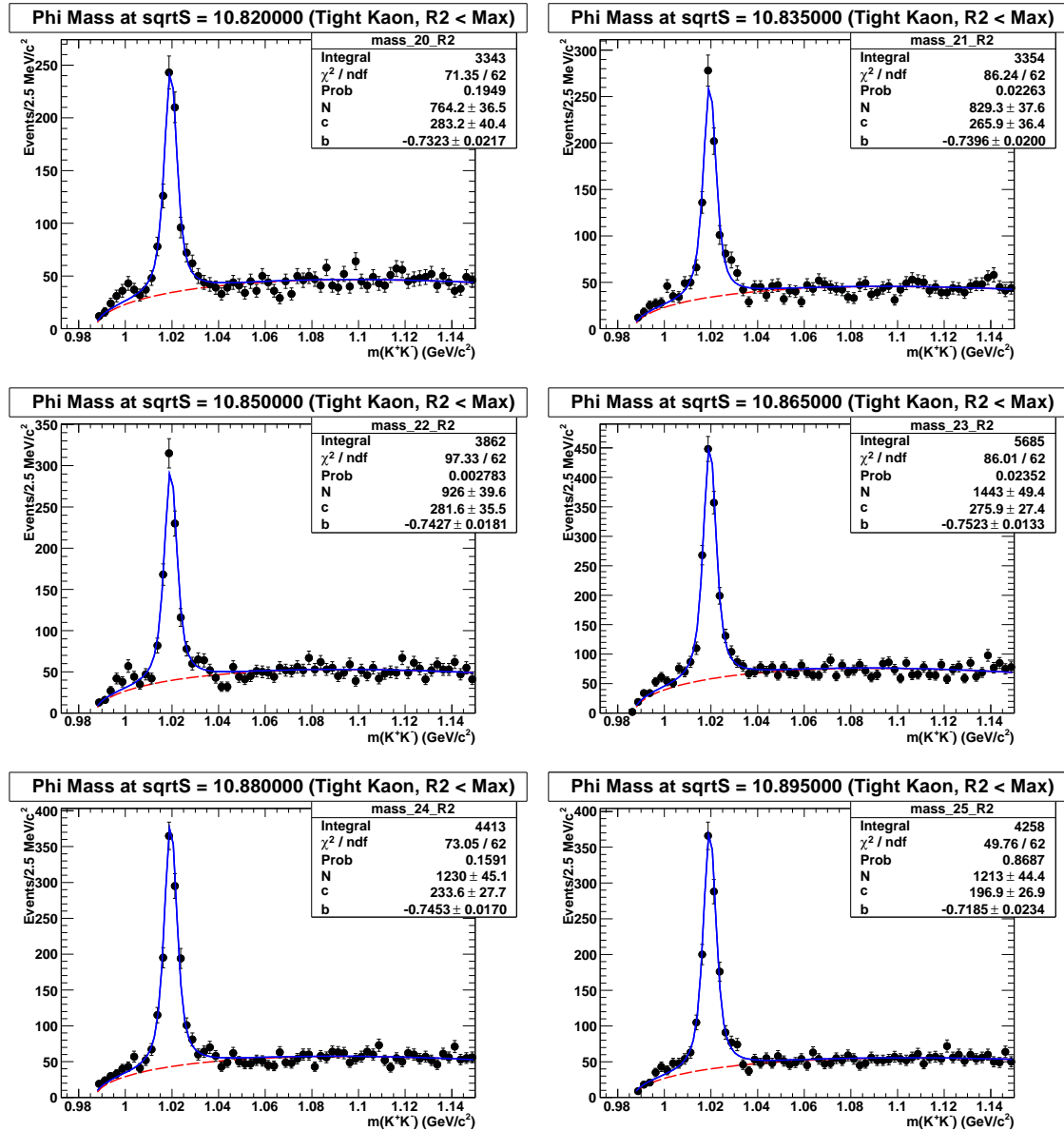


Figure A.4: Fits to  $K^+K^-$  invariant mass distributions in the region  $E_{CM} = 10.82 - 10.91$  GeV. The blue curve is the total fit, and the red curve is the background.

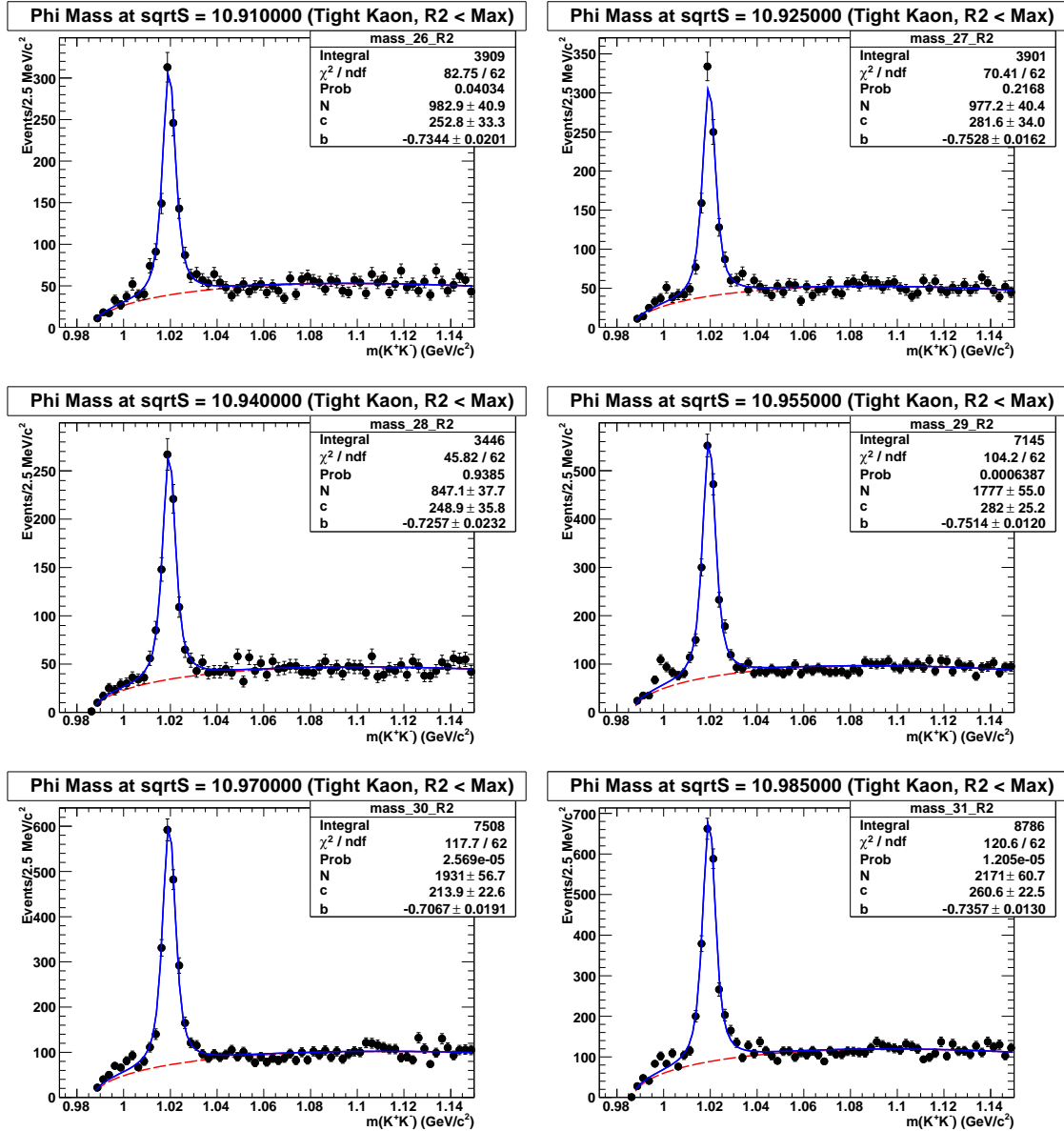


Figure A.5: Fits to  $K^+K^-$  invariant mass distributions in the region  $E_{\text{CM}} = 10.91 - 11.00$  GeV. The blue curve is the total fit, and the red curve is the background.

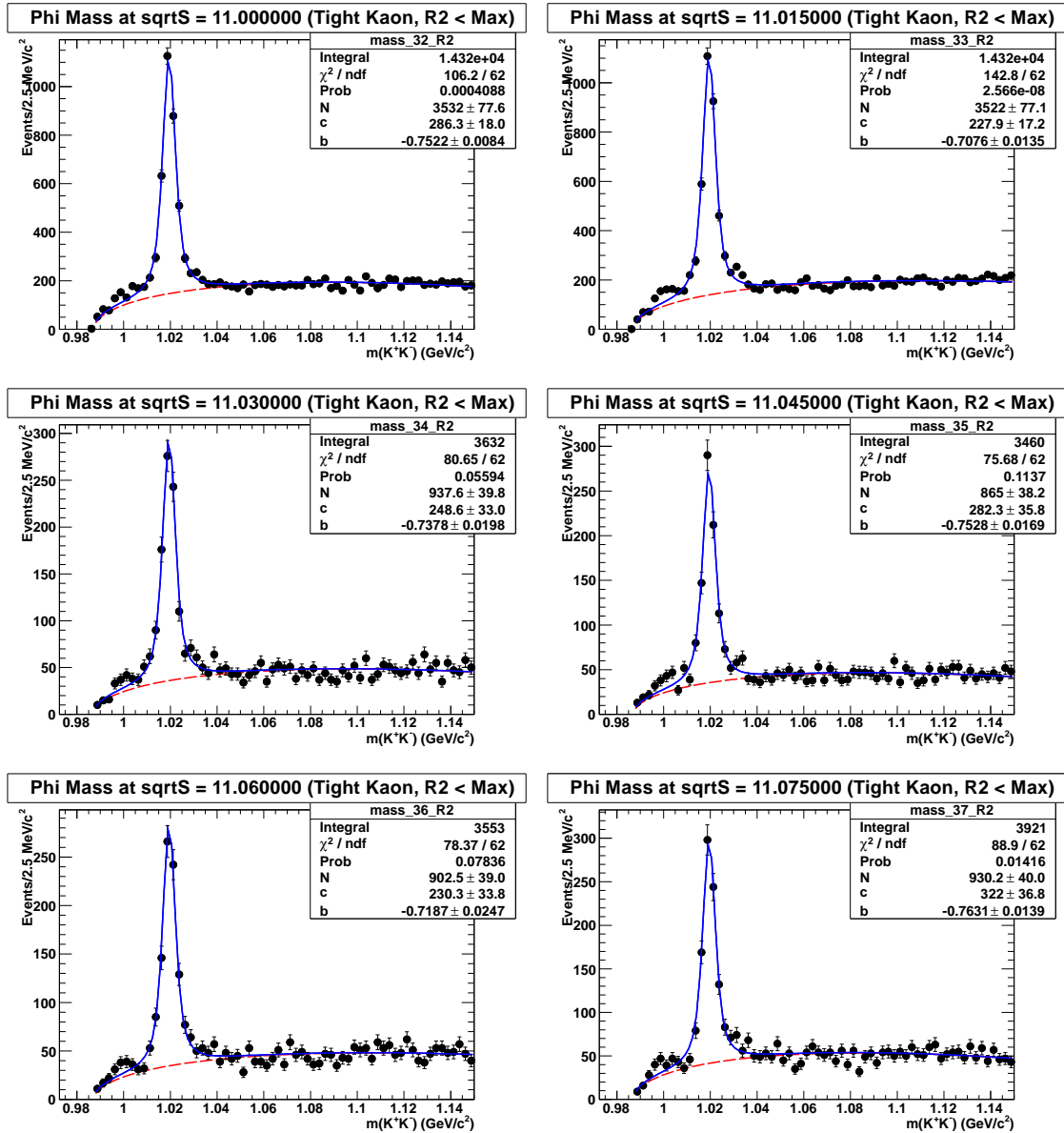


Figure A.6: Fits to  $K^+K^-$  invariant mass distributions in the region  $E_{CM} = 11.00 - 11.09$  GeV. The blue curve is the total fit, and the red curve is the background.

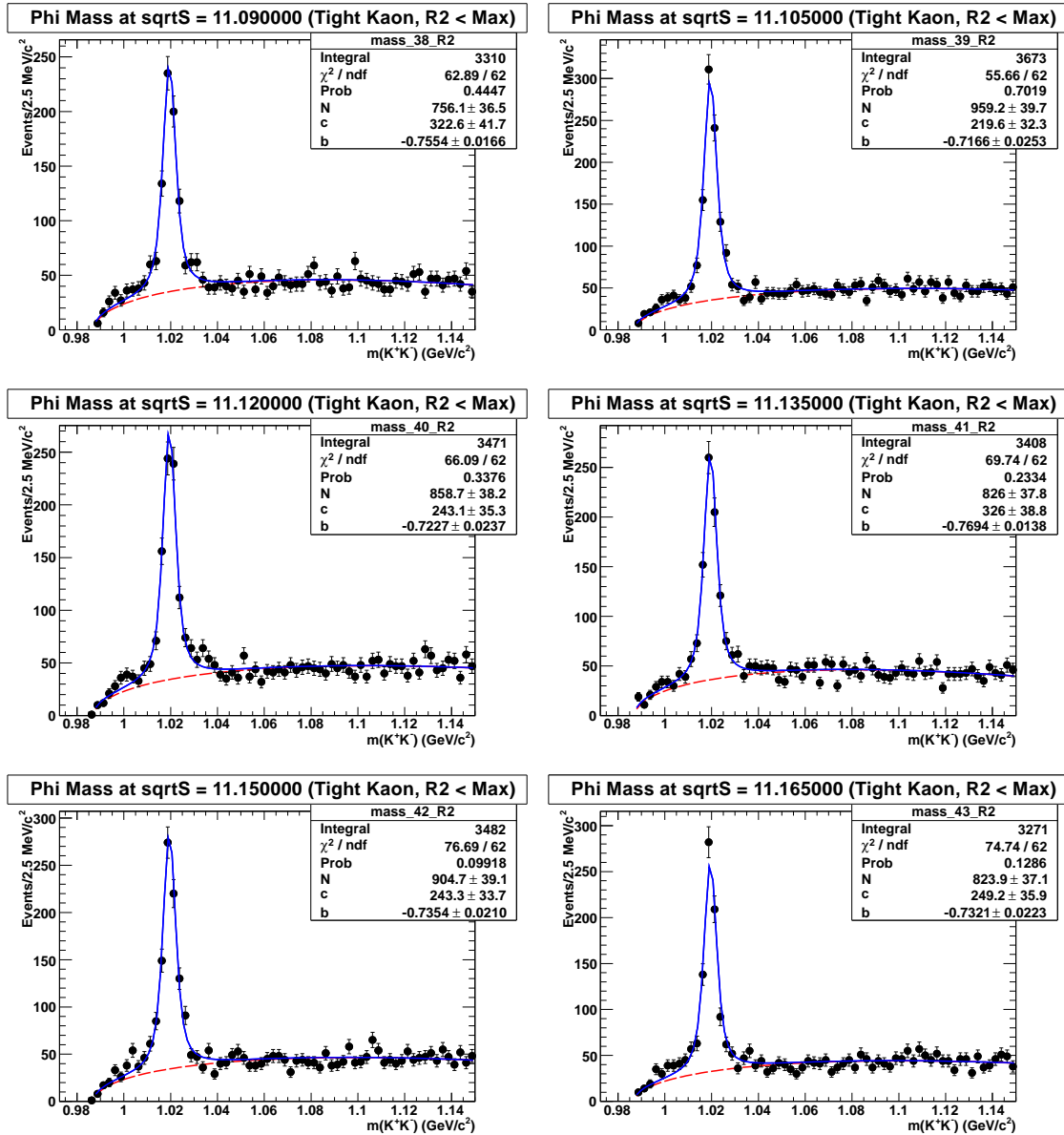


Figure A.7: Fits to  $K^+K^-$  invariant mass distributions in the region  $E_{CM} = 11.09 - 11.18$  GeV. The blue curve is the total fit, and the red curve is the background.

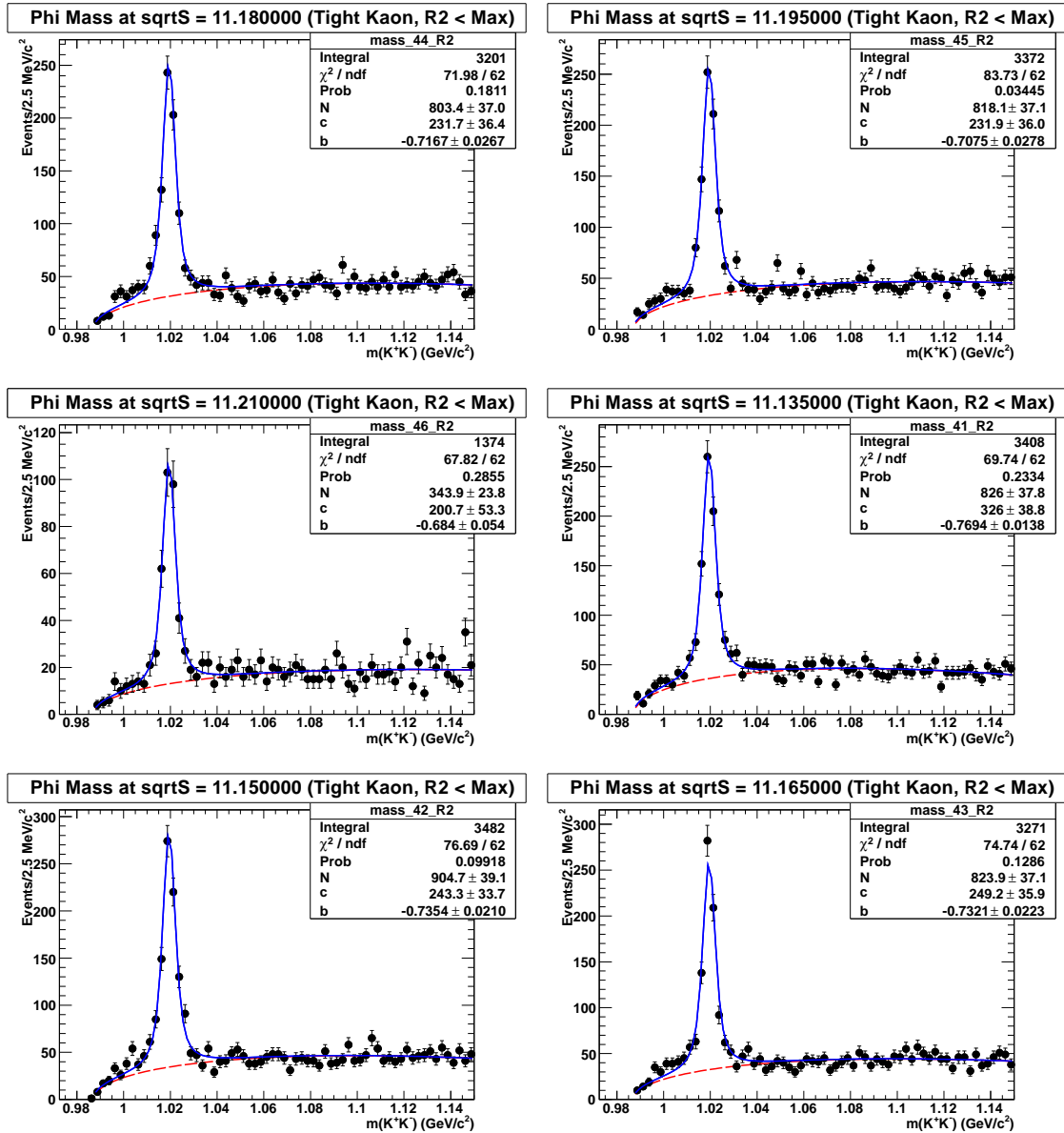


Figure A.8: Fits to  $K^+K^-$  invariant mass distributions in the region  $E_{CM} = 11.18 - 11.21$  GeV. The blue curve is the total fit, and the red curve is the background.

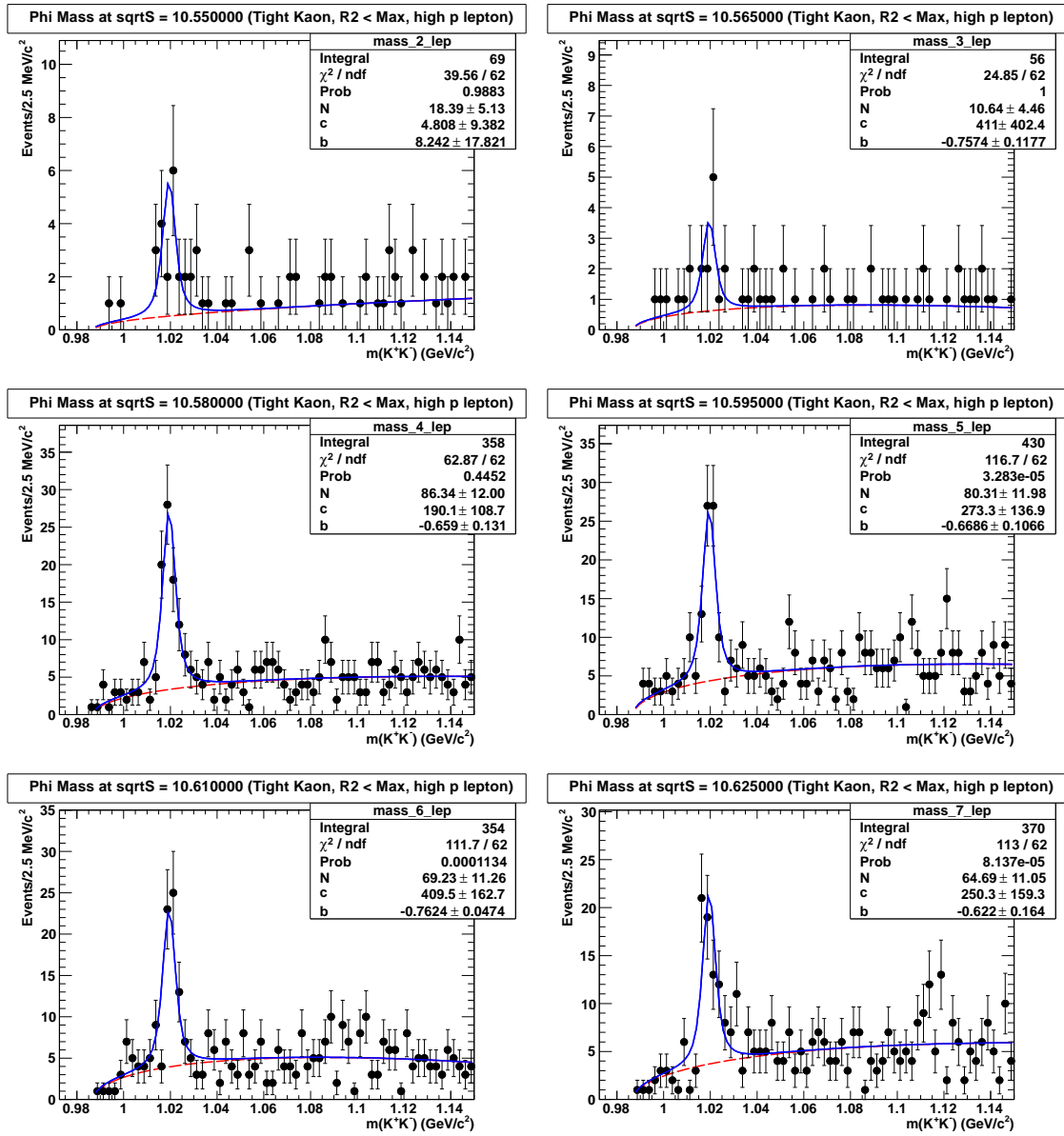
A.2  $\phi$ -lepton

Figure A.9: Fits to  $\phi$ -lepton sample  $K^+K^-$  invariant mass distributions in the region  $E_{CM} = 10.55 - 10.64$  GeV. The blue curve is the total fit, and the red curve is the background.

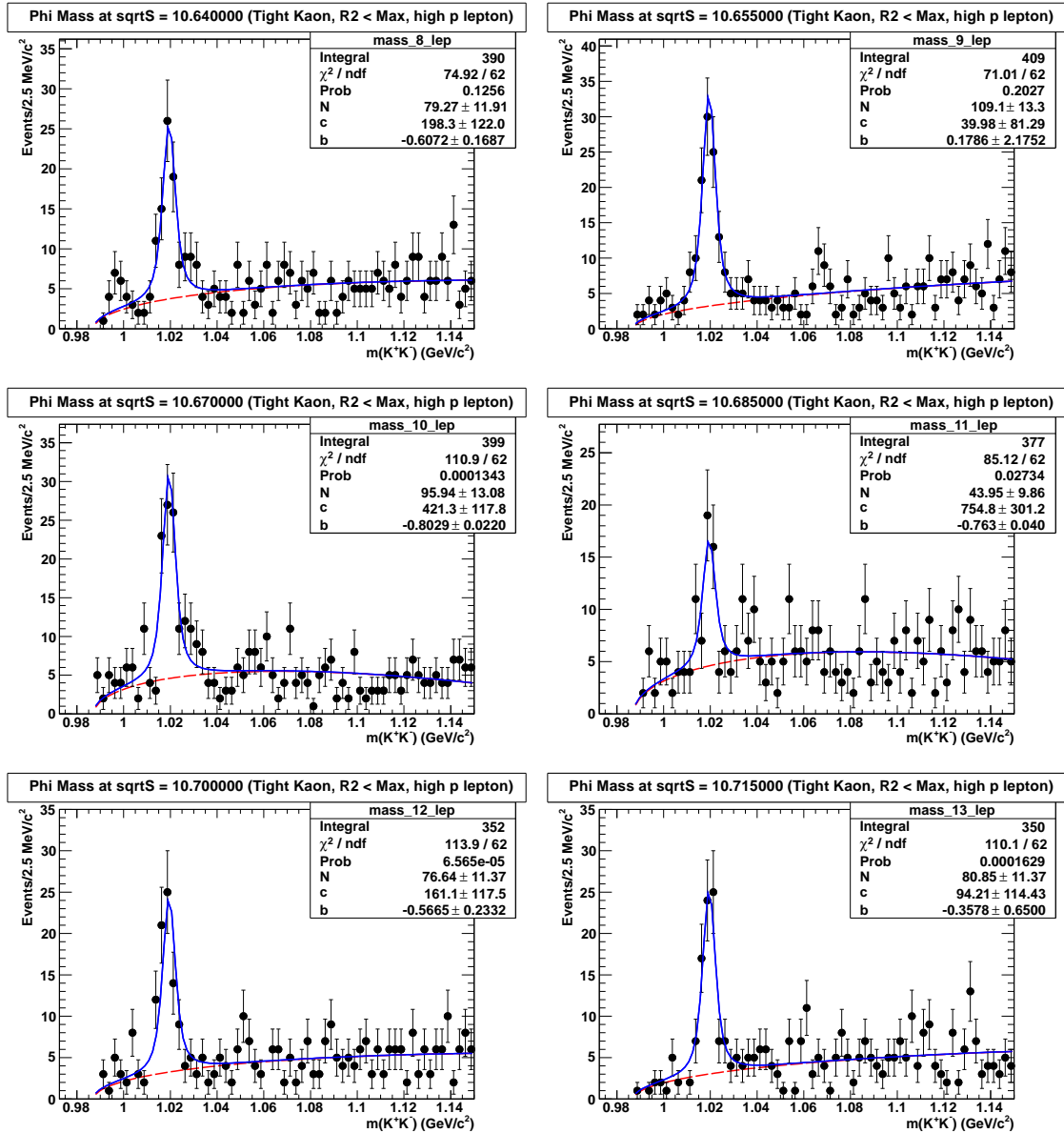


Figure A.10: Fits to  $\phi$ -lepton sample  $K^+K^-$  invariant mass distributions in the region  $E_{CM} = 10.64 - 10.73$  GeV. The blue curve is the total fit, and the red curve is the background.

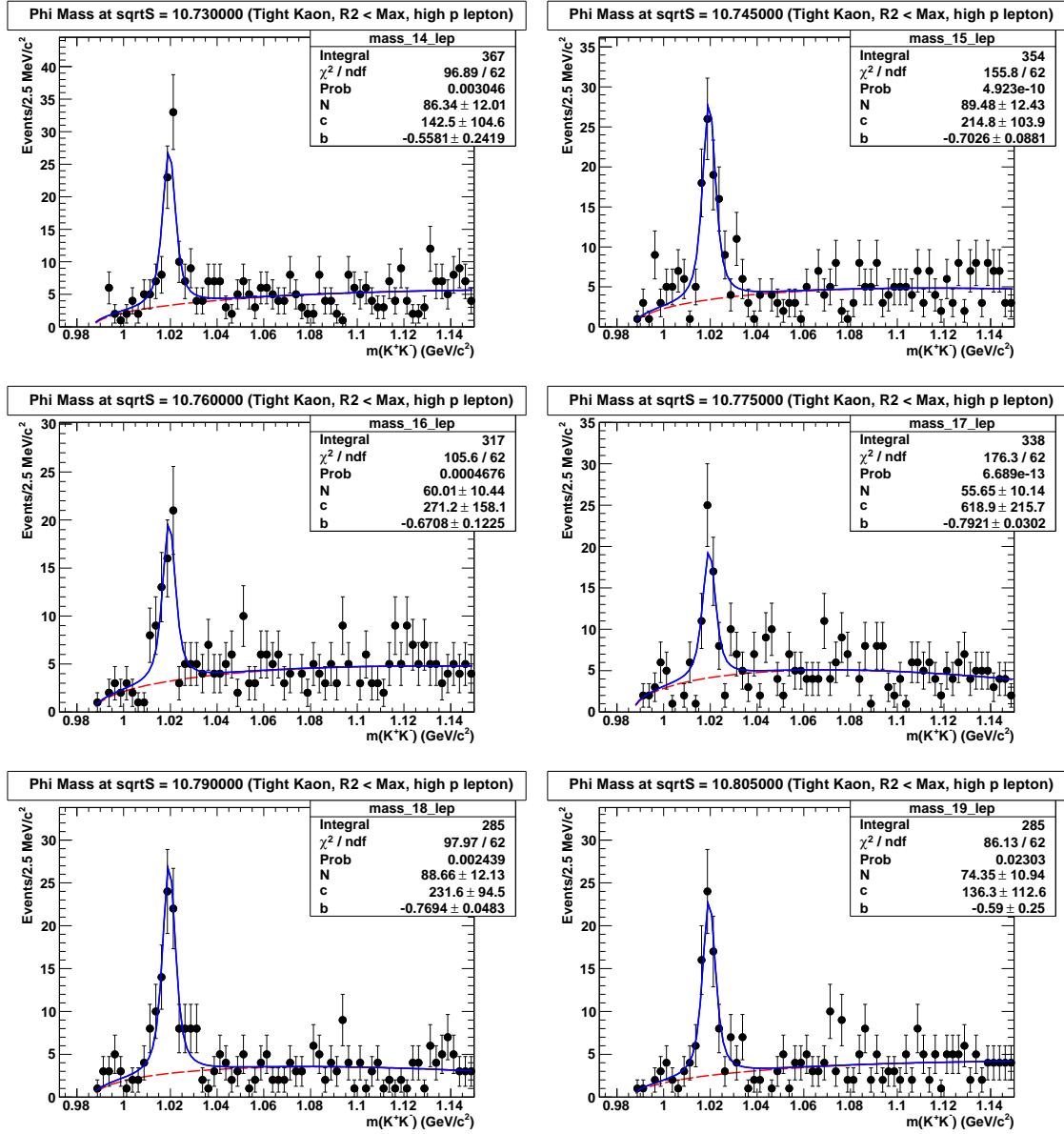


Figure A.11: Fits to  $\phi$ -lepton sample  $K^+K^-$  invariant mass distributions in the region  $E_{CM} = 10.73 - 10.82$  GeV. The blue curve is the total fit, and the red curve is the background.

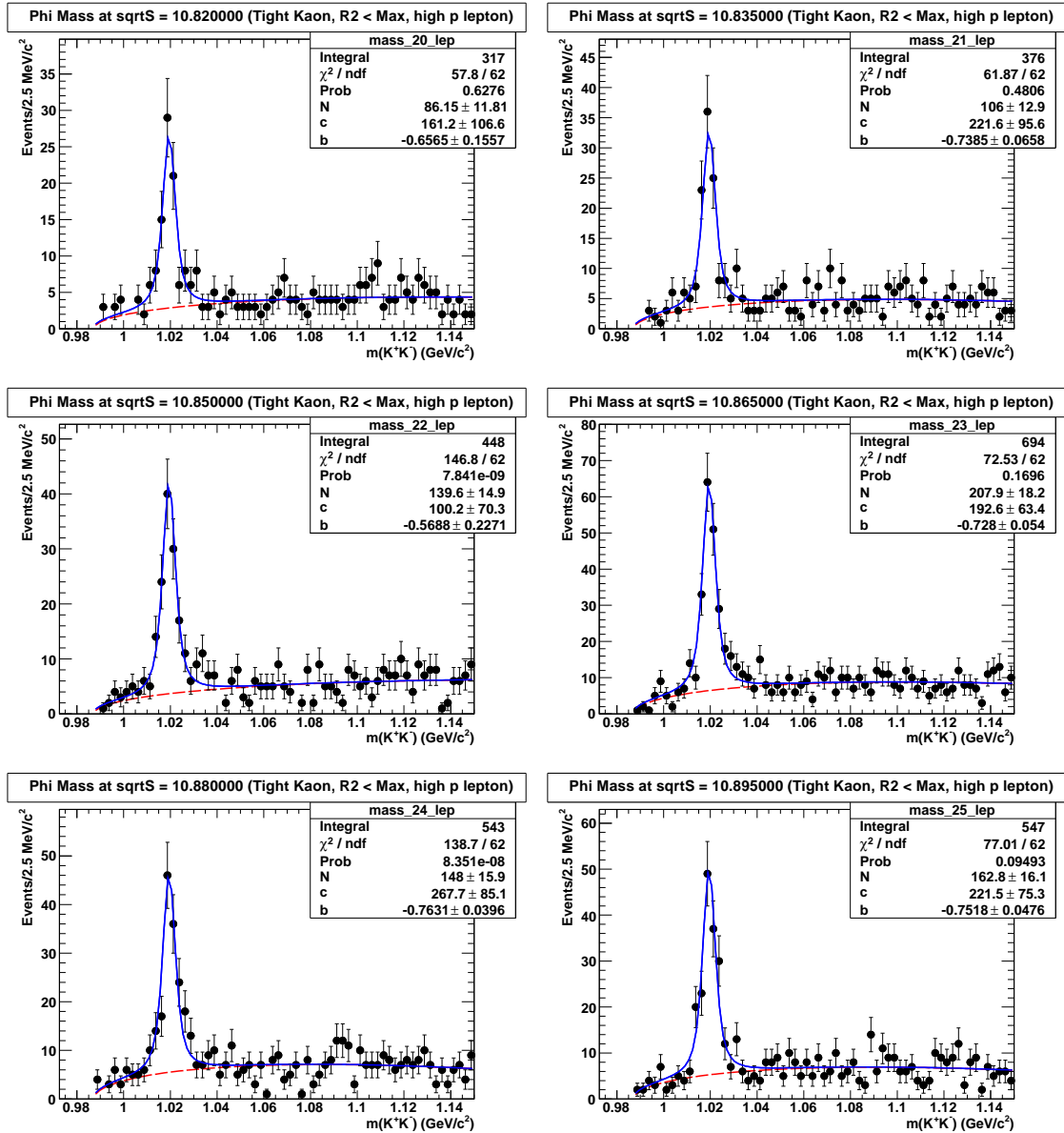


Figure A.12: Fits to  $\phi$ -lepton sample  $K^+K^-$  invariant mass distributions in the region  $E_{\text{CM}} = 10.82 - 10.91$  GeV. The blue curve is the total fit, and the red curve is the background.

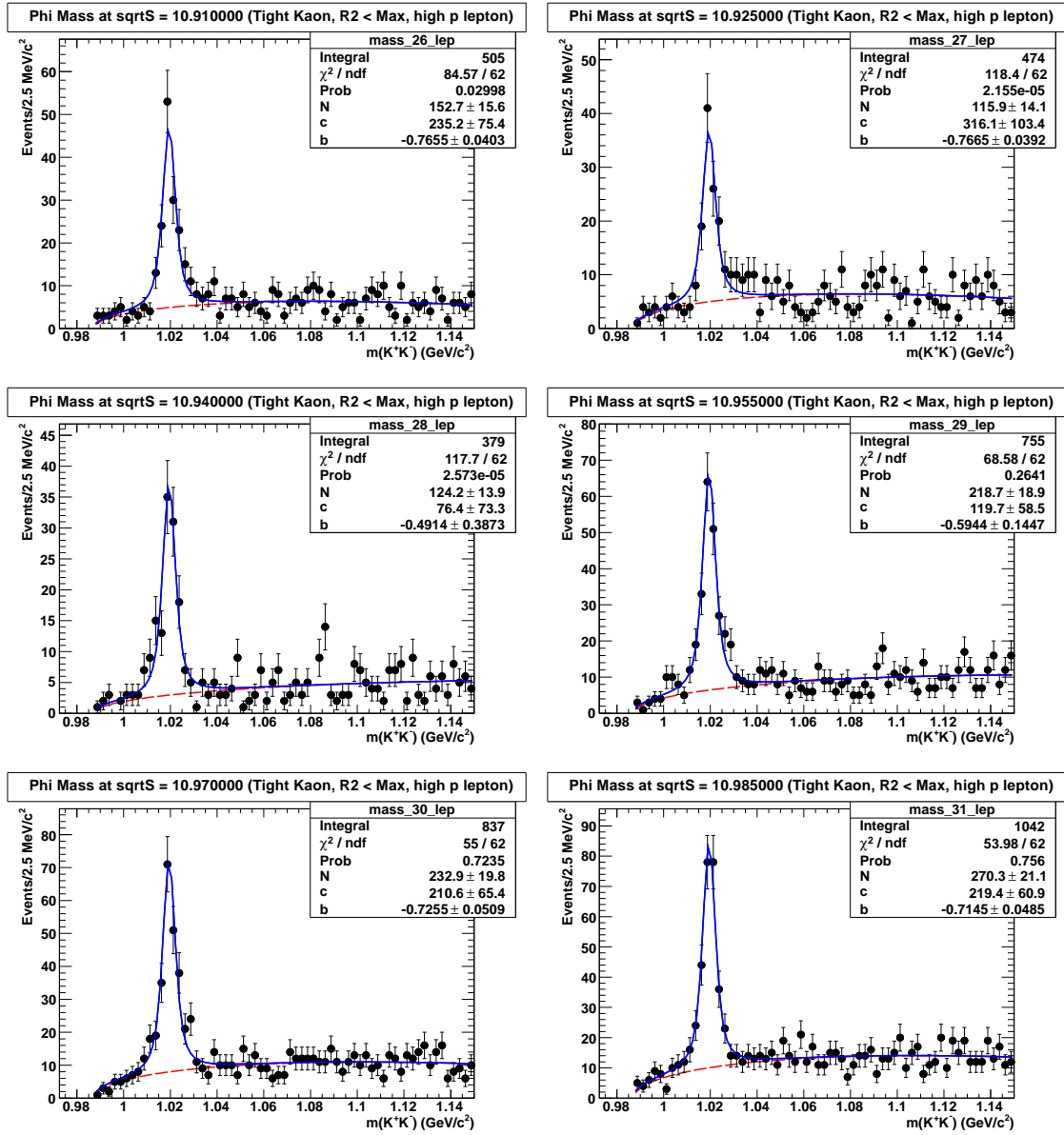


Figure A.13: Fits to  $\phi$ -lepton sample  $K^+K^-$  invariant mass distributions in the region  $E_{CM} = 10.91 - 11.00$  GeV. The blue curve is the total fit, and the red curve is the background.

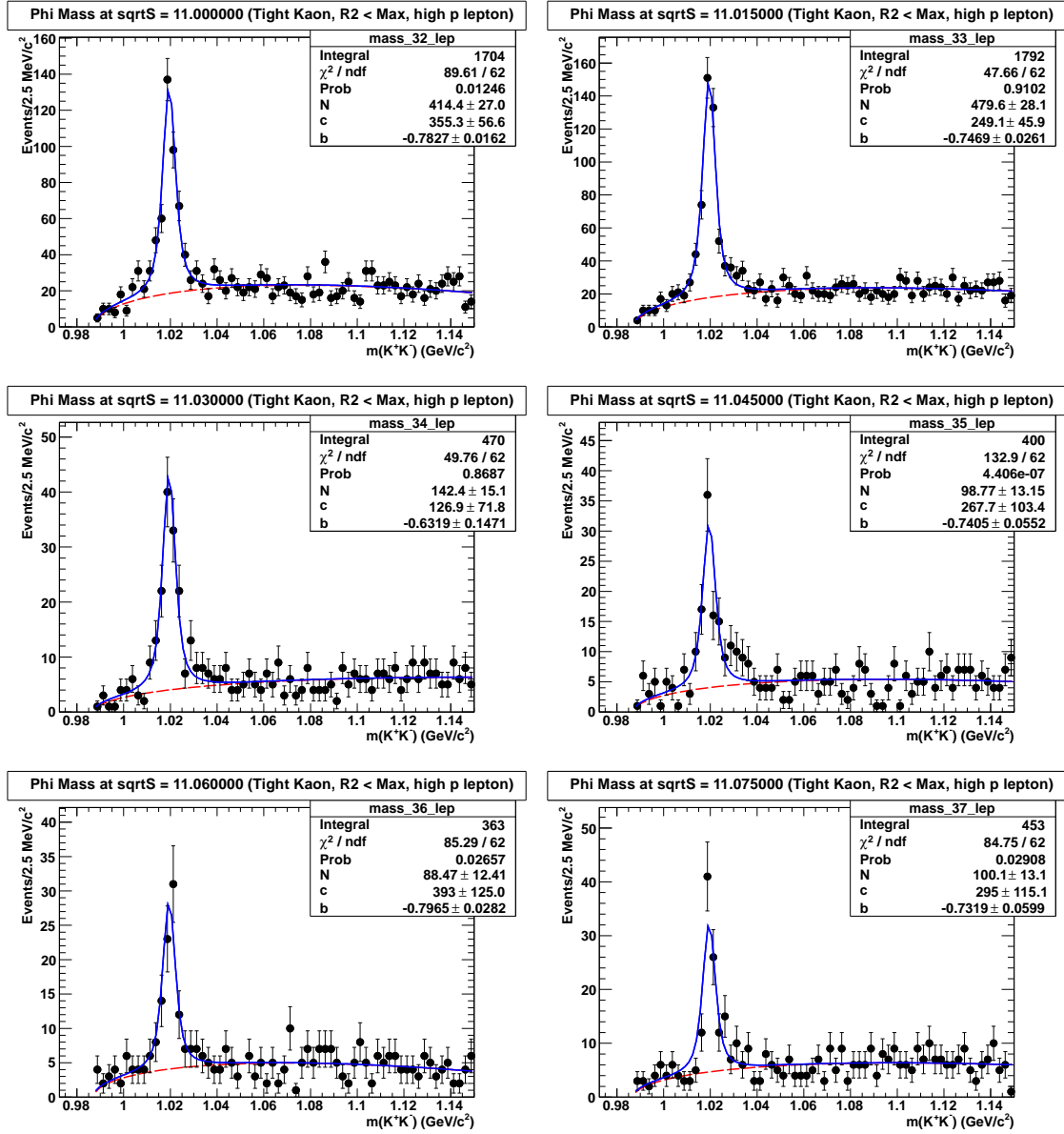


Figure A.14: Fits to  $\phi$ -lepton sample  $K^+K^-$  invariant mass distributions in the region  $E_{CM} = 11.00 - 11.09$  GeV. The blue curve is the total fit, and the red curve is the background.

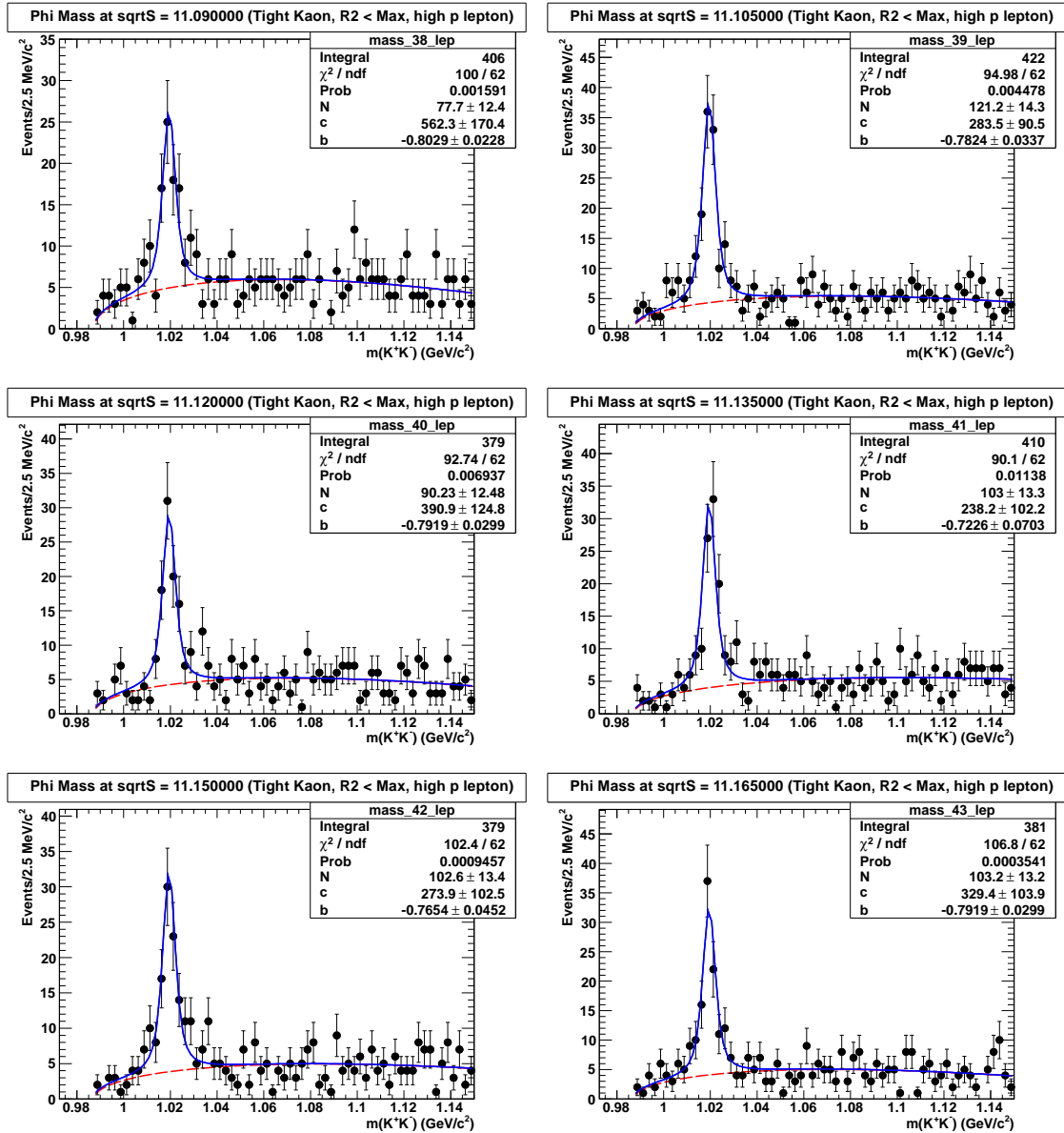


Figure A.15: Fits to  $\phi$ -lepton sample  $K^+K^-$  invariant mass distributions in the region  $E_{CM} = 11.09 - 11.18$  GeV. The blue curve is the total fit, and the red curve is the background.

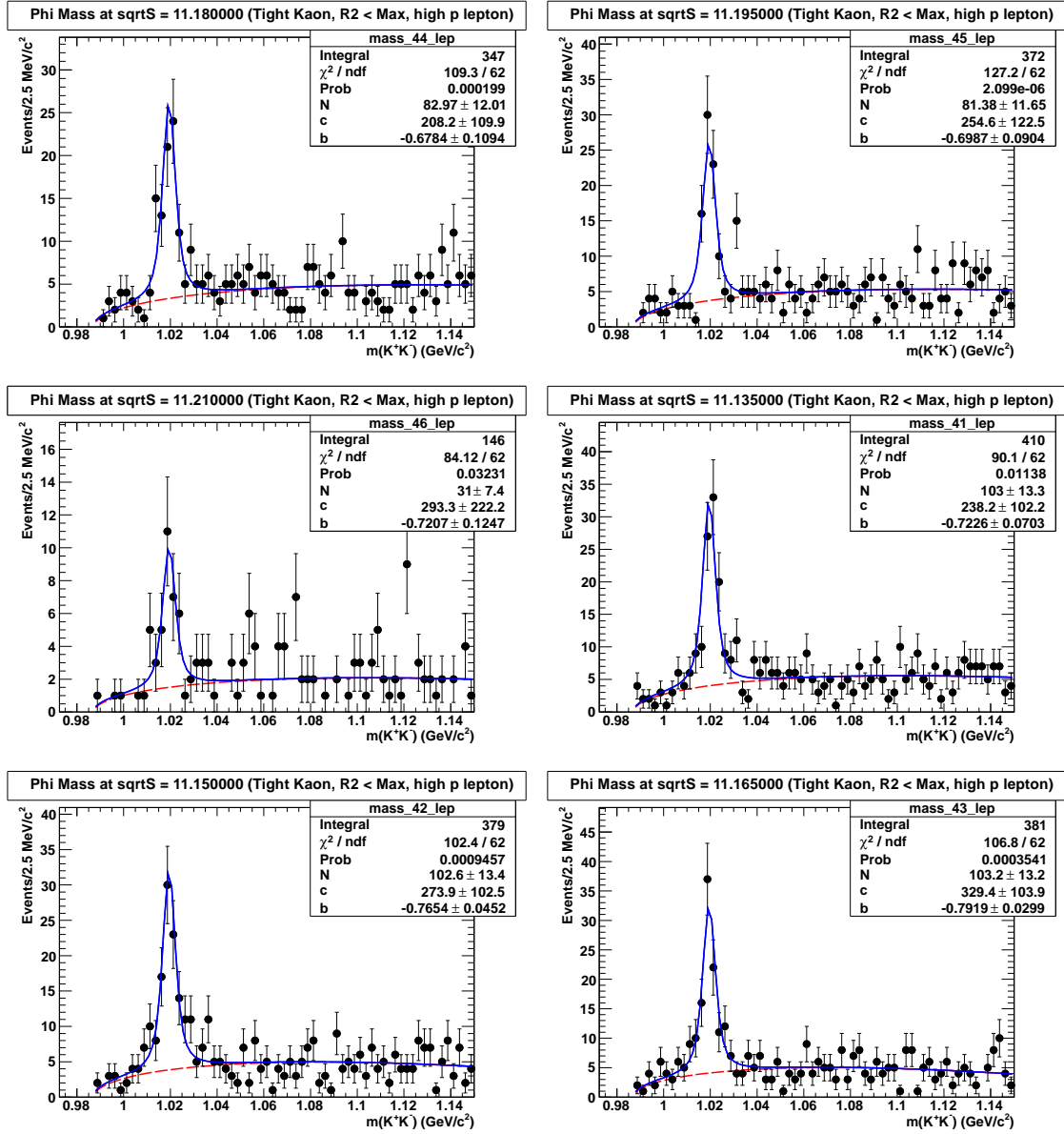


Figure A.16: Fits to  $\phi$ -lepton sample  $K^+K^-$  invariant mass distributions in the region  $E_{CM} = 11.18 - 11.21$  GeV. The blue curve is the total fit, and the red curve is the background.

Appendix B  
 Results of Antideuteron Yield Fits  
 B.1  $\Upsilon(2S)$

B.1.1  $\Upsilon(2S)$  on-resonance negative tracks

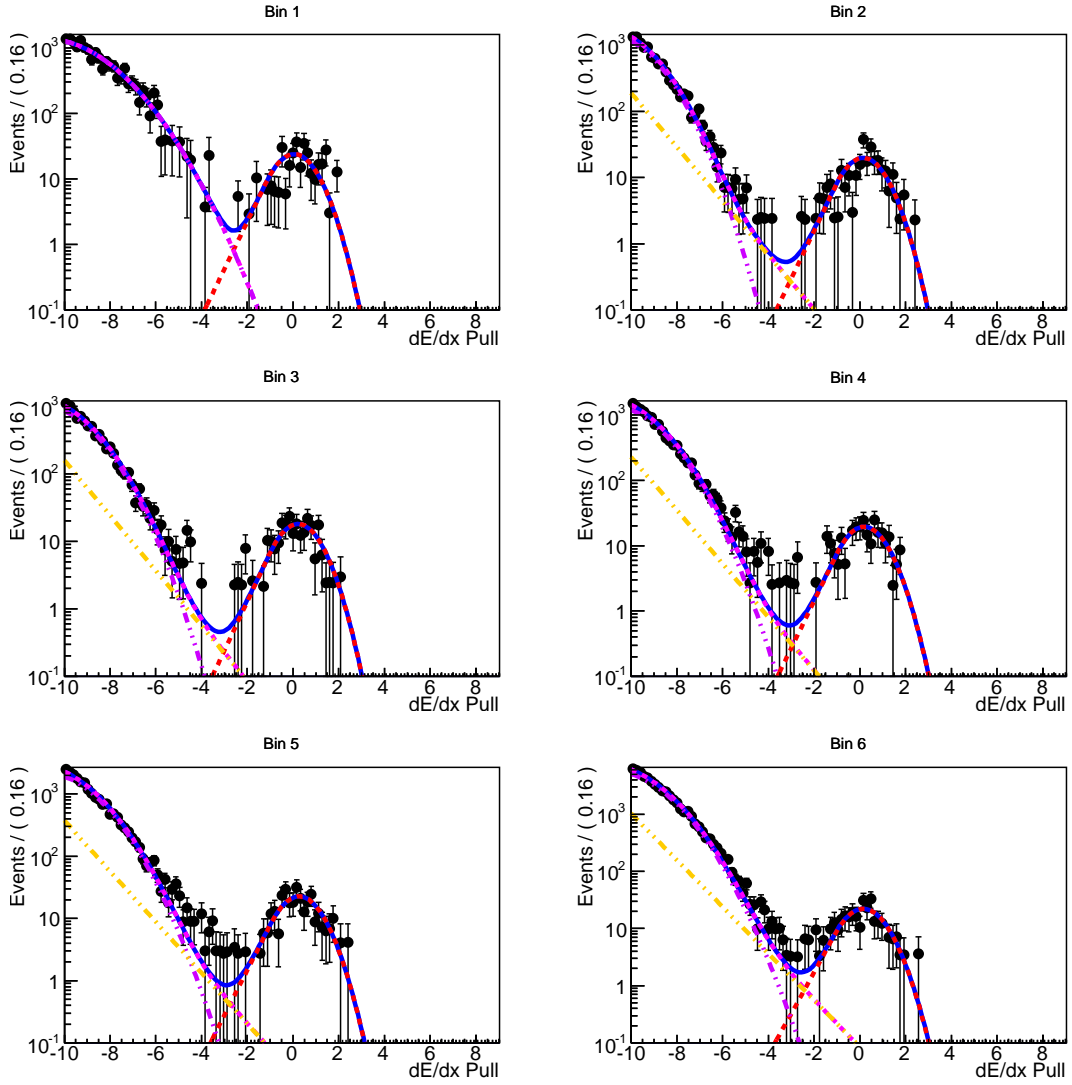


Figure B.1: Fit to  $\Upsilon(2S)$   $p_{CM}$  bin 1-6 for on-resonance negative tracks. The blue curve shows the total fit, the red, purple and yellow dotted curves the signal, Gaussian and Exponential components.

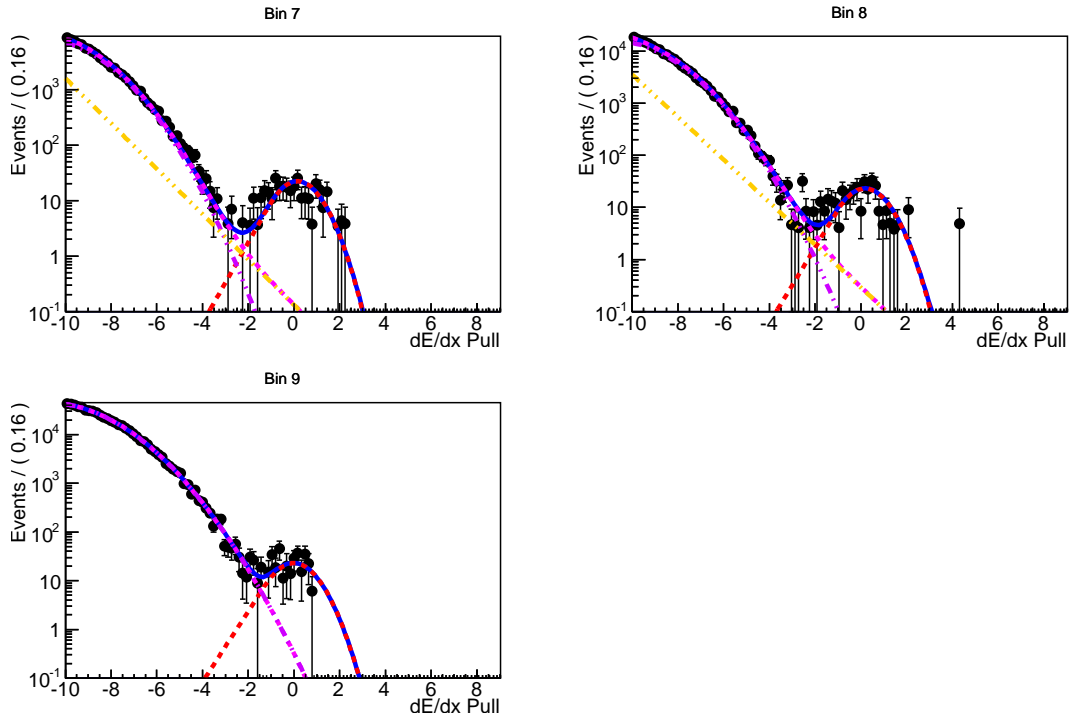


Figure B.2: Fit to  $\Upsilon(2S)$   $p_{\text{CM}}$  bin 7-9 for on-resonance negative tracks. The blue curve shows the total fit, the red, purple and yellow dotted curves the signal, Gaussian and Exponential components.

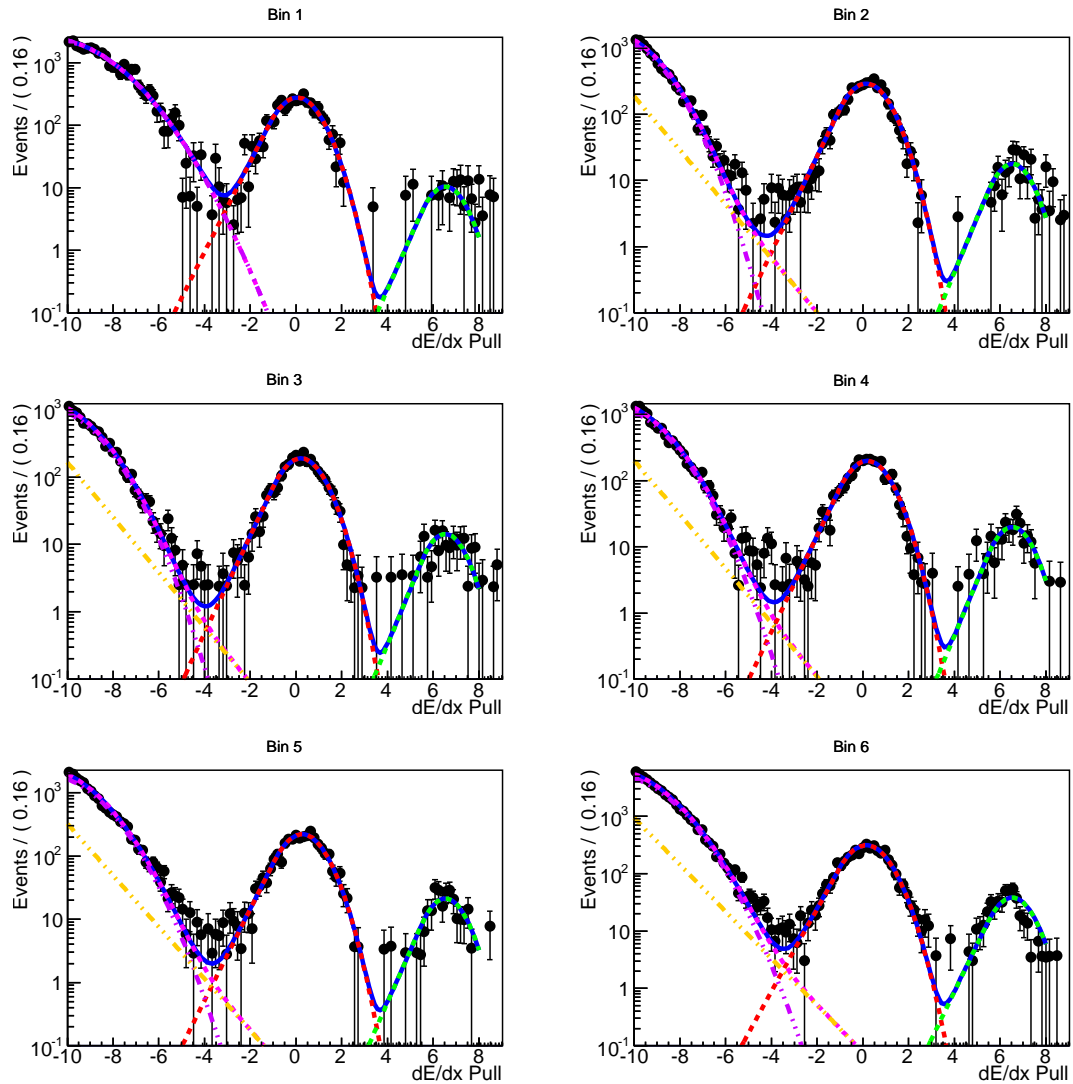
B.1.2  $\Upsilon(2S)$  on-resonance positive tracks

Figure B.3: Fit to  $\Upsilon(2S)$   $p_{CM}$  bin 1-6 for on-resonance positive tracks. The blue curve shows the total fit, the red, green, purple and yellow dotted curves the signal, triton, Gaussian and Exponential components.

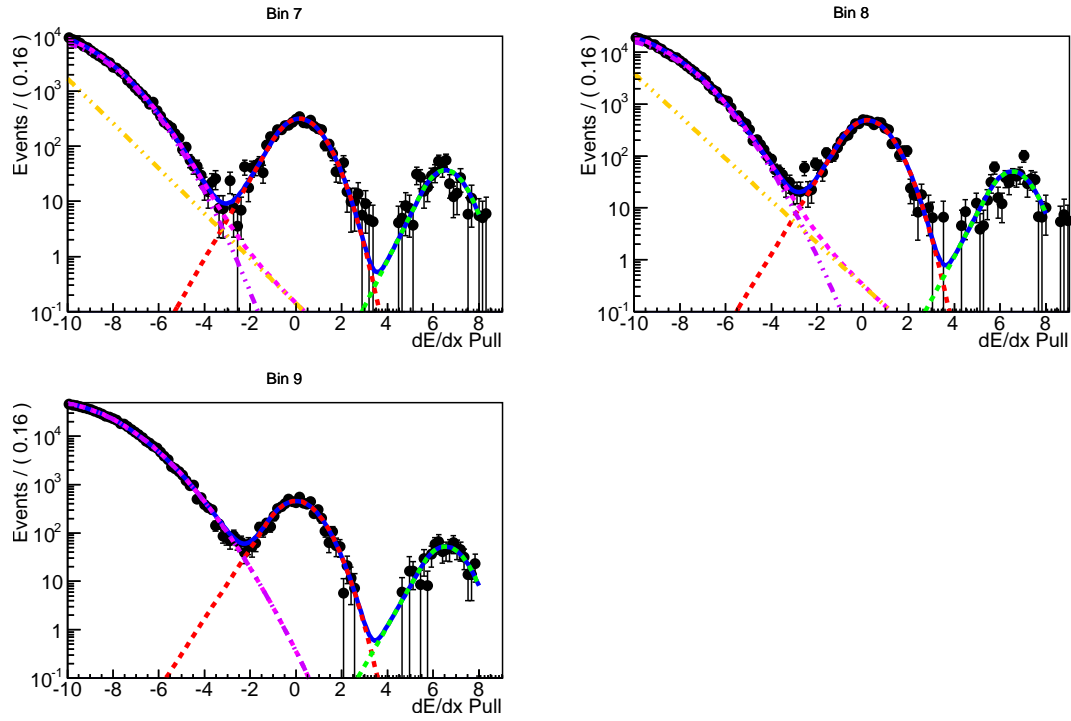


Figure B.4: Fit to  $\Upsilon(2S)$   $p_{CM}$  bin 7-9 for on-resonance positive tracks. The blue curve shows the total fit, the red, green, purple and yellow dotted curves the signal, triton, Gaussian and Exponential components.

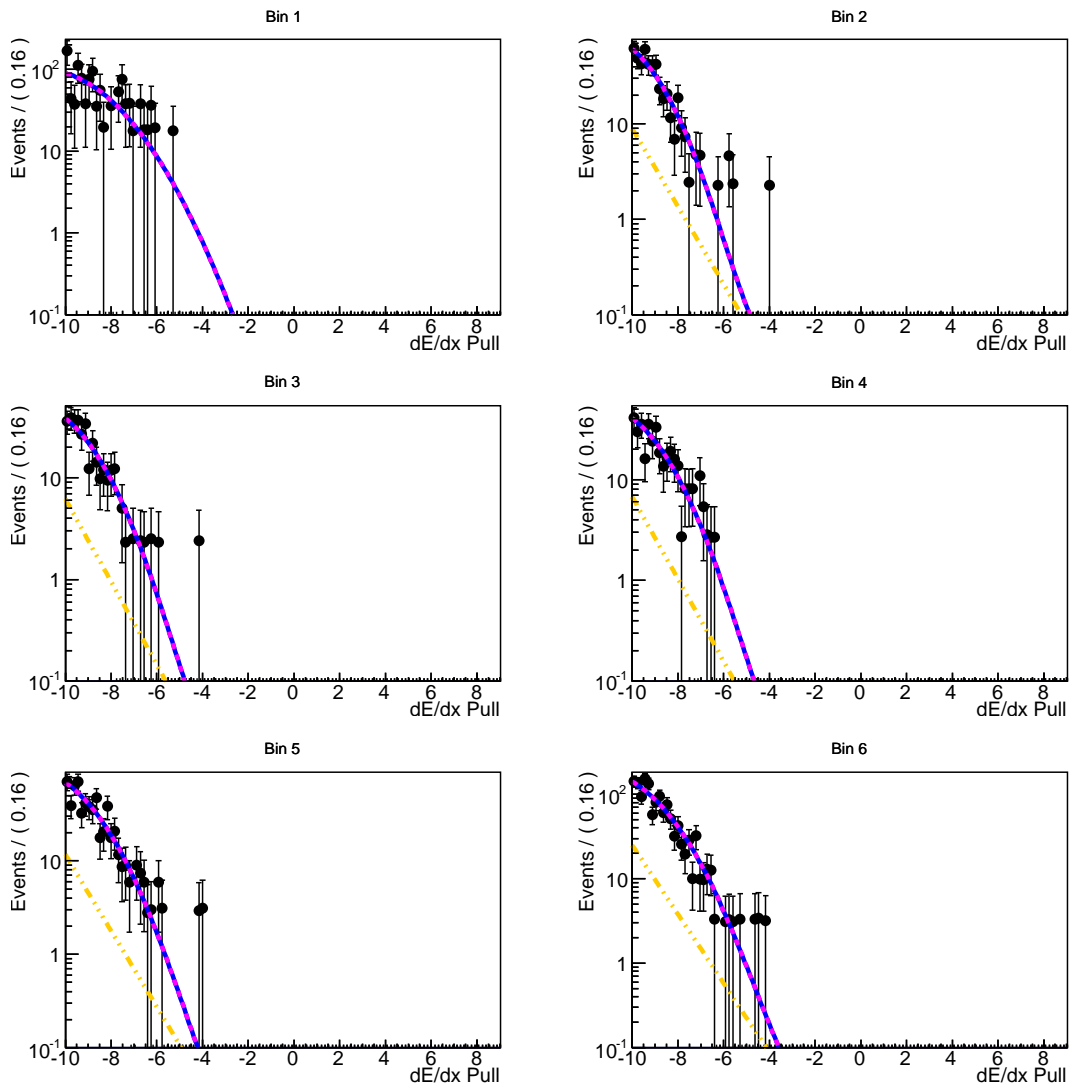
B.1.3  $\Upsilon(2S)$  off-resonance negative tracks

Figure B.5: Fit to  $\Upsilon(2S)$   $p_{\text{CM}}$  bin 1-6 for off-resonance negative tracks. The blue curve shows the total fit, the purple and yellow dotted curves the Gaussian and Exponential components.

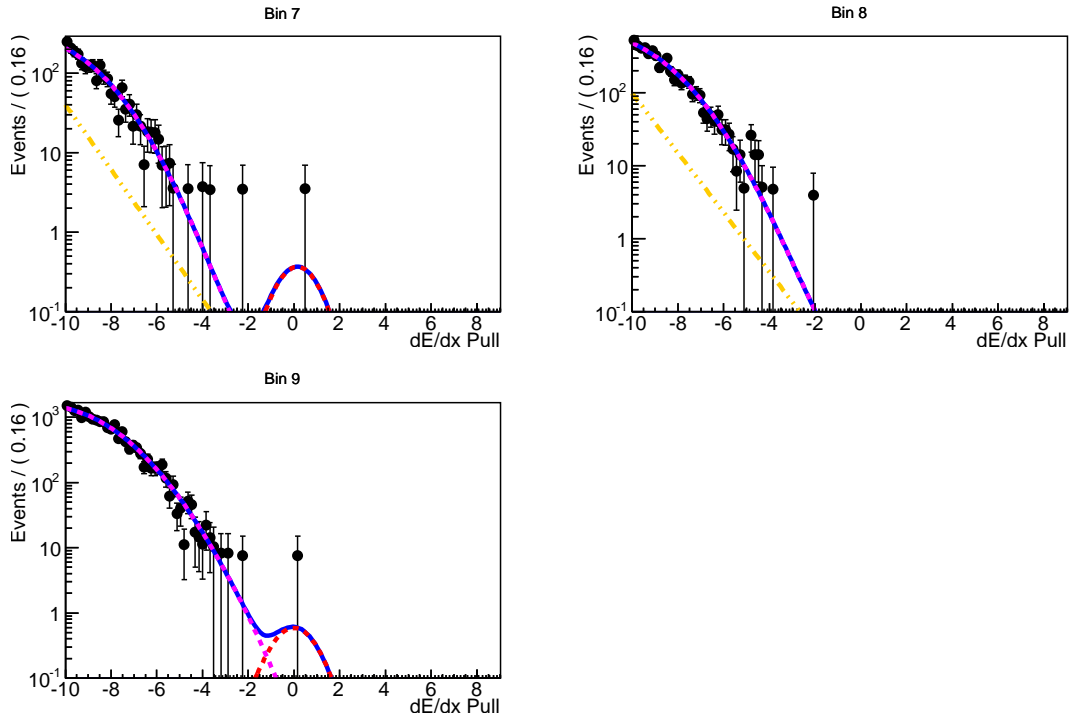


Figure B.6: Fit to  $\Upsilon(2S)$   $p_{\text{CM}}$  bin 7-9 for off-resonance negative tracks. The blue curve shows the total fit, the red, purple and yellow dotted curves the signal, Gaussian and Exponential components.

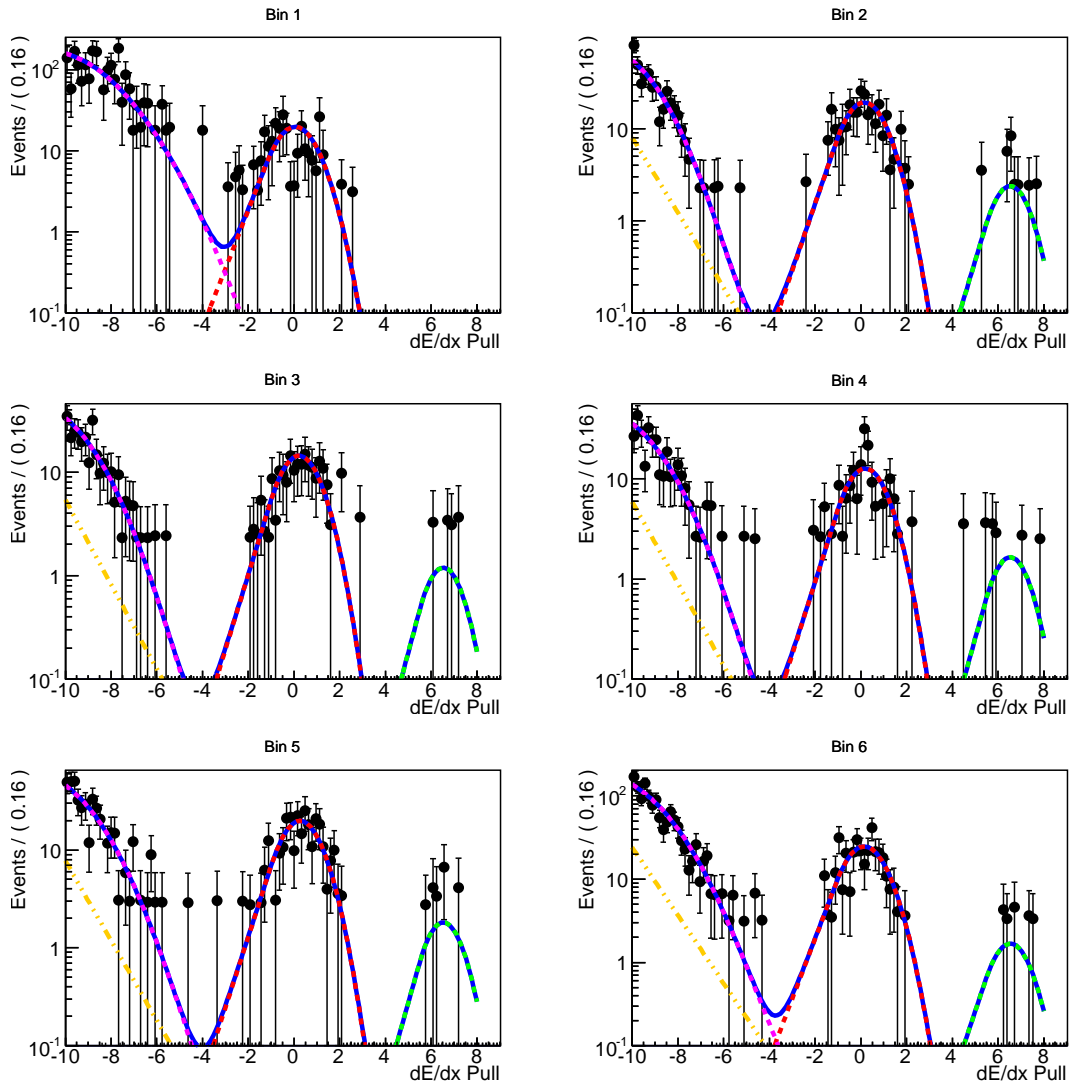
B.1.4  $\Upsilon(2S)$  off-resonance positive tracks

Figure B.7: Fit to  $\Upsilon(2S)$   $p_{CM}$  bin 1-6 for off-resonance positive tracks. The blue curve shows the total fit, the red, green, purple and yellow dotted curves the signal, triton, Gaussian and Exponential components.

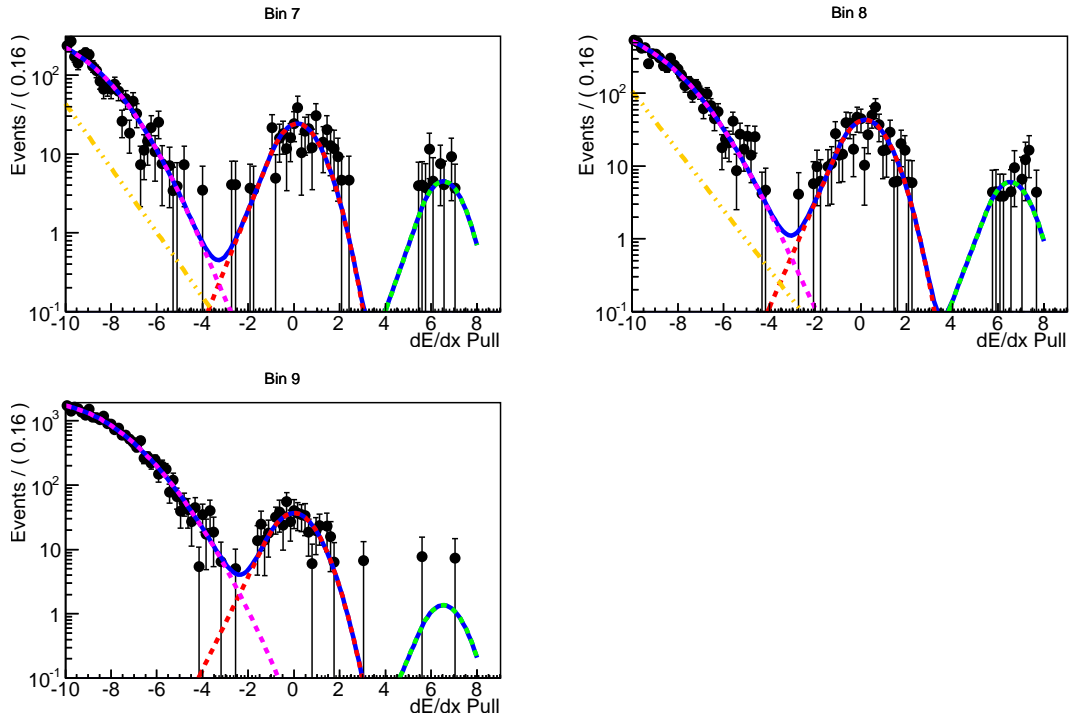


Figure B.8: Fit to  $\Upsilon(2S)$   $p_{CM}$  bin 1-6 for off-resonance positive tracks. The blue curve shows the total fit, the red, green, purple and yellow dotted curves the signal, triton, Gaussian and Exponential components.

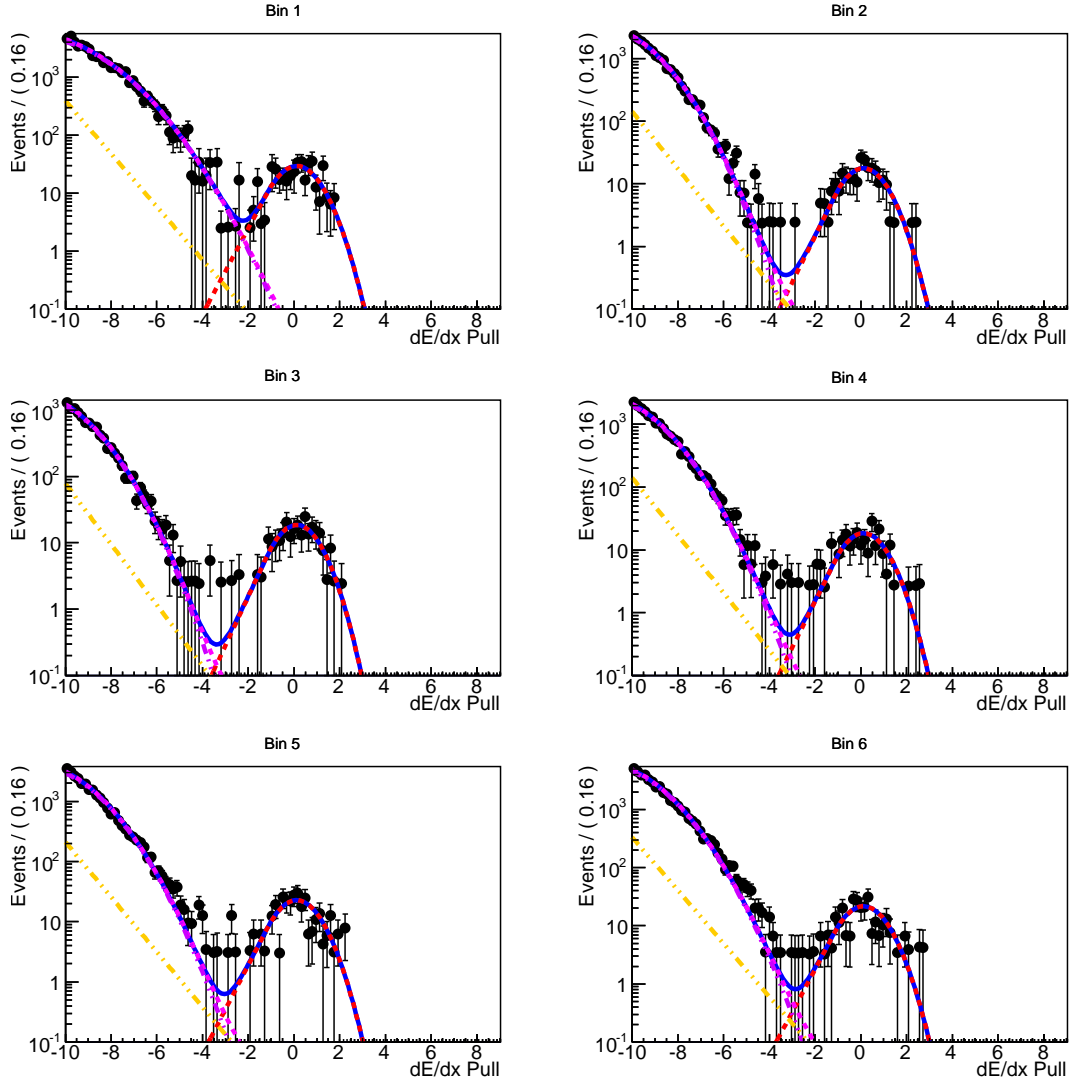
B.2  $\Upsilon(3S)$ B.2.1  $\Upsilon(3S)$  on-resonance negative tracks

Figure B.9: Fit to  $\Upsilon(3S)$   $p_{\text{CM}}$  bin 1-6 for on-resonance negative tracks. The blue curve shows the total fit, the red, purple and yellow dotted curves the signal, Gaussian and Exponential components.

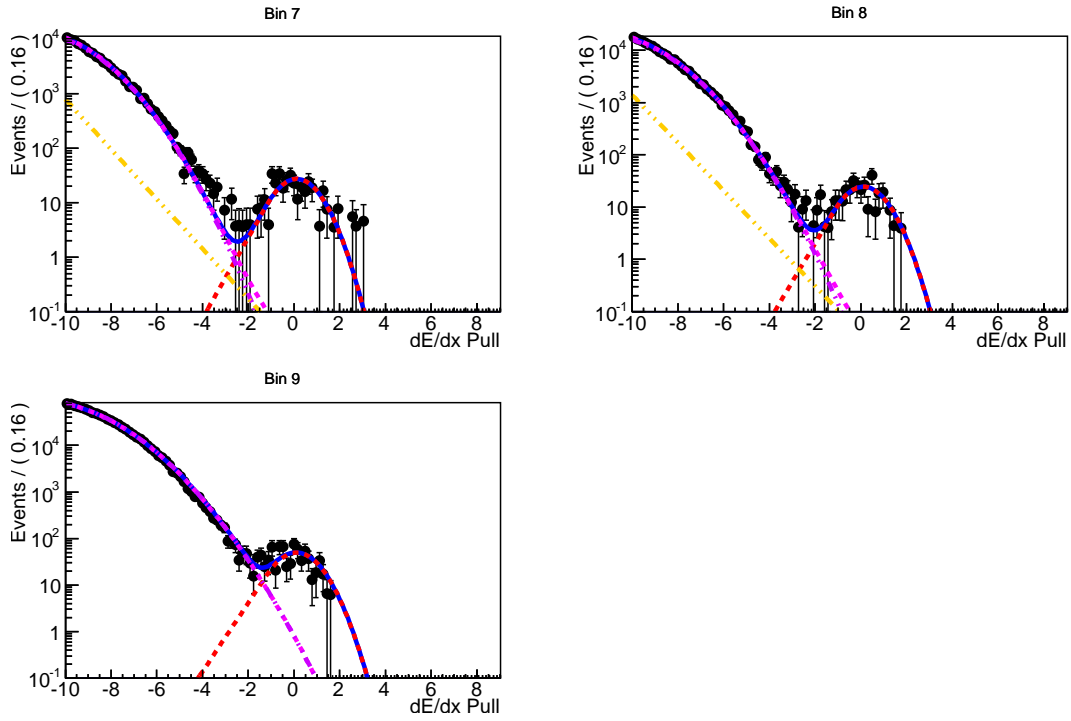


Figure B.10: Fit to  $\Upsilon(3S)$   $p_{CM}$  bin 7-9 for on-resonance negative tracks. The blue curve shows the total fit, the red, purple and yellow dotted curves the signal, Gaussian and Exponential components.

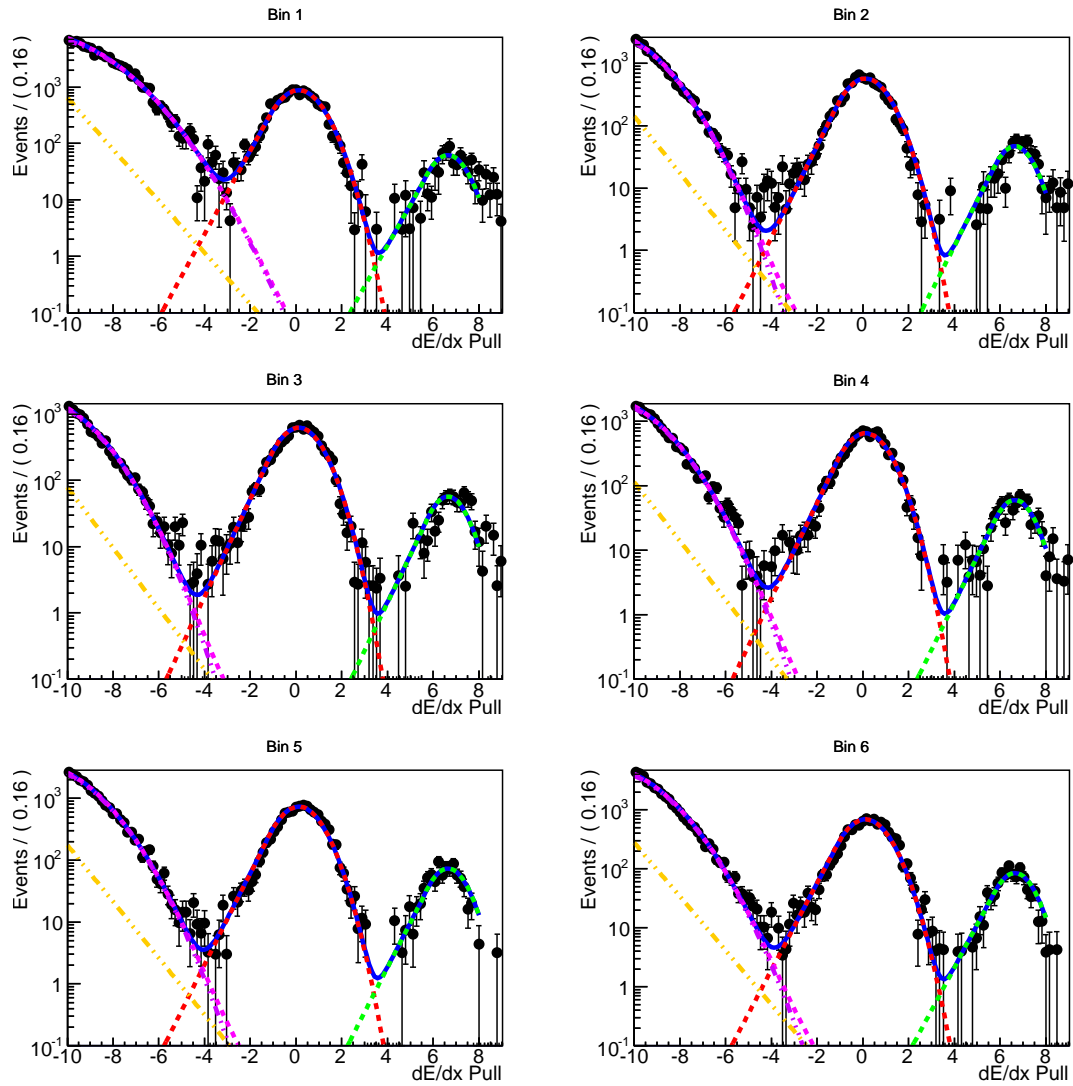
B.2.2  $\Upsilon(3S)$  on-resonance positive tracks

Figure B.11: Fit to  $\Upsilon(3S)$   $p_{CM}$  bin 1-6 for on-resonance positive tracks. The blue curve shows the total fit, the red, green, purple and yellow dotted curves the signal, triton, Gaussian and Exponential components.

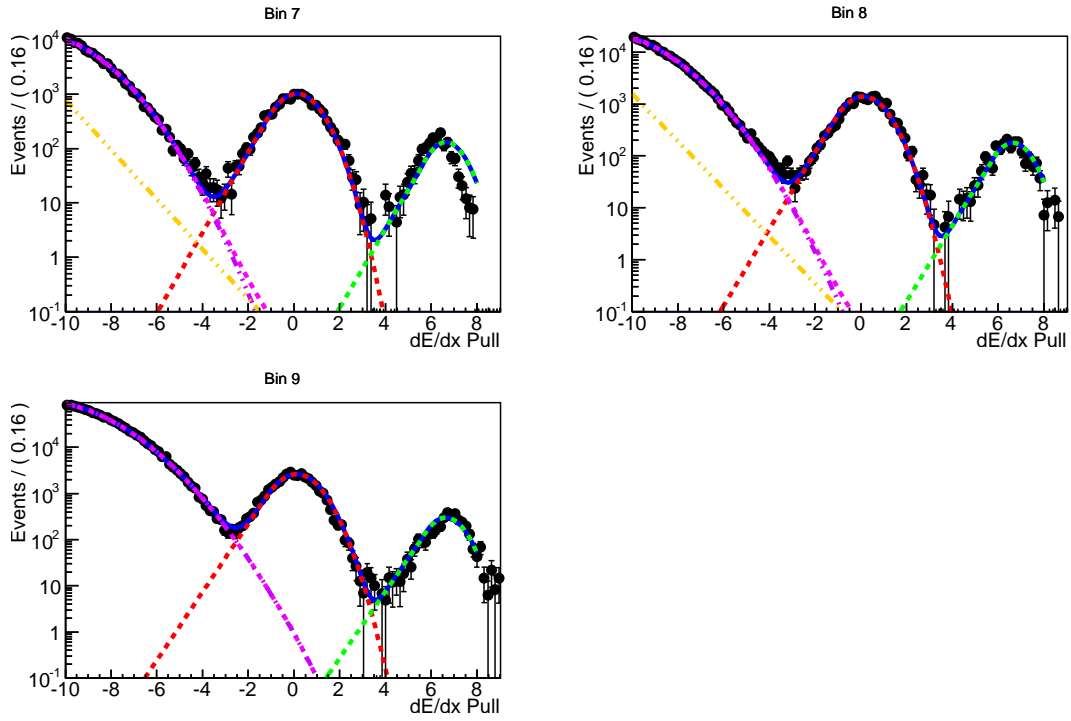


Figure B.12: Fit to  $\Upsilon(3S)$   $p_{\text{CM}}$  bin 7-9 for on-resonance positive tracks. The blue curve shows the total fit, the red, green, purple and yellow dotted curves the signal, triton, Gaussian and Exponential components.

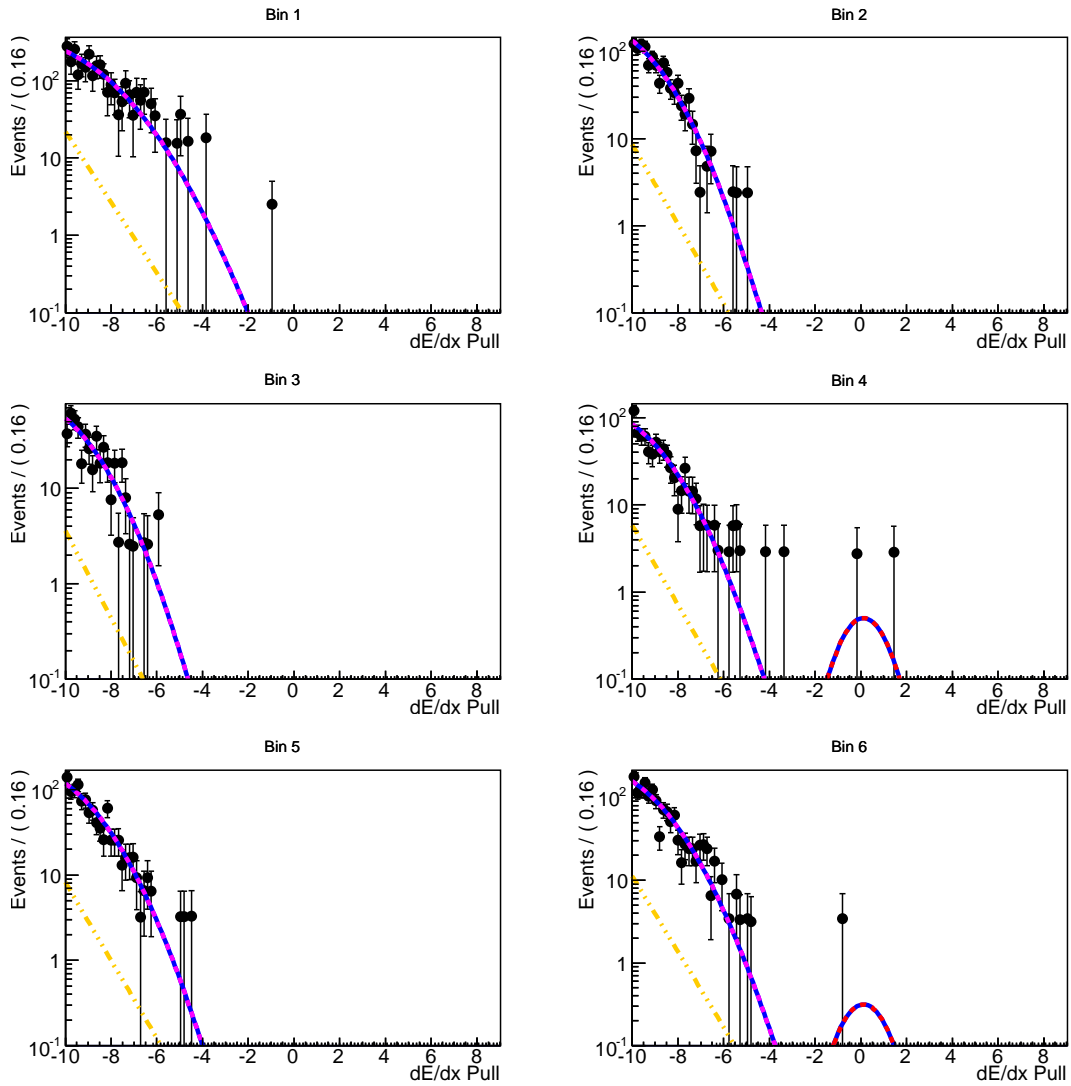
B.2.3  $\Upsilon(3S)$  off-resonance negative tracks

Figure B.13: Fit to  $\Upsilon(3S)$   $p_{CM}$  bin 1-6 for off-resonance negative tracks. The blue curve shows the total fit, the red, purple and yellow dotted curves the signal, Gaussian and Exponential components.

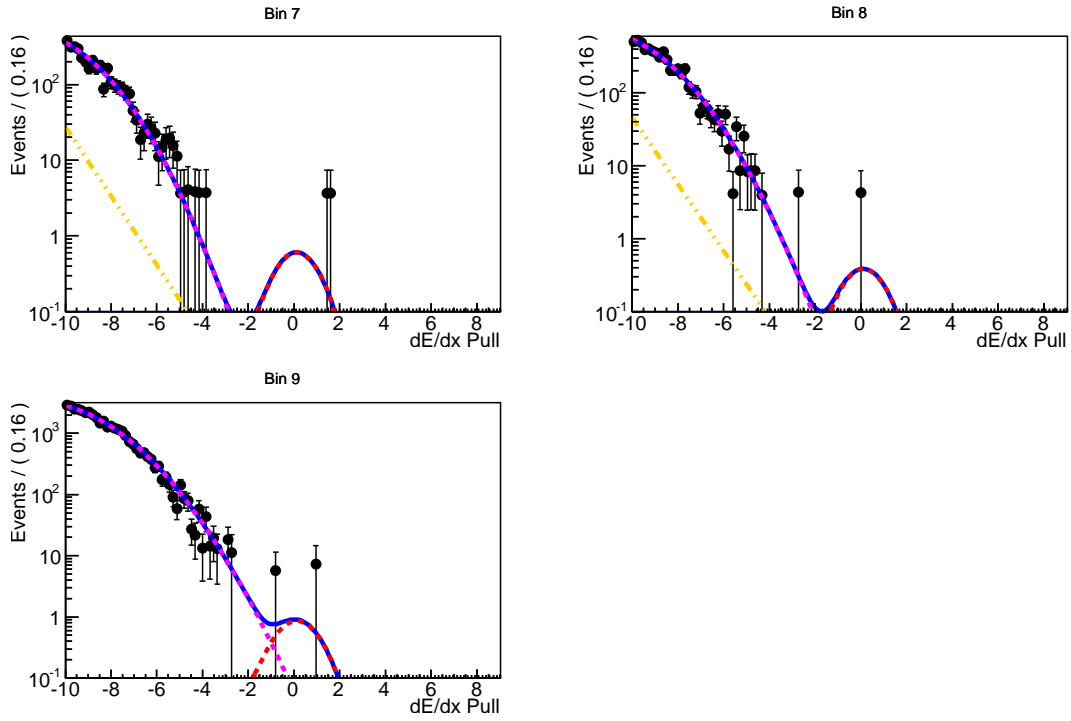


Figure B.14: Fit to  $\Upsilon(3S)$   $p_{CM}$  bin 7-9 for off-resonance negative tracks. The blue curve shows the total fit, the red, purple and yellow dotted curves the signal, Gaussian and Exponential components.

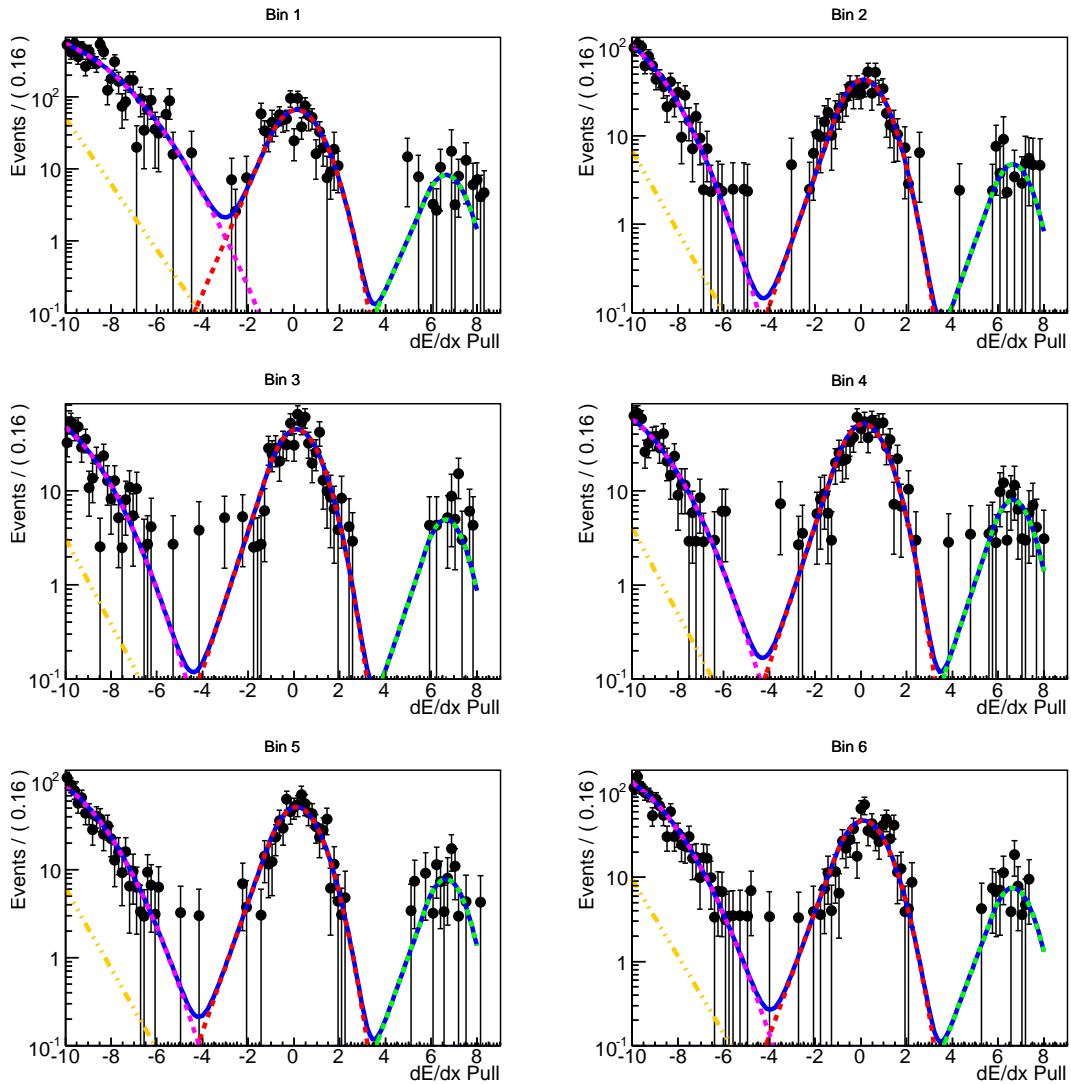
B.2.4  $\Upsilon(3S)$  off-resonance positive tracks

Figure B.15: Fit to  $\Upsilon(3S)$   $p_{CM}$  bin 1-6 for off-resonance positive tracks. The blue curve shows the total fit, the red, green, purple and yellow dotted curves the signal, triton, Gaussian and Exponential components.

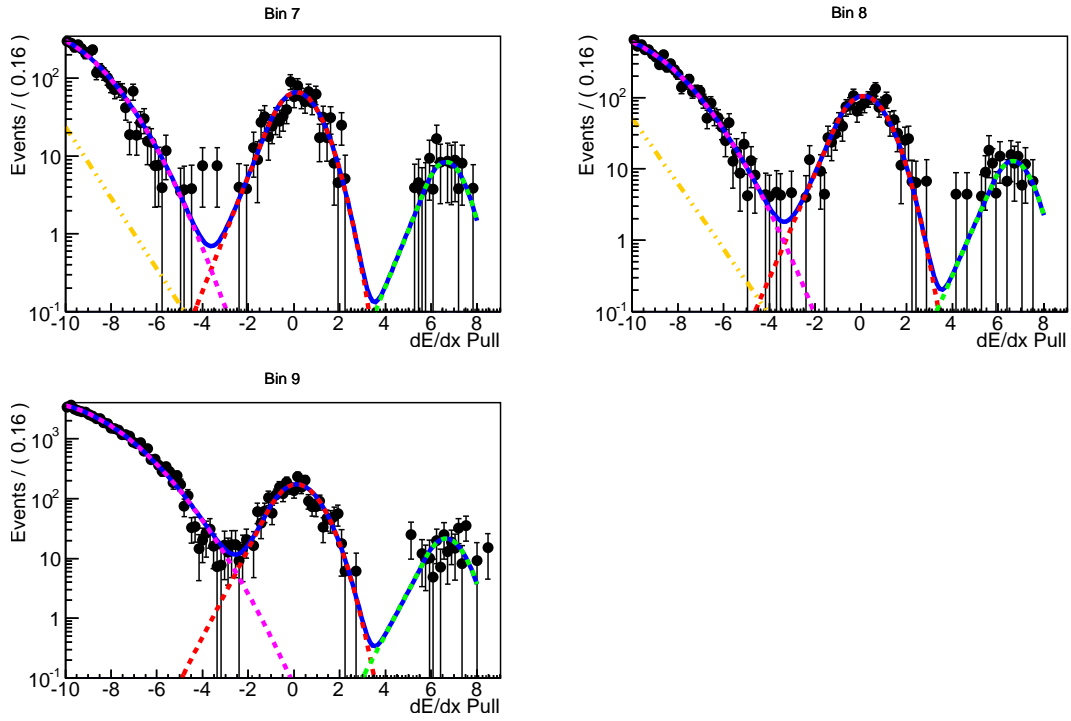


Figure B.16: Fit to  $\Upsilon(3S)$   $p_{CM}$  bin 1-6 for off-resonance positive tracks. The blue curve shows the total fit, the red, green, purple and yellow dotted curves the signal, triton, Gaussian and Exponential components.

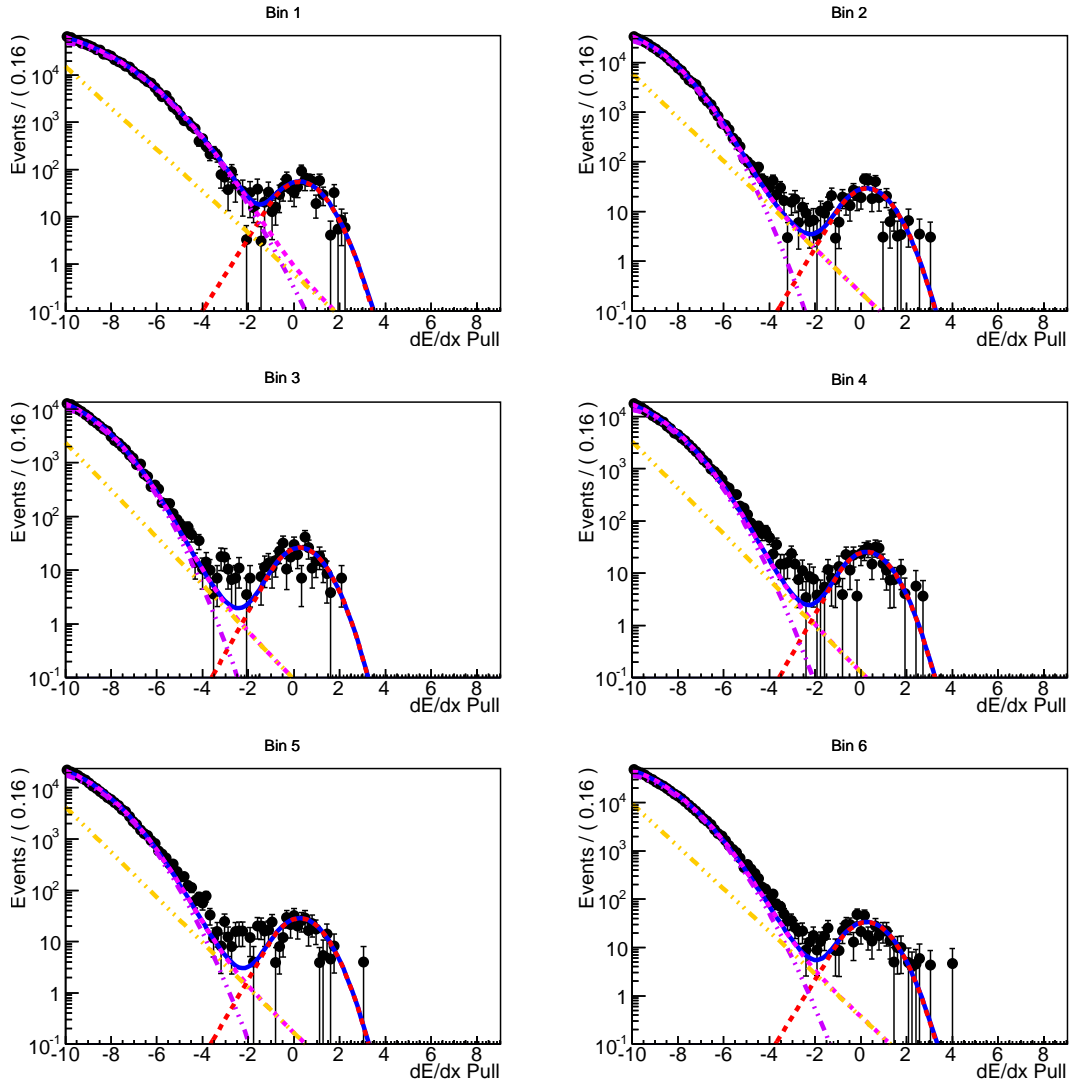
B.3  $\Upsilon(4S)$  and ContinuumB.3.1  $\Upsilon(4S)$  and Continuum on-resonance negative tracks

Figure B.17: Fit to  $\Upsilon(4S)$  data  $p_{CM}$  bin 1-6 for on-resonance negative tracks. The blue curve shows the total fit, the red, purple and yellow dotted curves the signal, Gaussian and Exponential components.

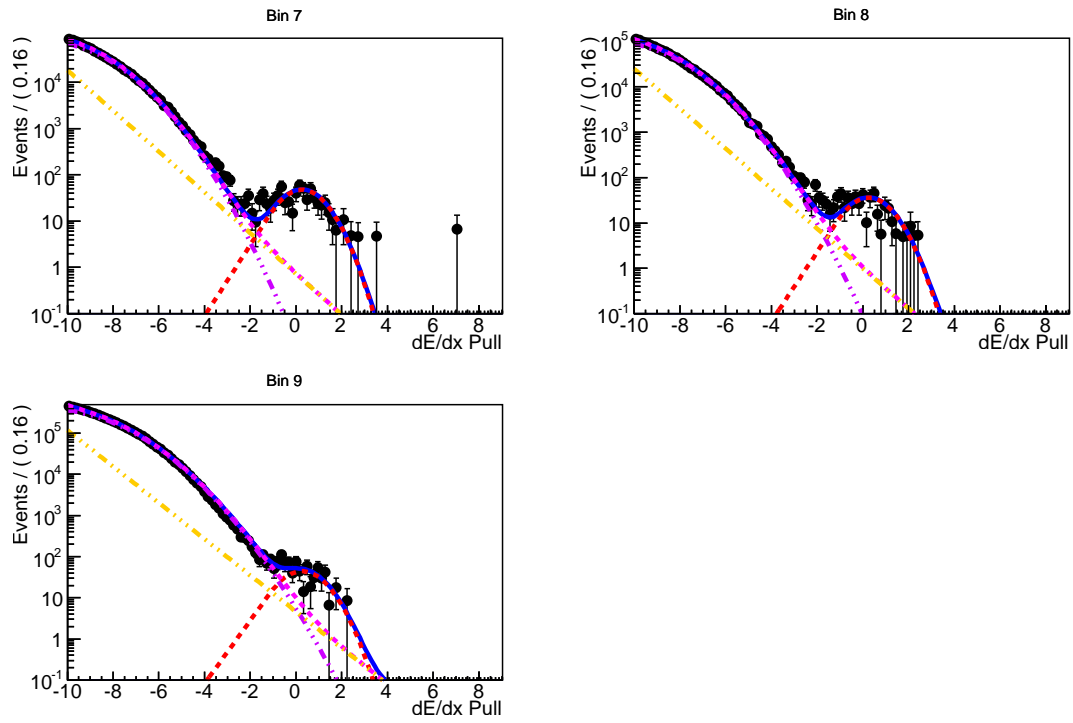


Figure B.18: Fit to  $\Upsilon(4S)$  data  $p_{CM}$  bin 7-9 for on-resonance negative tracks. The blue curve shows the total fit, the red, purple and yellow dotted curves the signal, Gaussian and Exponential components.

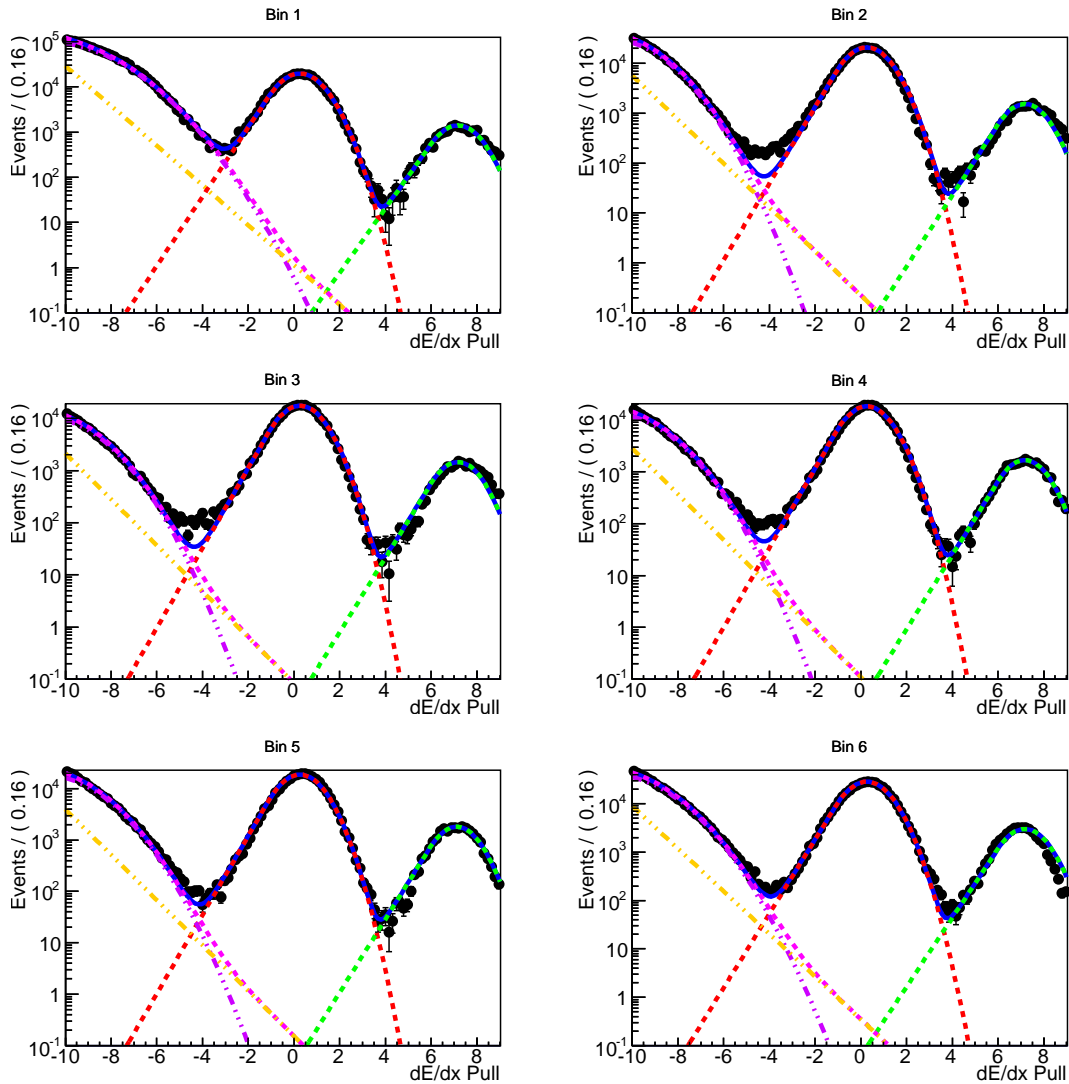
B.3.2  $\Upsilon(4S)$  and Continuum on-resonance positive tracks

Figure B.19: Fit to  $\Upsilon(4S)$  data  $p_{CM}$  bin 1-6 for on-resonance positive tracks. The blue curve shows the total fit, the red, green, purple and yellow dotted curves the signal, triton, Gaussian and Exponential components.

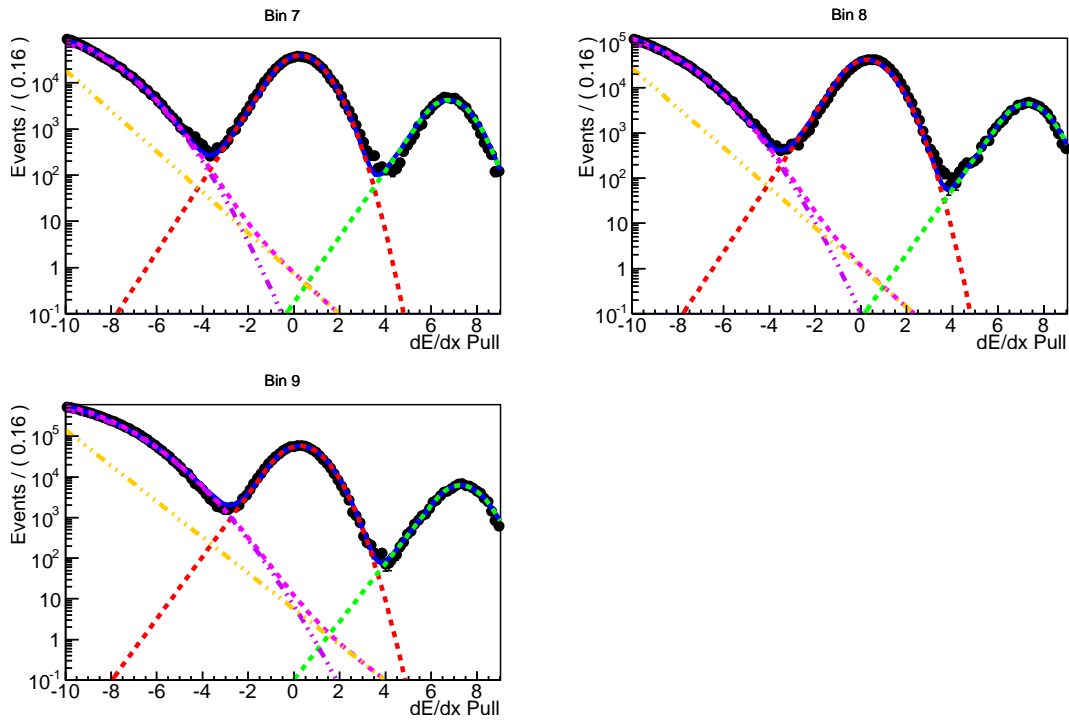


Figure B.20: Fit to  $\Upsilon(4S)$  data  $p_{CM}$  bin 7-9 for on-resonance positive tracks. The blue curve shows the total fit, the red, green, purple and yellow dotted curves the signal, triton, Gaussian and Exponential components.

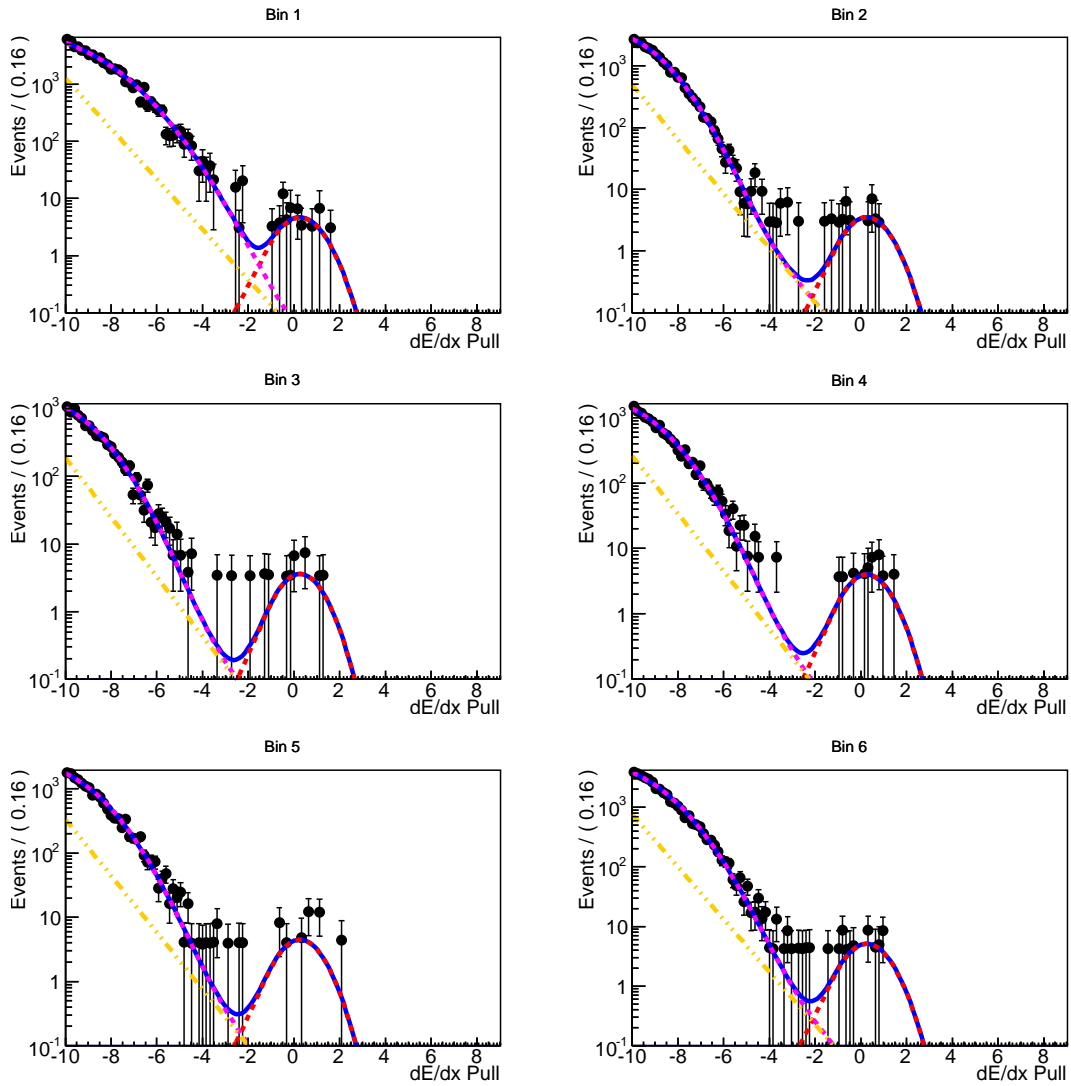
B.3.3  $\Upsilon(4S)$  and continuum off-resonance negative tracks

Figure B.21: Fit to  $\Upsilon(4S)$  data  $p_{CM}$  bin 1-6 for off-resonance negative tracks. The blue curve shows the total fit, the red, purple and yellow dotted curves the signal, Gaussian and Exponential components.

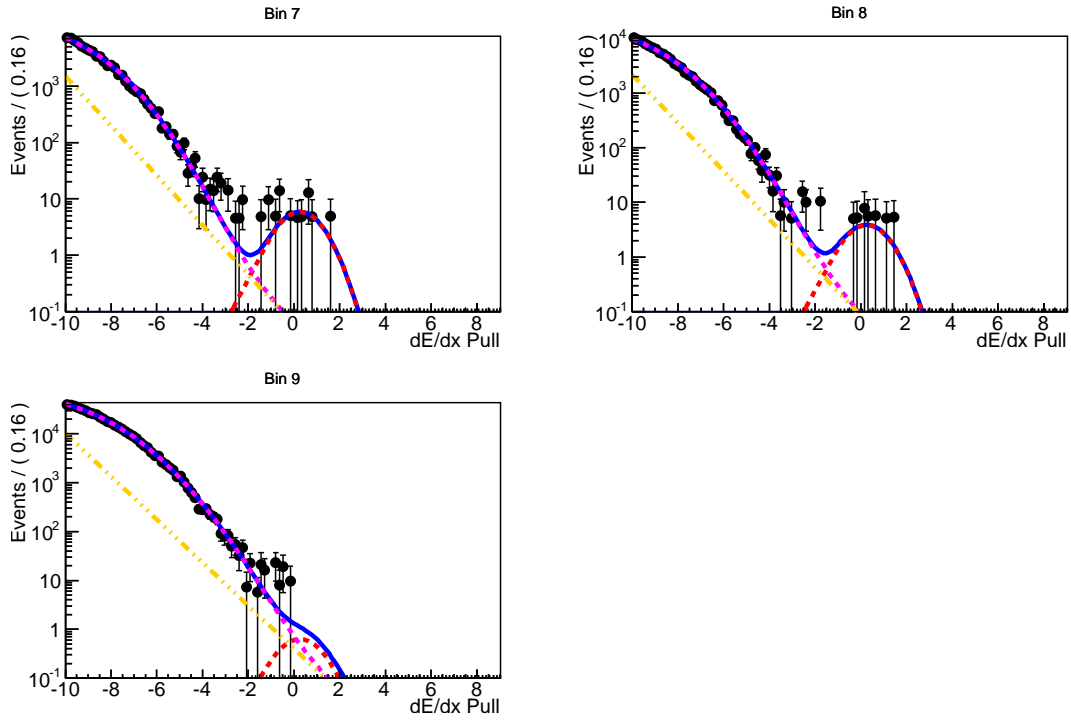


Figure B.22: Fit to  $\Upsilon(4S)$  data  $p_{CM}$  bin 7-9 for off-resonance negative tracks. The blue curve shows the total fit, the red, purple and yellow dotted curves the signal, Gaussian and Exponential components.

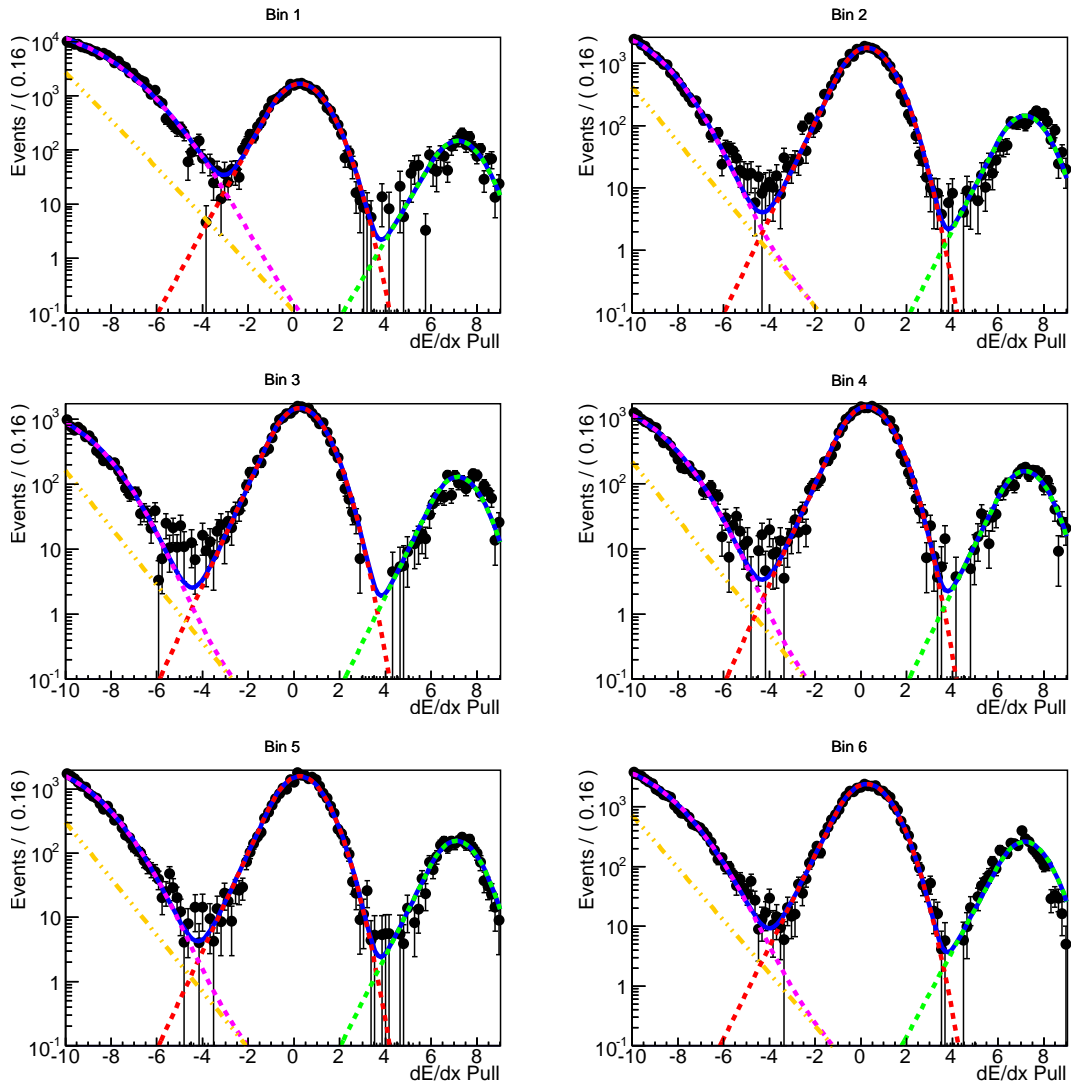
B.3.4  $\Upsilon(4S)$  and continuum off-resonance positive tracks

Figure B.23: Fit to  $\Upsilon(4S)$  data  $p_{CM}$  bin 1-6 for off-resonance positive tracks. The blue curve shows the total fit, the red, green, purple and yellow dotted curves the signal, triton, Gaussian and Exponential components.

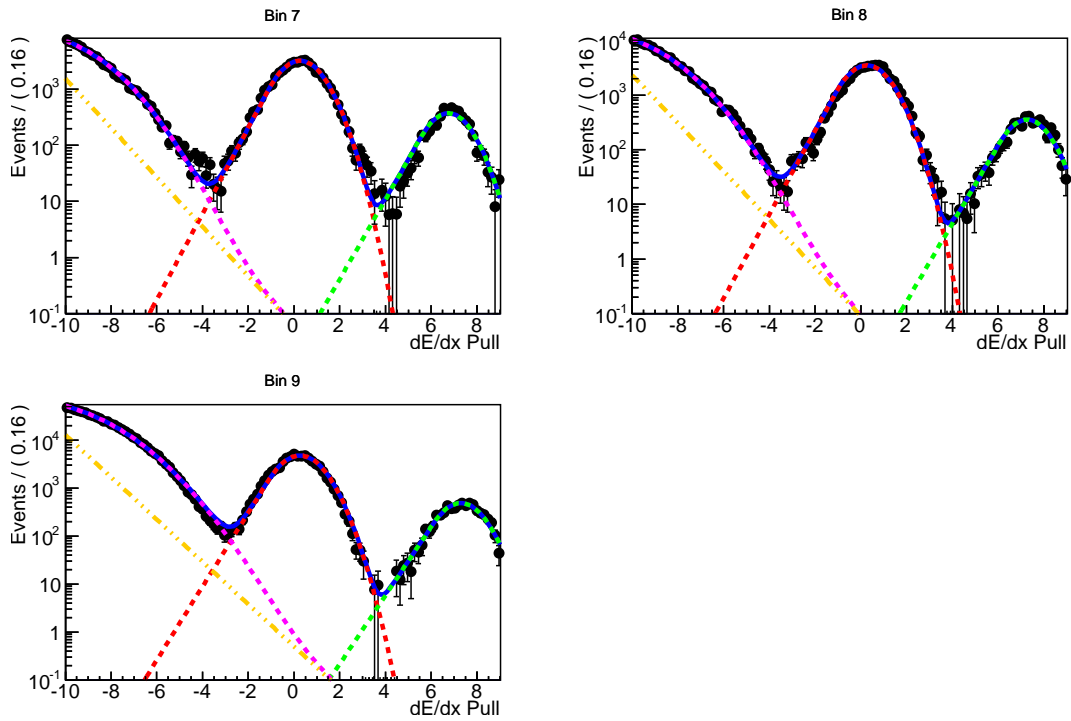


Figure B.24: Fit to  $\Upsilon(4S)$  data  $p_{\text{CM}}$  bin 1-6 for off-resonance positive tracks. The blue curve shows the total fit, the red, green, purple and yellow dotted curves the signal, triton, Gaussian and Exponential components.

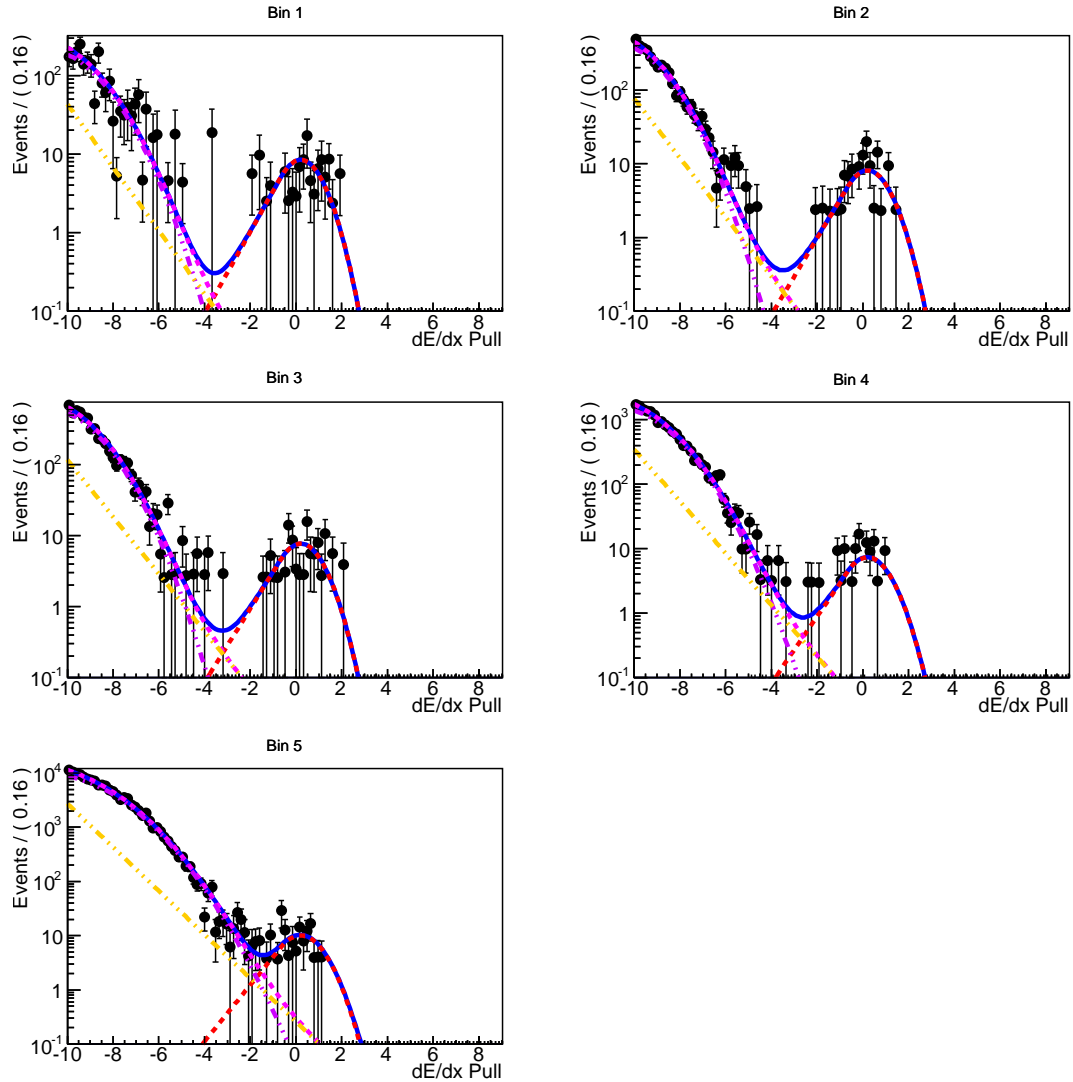
B.4  $\Upsilon(1S)$ B.4.1  $\Upsilon(1S)$  signal region negative tracks

Figure B.25: Fit to  $\Upsilon(1S)$   $p_{CM}$  bin 1-6 for negative tracks in the signal region. The blue curve shows the total fit, the red, purple and yellow dotted curves the signal, Gaussian and Exponential components.

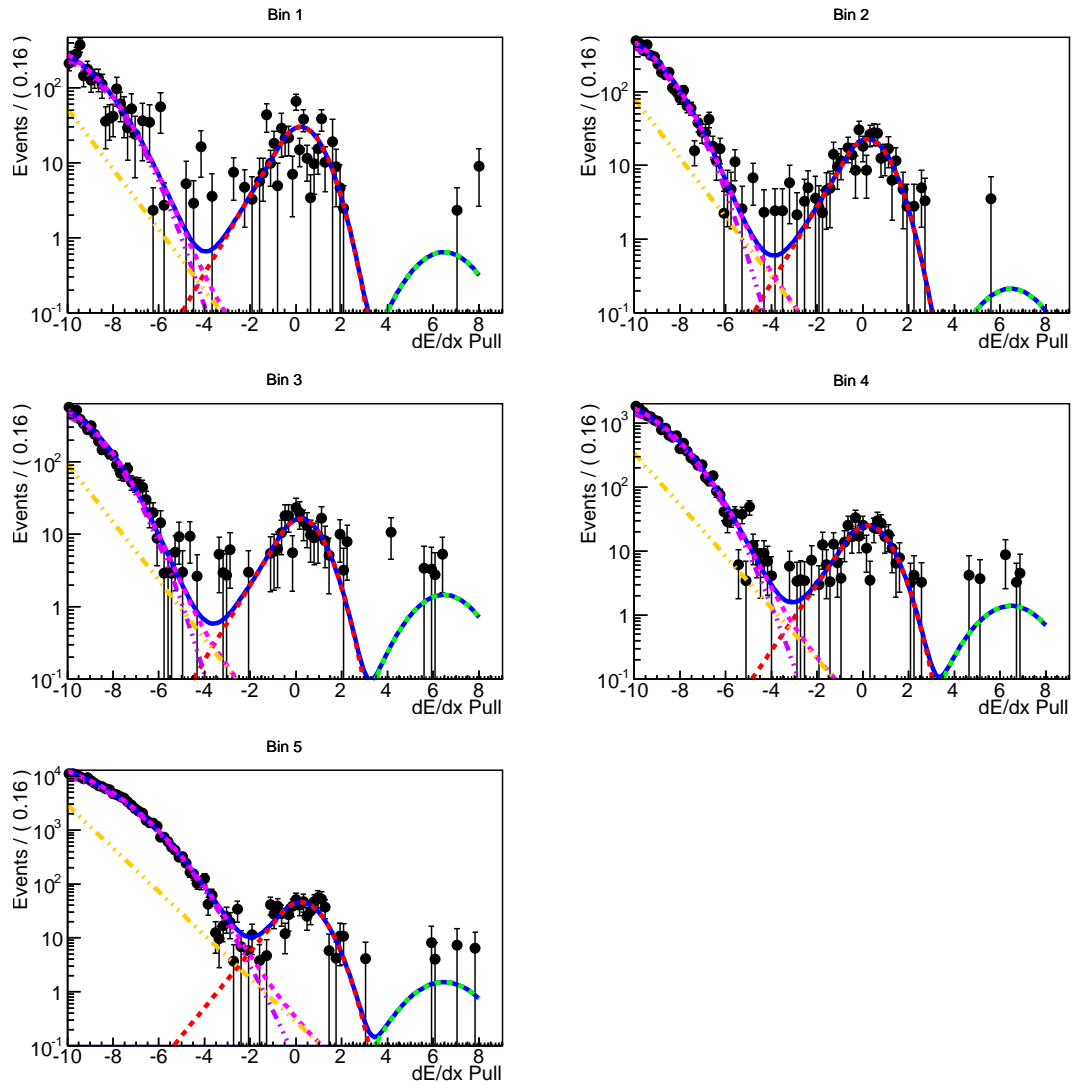
B.4.2  $\Upsilon(1S)$  signal region positive tracks

Figure B.26: Fit to  $\Upsilon(1S)$   $p_{CM}$  bin 1-6 for positive tracks in the signal region. The blue curve shows the total fit, the red, purple and yellow dotted curves the signal, Gaussian and Exponential components.

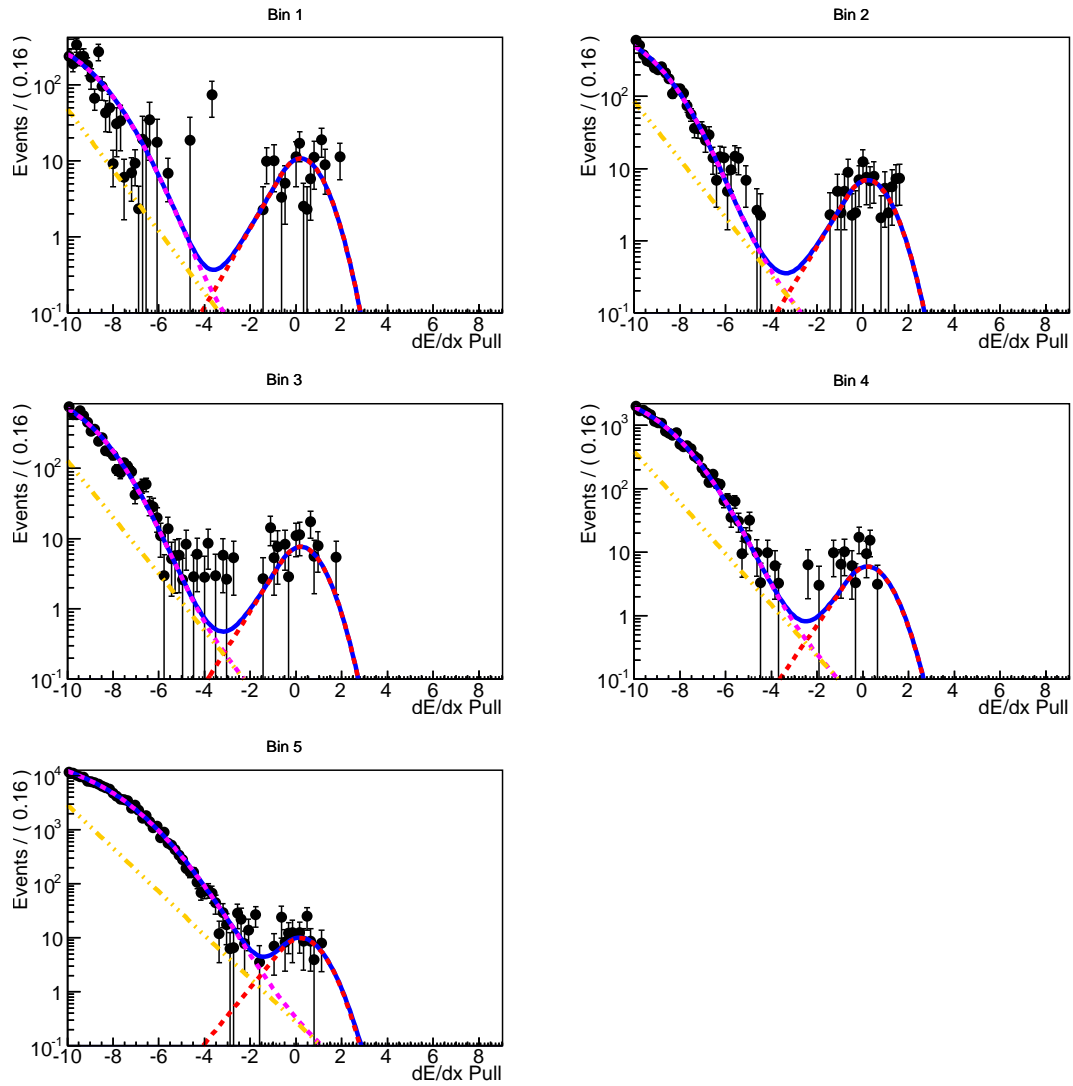
B.4.3  $\Upsilon(1S)$  sideband negative tracks

Figure B.27: Fit to  $\Upsilon(1S)$   $p_{CM}$  bin 1-6 for negative tracks in the sideband region. The blue curve shows the total fit, the red, purple and yellow dotted curves the signal, Gaussian and Exponential components.

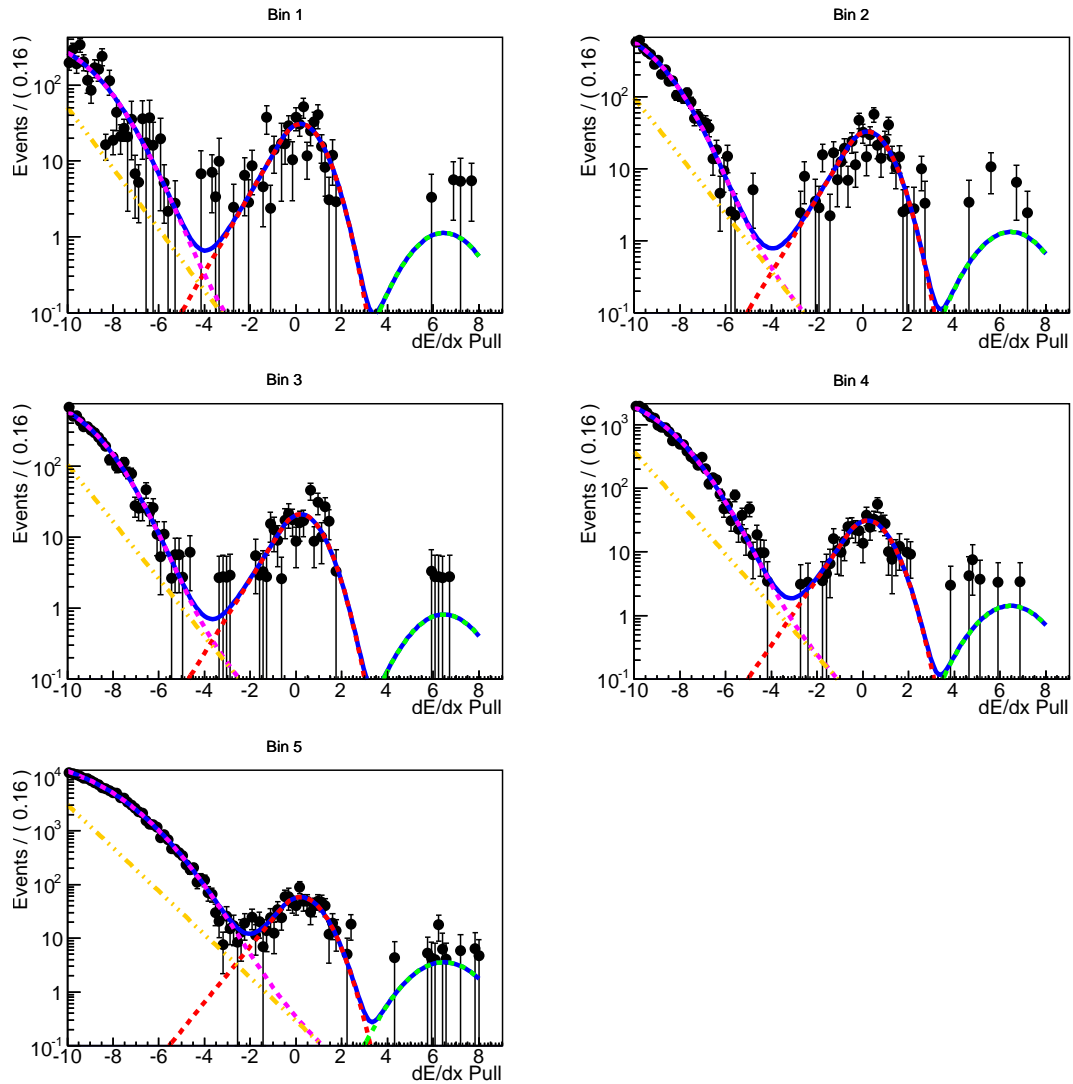
B.4.4  $\Upsilon(1S)$  sideband positive tracks

Figure B.28: Fit to  $\Upsilon(1S)$   $p_{\text{CM}}$  bin 1-6 for positive tracks in the sideband region. The blue curve shows the total fit, the red, purple and yellow dotted curves the signal, Gaussian and Exponential components.

## Bibliography

- [1] D. Besson and T. Skwarnicki, Annual Review of Nuclear and Particle Science **43**, 333 (1993).
- [2] S. Glashow, Nucl.Phys. **22**, 579 (1961).
- [3] S. Weinberg, Phys.Rev.Lett. **19**, 1264 (1967).
- [4] A. Salam, Weak and electromagnetic interactions, in *Proceedings of 8th Nobel Symposium, Lerum, Sweden*.
- [5] P. Higgs, Phys.Rev.Lett. **12**, 132 (1964).
- [6] P. Higgs, Phys.Rev. **145**, 1156 (1966).
- [7] F. Englert and R. Brout, Phys.Rev.Lett. **13**, 321 (1964).
- [8] H. C. Guralnik, G.S. and T. Kibble, Phys.Rev.Lett. **13**, 585 (1964).
- [9] N. Cabibbo, Phys.Rev.Lett. **10**, 531 (1963).
- [10] S. Glashow, J. Iliopoulos, and L. Maiani, Phys.Rev. **D2**, 1285 (1970).
- [11] M. Kobayashi and T. Maskawa, Prog.Theor.Phys. **49**, 652 (1973).
- [12] Particle Data Group, J. Beringer *et al.*, Phys.Rev. **D86**, 010001 (2012).
- [13] Particle Data Group, K. Nakamura *et al.* *Review of particle physics* Vol. G37 (, 2010).
- [14] (Super-Kamiokande Collaboration), Y. Fukuda *et al.*, Phys. Rev. Lett. **81**, 1562 (1998).
- [15] G. K. Yeghiyan, Phys.Rev. **D80**, 115019 (2009), arXiv:0909.4919.
- [16] B. Echenard, Mod.Phys.Lett. **A27**, 1230016 (2012), arXiv:1205.3505.
- [17] L. Dal and M. Kachelriess, (2012), arXiv:1207.4560.
- [18] Y. Cui, J. Mason, and L. Randall, Journal of High Energy Physics , 1 (2010).
- [19] ALEPH Collaboration, S. Schael *et al.*, Phys.Lett. **B639**, 192 (2006), arXiv:hep-ex/0604023.
- [20] B. Aubert *et al.*, Nucl.Instrum.Meth. **A479**, 1 (2002).
- [21] BABAR LST Group, W. Menges, IEEE Nucl. Sci. Symp. Conf. Rec. **5**, 1470 (2006), arXiv:physics/0609039.

- [22] G. C. Fox and S. Wolfram, *Phys.Rev.Lett.* **41**, 1581 (1978).
- [23] E. C. D.N. Brown and D. Roberts, The *BABAR* track fitting algorithm, in *Proceedings of CHEP 2000, Padova, Italy*, 2000.
- [24] T. Allmendinger *et al.*, (2012), arXiv:1207.2849.
- [25] D. Lange, *Nucl.Instrum.Meth.* **A462**, 152 (2001).
- [26] T. Sjostrand, *Comput.Phys.Commun.* **82**, 74 (1994).
- [27] S. Jadach, B. Ward, and Z. Was, *Comput.Phys.Commun.* **130**, 260 (2000), arXiv:hep-ph/9912214.
- [28] GEANT4, S. Agostinelli *et al.*, *Nucl.Instrum.Meth.* **A506**, 250 (2003).
- [29] *BABAR*, J. P. Burke *et al.*, *BABAR Analysis Document* **2186** (2011).
- [30] *BABAR* Collaboration, B. Aubert *et al.*, *Phys.Rev.Lett.* **103**, 161801 (2009), arXiv:0903.1124.
- [31] *BABAR* Collaboration, B. Aubert *et al.*, *Phys.Rev.Lett.* **102**, 012001 (2009), arXiv:0809.4120.
- [32] CLEO Collaboration, G. S. Huang *et al.*, *Phys. Rev. D* **75**, 012002 (2007).
- [33] N. Törnqvist, *Phys.Rev.Lett.* **53**, 878 (1984).
- [34] CLEO Collaboration, A. H. Mahmood *et al.*, *Phys. Rev. D* **70**, 032003 (2004).
- [35] *BABAR* Collaboration, B. Aubert *et al.*, *Phys. Rev. D* **74**, 091105 (2006).
- [36] Belle Collaboration, P. Urquijo *et al.*, *Phys. Rev. D* **75**, 032001 (2007).
- [37] ALEPH Collaboration, D. Buskulic *et al.*, *Physics Letters B* **361**, 221 (1995).
- [38] *BABAR* Collaboration, B. Aubert *et al.*, *Phys. Rev. D* **69**, 052005 (2004).
- [39] M. Gronau and J. L. Rosner, *Phys.Rev.* **D83**, 034025 (2011), arXiv:1012.5098.
- [40] I. Bigi, T. Mannel, and N. Uraltsev, *JHEP* **1109**, 012 (2011), arXiv:1105.4574.
- [41] ARGUS Collaboration, H. Albrecht *et al.*, *Phys.Lett.* **B236**, 102 (1990).
- [42] CLEO, D. M. Asner *et al.*, *Phys. Rev. D* **75**, 012009 (2007), arXiv:hep-ex/0612019.
- [43] Gorin and others, *Soviet J. of Nucl. Phys.* **13**, 334 (1972).
- [44] *BABAR*, C. Hearty and G. D. Mcgregor, *BABAR Analysis Document* **2069** (2008).
- [45] *BABAR*, C. Hearty and G. D. Mcgregor, *BABAR Analysis Document* **2126** (2008).